# Aerodynamic Phenomena of Propeller-Wing-Flap Interaction

Duivenvoorden, R.R.

**Important note**
To cite this publication, please use the final published version (if applicable).
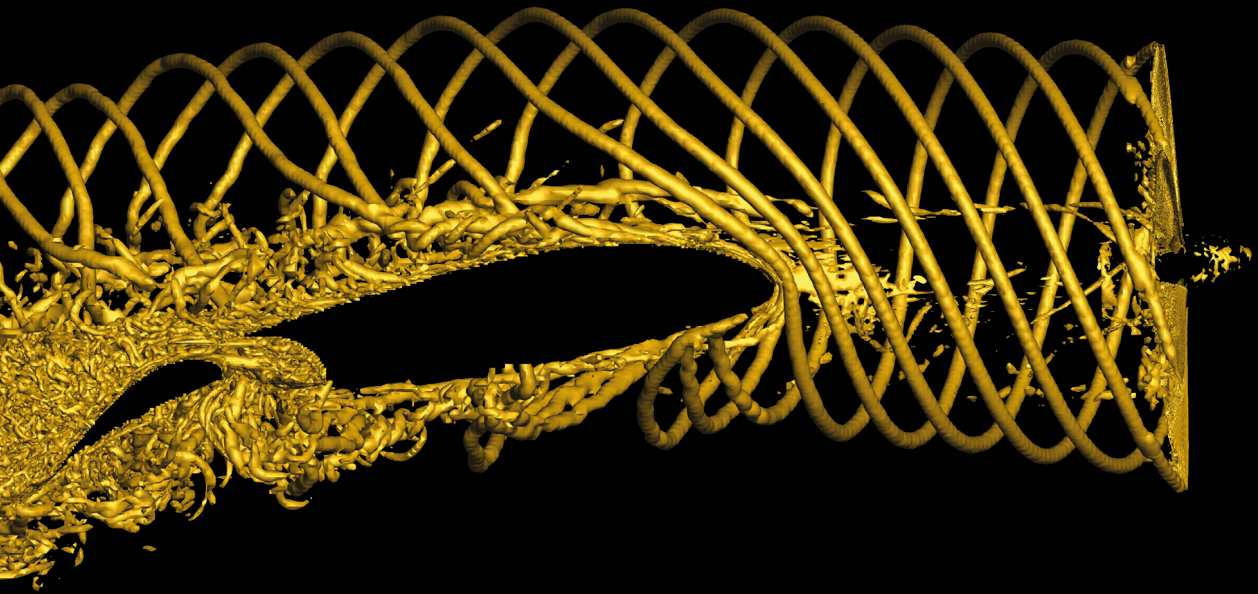Please check the document version above.

# Aerodynamic Phenomena of Propeller-Wing-Flap Interaction

R.R. Duivenvoorden

# Aerodynamic Phenomena of Propeller-Wing-Flap Interaction

# Aerodynamic Phenomena of Propeller-Wing-Flap Interaction

## Dissertation

for the purpose of obtaining the degree of doctor
at the Delft University of Technology,
by the authority of Rector Magnificus prof. dr. ir. T.H.J.J. van der Hagen,
chair of the Board of Doctorates,
to be defended publicly on June 5th 2025 at 15.00h.

by

## Ramon Robert Duivenvoorden

Master of Science in Aerospace Engineering
Delft University of Technology, Delft, The Netherlands,
born in Uden, The Netherlands.

This dissertation has been approved by the promotor and co-promotor.

Composition of the doctoral committee:

| | |
|---|---|
| Rector Magnificus, | Chairperson |
| Prof. dr. ir. L.L.M. Veldhuis, | Delft University of Technology (*promotor*) |
| Dr. ir. T. Sinnige, | Delft University of Technology (*co-promotor*) |

*Independent members:*

| | |
|---|---|
| Prof. dr. M. Kostonis, | Delft University of Technology |
| Prof. Dr.-Ing. J. Weiss, | Technical University Berlin, Germany |
| Prof. dr. T. Leweke | IRPHÉ, France |
| Dr. M. Felli | Institute of Marine Engineering, Italy |
| Prof. Dr.-Ing. G. Eitelberg, | Delft University of Technology, *reserve member* |

*Other members:*

| | |
|---|---|
| Prof. Dr.-Ing. J. Friedrichs, | Technical University Braunschweig, Germany |

Prof. Dr.-Ing. J. Friedrichs has contributed significantly to the preparation of this dissertation.

*"People who can change and change again are so much more reliable and happier than those who can't."*

- Stephen Fry

# SUMMARY

As the aviation industry faces growing environmental challenges, there is a critical push for innovations to reduce its climate impact. Advances in propeller technology present a promising, more efficient alternative to traditional turbofans, especially for short to medium-range flights. Propellers offer high propulsive efficiency and flexibility, though they pose challenges like increased noise and performance limitations at higher speeds. Recent developments explore propeller integration into airframes to harness aerodynamic benefits, such as distributed propeller systems that enhance lift during take-off. The design of such integrations requires a comprehensive understanding of the highly complex flow dynamics involved in the interaction between a propeller, wing, and flap.

The objective of this dissertation is therefore to *characterise the phenomena and mechanisms that govern the aerodynamic interaction between a propeller, wing, and flap.* The propeller-wing-flap aerodynamic interaction can be viewed as a combination of two fields which are already established in literature: propeller-wing aerodynamic interaction and multi-element airfoil aerodynamics. Using these foundations, the present research approaches the problem from two perspectives: the extension of propeller-wing interaction to include a flap, and the influence of a non-uniform flowfield induced by a propeller on the aerodynamics of a multi-element airfoil. Special attention is paid to the slipstream deformation, which is known to be substantial in propeller-wing interaction at high angles of attack and is likely to be very significant for the flow over a deployed flap. Additionally, the explorations of additional components in the system, such as distributed propellers and the role of the nacelle integration, are included to provide a basis for further research in the field.

The research discussed in this dissertation is conducted using a combination of experimental and numerical methods, and is mostly based around a single propeller-wing-flap design. The complexity of the flow requires the flexibility and information density of numerical simulations to facilitate in-depth analysis. The dominant viscous effects in the flow, on the other hand, make numerical methods expensive and less reliable, necessitating experimental measurements. Numerical methods employed include a version of the 2D multi-element aerodynamics solver MSES, modified to include a pressure jump in the domain, and high-fidelity Lattice-Boltzmann simulations. The modified MSES solver is verified using 2D RANS simulations. Experimental measurement techniques include oil flow visualization, surface pressure taps, a wake rake, multi-hole pressure probes and infra-red thermography. Both the model geometry and the experimental data are published as a validation dataset for other researchers in the field. Except for the study based on MSES, the dissertation is based on the same wing geometry, which is an NLFmod22(B) airfoil with deployable slotted flap in a 2.5D wing configuration without sweep or taper. Up to three propellers can be mounted on the wing, using cylindrical nacelles that blend into the leading edge of the propeller. In this dissertation, the TUD-XPROP-S reference propeller is used, which represents a typical turboprop propeller without sweep.

An early analysis using the modified MSES solver considers the interaction between a multi-element airfoil and a jet flow, providing a baseline understanding of how high-lift components behave under non-uniform inflow conditions. The jet serves as a simplification of the propeller slipstream in 2D. A design space of nine design parameters, such as flap deflection and angle of attack, is set up according to Design of Experiments principles, and analyzed using Response Surface Methodology. The study focuses on the relative dominance of design parameters on a range of responses such as aerodynamic coefficients and lift augmentation. The study shows that, compared to uniform inflow conditions, the dependency of the aerodynamic performance of multi-element airfoils on these parameters does not change under influence of a jet, unless transonic flow conditions are reached on the airfoil. The interaction between the wing circulation and the jet trajectory is found to be particularly important for the aerodynamic performance of the airfoil. Immersion of the flap in the jet is found to be critical to achieve the maximum augmentation of the lift coefficient.

The study then extends to three-dimensional configurations, examining how typical (low-lift) propeller-wing interaction phenomena change in high-lift conditions. This includes high angles of attack, flap deflections, and the combination of both. In high-lift conditions, additional interaction effects emerge that do not occur in low-lift conditions, such as flow separation on the wing at the outer edge of the slipstream. Furthermore, the flap is clearly affected by the part of the slipstream that moves past the pressure side of the main element. Slipstream deformation then results in an offset between the washed area of the main element and that of the flap. The differences in slipstream interaction between the main element and the flap are evident from the spanwise lift distributions as well. While the main element experiences a typical asymmetric disturbance to the lift distribution resulting from the tangential velocities in the slipstream, the flap lift is augmented more symmetrically and across a wider portion of its span compared to the main element.

The slipstream deformation is studied further using high-fidelity numerical simulation results, which were validated against the experimental data. They offer much more detailed insight into the development of the propeller slipstream as it interacts with the wing and flap. The fluid dynamics of the tip vortices interacting with the wing leading edge are compared to mechanisms of deformation defined in literature. Though it shows that the same mechanisms apply, the direction in which the main effects act can be very different in the high-lift condition. The development of the flow around the nacelle follows similar mechanisms to the tip vortex deformations and rolls into two strong vortices, one at each side of the wing. These vortices induce crossflow components on the wing surface, which leads to the accumulation of wing boundary layer within the borders of the slipstream. In high-lift conditions, this boundary layer accumulation may lead to local flow separation. Unlike the main element, no coherent vortex structures wrap around the flap. The effect of wing circulation on the helical vortex system of the slipstream causes early breakdown of concentrated vortices on the pressure side. Due to this effect, and the deformation of the tip vortices around the wing leading edge and interactions with the wing boundary layer, no concentrated vortices reach the flap. As a result, there is little tangential velocity in the flow just upstream of the flap. This explains the relative symmetry of the lift distribution of the flap. The slipstream deformation in

the wing wake is dominated by the velocities induced by the nacelle vortices.

The impact of propeller loading conditions on slipstream deformation is also investigated, aiming to understand how changes in torque and thrust coefficients affect flow behaviour around the wing. Based on the investigated mechanisms of slipstream deformation, distinct differences in deformation are expected depending on the amount of longitudinal and azimuthal vorticity shed by the propeller. These scale respectively with torque and thrust coefficient, which are controlled in a wind tunnel experiment by varying blade pitch, rotational speed and number of blades. Flow visualizations and seven-hole pressure probe measurements of various slices of the slipstream over and behind the wing reveal that the torque coefficient has a direct impact on the slipstream deformation, while the impact of thrust coefficient is comparably negligible. The various conditions differ in terms of the pressure losses originating from the nacelle and blade roots, which is attributed to combinations of advance ratio and inflow angle rather than the particular thrust or torque coefficient at which the propeller operates. The different propeller conditions are furthermore shown to change the development of regions of pressure losses on the wing surface that originate from the nacelle-wing junction.

Additionally, this dissertation includes two exploratory studies that are an extension of the simplified propeller-wing-flap configuration. This includes an exploration of distributed propeller systems in high lift conditions, and an exploration of nacelle interference effects on the wing flow in the absence of a propeller and in typical landing conditions (high angle of attack and low propeller thrust).

In the distributed propeller study, the same propeller-wing-flap geometry is fitted with two additional leading-edge mounted propellers. Based on experimental measurements of the distribution of total pressure behind the wing, the slipstream deformation is shown to be reduced in the distributed propeller case compared to the single propeller configuration. The impact of synchrophasing — where the relative angle between the blades of adjacent propellers is controlled — is studied and shown to particularly affect the slipstream development in high-lift conditions.

The nacelle interference study investigates how the particular nacelle placement and integration used in this dissertation influences the flow over the wing, when the propeller slipstream does not dominate the flow. This includes configurations where the propeller is removed entirely, and where it is operating at a very low thrust coefficient. Without a propeller present, the nacelle is shown to have a significant impact on the wing flow in high-lift conditions, inducing flow divergence behind the nacelle and large-scale flow separation on the main element. When a propeller is present, the propeller slipstream suppresses these effects, although not always completely. The asymmetric distribution of loading on the propeller disk resulting from the non-uniform inflow in high-lift conditions causes a significant presence of the slipstream on the downgoing blade side of the wing, even when the thrust coefficient is very small. The observations in this study lead to hypotheses regarding the interplay between the nacelle interference effects and the slipstream interaction with the wing.

Finally, several recommendations for future work are presented. Research in the field of propeller-wing-flap interaction would substantially benefit from a well-documented experimental dataset, because of the complexity of the flow and the difficulty to simulate it accurately. Although this dissertation provides a substantial dataset, all supplied exper-

imental data are time-averaged, which restricts the validation of time-accurate results from numerical simulations. Further expansion of the dataset with time-accurate or phase-accurate measurements would substantially increase its potential worth for future research in the field.

Additionally, the exact mechanisms of the flow separation induced by the slipstream outside its boundary were not fully explained in this dissertation. While various flow structures have been identified that will most likely play a critical role in the phenomenon, further investigation is required to fully appreciate the mechanisms behind it. This will require detailed investigation into the vortex-boundary layer interactions which were outside the scope of this dissertation. The exploration of slipstream deformation in distributed propeller configurations showed that distributed propellers have the potential to suppress several challenging aerodynamic phenomena that occur in the single propeller configuration. The fluid dynamics of the slipstream of distributed propeller-wing-flap configurations therefore warrants additional research. Lastly, the nacelle has been shown throughout the dissertation to play a significant role in the flow around the wing, both in powered and unpowered conditions. The interference of the nacelle in low thrust conditions may pose a significant challenge for the implementation of distributed propeller systems, and further research is required to understand the interplay between nacelle interference and its suppression by the slipstream. Additionally, the nacelle integration offers potential for synergistic aerodynamic benefits through unconventional and innovative design, which should be further explored.

The research presented in this dissertation provides in-depth analyses in the aerodynamic interaction between a propeller, wing, and flap, with a focus on flow dynamics and intuitive understanding of the complex flowfield. The insights gained from this research are essential for the optimization of propeller-wing-flap configurations and the development of innovative propeller-airframe integration concepts. The data presented in this dissertation, and in extension those in the published experimental validation dataset, will furthermore be invaluable for future research in the field.

# SAMENVATTING

De luchtvaartsector wordt in toenemende mate geconfronteerd wordt met milieuproblemen, wat resulteert in een dringende behoefte aan innovaties om de impact op het klimaat te verminderen. Ontwikkelingen in propellertechnologie bieden een veelbelovend, efficiënter alternatief voor traditionele turbofans, met name voor korte tot middellange vluchten. Propellers bieden een hoge voortstuwings-efficiëntie en flexibiliteit, doch ze ook uitdagingen met zich meebrengen, zoals meer geluid en prestatiebeperkingen bij hogere snelheden. Recente ontwikkelingen richten zich op de integratie van propellers met de vleugel om voordeel te halen uit aerodynamische interacties, zoals gedistribueerde propellersystemen die de lift verhogen tijdens het opstijgen en landen. Het ontwerpen van dergelijke integraties vereist een grondig begrip van de complexe stromingsphenomenen die optreden bij de interactie tussen een propeller, vleugel en uitgeslagen klep.

Het doel van dit proefschrift is daarom om *de aerodynamische verschijnselen en onderliggende mechanismen te karakteriseren die de interactie tussen een propeller, vleugel en klep beheersen.* De aerodynamische interactie tussen propeller, vleugel en klep kan worden gezien als een combinatie van twee reeds in de literatuur gevestigde vakgebieden: de aerodynamische interactie tussen propeller en vleugel, en de aerodynamica van vleugelprofielen met meerdere elementen. Vanuit deze onderliggende kennis wordt in dit onderzoek het probleem vanuit twee perspectieven benaderd: de uitbreiding van propeller-vleugelinteractie met een klep en de invloed van een niet-uniform aanstromingsveld, geïnduceerd door een propeller, op de aerodynamica van een meerdelig (*multi-element*) vleugelprofiel. Speciale aandacht gaat uit naar de vervorming van de propellerslipstroom als resultaat van de propeller-vleugelinteractie. Het is bekend dat deze vervorming extra significant is bij grote invalshoeken, hetgeen bepalend kan zijn voor de stroming over een uitgeslagen klep. Daarnaast is verkennend onderzoek naar extra componenten in het systeem, zoals interactie tussen gedistribueerde propellers en de rol van de integratie van de gondel, opgenomen om een basis te bieden voor toekomstige studies in het veld.

Het onderzoek dat in dit proefschrift wordt besproken, is uitgevoerd met een combinatie van experimentele en numerieke methoden, grotendeels gebaseerd op één specifiek propeller-vleugel-klepontwerp. De complexiteit van de stroming vereist de flexibiliteit en informatiedichtheid van numerieke simulaties voor een diepgaande analyse. Aan de andere kant maken de dominante viskeuze effecten in de stroming numerieke methoden duur en minder betrouwbaar, wat experimentele metingen en validatie noodzakelijk maakt. De gebruikte numerieke methodes omvatten: een aangepaste versie van de aerodynamische simulatietool voor multi-element vleugelprofielen MSES, aangepast om een druksprong in het domein op te nemen, en Lattice-Boltzmann simulaties. De aangepaste versie van MSES is verder gevalideerd met 2D RANS simulaties. Experimentele meetmethoden omvatten: stromingsvisualisatie door middel van fluorescerende olie, oppervlaktedruktappen, een zoghark, meergats druksondes en infraroodthermografie.

Zowel de modelgeometrie als de experimentele gegevens zijn gepubliceerd als een validatiedataset voor andere onderzoekers in het veld. Met uitzondering van de studie gebaseerd op MSES, is het proefschrift gebaseerd op dezelfde vleugelgeometrie, een NLFmod22(B)-profiel met een uitschuifbare Fowler-klep in een 2.5D-vleugelconfiguratie zonder pijlstand of tapsheid. Tot drie propellers kunnen op de vleugel worden gemonteerd, met behulp van cilindrische gondels die in de voorrand van de propeller overgaan. In dit proefschrift wordt de TUD-XPROP-S referentiepropeller gebruikt, die een typische turboprop-propeller zonder pijlstand vertegenwoordigt.

De eerste studie van dit proefschrift biedt een fundamenteel begrip van hoe hoogliftcomponenten zich gedragen bij niet-uniforme instroomcondities. Deze studie is uitgevoerd met de aangepaste MSES-oplosser, waarmee de interactie tussen een multi-element vleugelprofiel en een straalstroming (*jet*) wordt onderzocht. De jet stelt een vereenvoudiging van de propellerslipstroom in 2D voor. Een domein van negen ontwerpvariabelen, zoals klephoek en invalshoek, wordt opgezet volgens Design of Experiments-principes en geanalyseerd met behulp van Response Surface Methodology. De studie richt zich op het relatieve belang van ontwerpvariabelen op verscheidene reactievariabelen, zoals de aerodynamische coëfficiënten. Uit de studie blijkt dat, vergeleken met uniforme aanstroom, de afhankelijkheid van de aerodynamische prestaties van multi-element vleugelprofielen van deze variabelen niet verandert onder invloed van een jet, tenzij transone stromingscondities worden bereikt op het vleugelprofiel. De interactie tussen de vleugelcirculatie en het traject van de jet blijkt bijzonder belangrijk voor de aerodynamische prestaties van het vleugelprofiel. Het volledig omhullen van de klep met de jet is cruciaal om de maximale liftcoëfficiëntvergroting te bereiken.

Het onderzoek wordt vervolgens uitgebreid naar driedimensionale configuraties, waarbij wordt gekeken hoe typische (lage-lift) propeller-vleugelinteractieverschijnselen veranderen bij hoge-lift condities. Dit omvat grote invalshoeken, klephoeken en de combinatie van beide. Bij hoge-lift condities ontstaan aanvullende interactie-effecten die niet voorkomen bij lage-lift condities, zoals loslating op de vleugel aan de buitenrand van de slipstroom. Bovendien wordt de klep duidelijk beïnvloed door het deel van de slipstroom dat langs de drukzijde van het hoofdelement beweegt. Slipstroomvervorming resulteert vervolgens in een verplaatsing het door de slipstreoom beïnvloede gebied van het hoofdelement en dat van de klep. De verschillen in slipstroominteractie tussen het hoofdelement en de klep zijn ook duidelijk zichtbaar in de liftverdelingen over de spanwijdte. Waar het hoofdelement een typische asymmetrische verstoring van de liftverdeling ervaart, dankzij de tangentiële snelheden in de slipstroom, is de verstoring van de kleplift meer symmetrisch en over een groter deel van de spanwijdte verspreidt.

De slipstroomvervorming wordt verder onderzocht met behulp van resultaten van numerieke simulaties, die zijn gevalideerd aan de hand van experimentele data. De simulatieresultaten bieden een meer gedetailleerd inzicht in de ontwikkeling van de propellerslipstroom wanneer deze beïnvloed wordt door de vleugel en de klep. De vervorming van de tipwervels om de vleugelvoorrand wordt vergeleken met mechanismen van vervorming zoals beschreven in de literatuur. Hoewel wordt aangetoond dat dezelfde mechanismen van toepassing zijn, kan de richting waarin de hoofdeffecten werken aanzienlijk verschillen bij hoge-lift condities ten opzichte van lage-lift condities. De ontwikkeling van de stroming rond de gondel volgt vergelijkbare mechanismen als de

vervormingen van tipwervels en rolt op in twee sterke wervels, één aan elke zijde van de vleugel. Deze wervels induceren dwarsstroming op het vleugeloppervlak, wat leidt tot verdikkingen van de vleugelgrenslaag binnen de grenzen van de slipstroom. Bij hoge-lift condities kan deze grenslaagverdikking leiden tot lokale loslating. In tegenstelling tot het hoofdelement wikkelen zich geen coherente wervelstructuren rond de klep bij de bestudeerde klepuitslagen. Het effect van vleugelcirculatie op het helische wervelsysteem van de slipstroom veroorzaakt het vervroegd opbreken van geconcentreerde wervels aan de drukzijde. Als gevolg hiervan is er weinig tangentiële snelheid in de stroming stroomopwaarts van de klep. Dit verklaart de relatieve symmetrie van de liftverdeling van de klep. De slipstroomvervorming in het zog van de vleugel wordt gedomineerd door de snelheden geïnduceerd door de gondelwervels.

De impact van propellerbelasting op slipstroomvervorming wordt ook onderzocht, met als doel te begrijpen hoe veranderingen in koppel- en stuwkrachtcoëfficiënten het stromingsgedrag rond de vleugel beïnvloeden. Op basis van de onderzochte mechanismen van slipstroomvervorming worden duidelijke verschillen in vervorming verwacht, afhankelijk van de longitudinale en azimutale vorticiteit in de slipstroom van de propeller. Deze schalen respectievelijk met de koppel- en stuwkrachtcoëfficiënt, die in een windtunnelexperiment worden gecontroleerd door middel van specifieke combinaties van de bladhoek, rotatiesnelheid en het aantal bladen. Stromingsvisualisaties en metingen met een meergats druksonde van verschillende doorsneden van de slipstroom rondom de vleugel tonen aan dat de koppelcoëfficiënt een directe impact heeft op de slipstroomvervorming, terwijl de impact van de stuwkrachtcoëfficiënt relatief verwaarloosbaar is. De drukverliezen afkomstig van de gondel en bladwortels verschillen tussen de diverse condities, maar een systematische trend kan niet worden geïdentificeerd. Dit wordt toegeschreven aan de effecten van voortstuwingsverhouding en instroomhoek, in plaats van de specifieke stuwkracht- of koppelcoëfficiënt van de propeller. De verschillende propellerbelastingen blijken bovendien de ontwikkeling van drukverliezen op het vleugeloppervlak te veranderen die voortkomen uit de integratie tussen gondel en vleugel.

Verder bevat dit proefschrift twee verkennende studies, die een uitbreiding zijn van de vereenvoudigde propeller-vleugel-klepconfiguratie. Dit omvat een verkenning van gedistribueerde propellersystemen bij hoge-lift condities en een verkenning van interferentie door de gondel op de vleugelstroming in afwezigheid van een propeller en bij typische landingscondities (hoge invalshoek en lage propellerstuwkracht).

In de studie naar gedistribueerde propellers wordt dezelfde propeller-vleugel-klepgeometrie uitgerust met twee extra propellers, gemonteerd aan de voorrand. Op basis van experimentele metingen van de totale drukverdeling achter de vleugel, wordt aangetoond dat de slipstroomvervorming wordt verminderd in de configuratie met meerdere propellers ten opzichte van een enkele propeller. De impact van *synchrophasing*, waarbij de relatieve hoek tussen de bladen van aangrenzende propellers wordt gecontroleerd, wordt onderzocht en blijkt met name invloed te hebben op de slipstroomontwikkeling bij hoge-lift condities.

De studie naar gondelinterferentie onderzoekt hoe de specifieke gondelintegratie toegepast in het windtunnel model de vleugelstroming beïnvloedt. Er wordt speciale aandacht besteed aan de situatie waar de vleugelstroming niet wordt gedomineerd door de propellerslipstroom, zoals wanneer de propeller volledig is verwijderd of opereert met

een zeer lage stuwkrachtcoëfficiënt. Zonder propeller blijkt de gondel een aanzienlijke impact te hebben op de vleugelstroming bij hoge-lift condities, waarbij stromingsafbuiging achter de gondel wordt geïnduceerd en grootschalige loslating op het hoofdelement optreedt. Wanneer er wel een propeller gemonteerd is, onderdrukt de propellerslipstroom deze effecten, hoewel niet altijd volledig. De asymmetrische belastingsverdeling op de propeller, veroorzaakt door de niet-uniforme instroom bij hoge-lift condities, resulteert in een significante aanwezigheid van de slipstroom aan de neergaande bladzijde van de vleugel, zelfs bij een zeer kleine totale stuwkrachtcoëfficiënt. De observaties in deze studie leiden tot hypothesen over de wisselwerking tussen gondelinterferentie-effecten en de slipstroominteractie met de vleugel.

Tot slot worden in dit proefschrift verschillende aanbevelingen voor toekomstig onderzoek gepresenteerd. Onderzoek op het gebied van propeller-vleugel-klepinteractie zou aanzienlijk profiteren van een goed gedocumenteerde experimentele dataset, vanwege de complexiteit van de stroming en de moeilijkheid om deze nauwkeurig te simuleren. Hoewel er al een substantiële dataset wordt aangeboden bij dit proefschrift, zijn alle verstrekte experimentele gegevens enkel tijdsgemiddeld. Dit beperkt de mogelijkheden om tijd- of fase-accurate simulaties te valideren. Verdere uitbreiding van de dataset met tijd- of fase-accurate metingen zou de waarde ervan voor toekomstig onderzoek aanzienlijk vergroten.

Daarnaast worden de exacte mechanismen van de stromingsloslating aan de buitengrens van de slipstroom niet volledig verklaard in dit proefschrift. Hoewel verschillende stromingsstructuren zijn geïdentificeerd die waarschijnlijk een cruciale rol spelen bij dit fenomeen, is verder onderzoek nodig om de mechanismen erachter volledig te begrijpen. Dit vereist gedetailleerd onderzoek naar de interacties tussen wervels en grenslagen, wat buiten het bereik van dit proefschrift valt. De verkenning van slipstroomvervorming in configuraties met gedistribueerde propellers heeft aangetoond aan dat gedistribueerde propellers het potentieel hebben om verschillende uitdagende aerodynamische verschijnselen, die optreden bij configuraties met een enkele propeller, te onderdrukken. De ontwikkeling van de slipstroom in configuraties met gedistribueerde propellers, vleugels en kleppen rechtvaardigt daarom aanvullend onderzoek.

De gondel speelt door het hele proefschrift heen een significante rol in de stroming rond de vleugel, zij het met of zonder propeller slipstroom. De interferentie van de gondel bij lage stuwkrachtcondities kan een aanzienlijke uitdaging vormen voor de implementatie van gedistribueerde propellersystemen. Verder onderzoek is nodig om de wisselwerking tussen gondelinterferentie en de impact van de slipstroom te begrijpen. Bovendien biedt de gondelintegratie mogelijkheden voor synergetische aerodynamische voordelen door middel van onconventioneel en innovatief ontwerp.

Het onderzoek in dit proefschrift biedt diepgaande analyses van de aerodynamische interactie tussen een propeller, vleugel en klep. Hierbij ligt de focus op stromingsdynamica en een intuïtief begrip van het complexe stromingsveld. De inzichten die uit dit onderzoek worden uiteengezet, zijn essentieel voor de optimalisatie van propeller-vleugel-klepconfiguraties en de ontwikkeling van innovatieve propeller-integratie concepten. De gegevens die in dit proefschrift worden gepresenteerd, aangevuld door de gepubliceerde experimentele dataset, kunnen bovendien van grote waarde zijn voor toekomstig onderzoek op dit gebied.

# CONTENTS

# NOMENCLATURE

**Variables**

| | | | |
|---|---|---|---|
| $A$ | = | Area of slipstream cross-section | [m$^2$] |
| $c$ | = | Chord length | [m] |
| $C_d$ | = | Sectional drag coefficient | [-] |
| $C_{d,f}$ | = | Friction drag coefficient | [-] |
| $C_{d,p}$ | = | Pressure drag coefficient | [-] |
| $C_{d,tot}$ | = | Total drag coefficient | [-] |
| $C_{d,v}$ | = | Viscous drag coefficient | [-] |
| $C_{d,w}$ | = | Wave drag coefficient | [-] |
| $c_f$ | = | Skin friction coefficient | [-] |
| $C_l$ | = | Sectional lift coefficient | [-] |
| $C_m$ | = | Sectional moment coefficient | [-] |
| $C_p$ | = | Pressure coefficient | [-] |
| $C_{p,s}$ | = | Static pressure coefficient $\frac{p_s - p_{s,\infty}}{q_\infty}$ | [-] |
| $C_{p,t}$ | = | Total pressure coefficient $\frac{p_t - p_{s,\infty}}{q_\infty}$ | [-] |
| $D$ | = | Propeller diameter or Drag force | [m] or [N] |
| $D/c$ | = | Propeller diameter-to-wing chord ratio | [-] |
| $d_{base}$ | = | Base mesh element size | [m] |
| $\mathrm{d}s$ | = | Flap gap | [-] |
| $\mathrm{d}x$ | = | Flap overlap | [-] |
| $h$ | = | Heat transfer coefficient | [W/(m$^2$ K)] |
| $h_i/h_1$ | = | Relative cell size | [-] |
| $J$ | = | Propeller advance ratio | [-] |
| $k$ | = | Number of factors or power transform constant | [-] |
| $K_{C_l}$ | = | Lift augmentation factor | [-] |
| $k_f$ | = | Thermal conductivity of fluid | [W/(m K)] |
| $L$ | = | Lift force | [N] |
| $L/D$ | = | Lift-to-drag ratio | [-] |
| $M$ | = | Mach number | [-] |
| $N_b$ | = | Number of blades | [-] |
| $N_{cells}$ | = | Number of cells in mesh | [-] |
| $n_{crit}$ | = | Turbulence level indicator for $e^n$-method | [-] |
| $p$ | = | Pressure | [Pa] |
| $\dot{q}$ | = | Convective heat flux | [W/m$^2$] |
| $Q$ | = | Torque | [N m] |
| $Q_c$ | = | Torque coefficient $\frac{Q}{\rho_\infty V_\infty^2 D^3}$ | [-] |
| $Q_c^*$ | = | Equivalent torque coefficient $\int\int \frac{u \Delta v r^2}{V_\infty^2 D^2}\, dr\, d\psi$ | [-] |
| $q_\infty$ | = | freestream dynamic pressure | [Pa] |

| $r, R$ | = | Radius | [m] |
|---|---|---|---|
| $Re$ | = | Reynolds number | [-] |
| $\frac{t}{c}$ | = | Thickness-to-chord ratio | [-] |
| $T$ | = | Thrust | [N] |
| $T_c$ | = | Thrust coefficient $\frac{T}{\rho_\infty V_\infty^2 D^2}$ | [-] |
| $T_c^*$ | = | Equivalent thrust coefficient $\int \frac{(C_{p,t}-1)}{2D^2} dA$ | [-] |
| $T_W$ | = | Wall temperature | [K] |
| $T_\infty$ | = | Freestream temperature | [K] |
| $u$ | = | Streamwise velocity component | [m/s] |
| $v$ | = | Horizontal/spanwise velocity component | [m/s] |
| $V$ | = | Velocity | [m/s] |
| $V_j/V_\infty$ | = | Jet velocity ratio | [-] |
| $w$ | = | Vertical velocity component | [m/s] |
| $x$ | = | Longitudinal/Streamwise coordinate | [m] |
| $x_i, x_j, x_k$ | = | Factors in metamodel | [-] |
| $y$ | = | Horizontal/spanwise coordinate | [m] |
| $y^+$ | = | Dimensionless wall distance | [-] |
| $z$ | = | Vertical/normal coordinate | [m] |
| $z/D$ | = | Vertical position of the jet | [m] |
| | = | | |
| $\alpha$ | = | Angle of attack | [deg] |
| $\alpha^*$ | = | Star-point coordinate | [-] |
| $\beta$ | = | Regression term gain | [-] |
| $\beta_{0.7R}$ | = | Propeller blade pitch at 70% radius | [deg] |
| $\delta_f$ | = | Flap deflection angle | [deg] |
| $\epsilon$ | = | Error term | [-] |
| $\eta$ | = | Efficiency | [-] |
| $\lambda$ | = | Power transform exponential | [-] |
| $\lambda_2$ | = | Vortex criterion | [-] |
| $\lambda_{2D}$ | = | Shape factor for wind tunnel corrections | [-] |
| $v$ | = | Kinematic viscosity | [m$^2$/s] |
| $\rho$ | = | Density | [kg/m$^3$] |
| $\Delta\phi$ | = | Blade phase angle | [deg] |
| $\psi$ | = | Azimuthal angle | [deg] |
| $\omega$ | = | Vorticity | [1/s] |

**Sub- and superscripts**

| 0 | = | Sea-level condition or initial value |
|---|---|---|
| b | = | Blades |
| c | = | Coefficient |
| D | = | Diameter |
| f, flap | = | Flap element |
| i | = | Iterable |
| j | = | Jet or iterable |
| k | = | iterable |

| | | |
|---|---|---|
| m | = | Iterable |
| main | = | Main element |
| max | = | Maximum value |
| min | = | Minimum value |
| p | = | Pressure or metamodel iterable |
| prop | = | Propeller |
| s | = | Static |
| t, tot | = | Total |
| v | = | Viscous |
| w | = | Wave |
| x, y, z | = | Streamwise, spanwise, vertical direction |
| $\infty$ | = | Freestream condition |

**Acronyms & Abbreviations**

| | | |
|---|---|---|
| 7HP | = | 7-hole probe |
| ANOVA | = | Analysis of Variance |
| AAM | = | Advanced Air Mobility |
| BEM | = | Blade Element Momentum |
| BLI | = | Boundary Layer Ingestion |
| CCD | = | Central Composite Design |
| CFD | = | Computational Fluid Dynamics |
| CPU | = | Central Processing Unit |
| DoE | = | Design of Experiments |
| DP | = | Distributed Propulsion |
| eVTOL | = | Electric Vertical Take-Off and Landing |
| F | = | Flap |
| FLTE | = | Flap Trailing-Edge |
| HLP | = | High-Lift Propellers |
| IR | = | Infra-red |
| LBM | = | Lattice Boltzmann Method |
| LDV | = | Laser Doppler Velocimetry |
| LTT | = | Low-Turbulence Tunnel |
| METE | = | Main Element Trailing Edge |
| MELE | = | Main Element Leading Edge |
| N | = | Nacelle |
| NS | = | Navier-Stokes |
| P | = | Propeller |
| PIV | = | Particle Image Velocimetry |
| PWF | = | Propeller-Wing-Flap |
| PWFI | = | Propeller-Wing-Flap Interaction |
| PWI | = | Propeller-Wing Interaction |
| RANS | = | Reynolds-Averaged Navier-Stokes |
| RNG | = | Re-Normalisation Group |
| RSM | = | Response Surface Methodology |
| SA | = | Spalart-Allmaras |

| | | |
|---|---|---|
| SST | = | Shear-Stress Transport |
| STOL | = | Short Take-Off and Landing |
| TUD-PROWIM-3 | = | TU Delft Propeller-Wing-Flap Interaction Model 3 |
| UAM | = | Urban Air Mobility |
| VIF | = | Variance Inflation Factor |
| VLES | = | Very Large Eddy Simulation |
| VP | = | Verification Point |
| VTOL | = | Vertical Take-Off and Landing |
| W | = | Wing |
| uRANS | = | Unsteady Reynolds-Averaged Navier-Stokes |

# I

# BACKGROUND AND METHODS

# 1

## INTRODUCTION

As our world grapples with pressing environmental concerns and the escalating demand for aviation continues to soar, the need for innovative solutions that mitigate the climate impact of the aviation industry has never been more urgent. If air travel is to remain a viable mode of transport for the future, a comprehensive reform of the sector is necessary. Rapid advancements in renewable energy sources for aviation are promising, but they alone cannot address the industry's complex challenges. Disruptive change across the industry is necessary, challenging conventional norms and embracing new technologies. A prime example of such disruptive change is the rekindled interest in propeller technology, finding innovative and beneficial ways to integrate it into the airframe, and even redefining its primary purpose.

### 1.1. THE RESURGENCE OF PROPELLER PROPULSION

Since the 1960s, turbojets have been the preferred method of propulsion for commercial-class passenger aircraft. In the pursuit of improving fuel efficiency, these engines have developed over the years to include large fans with high bypass ratios (usually referred to as *turbofans*) in order to reduce the required velocity rise to achieve a certain thrust and boost propulsive efficiency. Increasing the bypass ratio to improve propulsive efficiency delivers diminishing returns, as the increase in fan size is associated with an increase in nacelle size. The additional drag due to the larger wetted area of the nacelle, along with the associated weight penalty and wing integration challenges, pose a limit on the effectiveness of increasing the bypass ratio of turbofan engines [1, 2].

Turboprops, propellers driven by gas-turbine engines, do not have outer ducts and are therefore not bound by the same limits. Large propellers can be fitted to reach higher propulsive efficiency than turbofans [3], leading to advanced turboprop design such as those used by the Airbus A400M and the GE36 counter-rotating open-rotor. Although development on the latter was ultimately abandoned, a modern version of the concept is currently being developed in the CFM RISE programme (Fig. 1.1), promising 20% improvement of fuel efficiency compared to the best engine in service [4].
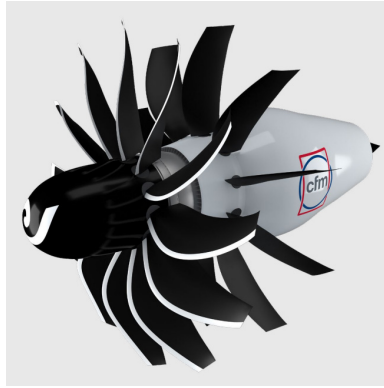
Figure 1.1: CFM International RISE engine, from [4].

Propellers come with a range of other potential drawbacks and benefits. Without a duct to act as a shroud for noise, both community and cabin noise are significantly higher with propeller systems compared to turbofans [5]. Propeller systems are also limited by the tip Mach number, which can reach transonic conditions in cruise, causing loss of performance [6]. As a result, propeller aircraft typically have to fly at a lower cruise velocity and altitude to preserve any propulsor efficiency over turbofan designs. On the other hand, pitchable blades allow propellers to operate at their maximum propulsor efficiency for a large portion of the flight envelope, unlike conventional turbofans. Propeller performance is also scalable and independent of the method of shaft power delivery, making propellers applicable to a wide range of aircraft sizes and motor types.

In the context of short to medium mission ranges, several of the drawbacks of propeller propulsion are mitigated while simultaneously amplifying the benefits. As the aircraft spends less time in cruise flight, the reduced cruise flight speed is less impactful on the mission block time compared to long range missions. The pitchable blades furthermore allow the propeller to operate efficiently outside of cruise conditions. Moreover, even for turbofan aircraft, a mission designed for minimal climate impact involves flying at reduced speed and altitude according to Thijssen, Proestman and Vos [7]. They show that at this optimized flight regime, turboprops would offer around 20% reduction in climate impact over turbofans without affecting total mission block time, rising to roughly 30% if mission block time is allowed to be varied.

It should therefore be no surprise that both industry and academia have committed to propeller propulsion as a fundamental building block towards a climate-neutral aviation sector. Most major aircraft manufacturers have adopted propeller-based aircraft in their next-generation line-up for short to medium range missions, such as the Embraer's Energia line (Fig. 1.2a). International collaborations such as the Clean Sky 2's IRON project have revisited propeller design for the next generation passenger-class aircraft (Fig. 1.2b).
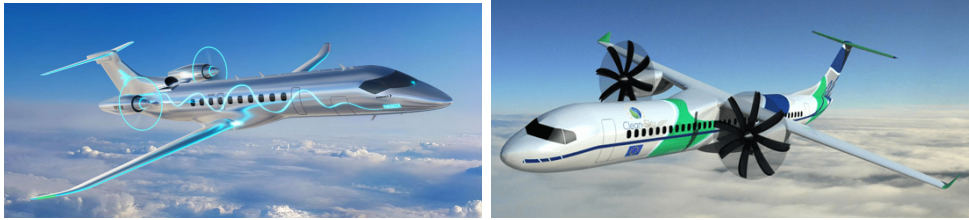
(a) Embraer Energia concept. Copyright: Embraer.      (b) Clean Sky 2 IRON concept. Copyright: DOWTY.

Figure 1.2: Impressions of next-generation propeller-based passenger aircraft concepts.

## 1.2. PROPELLER-AIRFRAME INTEGRATION

The resurgence of propeller technology comes alongside interest in novel propeller-airframe integration, to gain aerodynamic benefit through flexible and innovative integration of the propeller with the airframe. Historically, propulsion-airframe integration (for any mode of propulsion) has usually been designed to minimize and mitigate interference effects as much as possible, as they can negatively affect aerodynamic performance. This was further motivated by the inability to downscale gas-turbine engines without drastically impacting their performance. Together with the drive towards larger fan diameters to improve propulsive efficiency, this has led to modern passenger-class aircraft using a single, large-scale turbofan engine per wing. The scalability of propeller performance, their independence of shaft power delivery method and the advent of high performance electric motors, allows for the use of different scales of propulsion and flexible integration with the airframe. This, in turn, enables innovative solutions that capitalize on the aerodynamic interactions, rather than avoid them.

Closely-coupled design of the propeller system and airframe can lead to improvements that are greater than the sum of its parts, as they can benefit not only from the optimized components themselves, but also their interactions [8, 9]. Mounting propellers at the wing tip, for example, and rotating them against the tip vortex direction can simultaneously provide the required thrust and reduce induced drag by both swirl recovery and wingtip-vortex attenuation [10, 11, 12]. Other examples include drag reduction by boundary layer ingestion (BLI) [13, 14, 15], using distributed propeller (DP) configurations in attempts to improve aerodynamic performance [9, 11, 12] or reduce propeller noise [16] and high-lift propellers (HLP); applying propellers as active high-lift devices to augment wing lift during take-off and landing [17, 18, 19].

High-lift augmentation and distributed propeller systems have received particular attention in literature and industry, owing the NASA Maxwell X-57 (see Fig. 1.3). This concept aircraft demonstrates how utilizing distributed propellers as active high-lift devices allows for a reduction in total wing area and an increase in aspect ratio, thereby improving cruise performance [19]. Commonly in aircraft design, the wing sizing is dependent on the landing requirement rather than cruise conditions [9]. Traditional, passive high-lift devices consisting of leading-edge slats and (multi-slotted) trailing-edge flaps can only boost (total) lift coefficients to around 3 [20], and this requires highly complex systems that come associated with high mechanical complexity and weight penalties [21]. Using propellers as active lift augmentation devices can boost wing lift

coefficients much higher [22, 23], as readily demonstrated in the past by STOL aircraft such as the Breguet 941 (Fig. 1.4).

Although the Maxwell X-57 is the most popular example, the application of leading-edge mounted (distributed) propeller systems can be found in concepts across the aviation sector. The FUTPRINT50 project, funded by the European Horizon 2020 programme, aims to accelerate the delivery of propeller-driven hybrid-electric passenger aircraft in the class of 50 seats by 2040 [24]. In a similar effort, the German SynergIE project has investigated propeller-driven passenger aircraft up to 100 seats [11] and Airbus has adopted a distributed propeller concept in its ZeroE line-up (Fig. 1.5). Furthermore, wing-mounted propeller-technology is prominently featured in smaller scale applications, such as eVTOL and other Advanced Air Mobility concepts (e.g., NASA's VTOL UAM reference designs [25]).



Figure 1.3: NASA Maxwell X-57 demonstrator. Copyright: NASA.



Figure 1.4: Photo of the Breguet 941 STOL aircraft. Copyright: Wikimedia Commons.



Figure 1.5: Airbus ZeroE distributed propeller concept. Copyright: Airbus.

## 1.3. Propeller-Wing Aerodynamic Interaction

Clearly, propeller propulsion has a significant role to play in the future of aviation. Propeller technology is not just experiencing a resurgence, the focus now specifically lies on the integration of the propeller system with the airframe to capitalize on aerodynamic interactions. Consequently, properly understanding the aerodynamic interaction between the propeller and the wing is paramount. This *propeller-wing aerodynamic interaction* (PWI) features highly complex flowfields that involve a two-way interaction that cannot

be decoupled [26]. The propeller affects the wing by the imposition of axial and tangential velocities, swirl and turbulence, while the wing affects the propeller by the upwash induced by the wing circulation, as well as blockage effects. The impact of the propeller on the wing flow, thus influences the propeller performance, and vice versa.

Significant work has already been done on the aerodynamic interactions between propellers and wings. Prandtl [26] already noted the coupling between propeller and wing aerodynamics as early as 1921 and since then the interaction has been studied in more detail by, among others, Jameson [27], Kroo [28], Witkowski, Lee and Sullivan [29], Samuelsson [30] and Veldhuis [31]. An illustration of the main effects that these works discuss is given in Fig. 1.6. An installed propeller operates in a non-uniform inflow field due to influences of aircraft components such as the nacelle and upwash generated by the wing circulation. The wing, meanwhile, experiences disturbances to its spanwise lift distribution due to the axial and tangential velocities imposed on the wing by the propeller slipstream. The propeller swirl induces an apparent angle of attack on the wing, tilting the lift vector and affecting the induced drag of the wing. As the propeller slipstream is a highly three-dimensional flowfield, the position and inclination of the propeller ahead of the wing all change how the wing is influenced by the propeller, but also how the propeller is influenced by the wing.
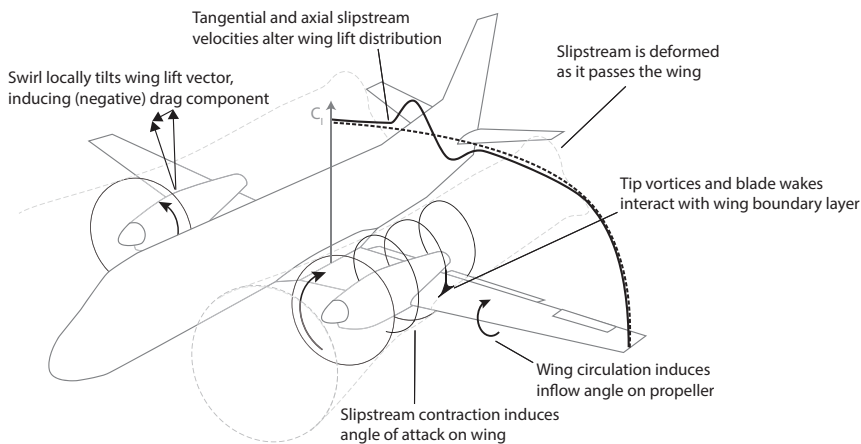


Figure 1.6: Illustration of the main effects of propeller-wing interaction.

The PWI also deforms the slipstream, which can impact how it affects downstream surfaces such as the flap and the empennage. Samuelsson [30] visualizes the velocity vectors at various streamwise positions in the slipstream, showing how they are affected by the wing and various nacelle geometries. However, this is only done in cruise conditions. The same goes for Aljabri and Hughes [32], who show the deformation of the propeller slipstream due to the interaction with a symmetric wing by means of distributions of total pressure in the wake of the wing, noting that the extent of the deformation is more significant than expected. Veldhuis [31] shows that this deformation changes significantly

with higher angle of attack. Whereas in cruise condition the slipstream mainly shears in spanwise direction, in high-lift conditions it completely deforms from its initial, circular shape (Fig. 1.7). The mechanisms behind the slipstream deformation are later studied by Felli [33], based on preceding work on propeller-rudder interaction in the field of marine engineering[1]. Key differences with installed propellers in aeronautical configurations remain, however, such as the presence of a lifting wing and the propeller operating in a non-uniform inflow field. Furthermore, Felli [33] uses a detached propeller, meaning nacelle integration effects are not included. These differences may critically influence slipstream deformation in aeronautical applications, but have not been studied in detail yet. In general, flow dynamics of the propeller-wing interaction are not as well-defined in aeronautical literature as the implications on wing and propeller performance are, particularly in high-lift conditions.

In the context of modern propeller-airframe integration concepts such as high-lift propellers and distributed propeller systems, the development of the flow deserves much more attention than it has received thus far in literature on PWI. The additional components involved in these systems, such as multiple propellers and wing elements, significantly increase the complexity of the resulting flowfields as they will all interact aerodynamically. If we are to optimize propeller integration, we will need to thoroughly understand how changes to performance are related to aerodynamic interaction mechanisms.

The potential importance of the slipstream deformation for the aerodynamic performance of an aircraft should not be understated. Besides the flow on the main wing, the deformation directly impacts the performance of any lifting surfaces downstream of the wing. Eshelby [34] notes the effect of the slipstream on the horizontal tail of a propeller-driven aircraft (see Fig. 1.8), noting that it introduces a secondary set of forces and moments to the equation of motion of the aircraft. They also note the drastic impact of the wing lift coefficient to the relative position between slipstream and horizontal tail. At the time, Eshelby [34] fails to recognize the extent of the deformation of the slipstream, however, which will further complicate the interaction. This is particularly true for the high-lift condition, as the deformation increases significantly [31]. Additionally, a deployed flap can — like the horizontal tail — be seen as a downstream surface that is thus strongly affected by the deformation of the slipstream induced by the upstream wing element.

The high-lift condition furthermore involves several viscous aerodynamic mechanisms that can generally be ignored in the cruise condition, making the PWI significantly more complex[2]. Furthermore, the aerodynamics of slotted (or *multi-element*) wings are well known to be highly interactional in their own right (see the seminal work of Smith [35]), where elements influence each other in a manner that, again, cannot be decoupled. Multi-element wings at high angles of attack are also particularly sensitive to Mach and Reynolds number effects [36]. The exact mechanisms that govern the maximum lift of multi-element wings are still not fully understood [37], as many multi-element

---

[1]The work by Felli [33] and his predecessors is further discussed in Section 5.2 of this dissertation

[2]Eshelby [34] notably calls the propeller slipstream behaviour at high wing lift coefficients an "enigma". Interestingly, they put forth the complex interaction and break-down of the tip vortex system as a potential explanation, an observation that is discussed in Chapter 5.

airfoils do not exhibit flow separation at maximum lift, unlike single-element airfoils which often exhibit sharp drops in lift due to flow separation. Compared to PWI in cruise conditions, the *propeller-wing-flap* (PWF) interaction results in a significant increase in complexity, where local changes in slipstream properties may drastically affect local wing performance.

## 1.4. PROPELLER-WING-FLAP AERODYNAMIC INTERACTION

Although propeller-wing-flap aerodynamic interactions (PWFI) have historically received less attention in literature compared to PWI in cruise conditions, it has not gone entirely untouched. Early research in the 50s and 60s (e.g., by Kuhn and Draper [38], Kuhn [39], Hayes, Kuhn and Sherman [40], and Newsom [41]) delved into fixed-wing Vertical Take-Off and Landing (VTOL) capability. They investigated how complex systems of slats, flaps, and vanes could be used to deflect the propeller slipstream and vector thrust to be used for short or even vertical take-off. This substantial body of work includes investigations of various flap systems, propeller positions and inclinations, and flap deflection angles. However, they focus on static thrust conditions and metrics such as the *slipstream turning ratio*, rather than understanding the aerodynamic mechanisms of PWFI. Ultimately, the
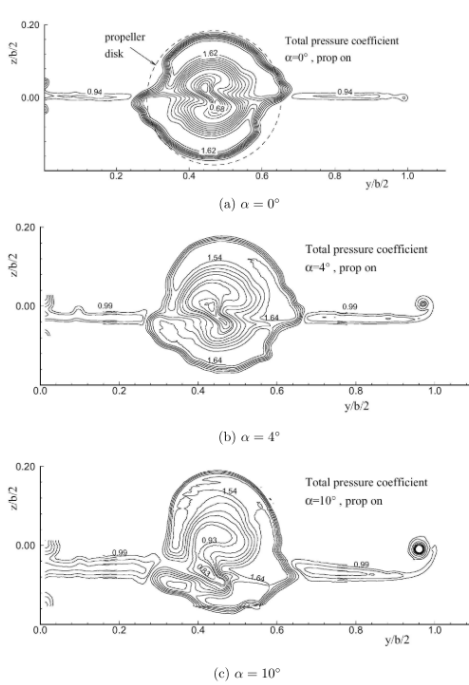


Figure 1.7: Distributions of total pressure coefficient behind a half wing model with a single propeller, visualizing the deformation of the slipstream due to the propeller-wing interaction. From [31].
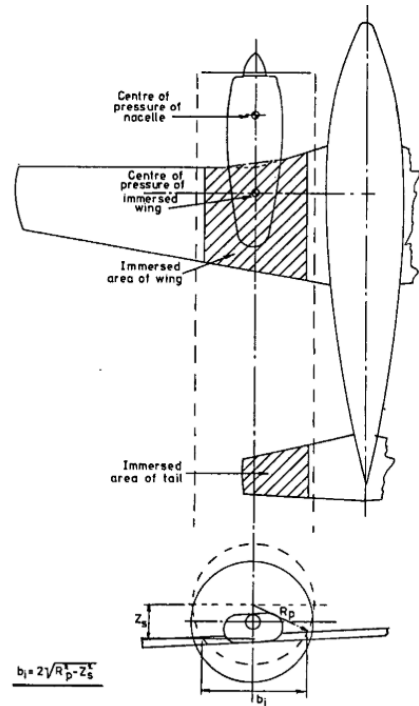
Figure 1.8: Illustration of the propeller slipstream affecting the horizontal tail of a propeller-driven aircraft. From [34].

Figure 1.9: Photo of the Ryan VZ-3YA Vertiplane. From Wikimedia Commons.

only fixed-wing VTOL concept from this era to have achieved full scale flight is the Ryan VZ-3YA Vertiplane [42], shown in Fig. 1.9.

Modern research on the PWFI has shifted from fixed-wing V/STOL capabilities and focuses more on achieving improvements in aerodynamic efficiency for the next-generation of aircraft through advanced propeller integration. Many projects (e.g., Cui et al. [43], Keller [11], Long et al. [44], Bongen et al. [45] and Beckers et al. [46]) investigate the performance of (distributed) PWF configurations. Similar to the established PWI research in cruise conditions, the results are typically discussed based on propeller and wing performance metrics. Of course, performance coefficients serve as crucial parameters for design and all of the complexities at aircraft design level have to be assessed when investigating the effectiveness of propeller-airframe integration concepts. In the author's opinion, however, the lack of fundamental understanding of the overall flow development often leads to a difficulty in providing generalized insight into the underlying aerodynamic mechanisms that drive the performance metrics. Specifically, the differences in dominant aerodynamic phenomena between traditional PWI in cruise conditions and high-lift conditions remain poorly understood. This includes both propeller-wing configurations with a single wing element at high angles of attack, and those with multi-element wings. Without proper understanding, we cannot recognize where opportunities in beneficial integration may lie, which fidelity of simulation is required in different conditions, or ensure safe operation at the limits of the flight envelope.

As the flap is positioned downstream of the main element, its interaction with the propeller slipstream is highly dependent on the preceding interaction between the slipstream and main element. As the slipstream is known to deform due to the interaction with the main element, the aerodynamics of the flap will be dependent on the extent of this deformation. This includes the deviation from the circular shape and how it intersects with the flap, but also the stretching, displacement and breakdown of individual vortices. It is highly likely that the orientation of the tip vortices with respect to the flap deviate significantly from the orientation with respect to the main element. Similar points can be

made for other downstream surfaces, such as the empennage. The interaction with the propeller slipstream will depend strongly on the deformation. Furthermore, the addition of the flap will further deform the slipstream, as well as displace it. The slipstream development in PWFI is thus crucial to understand for both local wing performance and from a flight dynamics perspective.

## 1.5. RESEARCH OBJECTIVES AND APPROACH

The main objective of this dissertation is therefore to **characterize the phenomena and mechanisms that dominate the propeller-wing-flap aerodynamic interaction**. Characterizing the dominant aerodynamic phenomena of PWFI is paramount to any focused attempt to optimize the interaction for aerodynamic benefit. The current state-of-the-art of PWFI lacks a proper understanding of the fluid dynamics behind the performance metrics. This work prioritizes visualizing and quantifying the flow structures, investigating which aerodynamic phenomena dominate the interaction and which mechanisms drive these phenomena. The purpose is to achieve an intuitive insight into the aerodynamic behaviour of PWF flows. This intuition will help analyse more complex configurations, predict limiting cases and determine suitable modelling methods for specific situations.

### 1.5.1. DEMARCATION OF THE INTERACTION MODES

We have readily established that propeller-wing-flap aerodynamic interactions are a fully coupled system that combines multi-element wing aerodynamics and propeller-wing aerodynamic interactions. The addition of the flap element increases the complexity of the interaction drastically. Whereas both propeller-wing aerodynamic interaction and multi-element aerodynamics only feature a single interaction mode (respectively the interaction between propeller and wing, and between wing and flap)[3], a propeller-wing-flap system consists of six modes: three primary interactions and three secondary interactions. Figure 1.10 illustrates the various interaction modes between propeller (P), wing (W) and flap (F).

Based on Fig. 1.10 we can approach the propeller-wing-flap aerodynamic interaction as extensions to propeller-wing aerodynamic interaction and multi-element airfoil aerodynamics, as follows:

- *How are typical multi-element airfoil aerodynamic interactions affected by an upstream jet of increased total pressure? (WF-P)*

- *How are propeller-wing aerodynamic interactions affected by the inclusion of a slotted flap? (PW-F) & (PF-W) & (WF-P)*

- *How does the aerodynamic interaction between the propeller and the flap differ from the interaction between propeller and wing? (P-F)*

- *How does the aerodynamic interaction between the propeller and wing affect the flap flow? (PW-F)*

---

[3]Note that each of these are still two-way coupled systems

**1**

Additionally, the state-of-the-art of propeller-wing interaction in high-lift conditions — be it by high angles of attack or deflected flaps — is lagging behind the equivalent in cruise conditions. It is not well understood how these flows that are dominated by viscous effects change the primary interaction between propeller and wing. We can then reach the additional question below. Note that we use *low-lift* rather than cruise, to signify that we do not attempt to achieve Reynolds number and Mach number similarity with cruise conditions in this dissertation.

- *How does the primary aerodynamic interaction between propeller and wing in high-lift conditions differ from low-lift conditions? (P-W)*

From literature, it is known that the slipstream deforms as a result from the propeller-wing interaction. Furthermore, this deformation changes substantially with angle of attack. We have also shortly discussed how this may not only affect the flap flow, but also surfaces further downstream. It then becomes important to understand:

- *How does the slotted flap affect the slipstream deformation?*

- *How does the slipstream deformation depend on the propeller loading?*

Finally, Fig. 1.10 shows that in the extension of PWFI lie interaction modes with distributed propulsion and the nacelle. Additional high lift elements also add to the interaction modes, but are excluded from the scope (see section 1.5.2). This leads to two additional research questions, listed below. We will not be able to decisively answer these questions within the scope of this dissertation. Rather, we will explore them within the bounds of our setup and provide a basis for further research on the topics. This is motivated further in section 1.5.2.

- *How does the aerodynamic interaction between a distributed propeller system and a wing-flap system differ from a single propeller setup?*

- *How does the nacelle and its integration affect the propeller-(nacelle-)wing-flap aerodynamic interaction?*

### 1.5.2. SCOPE OF THE SYSTEM CONFIGURATION

We have previously discussed that the complexity of applied (distributed) PWF systems often leads to a difficulty in analysing the fundamental phenomena and mechanisms. In this dissertation, we aim to provide the tools to analyse these complex systems by characterizing a simplified version of the system, illustrated by Fig. 1.11. We limit the configuration studied in this dissertation to a single propeller and a wing with a single-slotted flap. We ignore taper, sweep and end-effects, and generally limit the variation in wing geometry that we explore. Although airfoil design features or wing planform design will certainly affect the resulting aerodynamic performance, they will not change the fundamental phenomena and mechanisms that are involved like a separate wing element would. We therefore consider these additional design complexities as a next step in the analysis of PWFI and beyond the scope of this dissertation.
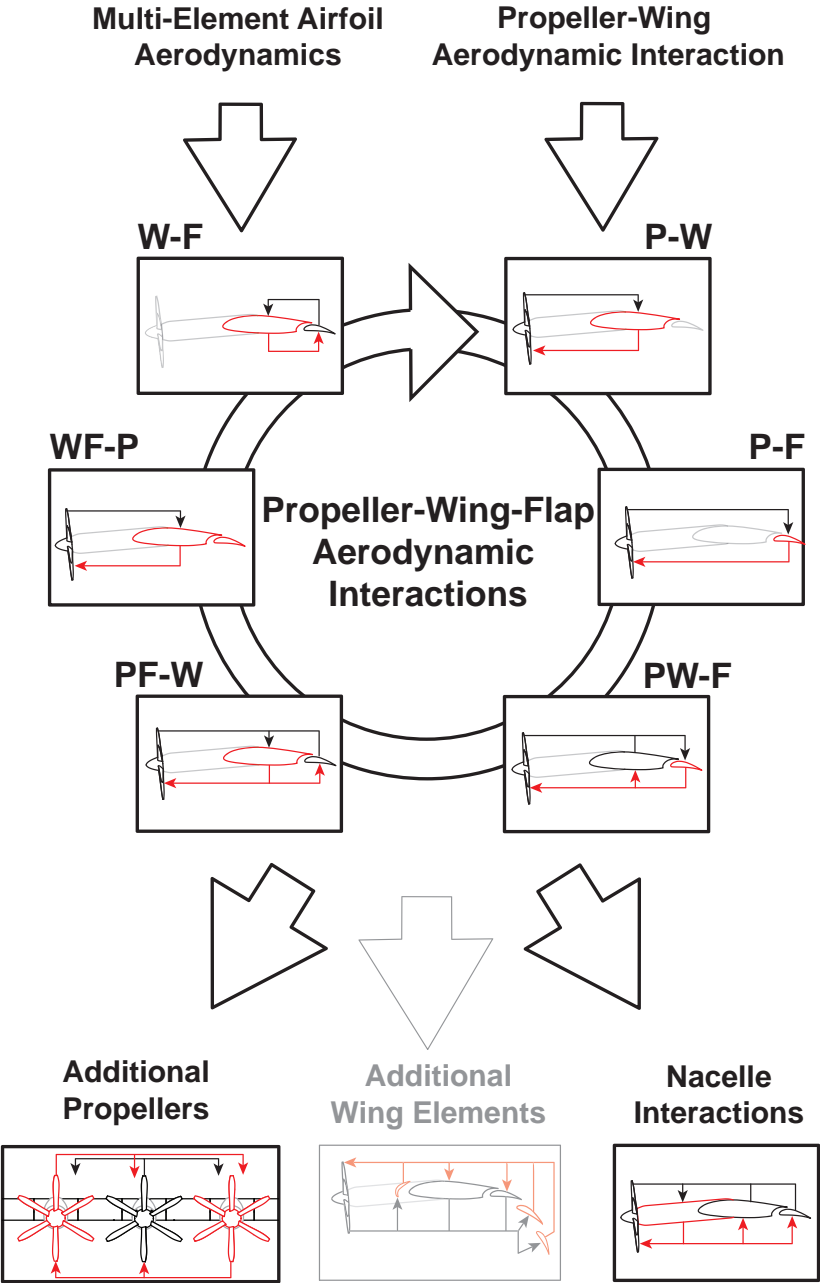
**1**



Figure 1.10: Illustration of the interactive modes that constitute the aerodynamic interaction between propeller (P), wing (W) and flap (F), and various systems of higher complexity that it relates to.
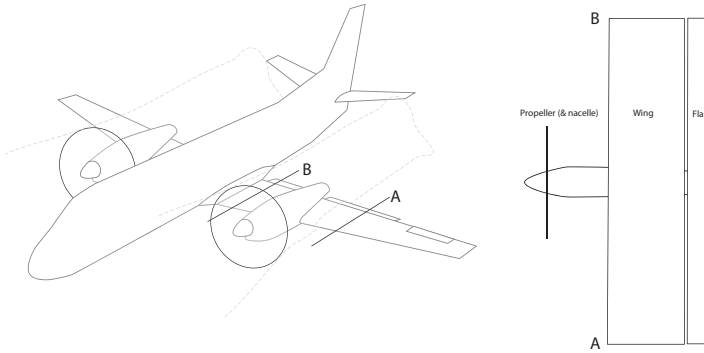
**1**



Figure 1.11: Reduction of a propeller-driven aircraft geometry to the essential testing components.

The nacelle can also be regarded as an active component in the propeller-wing-flap aerodynamic interaction (or rather *propeller-nacelle-wing-flap* aerodynamic interaction). Samuelsson [30] and Veldhuis [31] already noted the role of the nacelle in the propeller-wing-flap aerodynamic interaction. Many modern works on propeller-wing-flap aerodynamic interactions (e.g., Beckers et al. [47] and Oldeweme et al. [48]) feature propellers as detached from the wing, to benefit from the flexibility in placement of the propeller with respect to the wing. If the nacelle is to be considered an active component in the interaction, such setups should be interpreted as a specific nacelle integration configuration (or rather, lack thereof). In the main body of this dissertation, we consider the nacelle as an inherent part of the propeller system. As an extension of the primary research scope, we also explore the impact of a specific nacelle integration on the wing flow in the absence of a propeller and in low thrust conditions. Variations in the nacelle geometry and its integration with the wing are deemed out of scope.

We exclude any additional high-lift elements beyond the single slotted flap. Further increasing the number of components in the system, exponentially increases the number of interaction modes. This proliferation of interaction modes impedes analysis, as discussed previously. Moreover, while the addition of more flap elements would make the interaction more complex, it does not add phenomenological aspects to the system compared to a single slotted flap. The primary mechanisms of multi-element airfoil aerodynamics can be generalized to effects of upstream and downstream elements [35] and are all captured in a two-element system. Leading-edge high-lift devices, such as slats or droop noses, are also neglected. Slats are difficult to integrate with leading-edge mounted propellers and droop noses can be considered as a modification in airfoil camber, rather than a device that induces new aerodynamic mechanisms. The reduction of the number of high-lift elements also coincides with the trend in modern commercial-class aircraft design, as well as modern concepts utilizing HLP and DP, to minimize the complexity of passive high-lift devices.

Unlike the interaction modes with additional wing elements, we do explore the effect of additional propellers. In contrast to the effect of more than two wing elements, additional propellers are likely to change the aerodynamic phenomena that occur. De Vries et al. [49] show that adjacent propellers induce small deformations in slipstream

shape, though it is ultimately negligible when only considering an array of propellers. In presence of a downstream wing, however, this may change significantly as these small deformations can be amplified by the wing interaction. We therefore explore how the propeller-wing interaction of a single propeller differs from a distributed propeller setup. As with the nacelle integration analysis, this is deemed an exploratory extension of the primary research scope. While we do not include flap deflections in this exploration, high angles of attack are included.

### 1.5.3. METHODOLOGY

An effective investigation of the propeller-wing-flap aerodynamic interactions will require a combination of numerical and experimental methods. Multi-element wing aerodynamics are governed by both viscous and inviscid flow effects [50, 51]. Modern numerical simulation methods still struggle to accurately predict the aerodynamic behaviour of the viscous flow effects in high-lift conditions [37, 52]. In these conditions, the accuracy of turbulence models in traditional CFD methods such as RANS is inconsistent. Well established turbulence models such as the $\kappa - \omega$ Shear Stress Transform (SST) and Spalart-Allmaras (SA) models can result in completely different predictions of boundary layer separations on the flap of a propeller-wing configuration [53]. This emphasizes the necessity for experimental validation data whenever performing numerical simulations for such configurations, which are notably lacking in literature for propeller-wing-flap configurations.

On the other hand, the difficulty in reaching full-scale Reynolds numbers in wind-tunnel experiments is equally problematic as multi-element wings are highly sensitive to both Mach and Reynolds number effects [51]. Additionally, whereas the wing boundary layer can be tripped to avoid transition effects associated with low Reynolds number testing, such as laminar separation bubbles, this is generally difficult on small-scale propeller blades. Moreover, obtaining enough data to analyse the highly three-dimensional propeller slipstream in-depth using experimental methods is markedly more difficult than it is using numerical methods.

We therefore apply both numerical and experimental methods in this dissertation. Experimental data provides the validation data necessary to estimate the accuracy of numerical simulations, while the information density of the numerical simulations significantly increases the ability to investigate the intricate aerodynamic mechanisms at play. The use of coupled experimental and numerical methods inherently restricts the variations in geometry that can be investigated. While numerical simulations allow for variations in wing and propeller designs to be implemented easily (barring the time required to solve several high-fidelity simulations), this is not the case for experimental models. This dissertation is therefore mostly based on a single propeller-wing-flap design. The investigation of multi-element airfoil aerodynamics in a propeller slipstream is an exception, which uses a different airfoil design from the rest of the dissertation.

### 1.5.4. INTERPRETATION OF THE RESULTS

Although this dissertation is limited in its treatment of different propeller-wing geometries and Reynolds numbers, its conclusions are still valuable to achieve the purpose of achieving an intuitive insight into the propeller-wing-flap flowfield. The analyses in this

**1**

dissertation generally are performed from a phenomenological point of view, treating the aerodynamic phenomena that occur and the fundamental mechanisms that govern them. These are put into a broader context than the specific propeller and wing geometries. We do not focus on traditional performance metrics and their absolute values, which would certainly be subject to scaling effects.

Nonetheless, it is important to put the role of aerodynamic scaling into perspective. The performance of a particular multi-element wing is highly dependent on Reynolds and Mach numbers. A different Reynolds or Mach number affects the optimal overlap and gap for a given system, however not the mechanisms that governs this optimum. Barring boundary layer transition effects, the flap performance is governed by viscous flow mechanisms such as boundary layer separation, confluence of the main and flap boundary layers and bursting of the main element wake. While these effects generally become less dominant for a given angle of attack when Reynolds number increases, they still govern the limits of performance of the given airfoil. In this sense, understanding how the aerodynamic phenomena and mechanisms are affected by the propeller slipstream is transferable across a wide range of scales.

Whereas multi-element airfoil aerodynamics are governed by viscous flow effects, the propeller slipstream can be largely described by simple vortex element systems and potential flow equations, which are independent of Reynolds number. Interactions between viscous flow features such as blade wakes, vortex cores and boundary layers will, however, be subject to change at different Reynolds numbers. Again, this will mostly determine when certain effects become dominant, not whether they occur from a phenomenological point of view. Overall, viscous effects can be expected to become less prominent at higher Reynolds numbers. Furthermore, propeller-wing-flap aerodynamic interactions are important considerations in all scales of aviation, not just at the high Reynolds numbers of commercial-class passenger aircraft.

## **1.6.** DISSERTATION OUTLINE

Figure 1.12 illustrates the outline of the dissertation. The numerical and experimental models are detailed in Chapter 2, along with details on specific experiments, numerical setups and post-processing. Chapter 3 presents the validation and verification efforts performed for the numerical models that we employed.

The main body of the work is contained by Chapters 4 through 7, as illustrated by Fig. 1.12. Chapters 4, 5 and 6 contain the main matter regarding propeller-wing-flap aerodynamic interaction modes, while chapters 7 and 8 explore additional complexities of the system (as illustrated previously by Fig. 1.10).

In chapter 4, we investigate how typical multi-element airfoil aerodynamics are impacted by a 2D jet, serving as a simplified analogy for the propeller slipstream. It investigates which variables (and, crucially, interactions between variables) in the design space are dominant. Chapter 5 treats the main phenomena of propeller-wing-flap interaction as a three-dimensional system. It compares the aerodynamic interactions at cruise conditions with propeller-wing interaction at high-lift and propeller-wing-flap interaction. We discuss several aerodynamic phenomena that only occur in high-lift conditions and how the main element and flap element are affected differently by the slipstream. We furthermore illustrate the importance of slipstream deformation for the propeller-wing-flap
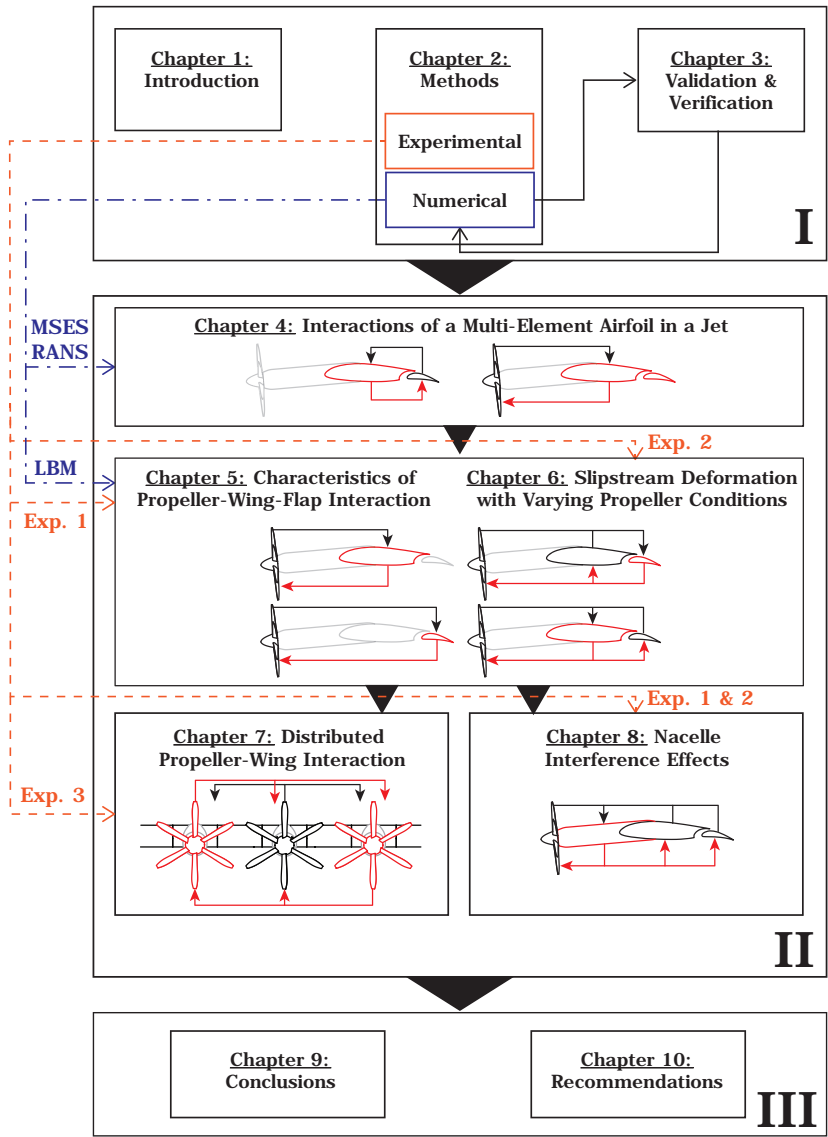
Figure 1.12: Outline of the dissertation, showing the links between the parts and chapters.

**1**

interaction and characterize different stages of deformation of the slipstream as it passes from the propeller over the wing. In chapter 6 we further investigate the mechanisms of the slipstream deformation and how the deformation is altered by characteristics of the helical vortex system. We vary the propeller thrust and torque coefficients to generate slipstreams with different ratios of longitudinally and azimuthally distributed vorticity and analyse how this impacts the slipstream deformation in various wing configurations.

Chapter 7 explores the impact of a distributed propeller system on slipstream deformation, as compared to the single propeller configuration. This serves as an outlook for future research and how the insights from the single propeller configuration can be used to interpret more complex systems. This chapter is limited to a flap nested configuration, although it does include analyses of high angles of attack. Similarly, we explore the interference effects of the nacelle on the wing flow in Chapter 8. This chapter specifically focuses on how the leading-edge mounted nacelle affects the wing flow, when the propeller slipstream does not dominate the flowfield. We investigate the impact of the nacelle integration without a propeller present, as well as a configuration where the propeller supplies very little thrust and the slipstream interaction effects are limited. This chapter is limited to the specific nacelle integration featured by the model used in this dissertation, which is detailed in Chapter 2.

Finally, the dissertation is concluded in Chapter 9, while Chapter 10 provides recommendations for future research.

# 2

## METHODS AND SETUP

*This dissertation relies on both experimental and numerical means of acquiring data, profiting from the relative strengths of both methodologies. This chapter contains details on each method employed in this dissertation. The experimental setups can be found in Section 2.1. This includes a description of the main wing and propeller design that was used for all studies in this dissertation, the only exception being the 2D simulations of Chapter 4. It furthermore includes descriptions of the various measurement techniques and details specific to each experiment. The numerical methods are detailed in Section 2.2, the validation and verification of which will be provided in Chapter 3. Besides the main numerical modelling methods, Section 2.2 also describes the main details of the regression analysis methodology used in Chapter 4.*

## 2.1. Experimental Setups

All wind tunnel experiments were performed at the Low Turbulence Tunnel (LTT) of the Delft University of Technology, a closed single-return tunnel with a maximum velocity of 120 m/s. The tunnel features interchangeable test sections with an octagonal cross-section. These test sections have a width of 1.8 m, a height of 1.25 m and length of 2.6 m, with the diagonal sections are at an angle of 135 deg and measure 0.425 m (see Fig. 2.1). The test section walls are slightly divergent to compensate for the streamwise pressure gradient induced by the boundary layer on the wind tunnel walls. In a cross-section at the centre of the (empty) test section, the variation of dynamic pressure is less than ±0.05% [59]. All experiments in this dissertation were performed at a freestream velocity of 30 m/s, at which the average turbulence intensity is 0.02% [60]. The experiments all utilize the same propeller-wing-flap design (dubbed the *TU Delft Propeller-Wing-Flap (TUD-PWF) model*), detailed in Section 2.1.1. The model was always mounted vertically in the test section, spanning the entire height of the test section (a quasi-2D wing setup), and was mounted to a turntable at each end. These turntables are flush with the floor and ceiling of the test section.
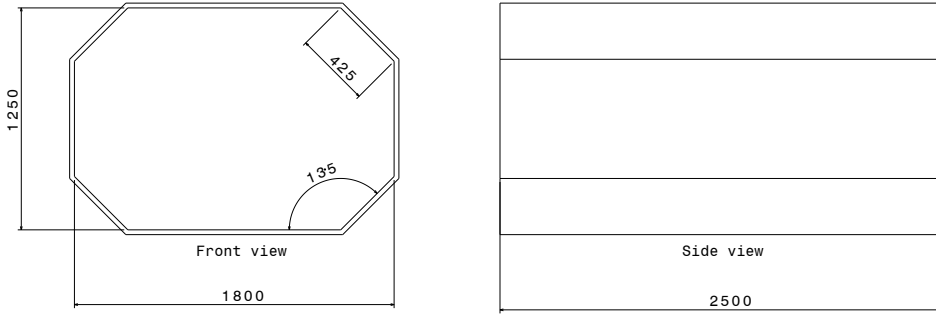


Figure 2.1: Schematic of the test section. Dimensions in mm.

The results presented in this dissertation are all as measured, with no wind tunnel corrections applied. For many of the measurements, such as the distributions of total pressure in planes perpendicular to the freestream (see Section 2.1.2), corrections cannot be applied. For sake of consistency of the measurements throughout the dissertation, also all polar data and pressure distributions presented in this document are uncorrected. Moreover, the impact of classical wind tunnel corrections (e.g., the methods of Barlow, Rae and Pope [61]) is very small due to the relatively small model size compared to the dimensions of the test section (Fig. 2.1). The solid blockage of the model is less than 0.2%, based on the airfoil thickness-to-chord ratio of $\frac{t}{c} = 0.17$ and $\lambda_{2D} \approx 3$ (from the graphs by Barlow, Rae and Pope [61]). As we did not measure the total drag coefficient of the wing, the wake blockage cannot be calculated. However, based on the original measurements of the wing profile by Boermans and Rutten [62], it is expected to be less than 0.1% for all tested configurations. Slipstream blockage at the maximum tested thrust coefficient is less than 0.3%.

### 2.1.1. EXPERIMENTAL MODEL

The experimental model consists of a straight, untapered wing with a single-slotted flap of 30% chord. It features an NLF-mod22(B) airfoil [62], with a chord of 0.3 m and a span of 1.248 m. The main wing is mounted to the wind tunnel walls with 1 mm shims at both sides, leaving no gap with the wall. The flap is mounted to the main element using six brackets, thus leaving a gap of 1 mm on both ends of the flap, which are taped off during the experiments to prevent bleed flow. The brackets can be swapped to deploy the flap to various positions, which in this dissertation include: the nested position, a deployment of 15 deg with 2% gap and 8% overlap, and a deployment of 30 deg with 3% gap and 0% overlap. These positions respectively represent a low-lift, take-off, and landing configuration. Definitions of deflection ($\delta_f$), overlap (d$x$) and gap (d$s$) are given in Fig. 2.2. The airfoil design and the various flap positions are illustrated in Fig. 2.3. A technical drawing of the wing with a single nacelle and propeller mounted, is given in Fig. 2.4.
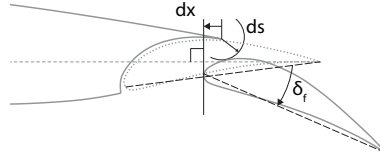


Figure 2.2: Definition of deflection ($\delta_f$), gap (d$s$) and overlap (d$x$).
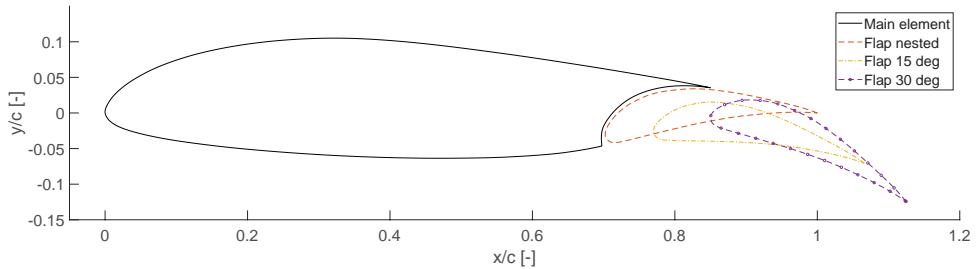


Figure 2.3: NLFmod22(B) profile with flap nested, flap deployed at 15 deg (d$x$ = 8%, d$s$ = 2%) and flap deployed at 30 deg (d$x$ = 0%, d$s$ = 3%).

The wing can be equipped with up to three nacelles, each housing an electric motor to drive a propeller. The nacelles attach to the wing leading edge, blending into the wing, and have a downwards angle of 5 deg with respect to the wing chord. They are cylindrical and relatively long, measuring 56 mm (0.187c) in diameter and 173.5 mm (0.578c) from the wing leading edge to the start of the propeller hub. All experiments utilize the TUD-XPROP-S reference propeller, a six-bladed propeller with straight blades and a diameter of 203.2 mm. The single propeller configuration shown in Fig. 2.4 was used for the majority

**2**
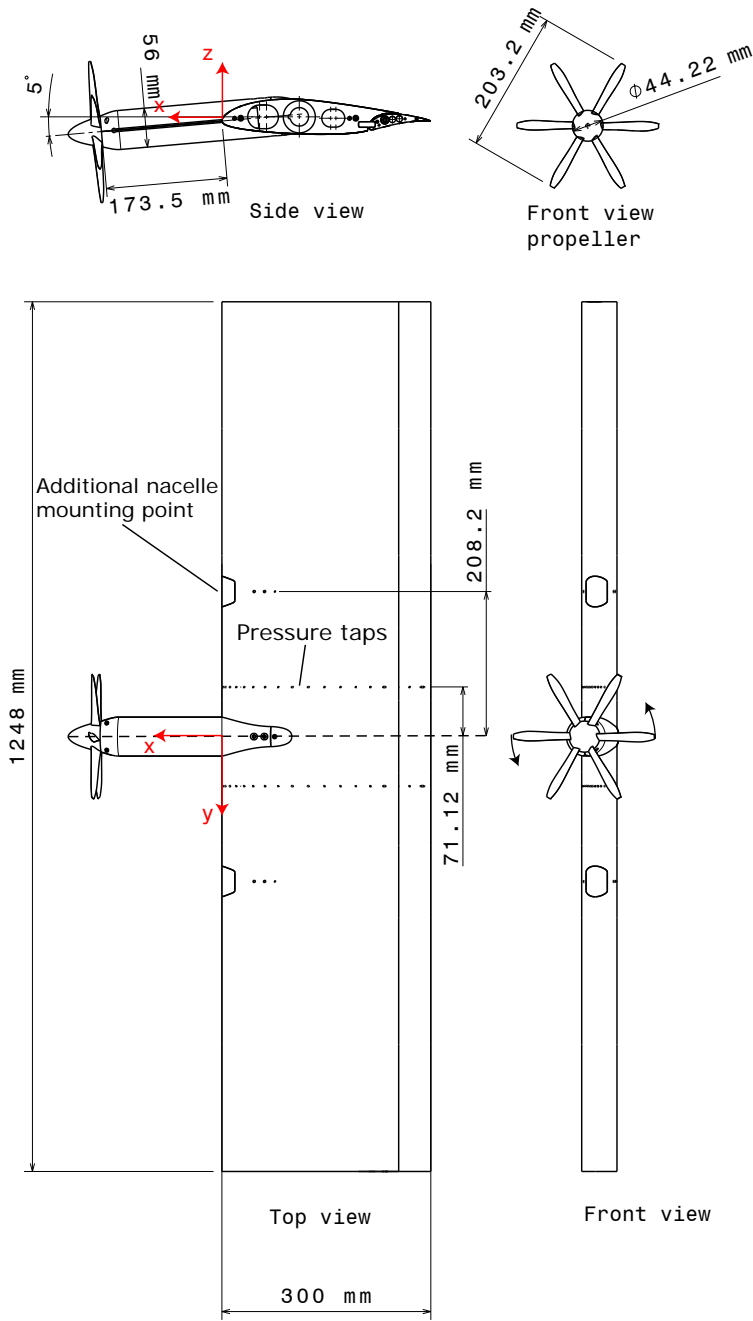


Figure 2.4: Technical drawing of wind tunnel model. Dimensions in mm.

of the studies in this dissertation, except for Chapter 7, which investigates the slipstream deformation in a distributed propeller-wing configuration. For that study, two additional nacelles and propellers were mounted at the locations indicated in Fig. 2.4, yielding a blade tip distance of 5 mm.

Figure 2.4 also shows the reference axes that are used throughout this dissertation (unless mentioned otherwise). We chose a coordinate system such that the y-axis was positive to the right and the z-axis was positive upwards when viewing the wing from the front. We deemed this the most logical system when investigating distributions and deformations of the slipstream in the $yz$-plane. Note that as a result, the $x$-coordinate is defined as positive upstream to maintain a right-handed system, which is somewhat unconventional.

The model also features two rows of pressure taps. These are located at $y/R = 0.7$ on either side of the central nacelle, and are thus positioned within the slipstream of the centre propeller. There was no telemetry on the propellers, apart from encoders to measure frequency and thermocouples to monitor motor temperature. The wing boundary layer was tripped by a zigzag strip at $0.1c$, on the main element suction side only. The purpose of the trip strip is to mitigate low Reynolds number effects such as laminar separation bubbles, as well as to match the turbulent state of the boundary layer that is normally imposed in numerical simulations, to facilitate validation. During testing, we found the performance of the clean wing (without nacelles or propellers installed) at high angles of attack to be highly sensitive to the tripping method. A short report on this can be found in Appendix A.3. Ultimately, a zigzag strip of 0.255 mm height and 12 mm width, with an angle of 60 deg, was found to least affect the high-lift performance of the wing, while still satisfying the intended purpose of tripping. Since this strip is too physically large to be applied properly to the flap, the flow was left to transition naturally. Furthermore, no strip was applied to the pressure side of the wing, as this was deemed non-critical since the pressure side (generally) is not affected by laminar separation bubbles at high angles of attack. The general setup of the wing in the wind tunnel is shown in Fig. 2.5. The wall boundary layer suction system indicated in Fig. 2.5b was found to be redundant and is not used in the results presented in this dissertation. More details can be found in Appendix A.2.

The geometry of both the propeller and the wing are available on request. The propeller geometry can be found at [63], while its performance is described in [64] and [49]. The wing geometry is available from [65]. Experimental data on the wing performance, both in clean wing configuration and with the central propeller mounted, as well as extensive measurements of the slipstream flow are provided as validation dataset at [66]. Performance graphs of the clean wing and the wing with a single propeller are also provided in this dissertation in appendix A.

(a) Pressure side                                    (b) Suction side
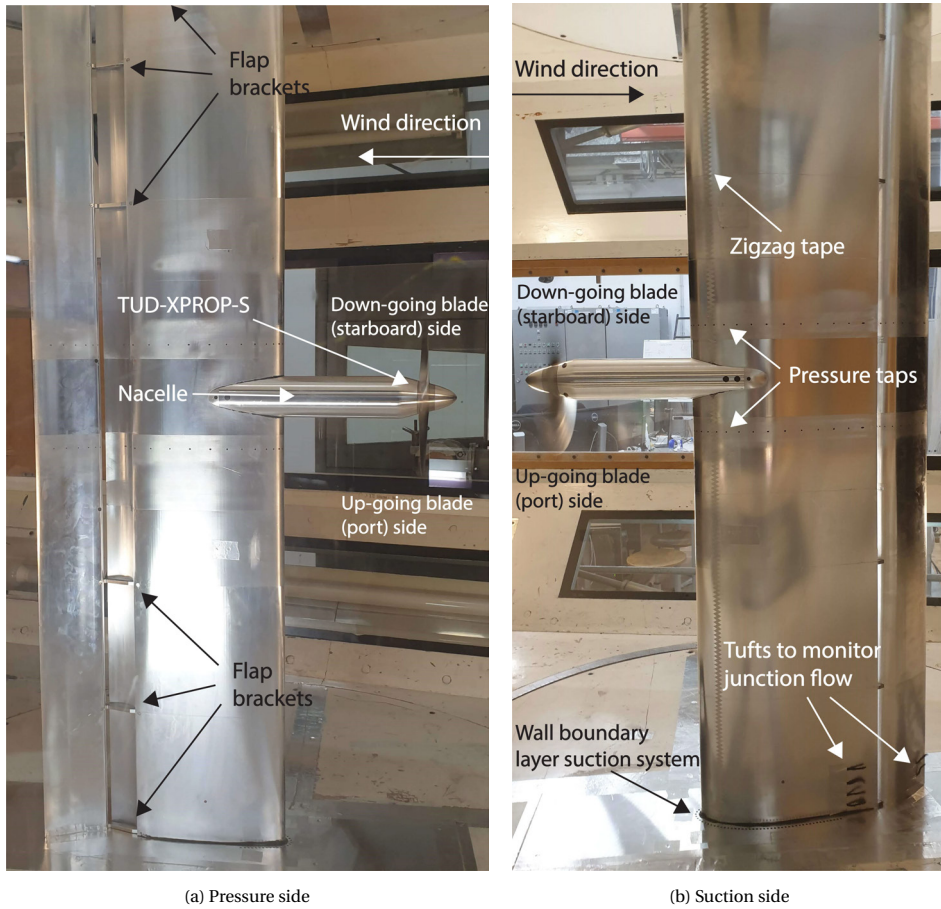
Figure 2.5: Wing as placed in the test setup with flap deployed and nacelle and prop attached.

### 2.1.2. Measurement Techniques

Across the various experiments, a range of measurement techniques were applied, including: a wake rake with total and static pressure probes, fluorescent oil flow visualization, digital 7-hole probe measurements and infra-red (IR) thermography. As the pressure taps on the wing have already been noted, they are not specifically treated in this section. Not every measurement technique was applied to every experiment. The specifics of each experiment, including which measurement techniques were applied and any small differences from the general setup, are detailed in Section 2.1.3.

#### Wake Rake

A wake rake with total and static pressure probes was placed at a downstream location of $x/c = -2$ (note again that the $x$-axis is defined positive upstream, as explained in Section 2.1), meaning the tips of the probes were positioned one chord-length from the wing trailing edge at $\alpha = 0$ deg. The position of the wake rake with respect to the wing in the test

section is illustrated in Figure 2.6, while Figure 2.7 shows the dimensions and spacing of the probes. The wake rake was traversed in vertical and spanwise directions with respect to the test section, meaning measurement planes are always perpendicular to the freestream. Resolution of measurement points was 10 mm in spanwise direction, while in normal direction the wake rake was aligned with the centre of the wing wake, with additional measurements at ±99 mm from the wake centre. This ensured a spatial resolution of 3 mm within ±400 mm from the test section centreline due to the distribution of probes on the wake rake.
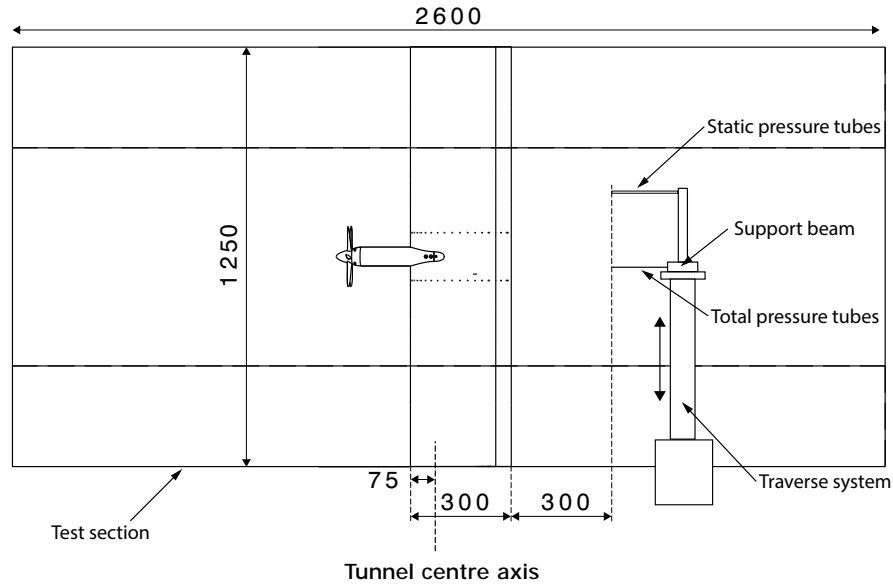
Figure 2.6: Positioning of the wake rake in the wind tunnel test section. Side view. Dimensions in mm.
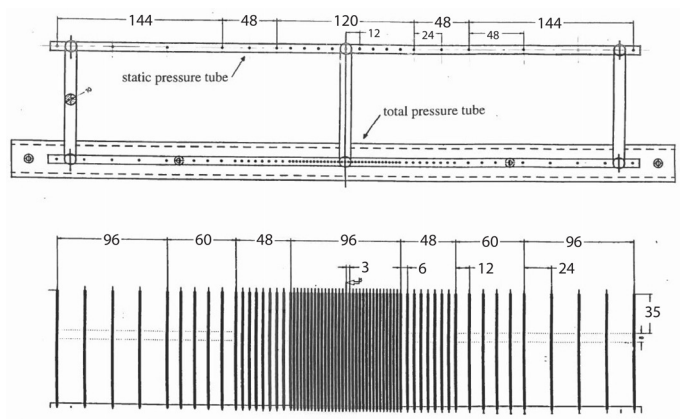
Figure 2.7: Wake rake top and front view.

## OIL FLOW VISUALIZATION

Application of fluorescent oil flow visualization provided qualitative insight into the wing surface flow. The oil was a mixture of paraffin oils of varying viscosity (i.e., 80% Shell Ondina 15 and 20% Shell Ondina 32) with 20 drops of A-680 fluorescent oil additive added per 30 millilitres of oil. The oil was illuminated using Philips TL-D BLB Blacklight Fluorescent Tube lights, in combination with a 400 W UV-spotlight. Images were captured with the wind tunnel turned on, using DSLR cameras mounted on tripods on both sides of the test section. Each camera was fitted with a 470 nm low-pass filter, which filters most of the light from the fluorescent tube lights and their reflections, but passes the wavelength of emitted by the fluorescent oil additive. Figure 2.8 illustrates the oil flow setup. Oil flow visualization images were post-processed using Adobe Lightroom (version 7.4.1). Image contrast was maximized and images were edited for highlights and shadows to improve the visibility of oil flow paths. All images were subsequently de-noised and sharpened using the AI assisted tools provided by Lightroom.

It should be noted that as the wing was mounted vertically in the wind tunnel, gravity plays a significant role in the transport of the oil, particularly in areas where the shear forces are low. The oil flow thus indicates dominant flow direction in regions of high shear, but cannot fully be interpreted as streamlines of the flow. Furthermore, although Fig. 2.8 shows the probe traverse system (as well as the black vinyl layer used for IR thermography), these components were not present for all experiments. See Section 2.1.3 for the specifics of each experiment.
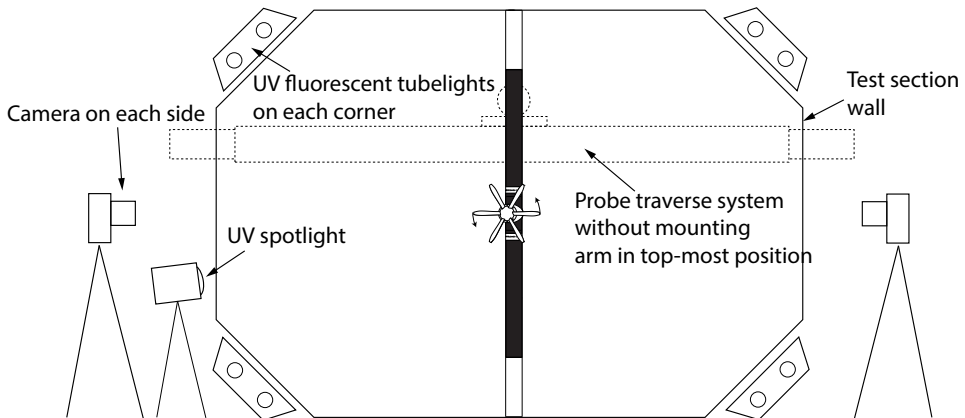


Figure 2.8: Experimental setup for the oil flow visualizations. Front view. Dimensions in mm.

## DIGITAL 7-HOLE PRESSURE PROBE

Distributions of total and static pressure, as well as all three components of velocity, were acquired using a Surrey Sensors Ltd. USM-ID7HP-050224-3.0 Digital 7-hole Pressure Probe. It contains an internal 6.9 kPA FS differential pressure sensor with a sensor accuracy of $\pm 0.1\%$ FS. The probe outputs data at a maximum rate of 1 kHz. It can be fitted with one of two custom probe stings: a straight sting (Fig. 2.9a) and one with a 90-degree crank

2

(Fig. 2.9b), both with a tip diameter of 2 mm.

The straight probe was used for measurements on the wing upper surface and behind the wing. Figure 2.10 shows an illustration of the setup of the straight probe system. A three-axis traversing system was positioned downstream of the test section in the diffusor of the wind tunnel, with an articulated arm reaching upstream into the test section on which the probe was mounted. The probe sting was aligned with the test section central axis and the tip could reach from just behind the wing (in all configurations) up to around 30% chord, depending on the angle of attack of the wing.

The cranked probe was used to reach behind the propeller and the lower surface of the wing. The cranked probe setup is illustrated in Fig. 2.11. It was mounted on an aerodynamic profile that entered the test section from the side, using a traverse system aligned with the test section side. This system could only move perpendicular to the freestream direction when measuring, but could be repositioned along the test section between measurements, without losing its alignment to the wind tunnel.

We took pressure measurements of planes perpendicular to the freestream direction at various chordwise stations over the wing, as well as along spanwise lines just above the wing surface, as illustrated in Fig. 2.12. We scanned the measurement planes by moving the probe through the planes in straight lines at a traverse speed of 7.5 mm/s, while measuring continuously at a datarate of 250 Hz. Exceptions are the measurements with the three-bladed propeller, which were taken at a traverse speed of 15 mm/s to reduce measurement time and mitigate overheating of the electric motor that drives the propeller. We verified that at each traverse speed the response of the probe was fast enough to capture the gradients in pressure accurately by comparing the moving measurements to point-by-point measurements. The traverse paths for the measurement planes at $\alpha = 8$ deg and $\delta_f = 15$ deg are illustrated in Fig. 2.13. Note that these paths will vary slightly for each configuration, as the planes are always perpendicular to the freestream direction, not the wing chord, and hence are dependent on the wing model angle of attack and flap deflection. The streamwise coordinates of the propeller, nacelle, and cove planes are equal in all tested configurations, while their vertical coordinates are



(a) Probe with straight sting

(b) Probe with cranked sting

Figure 2.9: Technical drawing of the 7-hole pressure probe with each custom sting.

**2**



(a) Front view



(b) Side view

Figure 2.10: Illustration of the traverse setup for the straight probe sting. Dimensions in mm.

Test section wall

Aerodynamic profile

Traversing system

Straight probe traverse system without mounting arm in top-most position

Probe body with cranked sting

(a) Front view

Straight probe traverse system without mounting arm in top-most position

Wind tunnel diffusor

Test section

Secondary position (Cove plane)

Aerodynamic profile

Probe body with cranked sting

Traversing system

(b) Top view

Figure 2.11: Illustration of the traverse setup for the cranked probe sting.

**2**



Figure 2.12: Measurement plane locations

adjusted for the orientation of the model. The *METE* plane is adjusted for the location of the main element trailing edge (METE), while the wake plane is vertically centred on the flap trailing edge, and positioned at 5 cm downstream of it. The traverse paths were manually adjusted to minim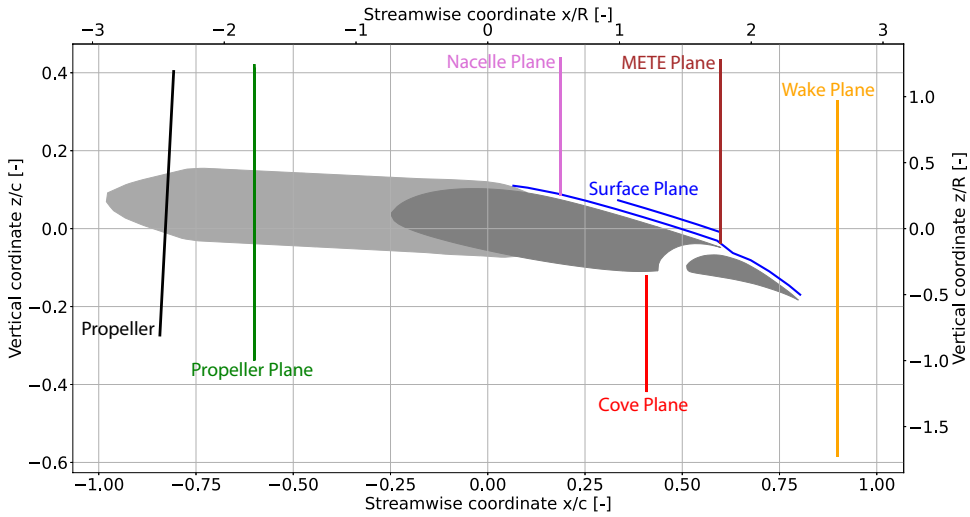ize the traverse distance (and therefore measurement time), while capturing the entire slipstream as it deforms and displaces over the wing.

In post-processing, the measurement data are passed through a Savitzky-Golay filter [67] to reduce noise of the pressure sensor while maintaining the sampling resolution. From the 7-hole pressure measurements, we calculate the local total and static pressure measurements, as well as all three components of velocity. For these calculations, we use the methodology of Shaw-Ward, Titchmarsh and Birch [68]. The required calibration of the pressure probes was performed by the manufacturer, for each of the probe stings separately. The calibrations were performed after the experiment, matching the orientation of the probe body during the experiments using the internal accelerometer.[1]

The measurement planes were chosen to visualize different stages of the deformation. The propeller plane gives the initial condition of the slipstream and is mainly used as a check for the selected theoretical operating conditions (see Chapter 6). The plane behind the nacelle blend captures the initial deformation of the slipstream from the interaction with the wing leading edge. Together with the planes at the main element trailing edge and the flap trailing edge plane, the entire deformation over the wing upper surface is visualized. Similarly, the cove plane and flap trailing edge plane show the deformation on the lower surface of the wing. Additionally, the cove plane yields the inflow condition of the flap when it is deflected. The planes on the upper surface of the wing and the flap

---

[1]During the experiment itself, the stings were aligned to the wind tunnel axes by laser. Data from the probe accelerometer was then recorded and reported to the manufacturer for subsequent calibration. The manufacturer aligned the probes by laser and checked the orientation via the accelerometer values.

(a) Propeller plane

(b) Nacelle plane

(c) Cove plane

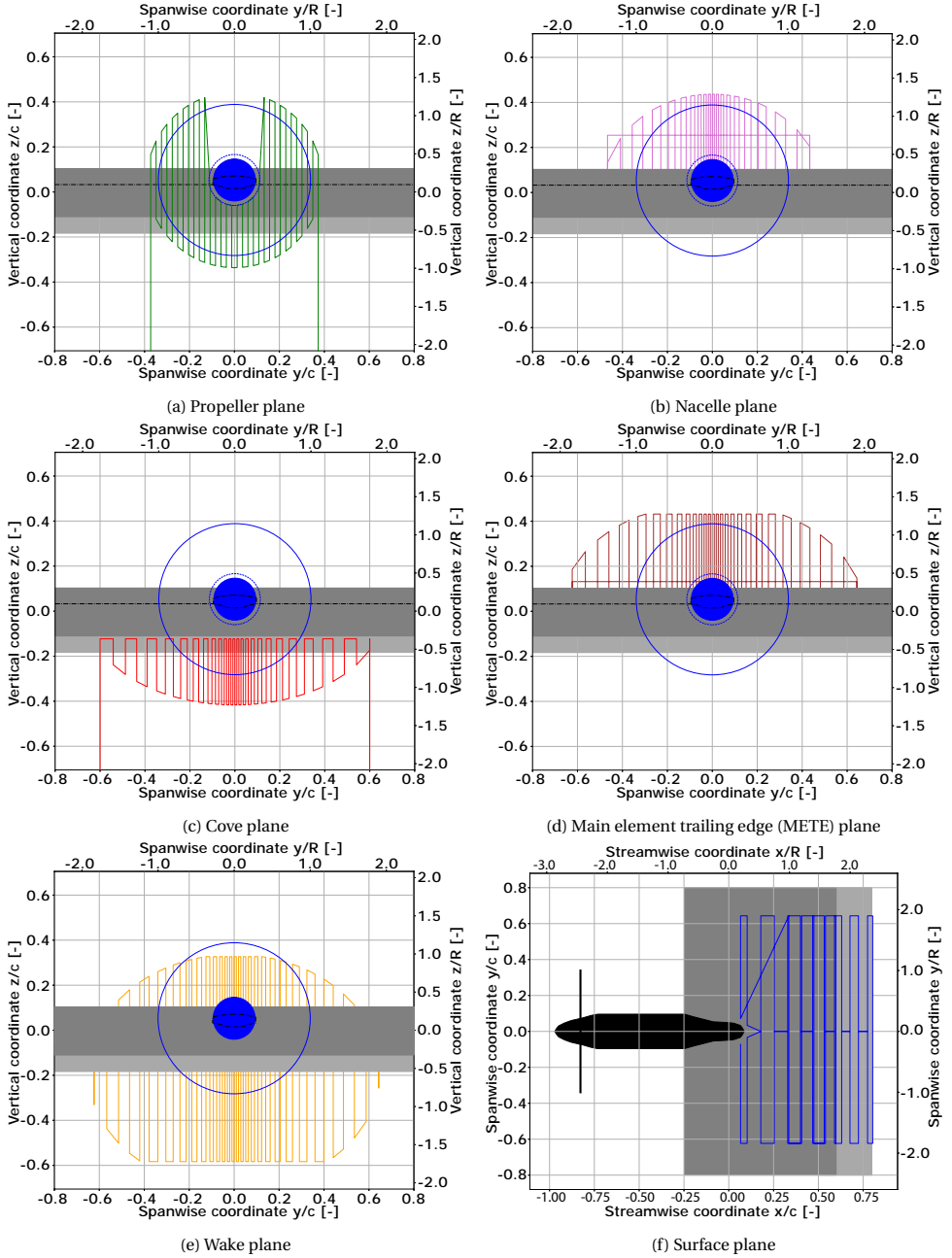(d) Main element trailing edge (METE) plane

(e) Wake plane

(f) Surface plane

Figure 2.13: Illustration of the measurement locations and corresponding paths of the measurement planes at $\alpha = 8$ deg and $\delta_f = 15$ deg.

trailing edge plane are all measured using the straight probe setup. The propeller and cove planes were captured using the cranked probe setup.

In all cases, a minimum normal distance between the probe centre and wing surface of 4 mm was maintained. We verified that this was the minimum distance required to avoid significant channel flow to occur between the probe tip and the wing surface. This was tested by placing the probe directly normal to one of the pressure taps on the wing and moving it closer until the pressure tap reading deviated from the initial value more than 5%.

The surface planes aligned with the wing upper surface consist of a primary plane at 4 mm from the surface and a secondary surface at 11 mm from the wing surface. The secondary plane was chosen based on numerical simulations (see Section 2.2.3) to be outside the boundary layer, since the calibration of the pressure probe to calculate the velocity vector can become unreliable if it operates within a strong pressure gradient over the width of the probe tip. This secondary plane therefore only covers a portion of the main element near the trailing edge, where the boundary layer is thickest (see Fig. 2.12). The surface planes are composed of spanwise continuous lines (see Fig. 2.13f). The (discrete) chordwise positions of these lines were selected to be aligned with the chordwise locations of the pressure taps of the wing, complemented with the most forward location reachable by the mounting arm, and the main element and flap element trailing edges.

### INFRARED THERMOGRAPHY

We utilized infrared (IR) thermography to measure the change in skin friction coefficient $c_f$ on the wing surface, resulting from the additional velocities in the slipstream. Numerical simulations (see Section 2.2.3) showed that $c_f$ was an effective parameter to determine the area of the wing that is washed by the slipstream, and thereby the displacement of the slipstream edge as it moves over the wing. Measuring this displacement on the wing surface based on total pressure or velocity gradients is generally difficult, due to the viscous losses in the boundary layer.

IR thermography is typically used for detection of flow separation and boundary layer transition fonts (see for instance Zuccher and Saric [69], and Simon et al. [70]). It relies on the convective heat transfer $\dot{q} = h(T_W - T_\infty)$, with heat transfer coefficient $h = \frac{1}{2}c_f V_\infty \frac{k_f}{v}$, where $T_W$ is the wall temperature, $T_\infty$ is the fluid temperature, $c_f$ is the skin friction coefficient, $V_\infty$ is the freestream velocity, $k_f$ is the thermal conductivity of the fluid and $v$ is the kinematic viscosity. By keeping $\dot{q}$ constant, for instance by heating the surface of the model externally by electric heating, the wall temperature $T_W$ will change with the local skin friction coefficient $c_f$. This is captured by measuring the emitted IR radiation using IR cameras.

The experimental setup for the thermography measurements consisted of two Optris PI 640 IR cameras, mounted on each side of the wind tunnel behind special IR bandpass windows. The cameras were covered with boxes lined with aluminium tape to shield them from external infrared sources. Since the wind tunnel model is made from aluminium, which has a high heat capacity and thus dissipates local changes in temperature, a black vinyl foil with an average thickness of 100 $\mu$m was placed on the wing. This allows a temperature contrast to be achieved in the thermography measurements. To achieve the necessary temperature difference between the wing surface and the fluid flow, the model

was heated externally using arrays of halogen lights. Halogen lamps fitted with infrared bulbs were placed on the diagonals of the test section, with additional regular halogen lights placed around the test section sides. Figure 2.14 summarizes the experimental setup of thermography measurements.

The workflow for thermography was as follows. The halogen lights were turned on during pressure probe measurements and left on until thermal equilibrium was reached on the wind tunnel model, monitored using the IR cameras. Once probe measurements were completed and thermal equilibrium was reached, the cameras were reset and thermography images were captured for various advance ratios in quick succession. This means the probe traverse mechanism, including articulating arm, was present in the wind tunnel during all of the thermography measurements. The probe was always centred in the wind tunnel, behind the model, when thermography measurements were taken. The various advance ratios include the design values for the experiment for each wing configuration, as well as an advance ratio near zero thrust. The latter served as a reference condition for the wing, minimizing the effect of the slipstream on the wing surface flow, resulting in a skin friction coefficient representative of the unblown wing. Each measurement consisted of 100 consecutive images captured by the cameras. In post-processing, these images are averaged to reduce noise. Subsequently, we subtracted the reference measurement near zero thrust from the measurement at design values. This yields a measurement of where the skin temperature changes significantly due to an increase in skin friction on the wing caused by the slipstream.
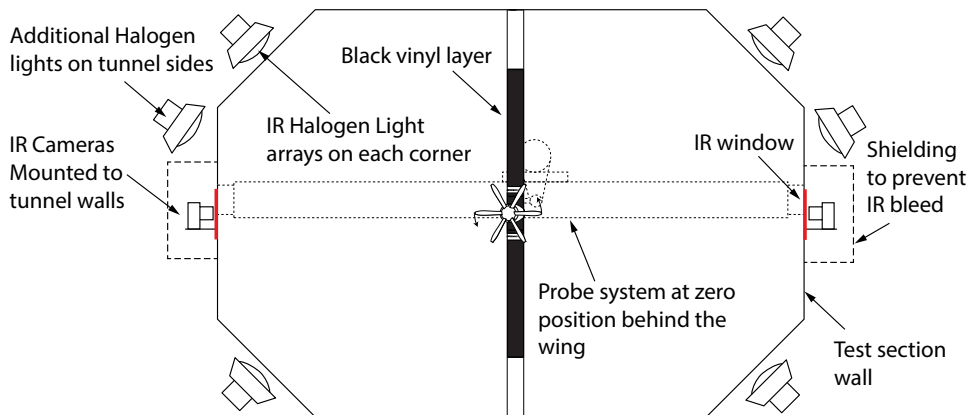


Figure 2.14: Experimental setup for the IR thermography.

ON THE EFFICACY OF IR THERMOGRAPHY

Our initial purpose to capture the change in $c_f$ caused by the propeller blowing on the upper surface (which was already tripped by the zigzag strip), rather than boundary layer transition, was met with mixed success. Based on numerical results (again, see Section 2.2.3), the change in $c_f$ between the unblown and blown parts of the wing surface was expected to be around a factor of 5. This is significantly lower than the typical change in

$c_f$ due to boundary layer transition, which is around a factor of 10 [70]. It was therefore unknown ahead of time whether the setup we used would result in enough contrast to visualize the slipstream path. In practice, we found that we were able to capture the change in $c_f$, but at a very low contrast. The measured change in temperature due to propeller blowing was close to the minimum temperature sensitivity of the cameras, resulting in a poor signal-to-noise ratio.

On the lower surface of the wing, however, we achieved much more consistent visualizations of the slipstream path. This opposed expectation, since the change in $c_f$ due to propeller blowing on the pressure side is much lower than on the suction side. The more consistent results can be attributed to the thermography actually visualizing the boundary layer transition. Unlike the suction side, the pressure side of the wing was not tripped, and the boundary layer likely remained laminar up to the cove of the main element in most configurations, since the airfoil was originally designed for natural laminar flow [62]. The turbulence in the slipstream, however, trips the wing boundary layer, resulting in a clear change in skin friction compared to the unblown parts of the wing.

Although the IR thermography did not fully work as originally intended, there is potential in using the method to visualize the slipstream deformation on the wing surface. This goes for both the method of measuring the slipstream-induced boundary layer transition of the wing, and the method of directly measuring the change in $c_f$ due to the increased velocities in the propeller slipstream. Results may be improved by improving the surface preparation, for instance by using conductive paint, to increase the achievable contrast. Additional (internal) surface heating and more sensitive cameras would also improve the setup.

The thermography measurements are only used to support interpretation of the oil flow images in Chapter 6. This combination leads to improved interpretation of the slipstream path on the wing surfaces. Figure 2.15 shows an example of how we combined these results to determine the slipstream paths. The correct overlap of oil flow images



(a) Processed oil flow image    (b) Extracted oil traces    (c) Thermography image    (d) Overlay of (b) and (c)
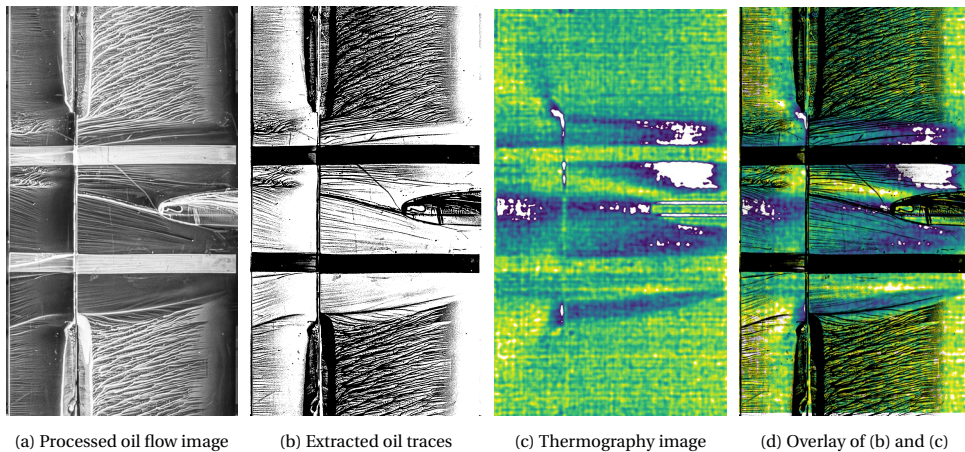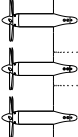
Figure 2.15: Example of processing steps to combine oil flow and thermography results. Wing lower surface view, freestream from right to left.

and thermography measurements was performed manually, using the nacelle and wing and flap trailing edges as reference.

### 2.1.3. Experiment Details

This dissertation contains results from a total of three wind tunnel experiments. The first experiment aimed to define the aerodynamic performance of the model and yield a first insight into the propeller-wing(-flap) aerodynamic interactions at high angles and with deflected flap. The second experiment expands on the first experiment by including different operating conditions for the propeller and improved measurement techniques. The purpose of this experiment was to investigate the relation between the slipstream characteristics and the deformation of the slipstream resulting from interaction with the wing and flap. The third experiment was designed to investigate the difference in slipstream deformation between a single propeller setup and a distributed propeller setup, and serves as an outlook for future research topics. A tabular overview of the experiments, the applied measurement techniques, and how they relate to the different chapters in this dissertation, can be found in Table 2.1.

Table 2.1: Overview of the models and measurement techniques used in each experiment.

| Experiment | Model config. | Measurement techniques | Relates to |
|---|---|---|---|
| 1 | | Pressure taps | Chapter 5 |
| | | Wake Rake | Chapter 8 |
| | | Oil Flow | |
| 2 | | Pressure taps | Chapter 6 |
| | | Digital 7HP | Chapter 8 |
| | | Oil Flow | |
| | | IR Thermography | |
| 3 | | Pressure taps | Chapter 7 |
| | | Wake Rake | |

#### Experiment 1: Identification of Aerodynamic Phenomena

The first experiment was meant to study the performance of the clean wing versus the wing with propeller (and nacelle), and to study the differences in the propeller-wing interaction caused by flap deflections. Measurement techniques included the pressure taps on the wing, the wake rake setup and oil flow visualization on the wing suction side. The setup of the oil flow visualizations was a simplified version of the setup discussed in Section 2.1.2. We used only a single camera, pointed at the wing upper surface for nearly all measurements. The wing was not fitted with a vinyl layer, so oil was applied directly to the aluminium surface. We also did not employ denoising and sharpening in Lightroom. In the experiment, each measurement technique was employed separately

to avoid interference effects. The pressure tap measurements specifically were taken without any other support structures in the tunnel.

Table 2.2 shows an overview of the configurations considered in the experiment. Due to time constraints, configuration 5 was limited to wake rake measurements only. All other powered cases were run at $J = 0.8$ and $J = 1.0$, corresponding to a high thrust coefficient ($T_c \approx 0.412$, where $T_c = \frac{T}{\rho_\infty V_\infty^2 D^2}$) and maximum propeller efficiency ($T_c \approx 0.177$). The high thrust coefficient setting was limited by the maximum torque that the electric motor could handle without overheating. The reported values of $T_c$ are based on isolated propeller performance curves from previous experiments by van Arnhem et al. [64] at the specified advance ratios, not direct measurements during the experiment. The propeller assembly was not equipped with any telemetry beyond temperature monitoring of the electric motors.

Table 2.2: Overview of tested configurations in the first experiment.

| Config | $\delta_f$ [deg] | d$s$ [-] | d$x$ [-] | Nacelle | Propeller |
|--------|------------------|----------|----------|---------|-----------|
| 1 | 0 | - | - | Off | Off |
| 2 | 15 | 0.02 | 0.08 | Off | Off |
| 3 | 30 | 0.03 | 0 | Off | Off |
| 4 | 30 | 0.03 | 0 | On | Off |
| 5 | 30 | 0.03 | 0 | On | On ($\beta_{0.7R} = 45$ deg) |
| 6 | 30 | 0.03 | 0 | On | On ($\beta_{0.7R} = 30$ deg) |
| 7 | 15 | 0.02 | 0.08 | On | On ($\beta_{0.7R} = 30$ deg) |
| 8 | 15 | 0.02 | 0.08 | On | Off |
| 9 | 0 | - | - | On | Off |
| 10 | 0 | - | - | On | On ($\beta_{0.7R} = 30$ deg) |

### Experiment 2: Effect of Helical Vortex System Characteristics

The second experiment was designed to study how the characteristics of the helical vortex system of the slipstream, such as the helix angle and the individual tip vortex strength, would affect slipstream deformation. The aim was to verify hypotheses based on the mechanisms of propeller-wing interaction proposed in literature [33]. Additionally, it was a direct extension of the first experiment, with the goal of obtaining an extensive validation dataset for propeller-wing-flap aerodynamic interaction research. Open access data of this type of configuration, particularly one with a minimal geometric complexity (i.e., no sweep or taper, wing-tip-effects or more complex combinations of high-lift devices). A dataset of the combined first and second experiments is therefore published at [66].

In the second experiment, the flap is either in its nested configuration, or deployed to a 15 degree deflection, with an 8% overlap and 2% gap. The wing was fitted with a black vinyl layer with an average thickness of 100 microns to facilitate thermography measurements. This vinyl was left on the wing for all measurements taken in this experiment. The nacelle and outer wing sections, as well as a strip of 1 cm around the pressure taps, were not covered. The zigzag strip on the main element upper surface was placed on top of the vinyl layer. Measurements involved the digital pressure probe setups, the IR thermography setup and the full oil flow visualization setup, as described in Section

2.1.2. The traverse system for the straight probe was present in the wind tunnel during all measurements, positioned as illustrated in Section 2.1.2. The articulated probe mounting arm was removed during the oil flow visualizations, however.

**Main test matrix**    Slipstream characteristics were controlled by the selection of specific propeller operating conditions. The motivation for the selected propeller conditions is part of the analysis in Chapter 6. Table 2.3 summarizes the propeller conditions used during the experiment (also present in Chapter 6). The indicated values of thrust and torque coefficients are based on numerical simulations using a BEM-solver for isolated propeller conditions. The value of $T_c$ at $J = 0.8$ reported in table 2.3 therefore differs slightly from the experimental measurement by van Arnhem et al. [64] reported in the description of experiment 1.

Table 2.3: Summary of numerical predictions of propeller performance for operating conditions used in the second experiment. Configurations will be referred to by their handle.

| Condition | Handle | $N_b$ [-] | $\beta_{0.7R}$ [deg] | $J$ [-] | $T_c$ [-] | $Q_c$ [-] |
|---|---|---|---|---|---|---|
| 1 | High $T_c$/High $Q_c$ | 6 | 30 | 0.800 | 0.422 | 0.079 |
| 2 | Low $T_c$/High $Q_c$ | 6 | 45 | 1.195 | 0.284 | 0.079 |
| 3 | Low $T_c$/Low $Q_c$ | 6 | 30 | 0.984 | 0.210 | 0.044 |
| 4 | Three-bladed | 3 | 37 | 0.717 | 0.284 | 0.079 |

Measurements of each of the conditions summarized in Table 6.1 included three wing configurations: $\alpha = 0$ deg with $\delta_f = 0$ deg, $\alpha = 8$ deg with $\delta_f = 0$ deg, and $\alpha = 8$ deg with $\delta_f = 15$ deg. Due to time constraints, the pressure probe measurements of the propeller plane were skipped for the $\alpha = 8$ deg, $\delta_f = 15$ deg configuration. The measurements of the $\alpha = 8$ deg, $\delta_f = 0$ deg configuration are not presented specifically in this dissertation, but are included in the published validation dataset.

**Secondary test matrix**    The second experiment also contained several measurements meant to explore whether nacelle-wing aerodynamic interactions become dominant at lower propeller thrust settings, when the propeller slipstream effects are less prominent. To this end, two main propeller conditions were tested: a *low thrust* coefficient setting ($J = 1.98$, $T_c \approx 0.05$) that is representative for landing regime and a *zero power* setting ($J = 2.42$, $T_c \approx 0.005$) where there was (almost) no power supplied to the electric motor of the propeller. These measurements include oil flow visualization of the wing upper surface and 7-hole pressure probe measurements at the nacelle blend, main element trailing edge and just downstream of the flap trailing edge, as defined in Section 2.1.2. Only high-lift conditions were considered, meaning the flap was deflected at $\delta_f = 15$ deg and the angle of attack was $\alpha = 8$ deg or 10 deg. We used the 6-bladed propeller with a blade pitch $\beta_{0.7R} = 45$ deg, as this configuration has the best efficiency at high advance ratios.

EXPERIMENT 3: DISTRIBUTED PROPELLER-WING INTERACTION

The third experiment was part of a larger experiment focused on the aeroacoustic performance of installed distributed propeller configurations. The results of the aeroacoustic measurements were published separately by Monteiro et al. [71] and are not absorbed in this dissertation. In addition to the acoustical measurements, we used the wake rake to capture the total pressure distribution in the wake of the wing, matching the setup of the first experiment. These distributions are again used to visualize the slipstream deformation in the wing wake in the distributed propeller configuration, serving as an exploratory study how the slipstream deformation differs between single and distributed propeller configurations. Due to time constraints, no flap deflections were applied, although high angles of attack were included.

Additionally, we investigated the impact of synchrophasing [2] on slipstream deformation in the installed condition. The control system of the propeller array allows us to lock the propellers in phase, with a specified relative blade phase angle between adjacent propellers. The definition of this angle is illustrated in Fig. 2.16. For all measurements in this experiment, the propellers were co-rotating in counter-clockwise direction when looking in streamwise direction. Besides measurements where the propellers were locked in phase, the experiment also includes measurements of randomized phase between propellers. This was achieved by forcing a difference in rotational speed of 0.03 Hz between each of the propellers. This ensures that they constantly vary the relative blade phase angle during measurements.
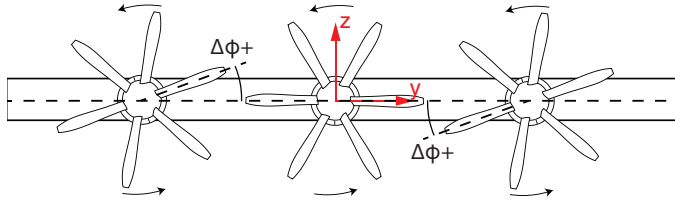


Figure 2.16: Definition of the relative blade phase angle $\Delta\phi$.

This experiment used a slightly different test section, which does not have divergent walls and where the diagonal sections of the wind tunnel contain acoustic lining, illustrated in Fig. 2.17. Since no flap deflections were applied in this experiment, the flap gap was taped off to prevent bleed flow. Otherwise, the setup was identical to the wake rake measurements performed in the first experiment, described in Section 2.1.2.

---

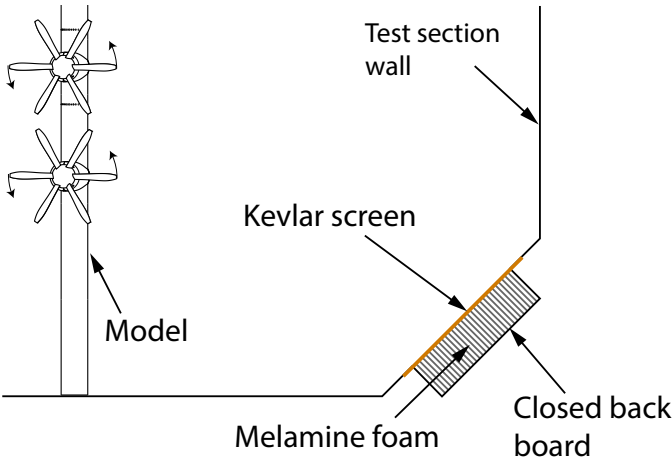[2]Varying the relative angle between the propellers in co-rotating mode

Figure 2.17: Kevlar lining on the diagonals of the acoustic test section used in the third experiment.

## 2.2. NUMERICAL SETUPS

This dissertation also includes the results of several numerical setups, the details of which are described in this section. The investigation of multi-element airfoil aerodynamics in 2D jet flows in Chapter 4 is based on simulations with a modified version of MSES, which is described in Section 2.2.1. This method is verified using 2D Reynolds-Averaged Navier Stokes (RANS) simulations (see Chapter 3), the setup of which is given in Section 2.2.2. A grid convergence study of the 2D RANS setup can be found in Appendix B. Finally, section 2.2.3 describes the setup of high-fidelity simulations that match the first experiment, which form the basis for a major part of the analysis in Chapter 5. Table 2.4 presents an overview of the various numerical methods and which chapters of the dissertation they relate to. Validation and verification efforts for the various numerical methods are described in Chapter 3.

Table 2.4: Overview of the numerical methods and the related chapters.

| Numerical method | Purpose | Relates to |
| --- | --- | --- |
| MSES (modified) | Flow simulations | Chapter 4 |
| 2D RANS | Verification of MSES | Chapter 4 |
| RSM | Response analysis | Chapter 4 |
| LBM | Flow simulations | Chapter 5 |

### 2.2.1. MSES with pressure jump modification

MSES is a 2D CFD solver, based on the Euler equations, able to handle multi-element airfoil simulations. It is a very computationally efficient solver, with average solution times in the order of minutes per configuration on a single CPU core. The streamline grid used by MSES is part of the solution, meaning it does not require pre-defined meshing for each configuration as is common in typical CFD simulations. This makes it very convenient for parametric studies. In this dissertation, we use a modified version of MSES where a pressure jump can be applied in the fluid domain. This mimics the jump in total pressure over a propeller disk. The implementation of this pressure jump utilizes another benefit of the streamline grid of MSES, which is expanded upon below. The downsides of MSES are its numerical instability and its inherent assumptions, such as the lack of viscosity outside the boundary layer and how it handles boundary layer confluence between airfoil elements. The numerical instability is improved by an automated solver process at the cost of some computational efficiency, discussed at the end of this section. The inherent assumptions of the method are addressed by a verification using a set of RANS simulations, which will be discussed in Chapter 3.

#### Solver setup

MSES employs an inviscid, compressible streamline grid coupled to a viscous boundary layer model based on the integral boundary layer equations. For a description of the basic functionality of MSES, we refer to the original literature by Drela [72, 73] and the MSES User's Guide [74]. The global variables and constraints are set to default as suggested by the User's Guide [74]. For the conservation law, entropy is conserved for all cells except those where dissipation contributes significantly to the loss of total pressure. All simulations are run on a domain of 30 by 30 chords (meaning a boundary distance of 15 chords with respect to the airfoil leading edge), with 81 streamlines in the top and bottom domain, 51 streamlines between element stagnation lines and 221 divisions per side on each airfoil. Due to the high lift coefficients that occur in the design space, the boundaries of the domain cannot be assumed as farfield, as significant pressure gradients still remain on the domain exit and streamlines are not yet parallel to the freestream. Therefore, the vortex+source+doublet farfield boundary conditions are used (which are default for MSES).

   The official source code of MSES comes readily equipped with code to apply an actuator disk in the domain, although this is not integrated in the front-end functionality of the software. Using these available resources, we implemented a total pressure jump at a specified location on the domain inlet, thereby creating a parallel, uniform 2D jet. Although the jet is initiated at the inlet, its position is controlled by a *jet constraint* perpendicular to the reference chord line positioned one chord length in front of the leading edge. The solver finds streamtubes that cross the jet constraint and adds the total pressure to their inlet position, after which it marches the grid to the next iteration. Figure 2.18 provides an illustration of the jet positioning. The initiation of the pressure jump is thus automatically adjusted such that the jet ends up at the desired location. This approach ensures that the airfoil is predictably immersed in the jet, despite the dependency of the jet development on the wing circulation, and is uniquely possible due to the streamline grid of MSES. In a 2D RANS approach (see Section 2.2.2), the pressure jump location is controlled rather than the resulting jet trajectory, which is unpredictable

due to its dependency on bound circulation of the wing (which in turn is a function of the trajectory of the jet over the airfoil).

To capture the edge of the jet and the associated velocity gradient accurately a refinement of streamlines is required at the jet edge. This is implemented by including a refinement in the grid initialization step of the solver, where the total pressure jump is not yet specified. The addition of the total pressure contracts that portion of the grid as it increases the local dynamic pressure, which needs to be compensated for in the grid initialization as shown in Fig. 2.18a. Because this compensation — much like the jet development itself — is a function of the airfoil lift, the refinement may not end up exactly where expected and the procedure is iterated until the centre of the refinement is positioned within 5% of the jet size from the edge of the jet constraint. The density of streamlines around the refinement position then ensure the solver resolves the jet edge accurately.
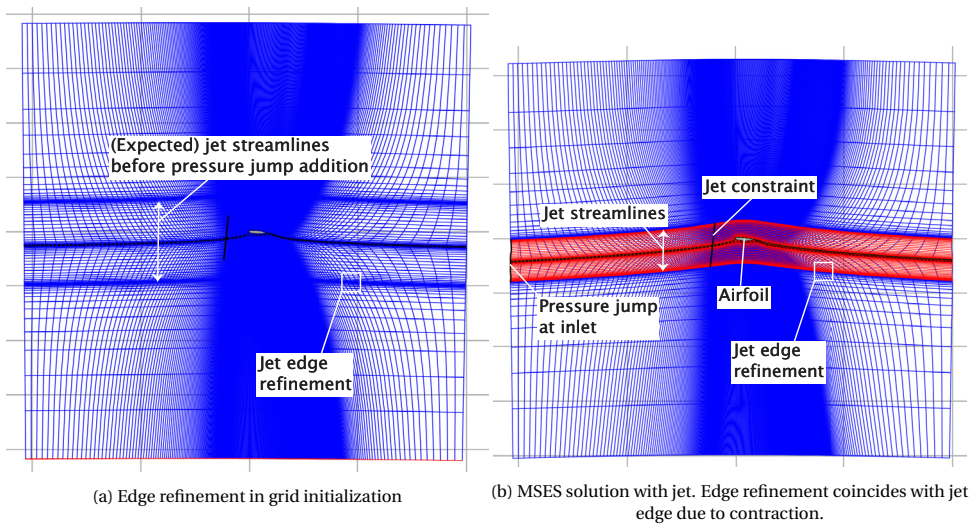


(a) Edge refinement in grid initialization

(b) MSES solution with jet. Edge refinement coincides with jet edge due to contraction.

Figure 2.18: Illustration of the jet constraint, total pressure addition and edge refinement in the MSES grid.

### BOUNDARY LAYER TRANSITION

MSES employs a hybrid viscous-inviscid formulation, where the viscous boundary layer is modelled by the Integral Boundary Layer (IBL) equations. Furthermore, it uses an $e^n$-transition model to determine the state of the boundary layer, where $n$ (or $n_{crit}$) is a measure of the inherent turbulence of the flow. It also allows for specification of fixed transition points of the boundary layer at each side of each element. For an airfoil in the slipstream of a propeller, it is commonly assumed that the boundary layer is fully turbulent. Unfortunately, many configurations in this study suffered from numerical instability when fixing the transition point. Instead, free transition was applied with a very low value of $n_{crit}$. As a result, the suction side boundary layer on the main element becomes turbulent within 0.05c for all configurations in the design space. The pressure side boundary layer, as well as the flap boundary layers, have a wider range of transition

**2**

locations. When analysed against the reported displacement thickness, however, the transition point does not have a dominant effect for the configurations in this study. We therefore assume that the boundary layer state has a negligible impact on the reported aerodynamic coefficients, except for friction drag due to the transitional nature of the boundary layer in MSES.

SOLUTION DEPENDENCIES

The addition of the jet in MSES increases the inherent numerical instability of the solver, causing frequent non-convergence, particularly when high streamline curvature or separation occurs. To mitigate this, the solver was set up to detect non-convergence and automatically re-initiate the simulation with slight variations to the value of $n_{crit}$ for the transition method or the $\alpha$ at which the solution is initiated. The value of $n_{crit}$ is initiated at 2.0 and is allowed to vary up to 3.0 before complete non-convergence is reported, while the initial $\alpha$ was reduced a maximum of 3 deg. The relaxation of these parameters greatly improved convergence. Whereas the change in initial $\alpha$ does not affect the result, as it is always marched to the target value, in the case of $n_{crit}$ it has some impact on the solution.

For a given configuration, we found the lift and moment coefficients would vary up to 0.5% depending on the value of $n_{crit}$. Drag coefficient is, predictably, more affected and varies up to 2.5%. However, most of the deviation is found for $n_{crit} > 2.5$ and all solutions remain within 0.5% deviation below that. Only 7% of the solutions in the datasets analysed using this method required $n_{crit} > 2.5$ to converge and thus the effect of differences in $n_{crit}$ on the analyses is limited.

An additional source of grid dependence is introduced by the addition of the jet refinement. MSES initializes a predetermined number of streamlines in the grid in five different domains, split by the jet edge refinement location and airfoil stagnation lines, bound by the upper and lower limits of the domain. Distribution of streamlines within the jet is dependent on the alignment between the jet and the airfoil stagnation lines, which introduces some grid dependency into the results. We investigated the sensitivity of the solution to number of streamlines, number of airfoil divisions and jet refinement distribution algorithm and found that lift, drag, and moment coefficients remained within 1% of the reference solution.

### **2.2.2.** 2D REYNOLDS-AVERAGED NAVIER STOKES SIMULATIONS

We verified the implementation of the jet in MSES by comparing the results of RANS-based simulations. This also allows us to test the validity of some inherent assumptions made in MSES, which are not present in RANS-based solvers. Assumptions such as the lack of viscosity outside the boundary layers and the lack of boundary layer confluence on the flap may significantly affect the resulting wing lift, drag, and moment coefficient. The results of MSES and 2D RANS for a selection of configurations are compared and discussed in Chapter 3. A grid convergence study of the 2D RANS simulations can be found in Appendix B.

SOLVER AND MESH SETTINGS

We performed the 2D RANS-based simulations with ANSYS Fluent 2020 R2, on an unstructured triangular mesh with Spalart-Allmaras turbulence model. The fluid was compressible and viscosity was calculated according to Sutherland's law. The solver was set
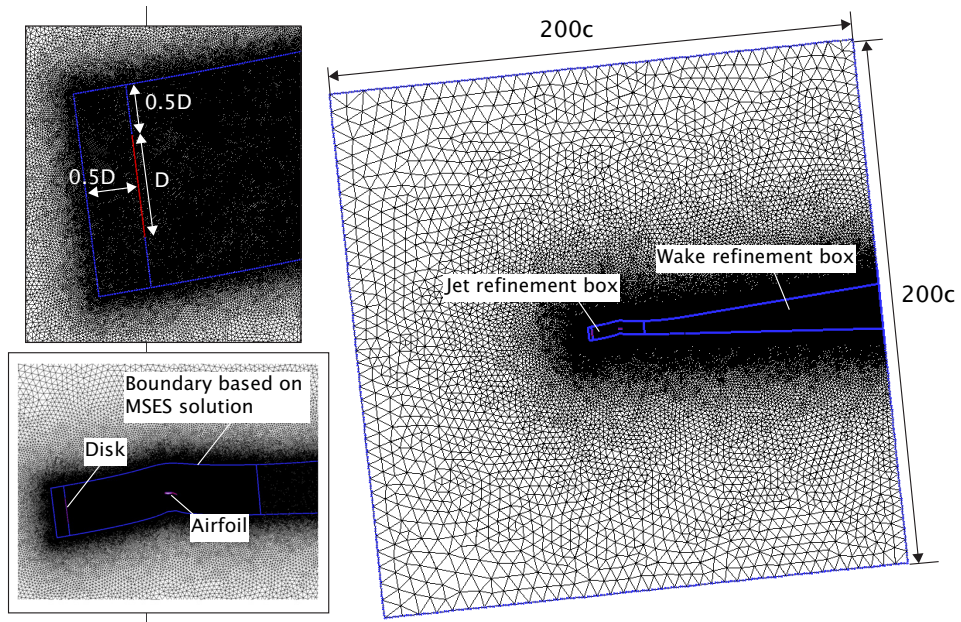
Figure 2.19: Illustration of RANS mesh setup showing the refinement areas.

to pseudo-transient, with least squares-based gradient discretization and third-order schemes on all values except for turbulent viscosity, which was set to second order upwind. The rectangular domain was 200 by 200 chords, angled to be aligned with the specified angle of attack (see Fig. 2.19). The upper and lower boundaries were specified as slip walls, while the inlet and outlet were configured as total pressure inlet and average static pressure outlet, respectively. The freestream was specified by the total pressure on the inlet and the chord length was set to satisfy the Reynolds number at the specified freestream Mach number. The jet was implemented by a constant total pressure jump within the domain using the *fan boundary condition* (hereinafter referred to as *disk*), at the same location as the inlet location of the jet in MSES. In MSES, the grid contracts automatically around the pressure jump on the inlet, yielding a fully contracted jet throughout the domain. The RANS-based simulation requires a much larger grid, however, and thus the contraction of the jet occurs within the domain. The height of the disk was corrected for this contraction based on conservation of mass, such that the fully contracted jet has the same size as the MSES simulation.

The mesh was unstructured and triangular, with two areas of refinement as shown in Fig. 2.19. The size of the *jet refinement box* was based on the streamlines extracted from the MSES results, scaled to twice the width of the disk (including compensation for contraction). It starts half the disk size ahead of the total pressure jump, continuing up to 10 chords downstream of the airfoil. The boundaries of the *wake refinement box* were straight lines at an angle of 5 deg from each other and tangential to the *jet refinement box*. The wake refinement was necessary to stabilize the continuity residuals. Both the main

and flap element feature inflation layers with a first layer height to satisfy $y^+ \approx 1$. The growth rate of the inflation layers was set to 1.15 and the number of layers was defined manually to achieve a smooth transition to the unstructured part of the mesh.

The mesh was discretized by maximum element size, relative to the main airfoil element size. This ensured the mesh generation was similar for different chord lengths, which were varied between verification points to satisfy the target Reynolds number. It also enabled a simple manner of consistent mesh refinement for grid convergence study (detailed in Appendix B). In the finest grid, which is used for all comparisons with MSES in this dissertation, the main airfoil element was divided into 1493 elements. Table 2.5 summarizes the relations between the element sizes specified in the grid generation. The maximum element size of the outer domain is left at the solver default (which depends on freestream condition) and the global mesh growth rate is 1.05.

Table 2.5: Mesh discretization settings for the 2D RANS setup.

| Element sizing | Relation |
| --- | --- |
| Base element ($d_{base}$) | $c/1493$ |
| Flap element | $d_{base}/1.5$ |
| Trailing edges | $d_{base}/12$ |
| Jet refinement | $d_{base} * 5$ |
| Wake refinement | $d_{base} * 10$ |

### 2.2.3. 3D LATTICE-BOLZMANN MODEL

Numerical simulations of the first experiment (Section 2.1.3) were performed in Power-FLOW ® (version 6-2021-R7), a commercial CFD solver that employs the Lattice-Boltzmann Method (LBM). LBM is based on statistical mechanics and represents fluid flow as interacting particles. The Boltzmann equation governs the behaviour of the particle distribution function, akin to the NS equations with time derivatives and advection terms. Specifically, the D3Q19 formulation is utilized, discretizing the particle velocities into 19 vectors, allowing particles to travel to adjacent cells.

We conducted simulations using the subsonic isothermal solver and Very Large Eddy Simulation (VLES) approach. This employs a $\kappa - \varepsilon$ Re-Normalisation Group (RNG) turbulence model with a swirl model, to reduce the eddy viscosity in the presence of resolved flow structures. The numerical setup involved a Cartesian mesh with variable cell sizes, refined near the propeller wake and flap surfaces. This mesh setup included a sliding mesh interface for propeller rotation, with a refined cylinder around the propeller wake to mitigate numerical dissipation. An illustration of mesh refinement regions near the wing is presented in Fig. 2.20.

The wind tunnel walls, simulated as free-slip boundaries, were included to eliminate the need for wall corrections. The propeller and wing surfaces were included with a no-slip condition and fully turbulent boundary layer flow. Furthermore, the flap brackets used to mount the flap to the main element were also included, as they locally dominate the flap flow. Boundary conditions consisted of a velocity inlet and a pressure outlet at the upstream and downwind faces of the numerical wind tunnel, respectively. The numerical dataset includes six configurations, consisting of two angles of attack ($\alpha = 0$
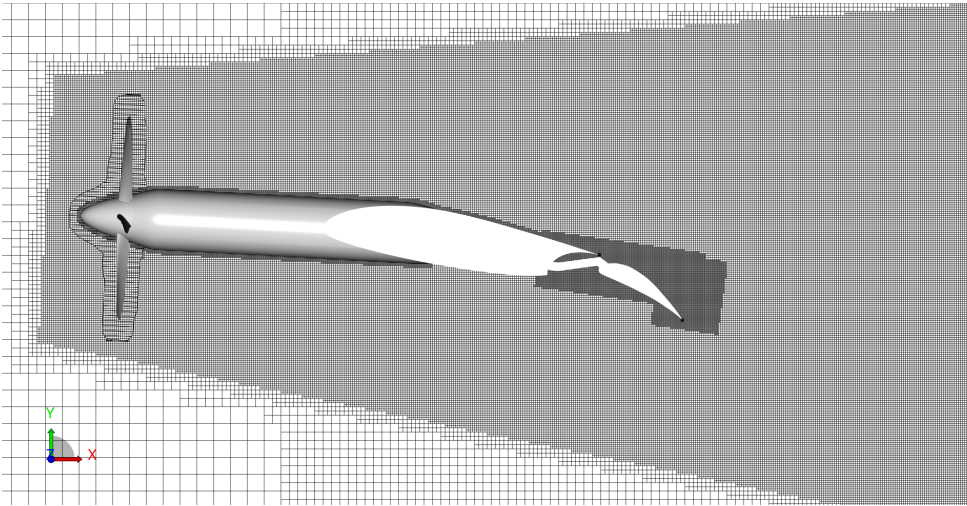
Figure 2.20: Illustration of the mesh refinement areas around the slipstream and the flap area, also showing the sliding mesh region around the propeller.

and 8 deg) and three flap deflections (0, 15 and 30 deg), matching the experiment. Each configuration considered only one advance ratio of $J = 0.8$.

### 2.2.4. RESPONSE SURFACE METAMODEL ANALYSIS

In chapter 4, we quantify the sensitivities of multi-element airfoils to a range of nine design parameters, or *factors*. To this end, we utilize principles from Design of Experiments (DoE) to define an orthogonal design space and select specific configurations to simulate and subsequently use Response Surface Methodology (RSM) to fit metamodels to these simulations. We selectively exclude terms from a metamodel and analyse how the remaining terms change. Due to the properties of orthogonal experimental designs, this then quantifies how much each term contributes to the variability of certain *responses*, such as lift, drag and moment coefficients, across the design space.

The simulations that serve as input to the metamodels were all performed with the modified MSES solver described in Section 2.2.1. For these simulations, we used the NLR 7301 airfoil with separate downstream flap. This airfoil was taken from van den Berg and Oskam [75] and is a transonic design with a relatively large leading edge radius and no flap nested position. Unlike the airfoil design of the experimental model, it thus avoids a cove and associated separation, which is beneficial to the convergence of MSES. This was a necessity due to the increased numerical instability of the MSES solver after the pressure jump modification.

The remainder of this section explains the various steps in the process of RSM metamodel analysis. The definition of the design space presents the included factors, the chosen experimental design and the ranges for each of the factors. We also describe the main metamodel, and give some notes on the multicollinearity of the designs and data transformations in the analysis.

### Definition of design space

The design space consists of nine main factors, illustrated in Fig. 2.21. It is further defined by a $k$-factor Central Composite Design (CCD), a typical DoE design used for RSM able to fit 2nd-order models[76]. This CCD consist of a $2^k$ factorial design with $2k$ star points to test for curvature and one centrepoint. For the 9-factor design of this study, this results in a total of 531 configurations. As the data are obtained from deterministic simulations, only a single centrepoint is necessary. Further information on CCDs can be found in classic textbooks on DoE, such as Montgomery [76], and will not be expanded upon in this document. The resulting CCD is summarized in Table 2.6 and motivated in section 2.2.4. The upper and lower bounds of each factor in the factorial part of the CCD (also called the *high* and *low* settings), along with their star points, are summarized in Table 2.6 and motivated below. In the remainder of this document, we will refer to this full 9-factor design space as the *jet design*.

The metamodel analysis used in Chapter 4 requires an orthogonal design to be able to fully separate contributions of each factor and interaction. Orthogonality of the CCD is achieved by specific placement of the star points. Unfortunately, the star points $\alpha^*$ required for a fully orthogonal 9-factor design are beyond the physical limitations of the configurations and the solver, unless the factor ranges are severely constricted. We therefore restricted $\alpha^*$ to $\pm 1.7321$, where $\alpha^*$ is the distance of the axial points to the
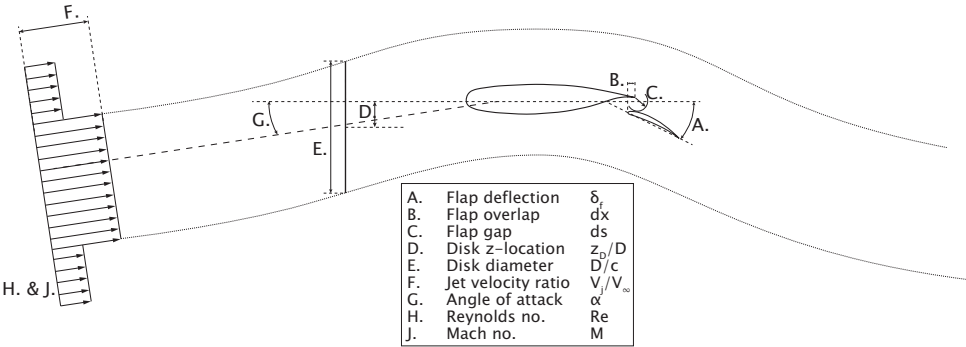


Figure 2.21: Illustration of the parametric design space of the jet-wing-flap configuration.

Table 2.6: Overview of the setpoints of the full 9-factor Central Composite Design.

| Coding | Factor | Unit | $-\alpha^{**}$ (-1.7321) | Low (-1) | Center (0) | High (+1) | $+\alpha^*$ (+1.7321) |
|--------|--------|------|--------------------------|----------|------------|-----------|------------------------|
| A | $\delta_f$ | [deg] | 11.34 | 15 | 20 | 25 | 28.66 |
| B | d$x$ | [deg] | -0.02928 | 0 | 0.04 | 0.08 | 0.10928 |
| C | d$s$ | [deg] | 0.022679 | 0.03 | 0.04 | 0.05 | 0.057321 |
| D | $z/D$ | [-] | -0.30981 | -0.2 | -0.05 | 0.1 | 0.20981 |
| E | $D/c$ | [-] | 0.77058 | 1.1 | 1.55 | 2 | 2.3294 |
| F | $V_j/V_\infty$ | [-] | 1.317 | 1.5 | 1.75 | 2 | 2.183 |
| G | $\alpha$ | [deg] | 0.5359 | 2 | 4 | 6 | 7.4641 |
| H | $Re$ | [-] | 5.44E+06 | 8.00E+06 | 1.15E+07 | 1.50E+07 | 1.76E+07 |
| J | $M$ | [-] | 0.1317 | 0.15 | 0.175 | 0.2 | 0.2183 |

centrepoint[3]. The multicollinearity that is introduced into the design in this way is minimal and will be treated at the end of this section.

The same CCD, but excluding the jet-related factors $D/c$, $z/D$ and $V_j/V_\infty$, serves as a baseline for multi-element airfoil behaviour in uniform flow. This *baseline design* thus considers 6 factors with 12 axial points and a centrepoint, resulting in a total of 77 configurations. Apart from the exclusion of the jet factors, factor ranges are equal to those in table 2.6. The baseline design is compared with *subset designs*, which follow the same CCD as the baseline design, but include a jet of fixed $V_j/V_\infty$, $D/c$ and $z/D$ in their domain. These thus represent a small portion of the full jet design and allow for direct comparison with the baseline.

### CHOICE OF FACTOR RANGES

The factor ranges for the CCD were chosen to represent a full-scale transport aircraft with highly loaded propellers in take-off configuration. Subsequently, the factor ranges were restricted based on solver limitations and to maintain design orthogonality. Design orthogonality is further addressed at the end of this section. The solver limitations restricted the use of high angles of attack, as the solver would not reliably converge when approaching $C_{l,max}$. Furthermore, the Mach number is chosen to avoid shocks in the majority of the design, as they also affect solver reliability negatively.

The factor range of the flap deflection, gap, and overlap was centred close to the original design of the flap of 20 deg with 5.3% overlap and 2.6% gap, with some adjustments to the respective ranges to avoid unfeasible configurations within the design space (for instance, $dx < ds$ cannot be achieved for most flap deflections). Generally, we have aimed to maintain as wide a range as possible.

The vertical position of the jet relative to the airfoil is chosen such that the airfoil stagnation lines remain within the jet in any configuration in the design space. This is a limitation of the numerical setup (see Section 2.2.1). Since the pressure jump is placed at the domain inlet, there is no contraction in the domain and there is no streamwise dependency of the jet constraint.

The range of jet velocity ratios is based on the ratios considered in the work by Ting, Liu and Kleinstein [77], which are also used by Patterson, Derlaga and Borer [78] in his work on lift-augmenting (distributed) propeller design. In the test matrix, the jet velocity ratios chosen are equivalent to thrust coefficients between $T_c \approx 0.29$ and $\approx 1.5$, depending on other factors in the system. This yields overall relatively high $T_c$, with some configurations on the edges of the design space even becoming practically unfeasible. In the context of (distributed) propeller-blown high-lift augmentation, it is worthwhile including relatively high thrust coefficients within the design space. Furthermore, high jet velocity ratios will make changes to the parametric sensitivities of the airfoil more pronounced. Configurations on the edge of the design space, even if practically unfeasible, test the potential nonlinearity of the theoretical responses.

### DEFINITION OF METAMODEL

Fitting a regression model (or *metamodel*) to a set of datapoints maps a response (e.g., lift coefficient) to the factors and interactions considered in the metamodel. For the jet

---

[3] In factorial designs, the centrepoint is 0 and the *high* and *low* settings of factors are defined as distance $+1$ and $-1$ from the centrepoint, respectively. The axial points are then at distance 1.7321 from the centrepoint.

design, we use a standard quadratic metamodel extended with three-factor interactions, given by Eq. (2.1). We include three-factor interactions because the jet design contains factors related to two systems known to each include two-way aerodynamic interactions (propeller-wing and wing-flap). Significant three-factor interactions are therefore likely to occur. Each term in Eq. 2.1 (also referred to as *model term*) relates to a factor or an interaction between factors. For instance, the model term $\beta_{1,2} x_1 x_2$ relates to the effect of the interaction of factors $x_1$ and $x_2$ on the response $y$, with $\beta_{1,2}$ being the gain obtained from the regression fit.

$$y = \beta + \sum_{i=1}^{p} \beta_i x_i + \sum_{i=1}^{p} \beta_{ii} x_i^2 + \sum_{i=1}^{p-1} \sum_{j=i+1}^{p} \beta_{ij} x_i x_j + \sum_{i=1}^{p-2} \sum_{j=i+1}^{p-1} \sum_{k=j+1}^{p} \beta_{ijk} x_i x_j x_k + \varepsilon \qquad (2.1)$$

We can rank the importance of each model term based on their relative contribution to the variance in response of all terms in the metamodel combined (or *total metamodel*). This is done by taking a ratio of the partial Sum of Squares of each term and the Sum of Squares of the total metamodel. This quantifies how much each term contributes to the total variability of the response across the design space. For a full overview of DoE/RSM, readers are again referred to standard textbooks on the topic, such as Montgomery [76]. Since the data considered in this study are obtained using deterministic numerical simulations, there is no random error. The typical approach using analysis of variance (ANOVA) to reduce the number of model terms can therefore not be applied, and all terms are kept in the metamodel for the jet design.

For the baseline and subset designs, however, we excluded the three factor interaction terms of Eq. (2.1), leaving only the quadratic metamodel. Since the baseline and subset designs do not include jet parameters as factors, three-factor interactions are unlikely to be significant. We confirmed this by analysing the baseline and some of the subset designs both with the quadratic metamodel only, and with the extended metamodel. In both cases, the dominant factors and interactions are identified with equal levels of contribution to the model. Three-factor interactions never contributed more than 0.14% to the baseline and subset models (with most three-factor interactions below 0.01%), unlike for the models for the full jet design (see section 4.3.1).

### Multicollinearity

The main reason to exclude three-factor interactions from the metamodels for the baseline and subset designs was to reduce the multicollinearity of model terms in one of the subsets (with $V_j/V_\infty = 2.0$, see section 4.2.1). For this design, insufficient design points could be converged to include the three-factor interactions. Low multicollinearity is required to independently determine the contribution of each term in the metamodel [76, 79]. The main purpose of the analysis in this dissertation is to determine the relative contribution of each model term to the chosen responses, rather than provide an estimation of the response for an arbitrary location within the parametric space. Therefore, we focus on minimal multicollinearity instead of optimal fit.

Multicollinearity of model terms can be measured by the Variance Inflation Factor (VIF), where a VIF of one means the term is completely independent. Standard practice is to reject a model when VIF of any term is greater than 10, or in more conservative cases

greater than 5 [79, 80, 81]. For all metamodels analysed, the VIF remains below 3 for all model terms, ensuring the terms can be interpreted as independent.

### DATA TRANSFORMATION
To improve fit of the metamodel, we apply data transformations in the analysis according to the Box-Cox approach. This determines a power transformation of the response $y^\lambda + k$ (where $y$ is the response data and $\lambda$ and $k$ are the power transform parameters) for which the error sum of squares is the minimum [76]. Response values reported in this document are always in the actual (not-transformed) space.

# 3

# VALIDATION AND VERIFICATION

*The numerical methods described in Chapter 2 require a form of validation or verification to contextualize interpretation of the results. Although MSES (described in Section 2.2.1) is a well documented tool for multi-element airfoil simulations, the modifications made to include the jet flow requires verification. The statistical analysis traditionally used to verify model fit in RSM (Section 2.2.4), furthermore, cannot be applied due to the deterministic nature of the simulations on which the RSM analyses are based and thus requires a different approach. Finally, the configurations simulated by LBM (Section 2.2.3) are highly sensitive to viscous flow effects and prone to flow separation. In the presence of such effects, the turbulent flow modelling used in LBM and uRANS simulations can become inconsistent and thus require validation. This chapter describes the validation and verification efforts performed to address these issues. Section 3.1 contains a verification of the MSES modifications using 2D RANS simulations. Section 3.3 describes an estimation of the model fit for the main metamodels used in the RSM analysis of Chapter 4. Finally, Section 3.2 compares the results of the LBM simulations to experimental data.*

---

Parts of this chapter have been published in Refs. [54, 55, 56].

## 3.1. Verification of MSES PWF with 2D RANS

Despite using resources available in the original source code, the inclusion of the jet required modifications not normally present in MSES. Therefore, a verification of the jet implementation is necessary. Furthermore, as MSES is not commonly used for jet flows, the inherent assumptions of the method require validation. Unfortunately, the setup cannot be reproduced experimentally. We therefore compare the results from MSES with RANS simulations for several configurations in the design space. Unlike MSES, RANS resolves much of the boundary layer, includes viscosity in the entire domain and inherently captures boundary layer confluence.

### 3.1.1. Verification points

We selected five verification points (VP) based on configurations predicted by MSES to have maximum $C_l$, maximum and minimum $C_d$, and maximum and minimum $L/D$. These configurations represent extreme cases in aerodynamic performance according to MSES and are therefore likely to challenge the assumptions of the model. Large discrepancies between the MSES and RANS solutions would indicate violations of these assumptions. Additionally, these verification points encompass combinations of main factors that fill the design space well. Table 3.1 summarizes the design parameters of the verification points that we included in the verification.

Table 3.1: Verification points chosen from the design space

|  | **VP1** | **VP2** | **VP3** | **VP4** | **VP5** |
|---|---|---|---|---|---|
| **Description** | Max $L/D$ | Min $C_d$ | Max $C_l$ | Max $C_d$ | Min $L/D$ |
| $\delta_f$ [deg] | 25 | 20 | 25 | 15 | 15 |
| d$x$ [-] | 0.00 | 0.04 | 0.00 | 0.08 | 0.08 |
| d$s$ [-] | 0.03 | 0.04 | 0.05 | 0.05 | 0.05 |
| $z/D$ [-] | -0.2 | -0.05 | 0.1 | 0.1 | -0.2 |
| $D/c$ [-] | 2 | 1.55 | 2 | 2 | 1.1 |
| $V_j/V_\infty$ [-] | 2 | 1.75 | 2 | 2 | 2 |
| $\alpha$ [deg] | 2 | 4 | 6 | 6 | 6 |
| $Re$ [-] | 1.50e7 | 1.15e7 | 8.00e6 | 1.50e7 | 8.00e6 |
| $M$ [-] | 0.15 | 0.175 | 0.15 | 0.2 | 0.2 |
| $C_l^*$ [-] | 8.634 | 6.573 | 10.74 | 7.278 | 6.794 |
| $C_d^*$ [-] | 0.0468 | 0.0417 | 0.1107 | 0.1372 | 0.1312 |
| $C_m^*$ [-] | -2.329 | -1.480 | -2.323 | -1.279 | -1.232 |
| * from MSES simulations | | | | | |

### 3.1.2. Comparison between MSES and RANS

Figure 3.1a shows the percentual difference between the RANS and MSES results, calculated as $\Delta_{(MSES-RANS)} = \frac{MSES}{RANS} - 1$. It compares lift, drag and pitching moment coefficients for the total airfoil, as well as for each element separately. From Fig. 3.1a it is clear that both lift and moment coefficients match well between RANS and MSES, but drag coefficient matches poorly. This may partly be explained by the transitional nature of MSES. Figure

3.1c show that the friction drag is systematically underestimated by MSES compared to RANS. Furthermore, the drag coefficient of multi-element airfoils is a combination of large pressure drag contribution of each element. These contributions have opposite signs and add to a small resulting value. This means that small differences in the drag of each element can sum to large differences in the total drag coefficient, as illustrated by Fig. 3.1b. Although the pressure drag of each element matches well for most configurations, percentual deviation of the total pressure drag is much larger.

VP4 and VP5 show very large deviation of the main element pressure drag between the two methods. This can be traced to shock-induced separation bubbles occurring in the RANS simulations, as shown for VP4 and VP5 in Fig. 3.2. Although MSES predicts a significant jump in displacement thickness due to the shock, it does not show evidence of a separation bubble. This is best observed from the pressure distributions.



(a) Main coefficients

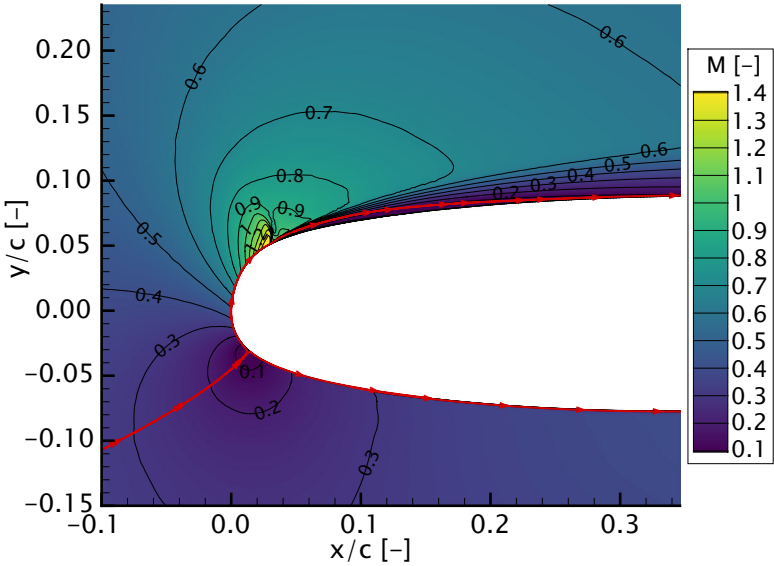(b) $C_{d,p}$



(c) $C_{d,f}$
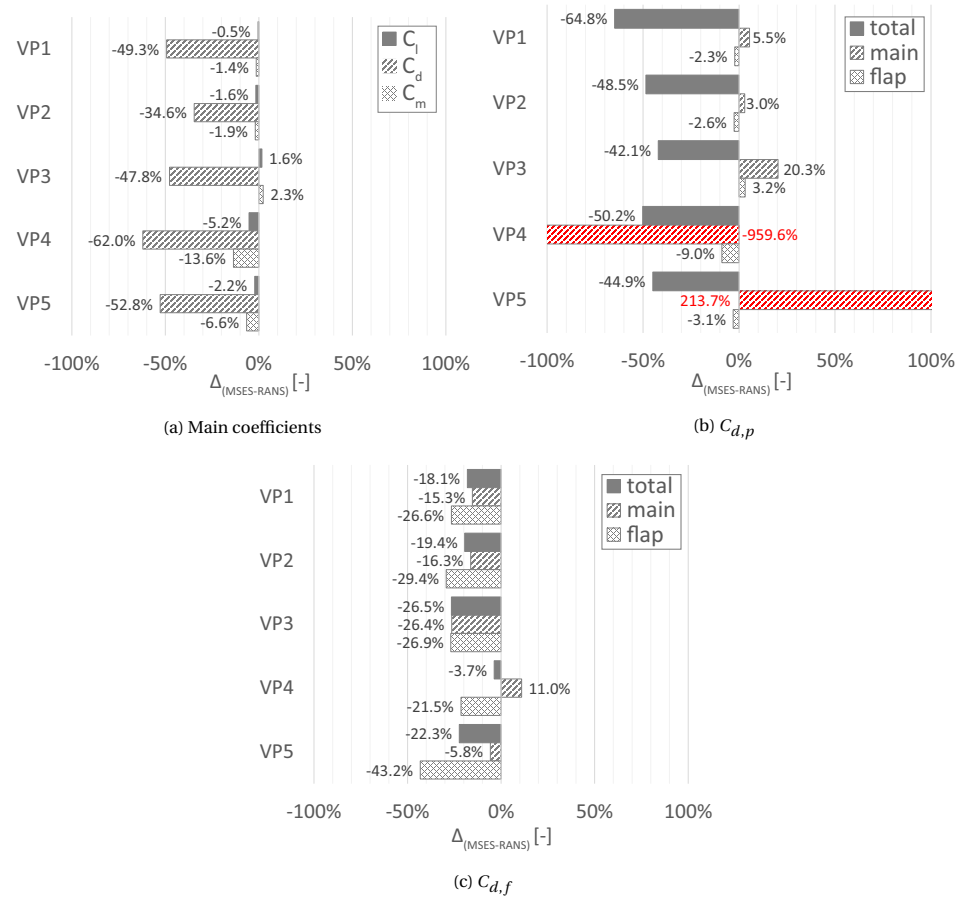
Figure 3.1: Deltas in coefficients predicted by MSES versus RANS.
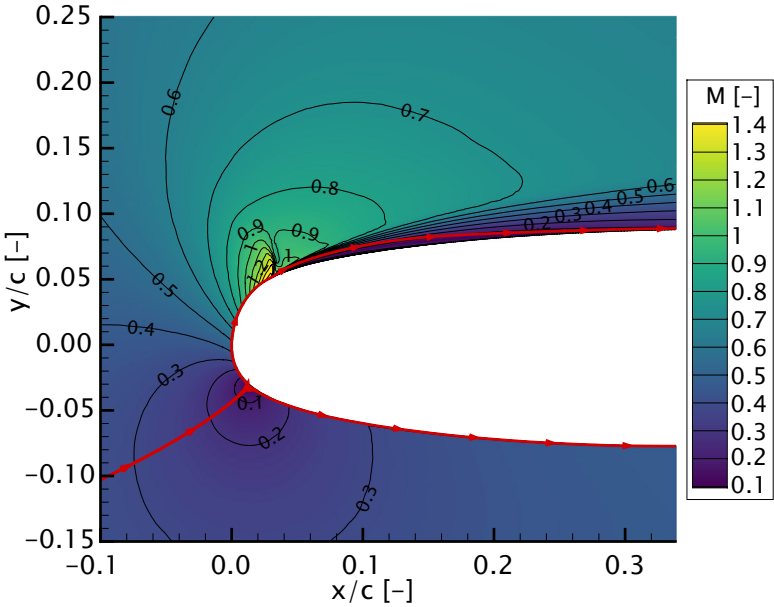
(a) VP4



(b) VP5

Figure 3.2: Mach contours around the main element leading edge and streamline showing separation bubble.
RANS simulation.

**3**

PRESSURE DISTRIBUTIONS

Figure 3.3 shows the pressure distributions from both MSES and RANS for each VP. VP 1, 2 and 3 show excellent match between both methods, as should be expected from the close match in lift, pitching moment and pressure drag coefficients. For VP4 and VP5, the RANS pressure distributions show the effects of the separation bubble as a thinner pressure peak with a change in its slope around $x/c = 0.03c$. MSES shows no evidence of this, resulting in a stronger pressure peak and thus a much larger negative pressure drag component for the main element. This explains the deviation of pressure drag on the main element for VP4 and VP5 in Fig. 3.1b. It should be noted that VP3 also has a transonic region at roughly the same location, but both MSES and RANS predict fully attached boundary layers and the aerodynamic coefficients show excellent agreement between both methods. MSES is thus able to resolve the transonic region in certain conditions, but not when it induces local separation.

JET VELOCITY AT THE CONSTRAINT LOCATION

The final metric to compare is the jet trajectory and velocity distribution, specifically the target position at $x/c = -1$. Since the pressure jump location in RANS is not iterated and the jet position at $x/c = -1$ is a function of airfoil circulation and can be considered as a metric of flowfield similarity between RANS and MSES.

Figure 3.4 shows the jet velocity profile at $x/c = -1$ for both methods. The gradient at the edge of the jet in the RANS solution, rather than a discrete jump as in the MSES solution, reveals the presence of viscous shear layers. From the gradients, we can see that the shear layers remain relatively thin close to the airfoil and do not influence the shape of the velocity distribution significantly. Overall, RANS and MSES predictions of the jet profile matches very well.

REFLECTION ON ACCURACY OF MSES FLOW MODELLING

The presented metrics show that across the design space, configurations that are significantly different from an aerodynamic perspective are represented by MSES at a similar fidelity as provided by RANS. The assumption of inviscid flow outside the boundary layer made by MSES does not appear to significantly change the solution in the verified cases. MSES consistently underestimates friction drag, likely a result from the transition model. Whereas the RANS simulations assume fully turbulent boundary layers, MSES applies a transition model (see Section 2.2.1). Furthermore, MSES is not able to resolve shock-induced separation bubbles in the same manner as RANS. However, this does not dominate the drag coefficient or the deviation between MSES and RANS. We therefore expect that the trends of drag coefficient in the design space are still captured with sufficient accuracy for the analysis in this dissertation, but note that the conclusions may require reassessment in the presence of stronger shocks.
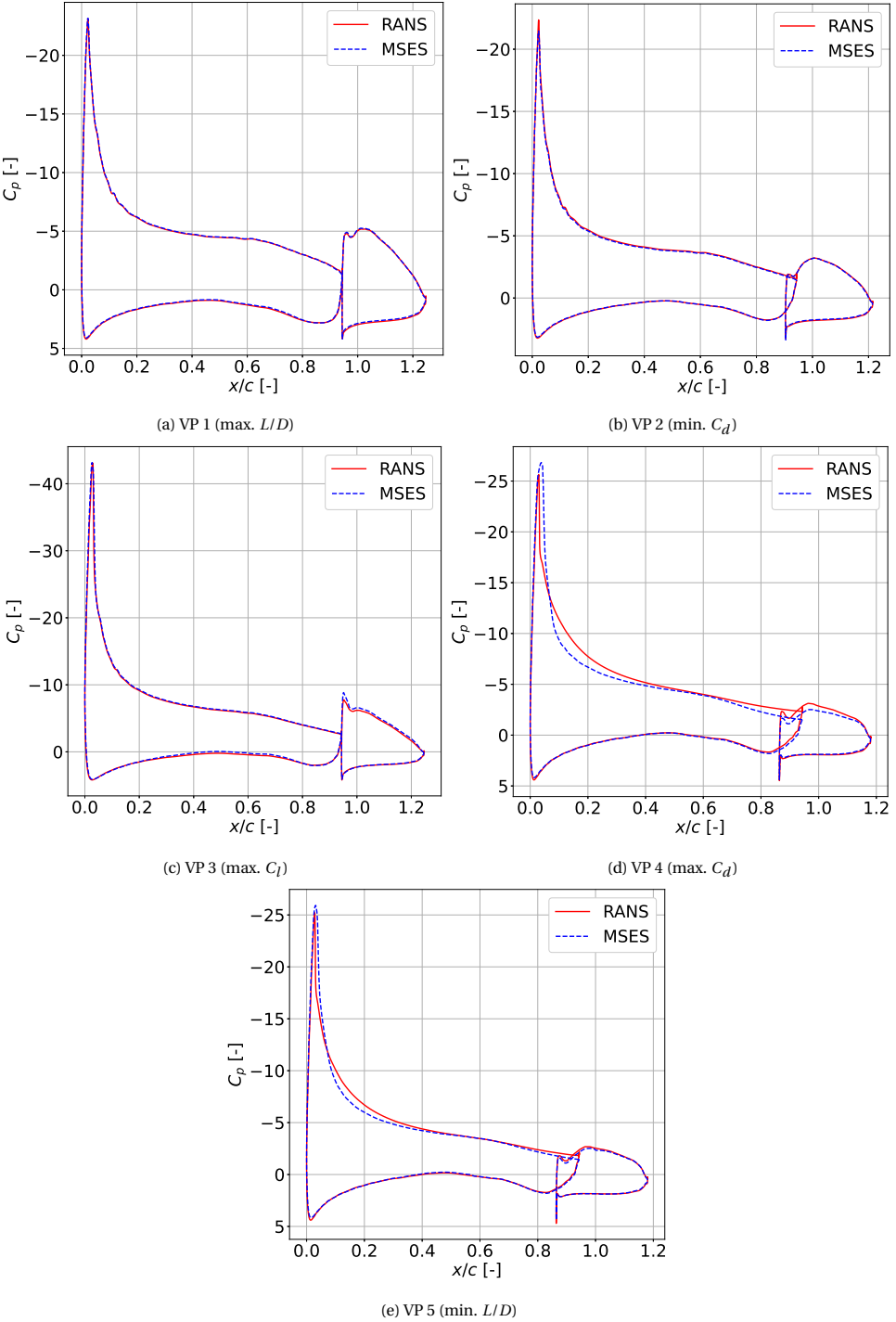
(a) VP 1 (max. $L/D$)

(b) VP 2 (min. $C_d$)

(c) VP 3 (max. $C_l$)

(d) VP 4 (max. $C_d$)

(e) VP 5 (min. $L/D$)

Figure 3.3: Comparison of pressure distribution as predicted by MSES versus RANS.

(a) VP 1 (max. $L/D$)

(b) VP 2 (min $C_d$)

(c) VP 3 (max. $C_l$)
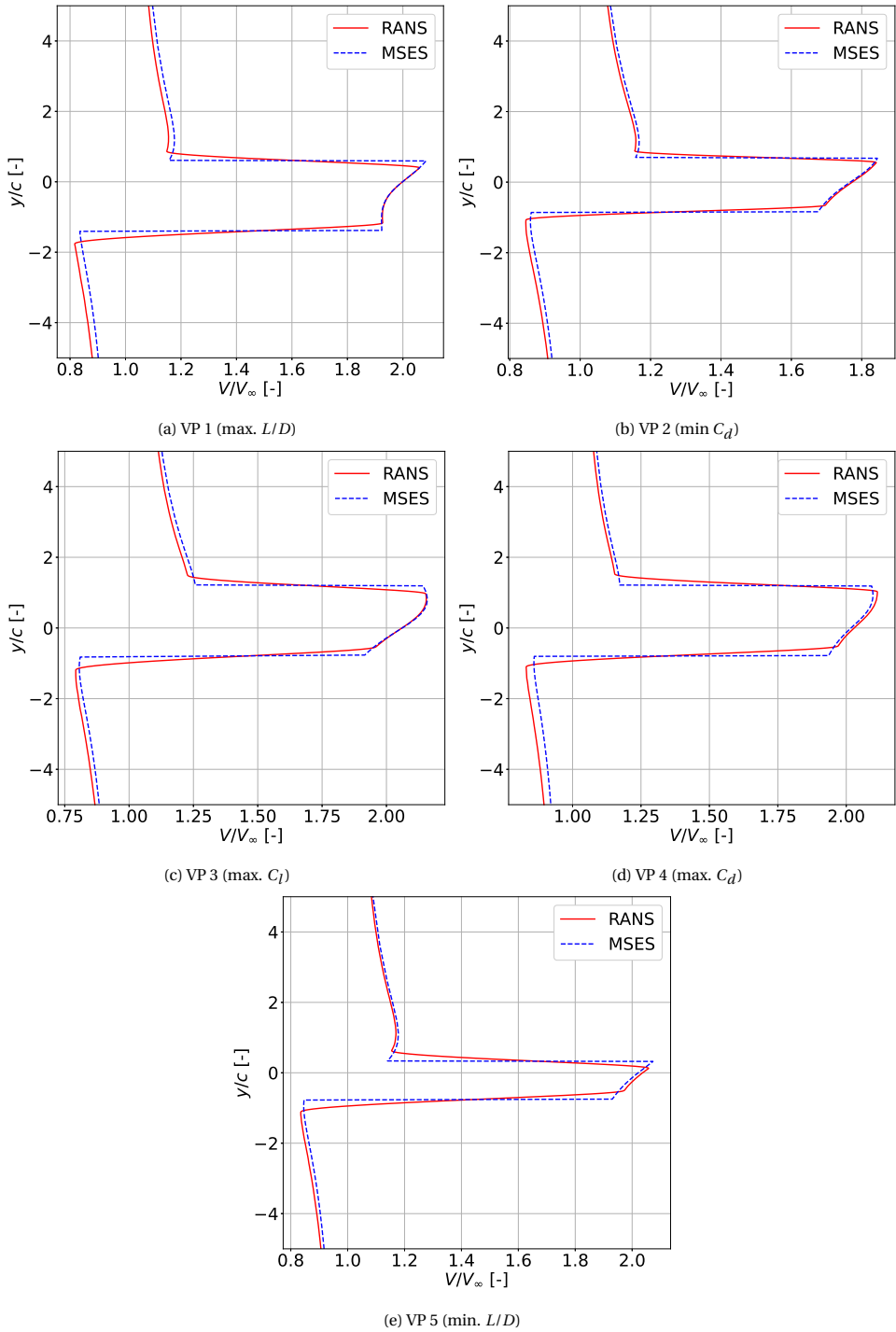
(d) VP 4 (max. $C_d$)

(e) VP 5 (min. $L/D$)

Figure 3.4: Comparison of velocity at the jet constraint as predicted by MSES and RANS.

## 3.2. VALIDATION OF LATTICE BOLTZMANN SIMULATIONS

This section describes the validation of the simulations performed with LBM-based solver PowerFLOW ®, with the experimental data from the first experiment (Section 2.1.3). Simulation results are validated against the reference propeller thrust coefficient, wing pressure distributions, surface oil flow visualizations and total pressure planes in the wake.

### 3.2.1. THRUST COEFFICIENT

From experiments by van Arnhem et al. [64], we know the thrust coefficient of the TUD-XPROP-S at $J = 0.8$ and $\alpha = 0$ deg in isolated conditions. We can use this as an approximate reference for our simulations and concurrently verify if the propeller thrust achieved in CFD is grid convergent. Note that since the simulations feature the propeller in installed conditions, the thrust coefficient will likely deviate slightly. The values of $T_c$ for the three resolutions simulated at $\delta_f = 30$ deg, $\alpha = 8$ deg are shown in Table 3.2, together with the experimental reference value. This combination of flap and wing angle settings is chosen as they feature the most complex aerodynamic features.

Table 3.2: Thrust coefficients for different grid resolutions at $\delta_f = 30$ deg, $\alpha = 8$ deg and experimental value for isolated propeller at $\alpha = 0$ deg.

| Resolution | $T_c$ |
|:---:|:---:|
| Coarse | 0.405 |
| Medium | 0.408 |
| Fine | 0.409 |
| Experiment | 0.412 |

Grid convergent behaviour is observed, with the difference between the fine and medium grids being over two times smaller than the difference from medium to coarse. The value of $T_c$ is within 1% of the reference for the isolated propeller, which we consider adequate.

### 3.2.2. WING PRESSURE DISTRIBUTION

As the simulations are set up to mimic the first experiment, we can use the experimental pressure distributions for the same purposes as the thrust coefficient. Figure 3.5 compares the experimental chordwise pressure distributions with the simulated results for three grid resolutions. Again, we select the highest flap deflection and angle of attack in our simulations, as it represents the most challenging case. Figure 3.5 shows that the smooth body separation over the flap is slightly affected by the resolution, in particular on the downgoing blade side, but the results do not change substantially with increase in grid resolution. Hence, we use the medium resolution for all of the LBM simulations.
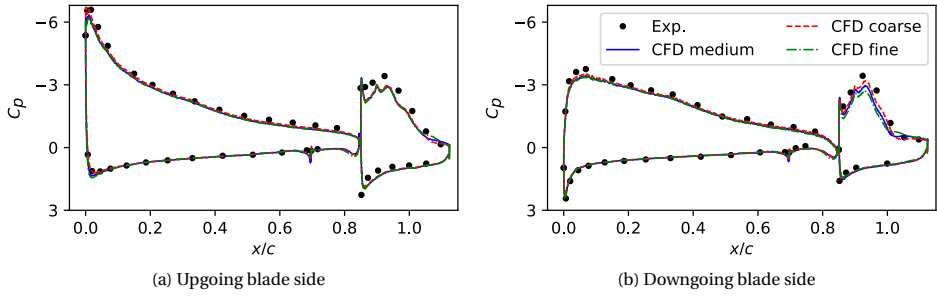
Figure 3.5: Effect of grid resolution on pressure coefficient along the wing chord for $\delta_f = 30$ deg, $\alpha = 8$ deg.

While the main element of the wing was tripped in the experiments, the flap was not. At such low Reynolds numbers (600,000 based on the clean wing chord), substantial regions of laminar flow can occur and laminar separation bubbles were observed on the flap in the experiments. To verify the sensitivity to such effects, we conducted simulations using a transition model [82] on the flap. This made the flap leading-edge laminar and the results of this are shown in Fig. 3.6. The pressure cuts show a small delay in the flap separation, improving the pressure distribution on the flap, and also the suction peak on the main element of the wing. Using a more advanced transition treatment, capable of accurately capturing separation bubbles [83] could lead to further improvements.

Although the results with the transition model show a slight improvement over the fully turbulent simulation, the differences are small enough that we set the remaining cases to fully turbulent. This avoids any uncertainties associated with using a transition model for a high-lift configuration [52]. It also facilitates the grid resolution study, as transition models have been shown to be sensitive to the mesh [84].

The rest of the simulated configurations thus feature the medium resolution and no transition model. Figure 3.7 shows a comparison of experimental measurement and simulated results for all simulated combinations of $\alpha$ and $\delta_f$. All configurations results show very good agreement with experiment. As $\delta_f$ increases, the simulations show discrepancies compared to experiments in the suction peaks, which can be connected to
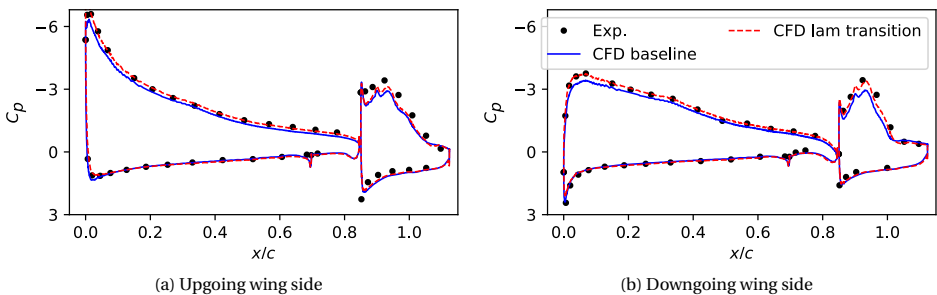


Figure 3.6: Effect of laminar to turbulent transition on chordwise pressure distribution at $y/R = \pm 0.7$ for $\delta_f = 30$ deg, $\alpha = 8$ deg.
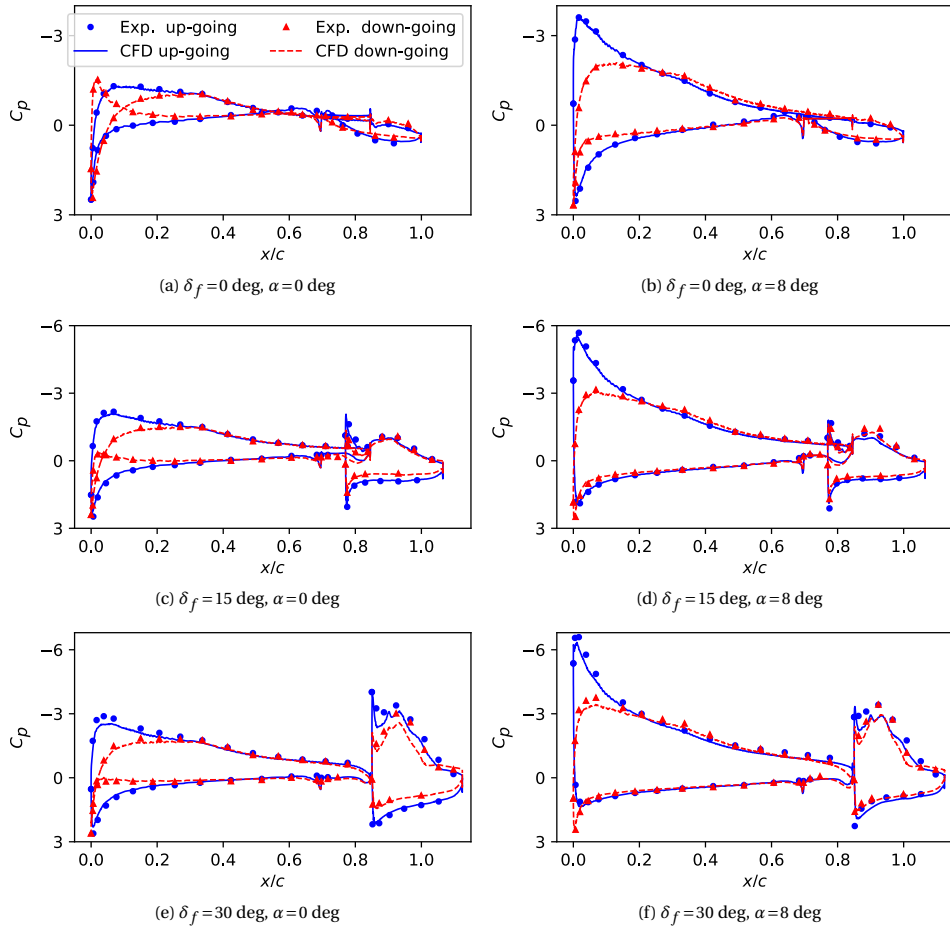
Figure 3.7: Pressure coefficient along the wing chord on the upgoing and downgoing blade sides of the propeller for different flap angles $\delta_f$ and angles of attack $\alpha$.
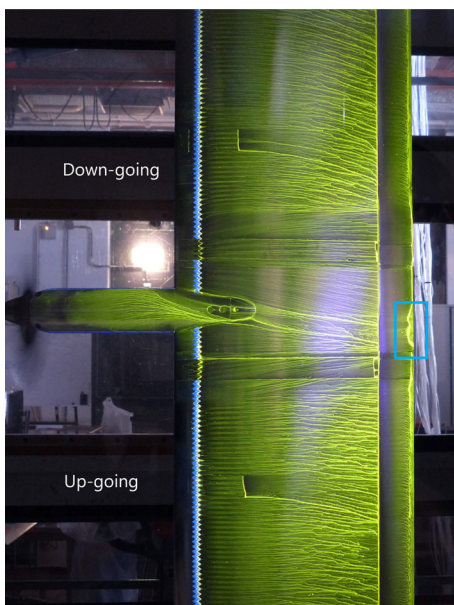
laminar-to-turbulent transition based on Fig. 3.6. In all simulations the additional total pressure generated by the propeller is well captured, as the $C_p$ values at the stagnation points agree with experimental values.
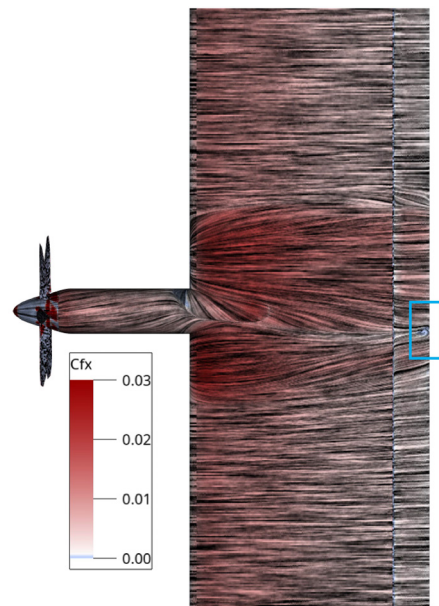
### 3.2.3. SURFACE OIL FLOW

In addition to the quantitative comparison of pressure distribution, we can use oil flow images to quantitatively compare complex flow structures on the wing surface between experiment and simulation. Figures 3.8 and 3.9 show a comparison of experimental oil flow visualization with numerical surface shear lines. Blue boxes are used to draw attention to several flow structures that match very well between the experimental oil flow and the simulated surface shear. Red boxes show distinct differences between simulations

and experiments. Figures 3.8a and 3.8b both show a slight separation due to nacelle vortex structure. With flaps deployed, the interference of the flap brackets on the flap flow is clearly visible in both experiment and simulation. The local separation on the flap is also captured well by the simulations, where the flow structures near the centre of the flap span in Fig. 3.8e and Fig. 3.8f are particularly of note. They also show the presence of the laminar separation bubble on the flap (marked in red in Fig. 3.8e), which is not present in the simulation and has some effect on the flap separation.

At $\alpha = 8$ deg (Fig. 3.9), the major flow structures, such as the effect of flap brackets and the crossflows directly behind the nacelle, are again captured well. The separated areas on the main element are captured by the simulation, but seem under-predicted (marked with orange boxes). They only occur on the upgoing blade side in the simulation, while Fig. 3.9c shows clear signs of separation on the main element on the downgoing blade side as well. The area of the flap that is affected by the slipstream also seems slightly larger in the oil flow images, although this cannot be fully judged from these images alone. Nonetheless, overall the simulated shear lines agree well with experimental oil flow visualization, which is very challenging to achieve in numerical simulations with smooth body separations [52].



(a) Exp. $\delta_f = 0$ deg                                (b) CFD $\delta_f = 0$ deg

(c) Exp. $\delta_f = 15$ deg

(d) CFD $\delta_f = 15$ deg

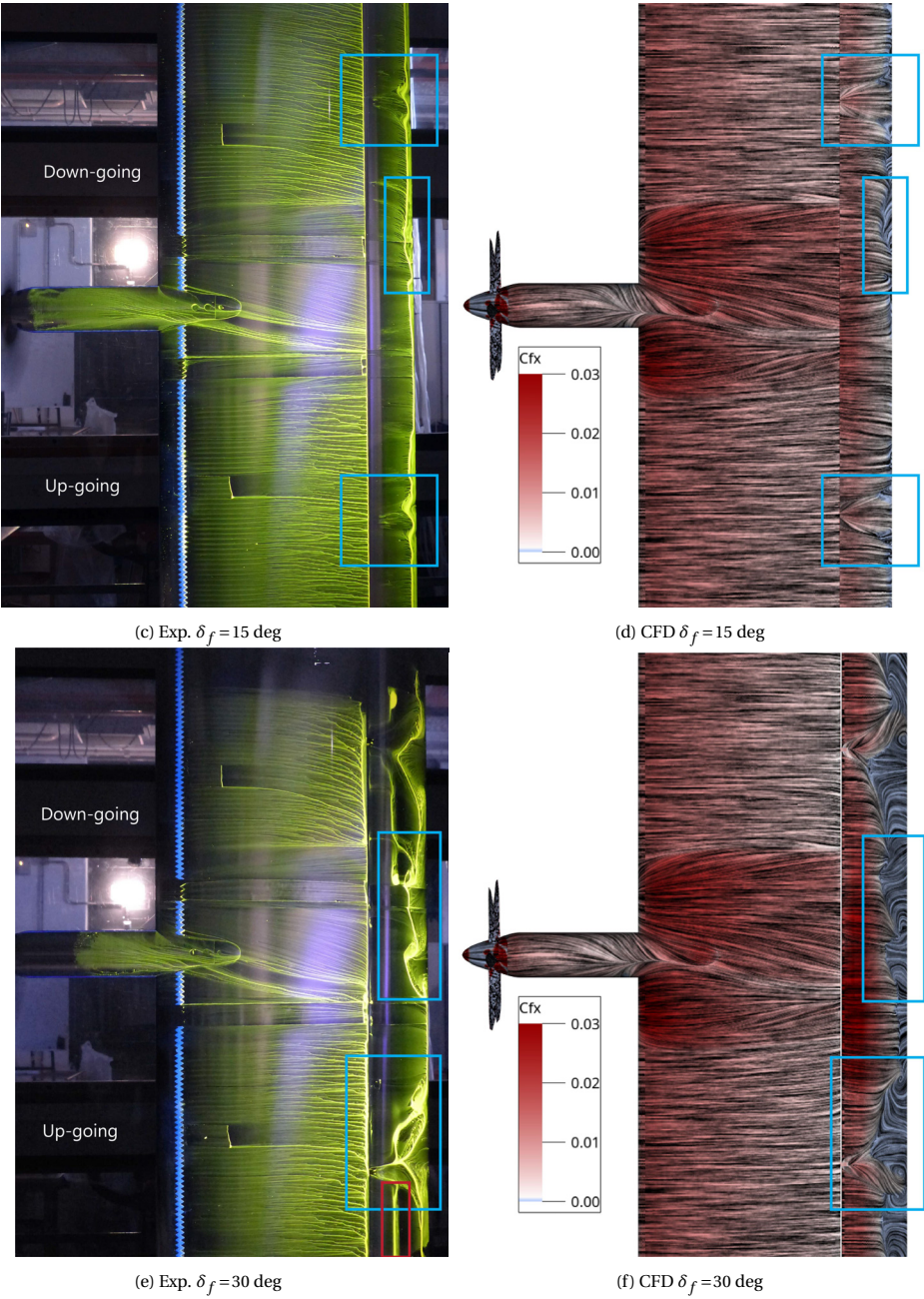(e) Exp. $\delta_f = 30$ deg

(f) CFD $\delta_f = 30$ deg

Figure 3.8: Surface shear lines on the wing suction side, represented by oil flow in the experiment and coloured by streamwise skin friction coefficient in simulations at $\alpha = 0$ deg. Boxes indicate notable flow features. Concluded.
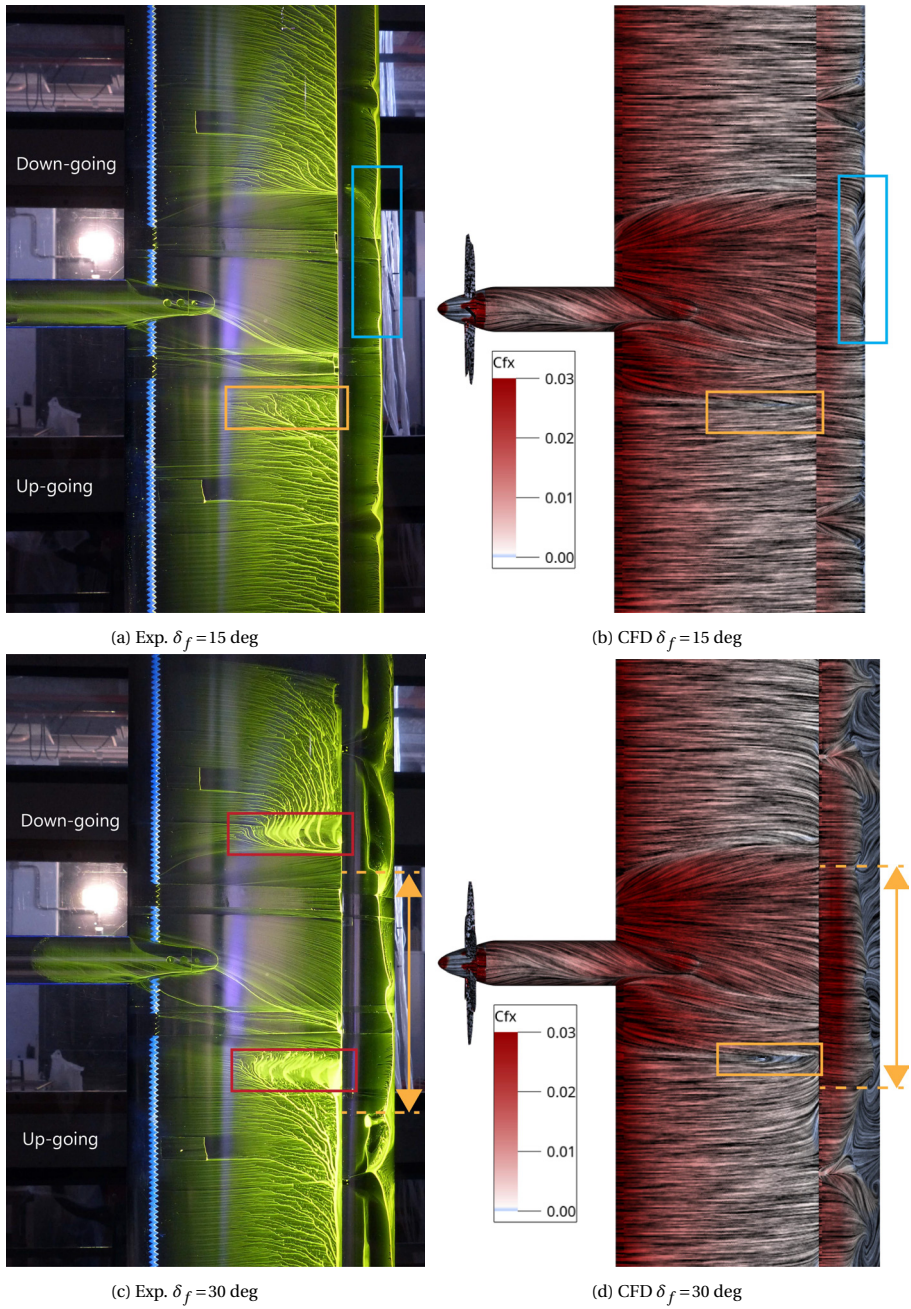
(a) Exp. $\delta_f = 15$ deg

(b) CFD $\delta_f = 15$ deg

(c) Exp. $\delta_f = 30$ deg

(d) CFD $\delta_f = 30$ deg

Figure 3.9: Surface shear lines on the wing suction side, represented by oil flow in the experiment and coloured by streamwise skin friction coefficient in simulations at $\alpha = 8$ deg. Coloured boxes indicate flow features of interest.

### 3.2.4. TOTAL PRESSURE WAKE PLANE

Finally, we compare distributions of total pressure coefficient $C_{p,t} = (p_t - p_{s,\infty})/q_\infty$ on a plane one chord downstream of the nested flap trailing-edge at $\alpha = 0$ deg. Experimental results are shown on the top rows of Figs. 3.10 and 3.11, while the simulations are shown in the bottom rows. The horizontal lines represent the wing leading edge and flap trailing edge, while the circles indicate the propeller position. The distributions clearly show the deformation of the slipstream, which can be identified by $C_{p,t} > 1$ since the propeller adds total pressure to the flow. The deformation is a direct result of the propeller-wing aerodynamic interaction. A close match of the distribution of total pressure coefficient in the wing wake is therefore representative of an accurate simulation of the upstream aerodynamics.
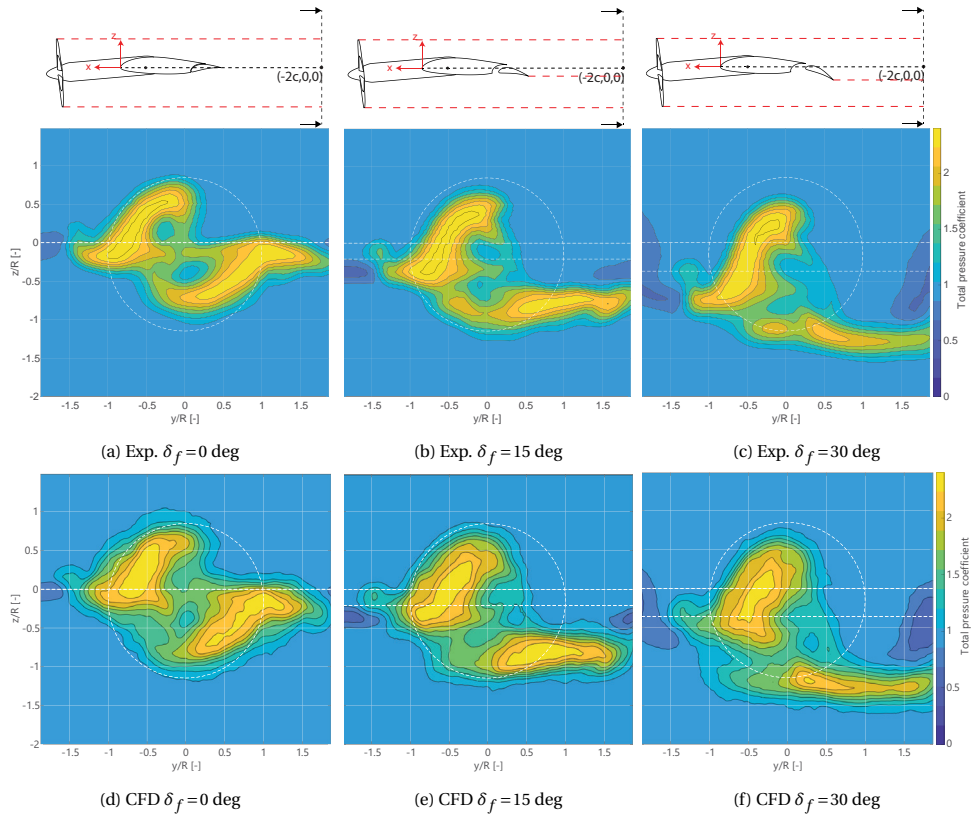


Figure 3.10: Distribution of total pressure coefficient in the wake of the wing. $\alpha = 0$ deg.

The flow features of the propeller wake being cut by the wing and the slipstream on the upper surface moving to the downgoing blade side, while the slipstream on the lower surface moves to the upgoing blade side are well captured by the simulations. The vortices that appear as pressure loss regions near the centre of the images are also well captured, with small differences that increase with $\alpha$ and $\delta_f$. At $\alpha = 8$ deg and flaps deflected

(Fig. 3.11) the general shape is captured, but the discrepancy between simulation and experiment is larger than for $\alpha = 0$. This can partly be attributed to differences in flow separation on the flap. Overall, the match between simulations and experiments is very good, particularly considering that resolving the slipstream downstream of the wing is generally a challenge for traditional N-S solvers due to the dissipation and diffusion of vorticity.
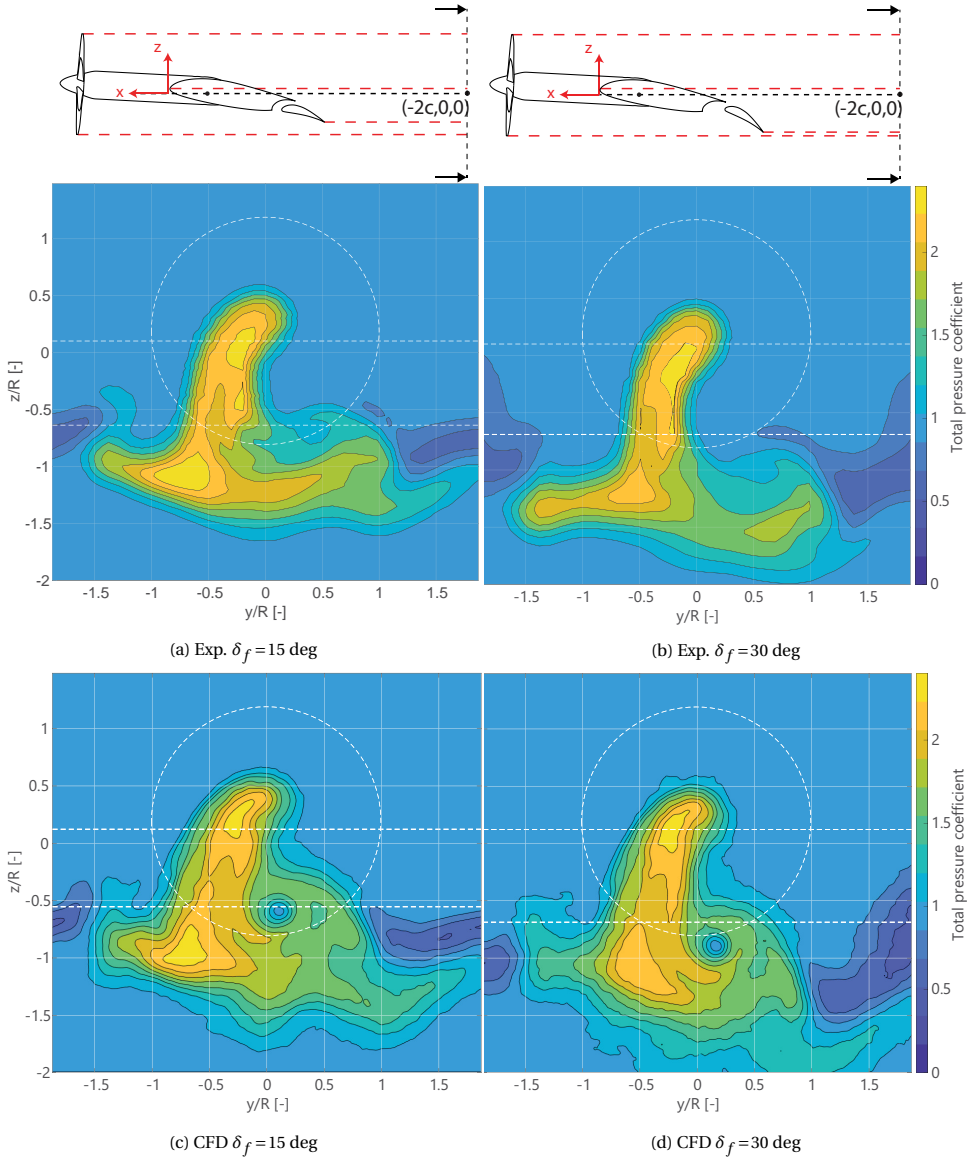


(a) Exp. $\delta_f = 15$ deg

(b) Exp. $\delta_f = 30$ deg

(c) CFD $\delta_f = 15$ deg

(d) CFD $\delta_f = 30$ deg

Figure 3.11: Distribution of total pressure coefficient in the wake of the wing. $\alpha = 8$ deg.

## 3.3. VERIFICATION OF RSM MODEL FIT

Applying the metamodel described by Eq. (2.1) in Chapter 2, inherently assumes that the factor dominance of the design space can be estimated using an extended quadratic model. Since all the main factors individually have either a linear or quadratic relation to the chosen responses within the considered values, combined with the focus on term ranking instead of response prediction, we believe this assumption to be valid. As there is no random error in the design and replicates are meaningless in the context of deterministic simulations, we cannot perform a standard lack-of-fit test. We therefore verify the metamodel fit using 300 confirmation points distributed throughout the parametric space. The points are chosen according to the I-optimality criterion, which attempts to reduce the prediction variance in the design space and are thus the points most critical for model fit.

Figure 3.12 shows histograms based on the number of runs with a residual of the predicted value within a certain range of the simulated value. The cumulative fraction of the total number of runs is displayed on the secondary axis. The model for lift predicts over 95% of the model points with a residual of less than 1.5% and all of the model points within 3.5%. The models for drag and moment show more deviation, but still predict 95% of the points within 5% of their actual value. All models show larger deviations for the confirmation points, although this is to be expected. Out of the confirmation points, 95% are predicted within 3.5% of their actual lift value, while their moment value is predicted within 4.5%. For drag, the 95% mark is reached with a maximum residual of around 7.5%. Towards the edge of the design space, particularly for the combination of high $\alpha$, $M$ and $V_j/V_\infty$, the prediction of drag becomes very poor. This is an indication of insufficient model order for that part of the design space. Nonetheless, based on the data in Fig. 3.12, we are confident the metamodels sufficiently represent the parametric space for the analysis in this dissertation. Only the drag response may become invalidated for configurations with high $\alpha$, $M$ and $V_j/V_\infty$. This is likely related to compressibility effects, which is further discussed in Chapter 4.
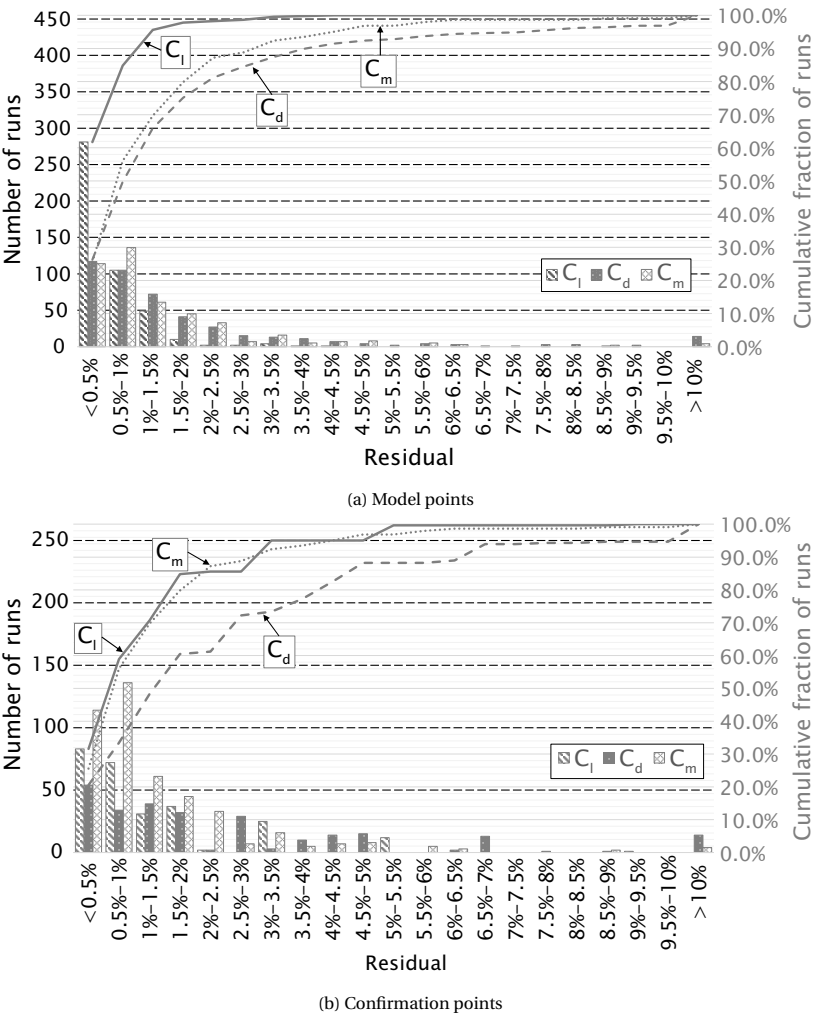
(a) Model points



(b) Confirmation points

Figure 3.12: Histogram of the percentual residual of the model points and the confirmation points for the metamodels used in the regression analysis of the main design.

# II

## RESULTS AND DISCUSSION

# 4

## INTERACTIONS OF A MULTI-ELEMENT AIRFOIL IN A JET

*In chapter 1, we divided the propeller-wing-flap aerodynamic interaction into two main perspectives: how traditional multi-element airfoil aerodynamics change due to the addition of the propeller, and how propeller-wing aerodynamic interaction changes due to the addition of a flap element. In this chapter, we investigate the former. The main aerodynamic mechanisms of traditional multi-element airfoils can be described from a 2D perspective. To this, we add a 2D analogy of the propeller, which reduces to a jet of increased dynamic pressure. Using principles from Design of Experiments and Response Surface Methodology, we can quantify which design parameters dominate lift, drag and moment responses, and particularly how these parameters interact and affect the flow. The general methodology of this analysis is presented in Chapter 2 (Section 2.2.4), but a short summary is provided for the comfort of the reader in Section 4.1. The results of the analysis methodology on a traditional multi-element airfoil configuration without jet is presented in Section 4.2 as a baseline, after which it is compared to the same analysis performed on a multi-element airfoil subjected to a jet of fixed velocity, size, and position in Section 4.2.1. This comparison reveals whether the typical interactions in a multi-element airfoil configuration change due to the presence of the jet. Sections 4.3 and 4.4 then continue to define the dominant interactions of the entire design space, showing how the dependencies change with variations in jet velocity, size, and position. The key findings of the chapter are summarized in Section 4.5. All aerodynamic data for this chapter was generated with the modified MSES solver described in Chapter 2.*

---

A version of this chapter has been published in Ref. [56].

## 4.1. SUMMARY OF DESIGN SPACE AND METHODOLOGY

The design space represents a simplified, two-dimensional equivalent of a propeller-wing-flap (or rather *jet-wing-flap*) configuration and consists of nine main *factors*, illustrated in Fig. 4.1. A total of 541 different combinations of these factors, determined by a central composite design, were simulated using the modified MSES solver. The simulations result in various *responses* including lift, drag, and moment coefficient and lift augmentation factor $K_{C_l}$. The latter is defined as the ratio of lift coefficient with a jet in the domain compared to the same airfoil configuration without the jet. A reduced design space, which excludes all terms that involve the jet, serves as a baseline design space. This baseline is used to characterize the dominant factors and interactions of a two-element airfoil when it is not subjected to a jet.

**4**



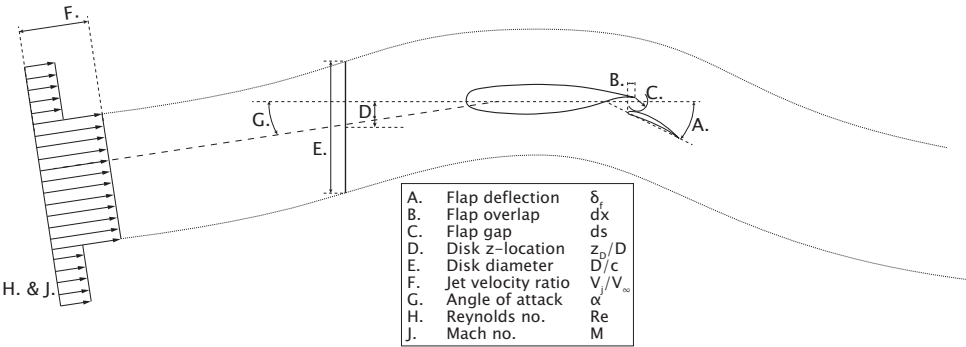| | | |
|---|---|---|
| A. | Flap deflection | $\delta_f$ |
| B. | Flap overlap | $dx$ |
| C. | Flap gap | $ds$ |
| D. | Disk z–location | $z_D/D$ |
| E. | Disk diameter | $D/c$ |
| F. | Jet velocity ratio | $V_j/V_\infty$ |
| G. | Angle of attack | $\alpha$ |
| H. | Reynolds no. | $Re$ |
| J. | Mach no. | $M$ |

Figure 4.1: Illustration of the parametric design space of the jet-wing-flap configuration.

Second-order metamodels (extended with three-factor interactions) are then fitted to each of the extracted responses using polynomial regression. Based on the resulting metamodel equations, we calculate the contribution of each term in the equation to the complete model. This quantifies how much each term in the metamodel changes the response (or *contributes* to the model), compared to how much the response varies in total across the entire design space (the model *variability*). The terms in the metamodel include *main factors* (i.e., angle of attack, flap deflection, etc.) and *interactions* between the main factors (up to three-factor interactions), and are represented by coded letters as given in Fig. 4.1.

Responses are always non-dimensionalised based on the freestream conditions, not the jet velocity. Note that these are responses relating to integral performance, not specific aerodynamic phenomena. The phenomena have to be identified by aerodynamic analyses, for which the relation between factors and performance coefficients can serve as effective guidance. We can also compare different design spaces, such as jet flow conditions with regular uniform freestream conditions, and test whether the dominant relations change. This would indicate fundamental changes in aerodynamic interactions.

## 4.2. BASELINE DESIGN SPACE RESULTS

For the baseline design space, a two-element airfoil in a uniform freestream, the main factors alone are directly responsible for nearly all change to the aerodynamic responses in the design space. Figure 4.2 shows a graph of the contributions of various terms in the metamodels fitted to the lift, drag, and moment coefficient responses in the baseline design space. Only factors and interactions contributing at least 1% to any response are shown for clarity, with all terms retained in the metamodel. The "main factors" bar represents the sum of all main factors, which represent over 97% of the model variability in each response. This suggests that interaction effects between factors are not dominant for the responses within the design space. The most important factors are clearly flap deflection $\delta_f$ and $\alpha$. For moment coefficient, $\alpha$ hardly contributes to the variability, and d$x$ is one of the dominating factors instead.
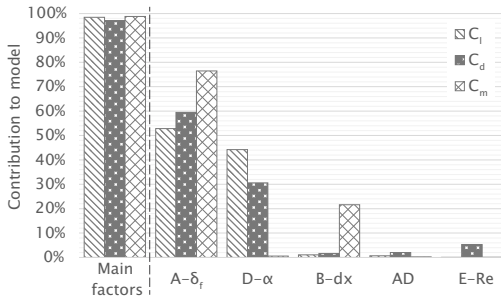


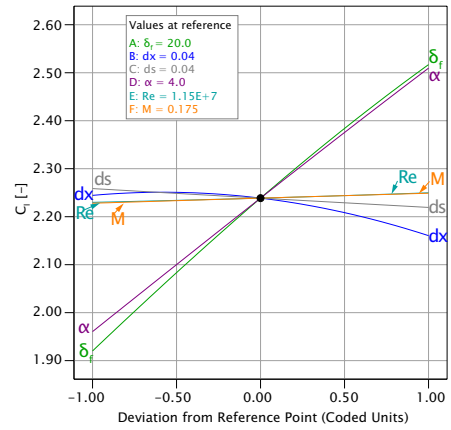Figure 4.2: Factor contributions to the lift, drag, and moment responses for the baseline model.



Figure 4.3: Perturbation plot of lift coefficient around the centrepoint of the baseline model.

The factor contributions alone do not show how the factor affects the response in absolute terms. This is better visualized by a perturbation plot, as shown in Fig. 4.3 for the lift response. This plot depicts response deviations from a reference point (centrepoint of the design space) as factors change individually. Lines show response changes when a single factor is varied between low (-1) and high (+1) values[1], while others remain constant. This does not show interactions, which would cause the trends to change depending on the value of interacting factors. Since Fig. 4.2 indicates no significant interactions, this suggests stable trends in the perturbation plot across the design space.

### 4.2.1. COMPARISON BETWEEN UNIFORM AND JET FLOWS

We can compare the baseline design with subsets of the jet design, where the jet-related factors $V_j/V_\infty$, $D/c$ and $z/D$ are kept constant. These subsets then have the same 6-factor CCD as the baseline design, but with a jet of fixed velocity, size, and position in the domain.

---

[1] Note that *low* and *high* refer to the corresponding settings (-1) and (+1) in the CCD (see Chapter 2), and do not comment on the magnitude of the variable.

This comparison will reveal whether the airfoil responds differently when immersed in a jet compared to uniform freestream. Figure 4.4 shows the factor contributions to the lift, drag, and moment responses for the baseline design space and subsets with specified combinations of jet size, velocity, and position. Table 4.1 summarizes the four subsets considered for comparison with the baseline.

Table 4.1: Summary of subset jet settings.

| Subset | $V_j/V_\infty$ [-] | $D/c$ [-] | $z/D$ [-] |
|--------|--------------------|-----------|-----------|
| 1 | 1.5 | 2.0 | 0.1 |
| 2 | 1.5 | 1.1 | -0.2 |
| 3 | 1.5 | 2.0 | -0.2 |
| 4 | 2.0 | 2.0 | -0.2 |

**4**

Figure 4.4 reveals that for low (-1) jet velocity ratios (Subsets 1 through 3), the same factors and interactions contribute to the response as for the baseline, matching within a few percent of contribution. The slight differences between cases can be attributed to a combination of inherent error of the solver and any interactions between the displayed factors and the fixed jet parameters. For the high (+1) jet velocity (Subset 4), however,



(a) Lift coefficient

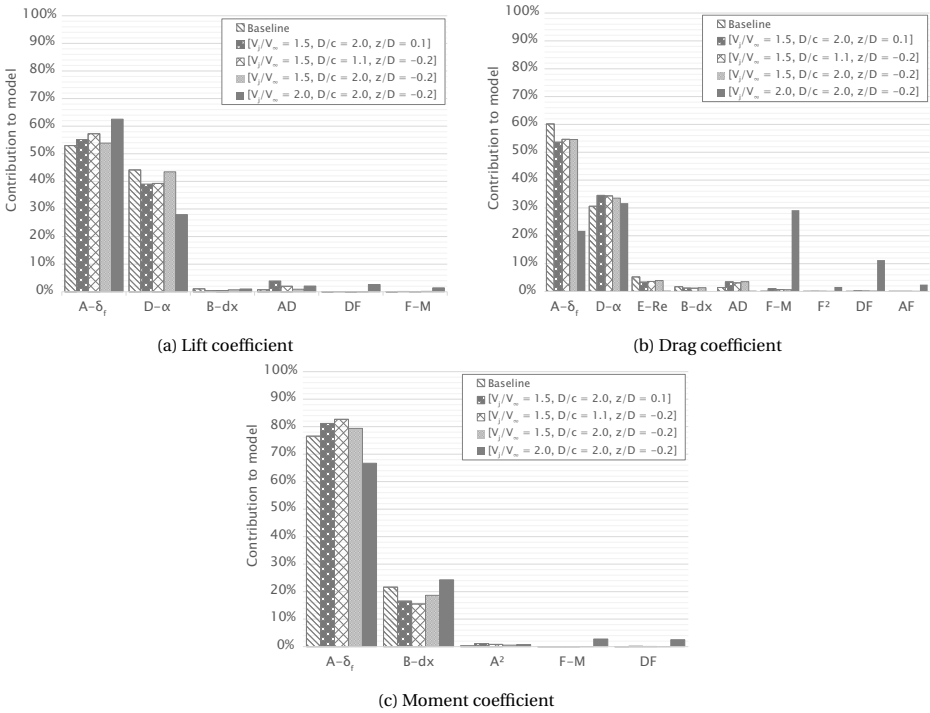(b) Drag coefficient

(c) Moment coefficient

Figure 4.4: Comparison of the relative contribution to the model with and without jet. Only terms with a contribution above 0.5% are shown.

the factor contributions change significantly. Lift and moment coefficient responses show significant variations in contribution of their dominant factors, but overall show the same terms to be dominant. Mach number and the interaction DF ($\alpha$-$M$) are added as significant contributors. For the drag response however, the dominant terms change drastically. Flap deflection contributes much less to the model compared to the other subsets and the baseline, while Mach number becomes the second-most dominant factor. Interactions DF ($\alpha$-$M$) and AF ($\delta_f$-$M$) also significantly increase their contributions.

The change in the dominant factors and interactions for subset 4 can be attributed to the occurrence of transonic flow on the main element. This adds wave drag and can increase the boundary layer displacement thickness (and thus viscous drag) significantly, as illustrated in Fig. 4.5. Out of all design points in Subset 4, roughly 70% has a shock on the main element, with wave drag on average contributing 10% of the total drag. For the other subsets, only about 20% of the design points contain transonic flow and the wave drag contributes on average only around 1% to the total drag. The baseline design contains no configurations with transonic flow at all. The occurrence of transonic flow is, of course, highly configuration dependent and the jet velocity ratios considered in this study are relatively large. Nonetheless, the addition of a jet to the domain can trigger a significantly different airfoil response compared to a uniform flow due to transonic effects. This may pose a crucial limit to propeller-blowing as a high-lift system.
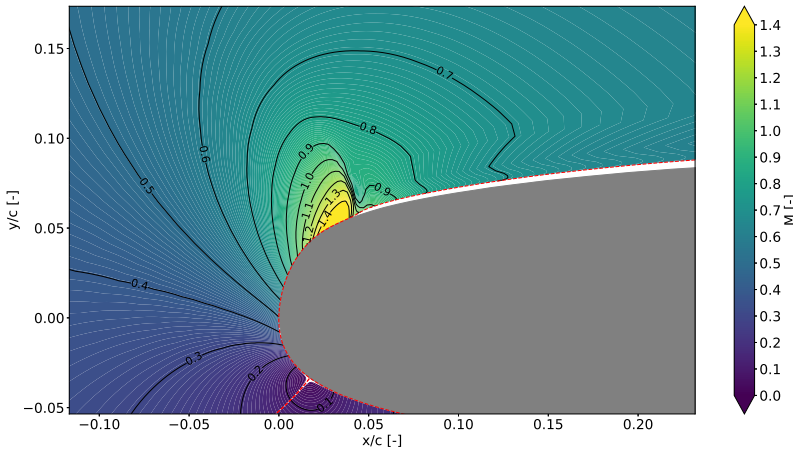


Figure 4.5: Mach contour of the flowfield of an example run from Subset 4, showing the shock on the main element and associated increase in displacement thickness (red dashed line).

## 4.3. JET DESIGN SPACE RESULTS

Figure 4.6 shows the relative contributions of model terms to the responses in lift, drag, and moment coefficients for the full jet design space. Only model terms that contribute more than 0.5% to the total variability in the response are shown. It is clear that jet velocity ratio $V_j/V_\infty$ (factor F) is the most dominant factor for all aerodynamic coefficients. Only varying $V_j/V_\infty$ and keeping all other terms in the model constant accounts for around 55% of the variation in lift across the design space. For drag and moment coefficients, this is 50% and 45%, respectively. Further dominant factors include angle of attack $\alpha$ (factor

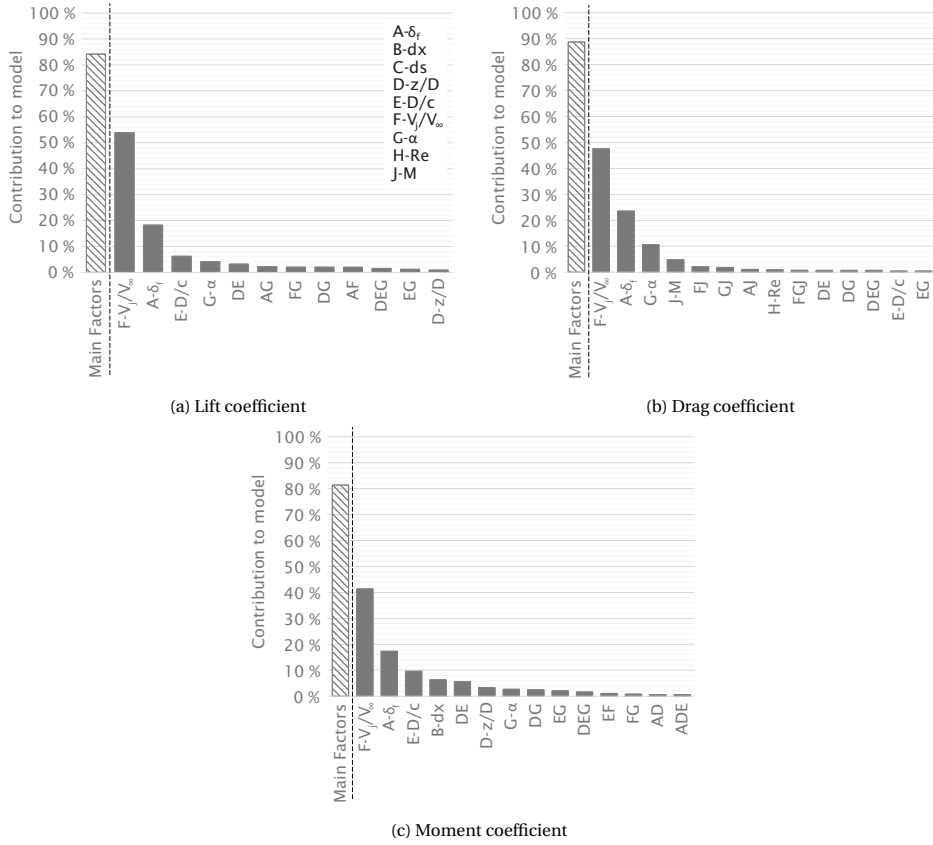(a) Lift coefficient

(b) Drag coefficient

(c) Moment coefficient

Figure 4.6: Relative contribution of terms to the lift, drag, and moment responses. Only shows terms with a contribution ≥ 0.5%. Dashed bar indicates sum of main factors only.

G), flap deflection angle $\delta_f$ (factor A) and diameter-to-chord ratio $D/c$ (factor E). The latter contributes primarily to lift and moment response and not as much to the drag response.

Figure 4.7 displays the perturbation plots around the centrepoint, showing how factors affect the responses. Increasing jet velocity ratio increases both lift and drag coefficients, while decreasing the moment coefficient. While lift and moment coefficient behave (nearly) linearly, the drag coefficient increases non-linearly with increasing jet velocity ratio. The linear scaling of $C_l$ and $C_m$ with $V_j/V_\infty$ is readily explained by the fact that they are normalized by the freestream instead of the jet velocity. The same would be expected for $C_d$ in fully incompressible conditions. However, we have already established that a portion of the design space contains significant transonic flow effects. Across the full jet design space, transonic flow occurs in about 25% of the design points, resulting in a non-linear relation of $C_d$ with both $V_j/V_\infty$ and $M$. This becomes evident from Fig. 4.8, showing the interaction between $V_j/V_\infty$ and $M$ for the drag response. For $M = 0.15$, the drag coefficient scales linearly with $V_j/V_\infty$, while for $M = 0.2$ it becomes non-linear.

(a) Lift coefficient

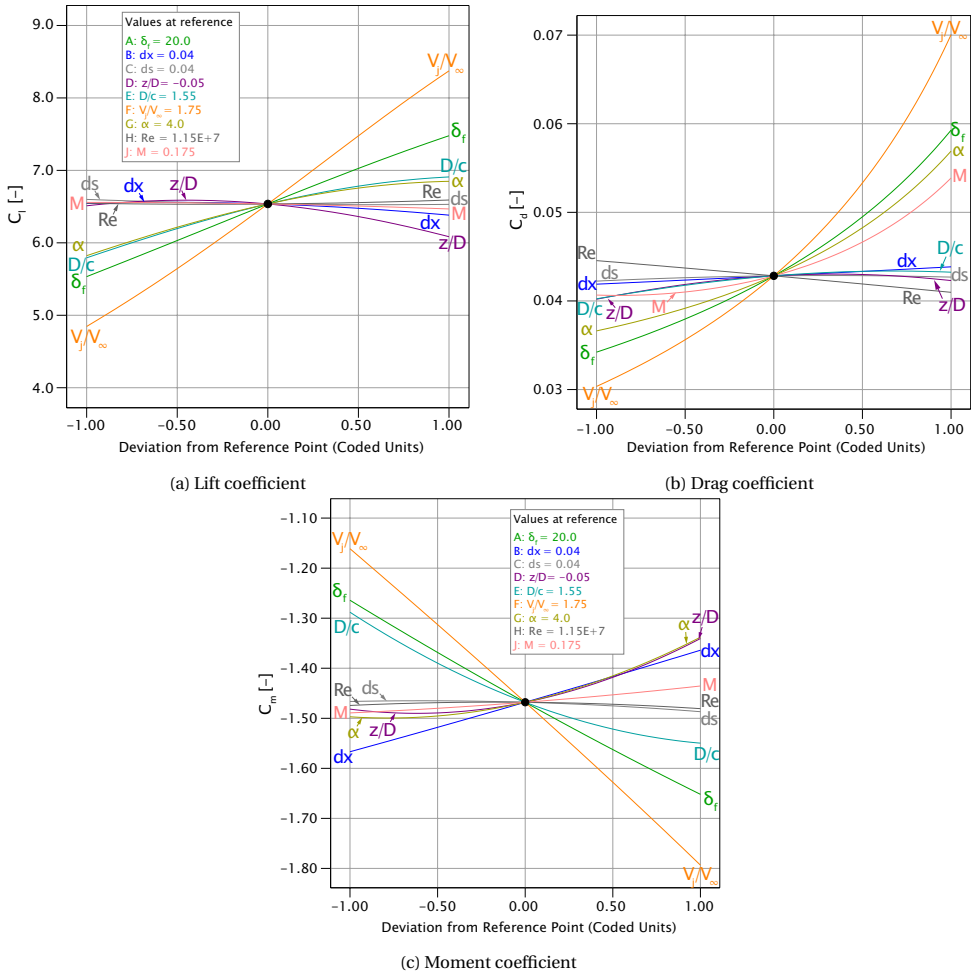(b) Drag coefficient

(c) Moment coefficient

Figure 4.7: Perturbation of responses around the centrepoint by each of the main factors. Coded units refer to the low (-1) and high (+1) values in the CCD.

Figure 4.9 presents Mach number contour plots for the two design points indicated in Fig. 4.8, showing the transonic region for the $M = 0.2$ configuration. Table 4.2 contains a drag breakdown for both configurations shown in Fig. 4.9, showing that wave drag contributes nearly one-third to the total drag coefficient for the $M = 0.2$ case.

Figure 4.8 also demonstrates that a relatively small contribution to the total model variability does not necessarily mean it is negligible in terms of absolute response value. Although the $V_j/V_\infty$-$M$ interaction only contributes a few percent to the model, change in drag coefficient varies between roughly 0.03 and 0.1 due to the interaction. The presence of $V_j/V_\infty$ in the model thus obscures the significance of other factors and interactions due to it having a disproportional impact on the responses. Visualizing the interactions and analysing how they affect the relation between factors and responses is thus important.
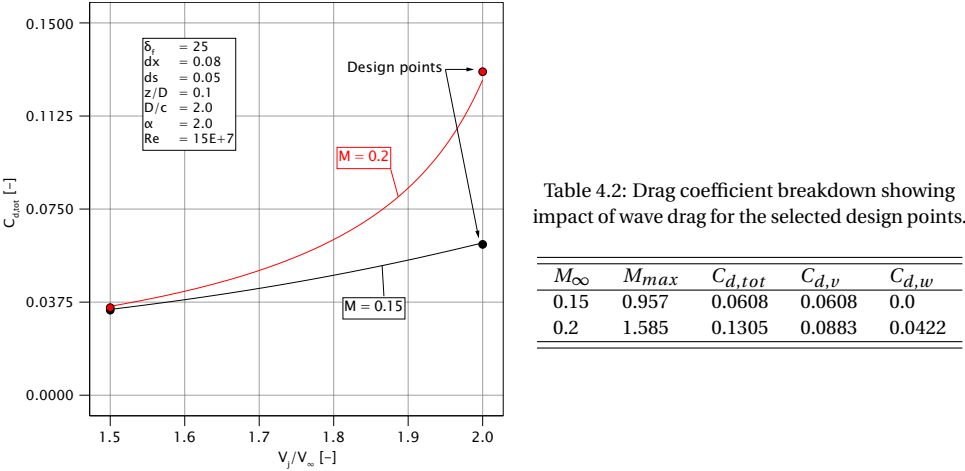
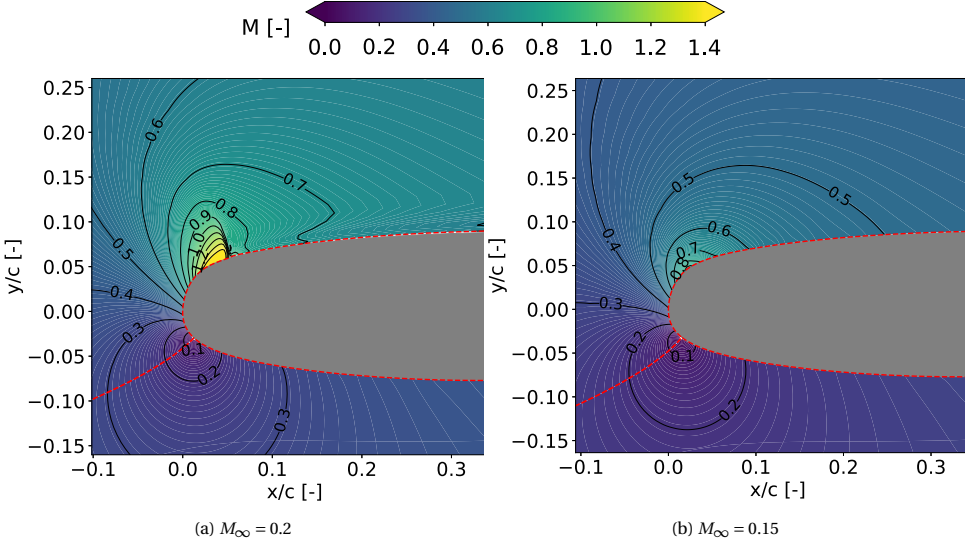Figure 4.8: $C_d$ vs. $V_j/V_\infty$ for varying $M$.

Table 4.2: Drag coefficient breakdown showing impact of wave drag for the selected design points.

| $M_\infty$ | $M_{max}$ | $C_{d,tot}$ | $C_{d,v}$ | $C_{d,w}$ |
|------------|-----------|-------------|-----------|-----------|
| 0.15       | 0.957     | 0.0608      | 0.0608    | 0.0       |
| 0.2        | 1.585     | 0.1305      | 0.0883    | 0.0422    |



(a) $M_\infty = 0.2$                    (b) $M_\infty = 0.15$

Figure 4.9: Mach contours for $M_\infty = 0.15$ and $M_\infty = 0.2$, showing transonic conditions occurring on the wing suction side. $\alpha$ set to (-1), other factors to (+1).

## 4.3.1. IMPORTANT INTERACTIONS IN THE JET DESIGN SPACE

From the summed contribution of all main factors (the dashed bars in Fig. 4.6) we see that, compared to the baseline design, a significant portion depends on interactions. For the lift coefficient, roughly 15% of the response depends on interactions, while for the drag and moment coefficients this is 10% and 23%, respectively. The most important interactions can be split into two sets. For lift and moment coefficients, the main interactions involve $\delta_f$ (A), $z/D$ (D), $D/c$ (E), $\alpha$ (G), and $V_j/V_\infty$ (F). For the drag coefficient, a second set of important interactions exists between $\alpha$ (G), $V_j/V_\infty$ (F), $\delta_f$ (A) and $M$ (J). The latter set of interactions can again be attributed to transonic flow conditions mentioned previously.

The maximum velocity in the domain is mostly dictated by the upstream velocity (i.e., $V_j/V_\infty$ and $M$) and the streamline curvature (i.e., $\alpha$ and $\delta_f$). We can therefore attribute the contributions of interactions FJ ($V_j/V_\infty$-$M$), GJ ($\alpha$-$M$), AJ ($\delta_f$-$M$) and FGJ ($V_j/V_\infty$-$\alpha$-$M$) to the occurrence of transonic flow in the design space.

The other set of interactions ($\delta_f$ (A), $z/D$ (D), $D/c$ (E), $\alpha$ (G), and $V_j/V_\infty$ (F)) can again be split into two groups. The first group consists of interactions between $\alpha$, $\delta_f$ and $V_j/V_\infty$. They are visualized through the lift response surface in Fig. 4.10. An interaction means



(a) $V_j/V_\infty$ versus $\alpha$



| Other Factors: | dx=0.04 | ds=0.04 | z/D=−0.05 | D/c=1.55 |
| | α=4.0 | Re=11.5E6 | M=0.175 | |

(b) $V_j/V_\infty$ versus $\delta_f$
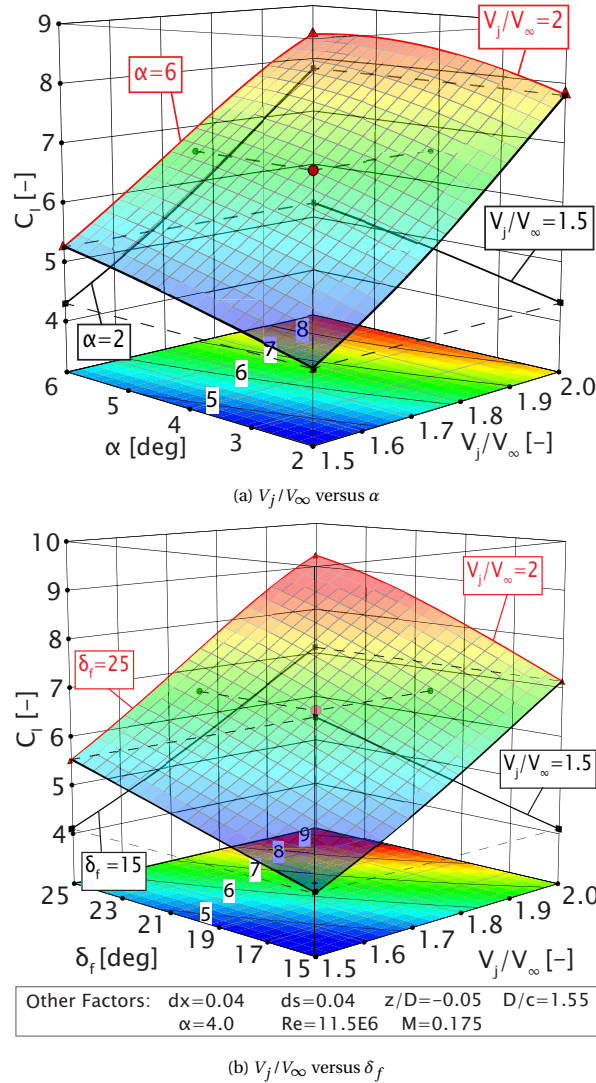
Figure 4.10: Response surfaces of the lift coefficient for the two main interactions involving $V_j/V_\infty$. All other factors are set to the centrepoint. Vertical planes show projections of the edges of the surface.

that the response curve of one factor changes when another factor is changed. The edges of the response surfaces are projected on the vertical planes to make this more visible. Slight interaction effects are visible, where for higher $V_j/V_\infty$ the lift response becomes non-linear with $\alpha$ and steeper with $\delta_f$. However, the effect of these interactions are small compared to the impact of the jet velocity ratio itself.

The second group features factors $\alpha$ (G), $z/D$ (D) and $D/c$ (E). Figure 4.11 shows the response surface of the lift coefficient for $z/D$ and $D/c$ for various levels of $\alpha$, with all other factors at the centrepoint value. Two-factor interactions, such as $z/D$-$D/c$ (DE), are illustrated by the significant change in slope in the projections on the vertical planes. We can see that the response surface shape changes significantly for different $\alpha$, a result from the interactions $\alpha$-$D/c$ (EG), $\alpha$-$z/D$ (DG) and $\alpha$-$z/D$-$D/c$ (DEG). Unlike the interactions with $V_j/V_\infty$, the impact of this group of interactions is in the order of magnitude of the impact of the factors on their own. The jet position $z/D$ particularly does not contribute much to the lift response by itself, but drastically changes the response to $D/c$.

The response surfaces show that a small jet generates more lift at a lower position, while a larger jet benefits from a higher position. However, the impact of vertical position on the lift response with a small jet is generally larger than for a large jet, particularly at higher angles of attack. At low (-1) $\alpha$, a higher position $z/D$ is always beneficial to lift, while at higher $\alpha$ this fully inverts and a lower $z/D$ yields higher lift coefficient for any $D/c$. For an explanation, we look at the immersion of the flap. Ting et al. [77] already showed that the lift of a single airfoil immersed in a jet depends on the ratio between jet height and airfoil chord. Relatively large ratios are necessary to get the full effect of the additional velocity within the jet. In the present study, the jet passes the airfoil mostly on the suction side, as its trajectory is affected by angle of attack and circulation on the airfoil.
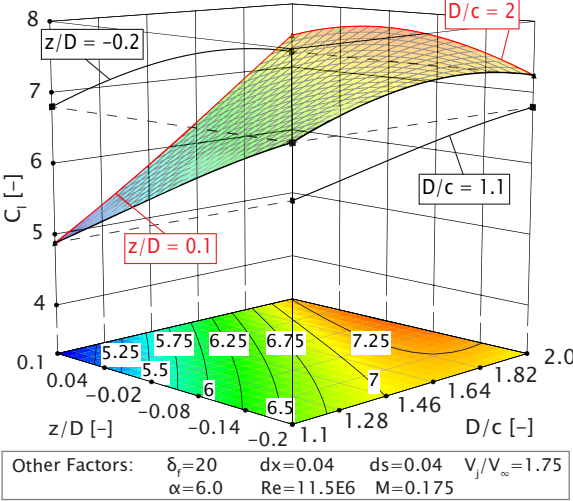
Figure 4.12 illustrates how the flap immersion is a function of the interaction of $D/c$
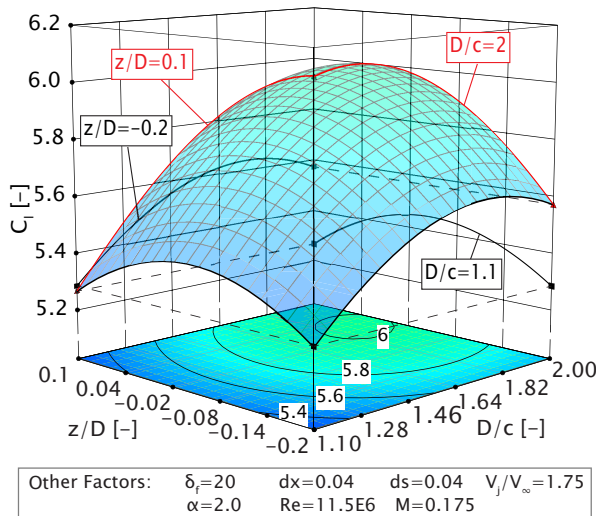


(a) $\alpha = 2$ deg
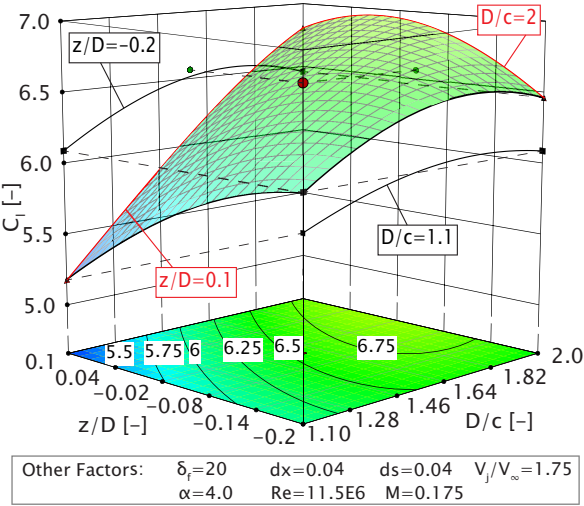
(b) $\alpha = 4$ deg



(c) $\alpha = 6$ deg

Figure 4.11: Response surfaces of the lift coefficient for the interaction of $D/c$ and $z/D$ for various settings of $\alpha$ and all other factors set to the centrepoint. Vertical planes show projections of the edged of the surface. Concluded.

and $z/D$, by visualizing the jet edge for various configurations. The pressure distributions of these configurations are displayed in Fig. 4.13, while Table 4.3 presents a lift breakdown. For a small jet, the lower jet edge approaches the flap very closely, in the case of Fig. 4.12b even travelling over the flap. This drastically reduces the flap lift, which in turn affects the main element lift. For the larger jet, the lower jet edge travels well below the flap for both

vertical positions, with little change to lift or pressure distribution as a result. It is easy to imagine how this will be further affected by $\alpha$, due to its effect on lift and thus upwash. Overall, the interactions between $\alpha$, $z/D$ and $D/c$ suggest that a high position is generally beneficial to the lift coefficient, on the condition that the flap is sufficiently immersed.
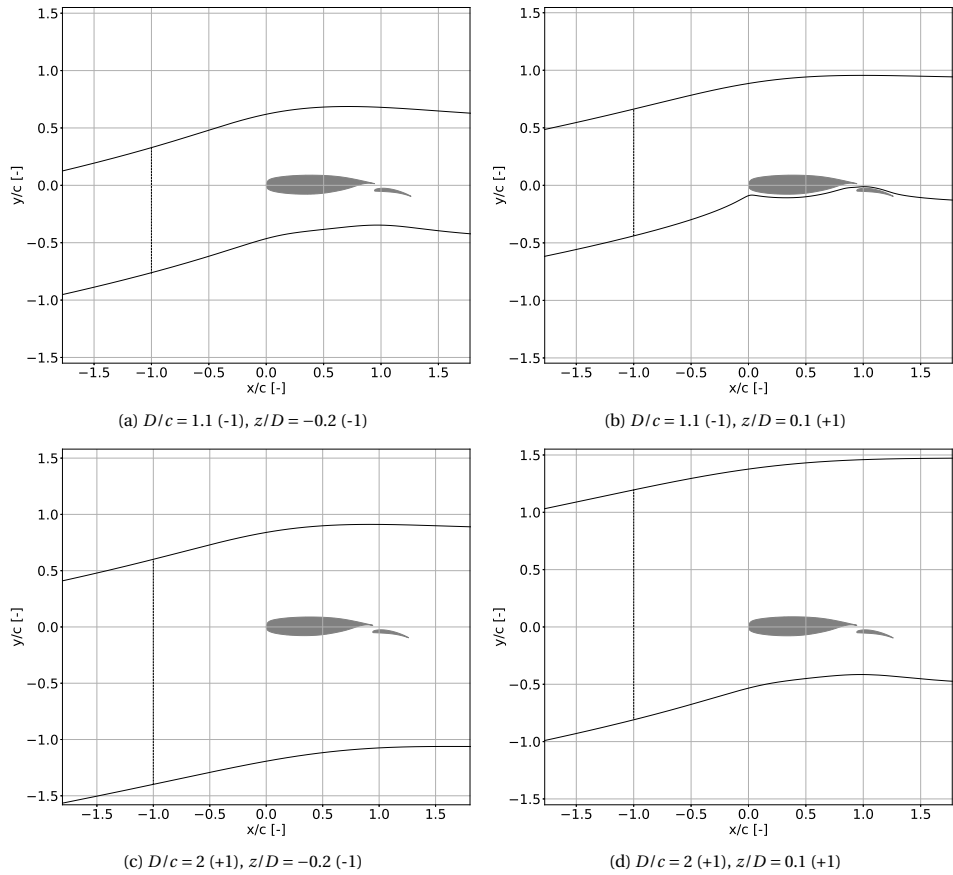


(a) $D/c = 1.1$ (-1), $z/D = -0.2$ (-1)    (b) $D/c = 1.1$ (-1), $z/D = 0.1$ (+1)

(c) $D/c = 2$ (+1), $z/D = -0.2$ (-1)    (d) $D/c = 2$ (+1), $z/D = 0.1$ (+1)

Figure 4.12: Visualization of the jet trajectory for various $D/c$ and $z/D$. From MSES simulations. Jet constraint indicated by dashed line. Other factor values: $V_j/V_\infty = 1.5, \alpha = 6, \delta_f = 15, dx = 0, ds = 0.05, Re = 15e6, M = 0.15$.

Table 4.3: Lift coefficient breakdown showing impact of jet position for different jet sizes.

| $D/c$ | $z/D$ | $C_{l,tot}$ | $C_{l,main}$ | $C_{l,flap}$ |
|-------|-------|-------------|--------------|--------------|
| 1.1 | 0.1 | 3.666 | 3.223 | 0.440 |
| 1.1 | -0.2 | 4.451 | 3.706 | 0.745 |
| 2 | 0.1 | 4.840 | 4.053 | 0.787 |
| 2 | -0.2 | 3.915 | 3.915 | 0.770 |

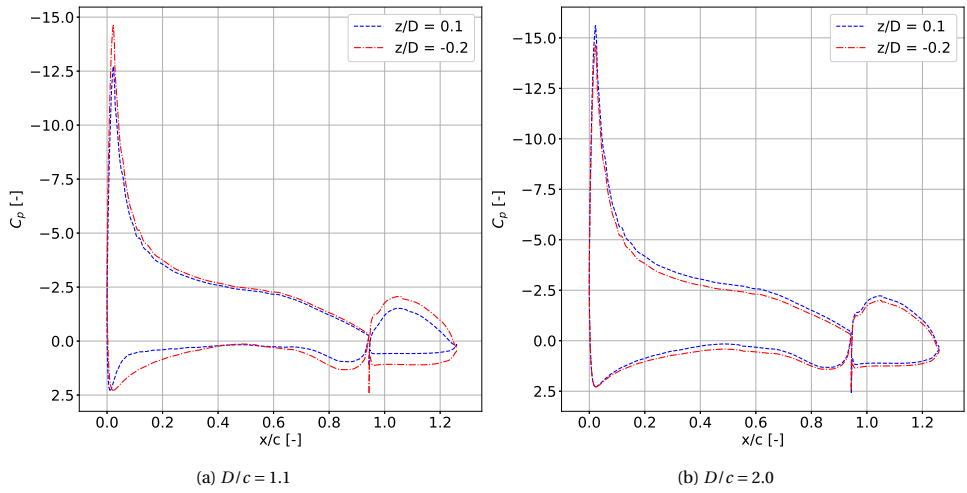(a) $D/c = 1.1$                           (b) $D/c = 2.0$

Figure 4.13: Pressure distributions showing the effect of vertical jet position for small and large jet sizes.

### 4.3.2. Lift response separated by element

To further investigate the interactions in the jet design space with the flap immersion and its effect on the lift response, we investigate models based on the main element and flap element lift responses separately. The factor contributions for these models are shown in Fig. 4.14 and compared to the total lift model. The factor contributions for main element lift are very similar to the total lift coefficient. The jet velocity ratio is dominant and the
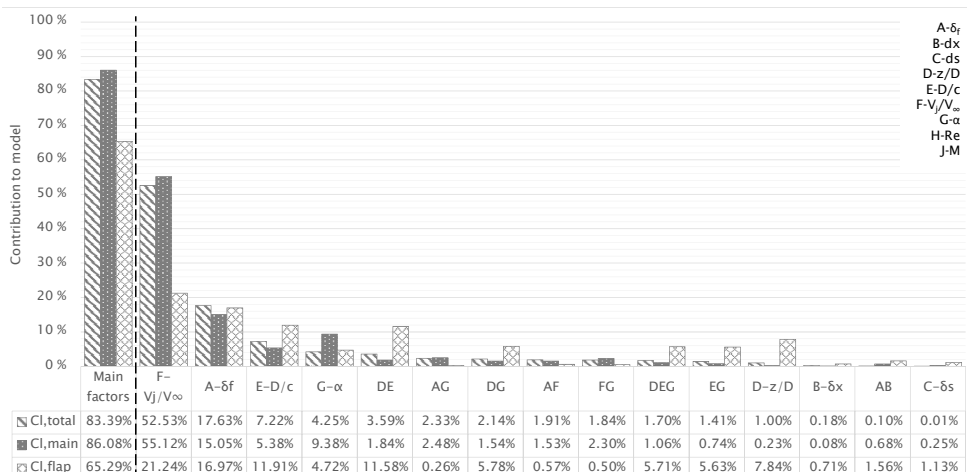


Figure 4.14: Comparison of dominance of terms to lift response of total airfoil, main, and flap element. Summed contributions of all main factors (no interactions) is shown left of the dashed line, individual contributions reported to the right.

large contribution of the flap deflection underlines the interactive effect between both elements. However, contributions to the flap lift response deviate from the total and main element lift responses. The contribution of $V_j/V_\infty$ is more than halved, as are its interactions. Contributions of $\alpha$ are much lower than for the main element lift. The flap lift coefficient is more dependent on $D/c$, $z/D$ and interactions between $D/c$, $z/D$ and $\alpha$. In fact, the contribution of $D/c$, $z/D$ and $\alpha$ — which are dominant in the trajectory of the jet — together contribute more to the model variability than $V_j/V_\infty$.

Figure 4.15 shows the perturbation plots for the flap lift response at different settings of $\alpha$ (all other factors set to the centrepoint). For low (-1) angles of attack, $z/D$ and $D/c$ have a relatively minor effect on flap lift coefficient and are optimal around the centrepoint. As $\alpha$ increases, however, the impact of $z/D$ and $D/c$ increases due to their interactions with $\alpha$. The optimum for flap lift coefficient shifts to lower $z/D$ and higher $D/c$, and the
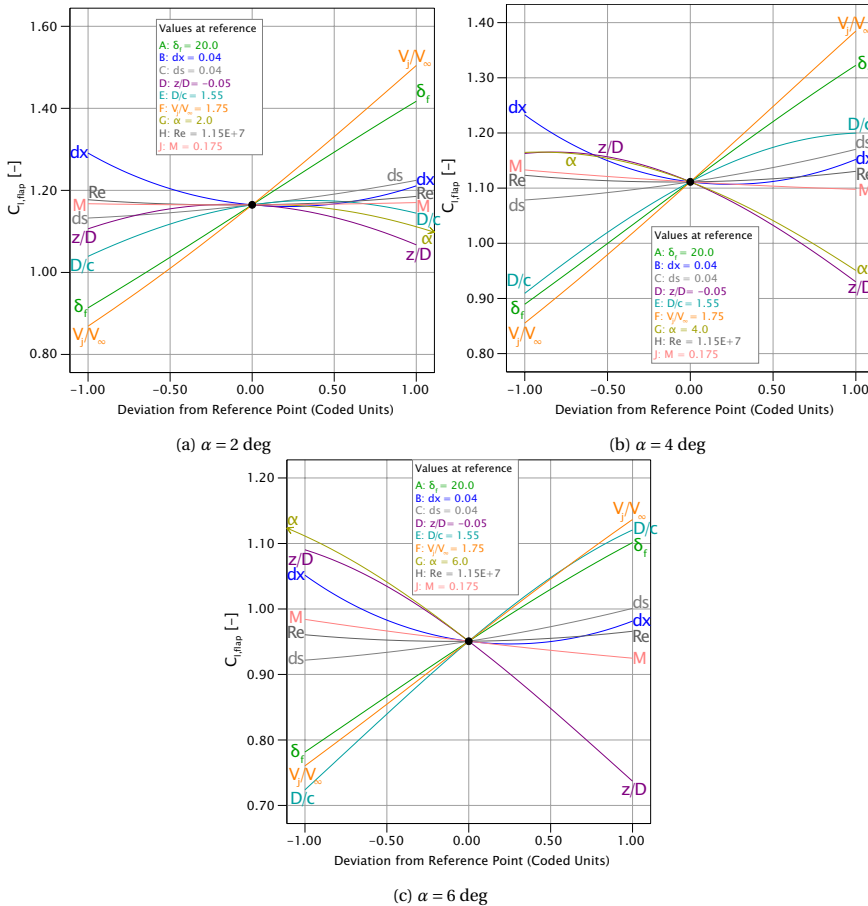


Figure 4.15: Perturbation of flap lift coefficient by main factors at different angles of attack. Other factors are set to the centrepoint value. Coded units refer to the low (-1) and high (+1) values in the CCD. Factors with small perturbation are excluded for clarity.

influence of these factors exceeds that of the jet velocity ratio.

The flap lift response is thus mostly dependent on factors that affect the jet trajectory and how much of the jet passes each side of the airfoil. Furthermore, the perturbation plots show that an optimum for $z/D$ and $D/c$ exists within the design space. This aligns with the conclusion that the flap requires a minimum immersion in the jet. As $\alpha$ is increased, this optimum shifts to lower $z/D$ or higher $D/c$. After minimum immersion of the flap is reached, a larger jet or a lower position no longer benefits the flap lift response and more lift is achieved by increasing the extent of the jet on the suction side of the airfoil. This follows standard circulation theory, where additional dynamic pressure on the suction side should increase airfoil circulation. Unfortunately, we cannot determine the exact relation of required immersion for the flap from the current dataset. The CCD only contains two different jet positions for each combination of all other factors, so it does not include the flowfield data to investigate systematically marching the jet edge closer to the flap. This will therefore be left to future research.

## 4.4. LIFT AUGMENTATION

The final response of interest is the lift augmentation factor, defined as $K_{C_l} = \frac{C_{l,jetflow}}{C_{l,uniformflow}}$. This quantifies how much the presence of the jet in the flowfield augments the lift response compared to the equivalent baseline configuration. Figure 4.16a shows the factor contributions to the lift augmentation factor. The lift augmentation is clearly dominated by $V_j/V_\infty$, which contributes nearly 70% to the response variability. The remaining 30% are mostly a function of $D/c$, $z/D$, $\alpha$ and their interactions. The perturbation of $K_{C_l}$ about the centrepoint is given in Fig. 4.16b, showing that $K_{C_l}$ increases linearly with $V_j/V_\infty$.



(a) Model contributions to $K_{C_l}$ response          (b) Perturbation of $K_{C_l}$ about centrepoint
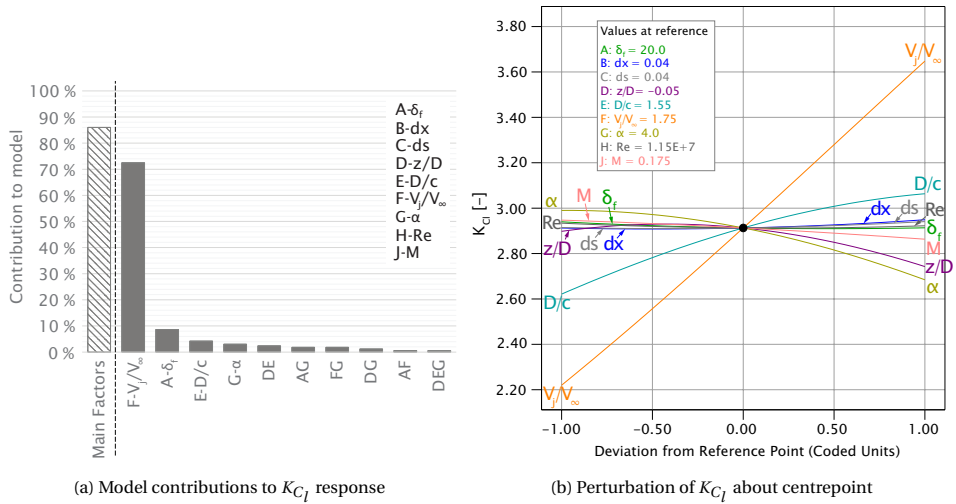
Figure 4.16: Model contribution summary and perturbation plot of the metamodel for lift augmentation factor $K_{C_l}$. Factors with small perturbation are excluded for clarity.

The perturbation curves for $D/c$, $z/D$ and $\alpha$ are similar to those for the flap lift

response. We have shown that the total lift response is significantly affected by these factors and their interactions, which is attributed to their impact on the flap lift more than the main element lift. Of all simulations, the configurations that yield the maximum $C_{l,tot}$ are mostly also the configurations yielding maximum $C_{l,main}$, but not with maximum $K_{C_l}$. The latter is more strongly correlated with maximum $C_{l,flap}$. We can therefore conclude that for a given jet velocity ratio, the flap immersion is a critical to the achieved lift augmentation.

## 4.5. Key Findings

We investigated the impact of a jet of higher dynamic pressure on the aerodynamic performance of a two-dimensional multi-element airfoil. We simulated a wide range of configurations that varied nine different factors, which together controlled jet and freestream velocity, jet position and flap position. Quantifying which of these factors and interactions between factors are dominant with respect to lift, drag and moment coefficient, revealed that the jet velocity ratio is dominant for all of the responses. We have shown that the jet can induce transonic flow regions on the main element, which severely affect the aerodynamic responses, in particular drag coefficient. In the absence of critical Mach numbers, the factor dependency is comparable to uniform flow conditions, showing the aerodynamic mechanisms of multi-element airfoils are not fundamentally affected by the presence of the jet. This is not to be confused with the magnitude of the aerodynamic coefficients, which can be significantly altered by the jet.

We furthermore analysed the interactions between jet size $D/c$, jet position $z/D$ and angle of attack $\alpha$. We established that these interactions influence the jet alignment with the airfoil and how much the flap is immersed in the flow. The optimal position of the jet with respect to the airfoil is found to change between smaller jets, which benefit from lower positions, and larger jets, which generally favour higher positions. We quantified the dominant factors and interactions for the main element and flap lift coefficients separately, concluding that the impact of $D/c$, $z/D$, $\alpha$ and their interactions stems mostly from their influence on the flap lift. We conclude that a minimum flap immersion is critical to the lift augmentation resulting from the jet, after which passing the jet over the suction side of the airfoil yields most impact on lift coefficient.

Extrapolating the results of this chapter to a full propeller-wing-flap configuration, results in several key insights:

- The current state-of-the-art in propeller-wing-flap interaction studies generally accepts that a lower position of the propeller is more beneficial for lift augmentation (e.g., Beckers et al. [47]). This general rule is confirmed by the presented results, when $D/c$ is small and only the dynamic pressure increase is considered. However, the results in this chapter also suggest that this could change for larger $D/c$, assuming it is not dominated by the effects of other slipstream characteristics.

- The importance of the flap immersion highlights the impact of slipstream deformation on the lift augmentation by propeller blowing. Literature (e.g., [30, 31]) shows the deformation of the slipstream due to wing interference, leading to spanwise variations in wing immersion. This will strongly affect the local lift augmentation as a result.

- For large angles of attack or strong wing circulation, the longitudinal distance between propeller and wing cannot be overlooked, due to the dependency of the slipstream trajectory on the relative position, angle of attack and wing-induced upwash.

- The induction of shocks due to the increased flow velocity within the slipstream may pose a limiting factor on full-scale applications of high-lift propellers.

- The optimal flap gap and overlap will change due to the slipstream interactions and will be a function of spanwise location.

**4**

# 5

## CHARACTERISTICS OF PROPELLER-WING-FLAP INTERACTION

*In the previous chapter, we investigated how the aerodynamic response of a multi-element airfoil is affected by the additional dynamic pressure of a jet, as an analogy for a propeller slipstream. In reality, the propeller slipstream is a highly three-dimensional flowfield, which involves more effects than just the additional dynamic pressure imposed on the flow. This chapter explores the propeller-wing-flap aerodynamic interaction in three dimensions. We first define the performance of the wing and flap when immersed in the propeller slipstream in Section 5.1. Performance measurements of the clean wing (i.e., without any propeller and nacelle mounted) are included in Appendix A. Sections 5.1.1 through 5.1.3 identify critical aerodynamic phenomena on the surface and in the wake, while Section 5.1.4 discusses the impact of slipstream deformation on the wing performance coefficients. Literature on the driving mechanisms of this slipstream deformation is discussed in Section 5.2. Section 5.3 subsequently characterizes the development of the slipstream as it passes the wing using high-fidelity numerical simulations, reflecting on the existing literature on slipstream deformation and the other critical aerodynamic phenomena identified in Sections 5.1.1 through 5.1.3. The data used in this chapter were acquired during the first experiment, as well as from the LBM simulations, all treated in Chapter 2.*

---

Parts of this chapter have been published in Refs. [54, 55] or are under review.

## 5.1. AERODYNAMIC PERFORMANCE OF THE BLOWN WING

The basic effects of the slipstream on wing performance can be captured by viewing the slipstream as an increase in dynamic pressure, increasing lift generation, and a tangential velocity (or *swirl*) that induces a local change in angle of attack [31]. These effects are immediately obvious from the sectional aerodynamic coefficients presented in Fig. 5.1 through 5.3, respectively showing the local integrated aerodynamic coefficients for flaps at 0, 15 and 30 deg at various advance ratios (no propeller, $J = 1.0$ and $J = 0.8$). The clean wing configuration excludes both the propeller and the nacelle. We chose this as a reference over the unpowered configuration with nacelle mounted, as the nacelle significantly affects the local flow at high angles attack. Near maximum lift, the aerodynamic coefficients would therefore be influenced by the nacelle interference effects and no longer be comparable with the propeller-on configurations. Nacelle interference effects in high-lift conditions are further discussed in Chapter 8.

Generally, the lift, drag, and moment coefficients are all increased in magnitude by the propeller blowing. Clear differences between the upgoing and downgoing blade sides occur due to the effect of swirl, which induces a local apparent angle of attack. As angle of attack increases, the offset between the lift coefficient of the port and starboard sides decreases. This may be attributed to the swirl recovery effect which becomes stronger with increasing wing circulation [31], and to asymmetric disk loading due to the angle of attack [85].

The flow behaviour at maximum lift is also clearly affected by the propeller blowing. The angle of maximum lift is generally reduced compared to the clean wing. At $\delta_f = 30$ deg (Fig. 5.3), the $J = 1.0$ configuration reaches a lower maximum lift coefficient than the unpowered configuration. Additionally, the stall behaviour is much milder in the powered configurations than the unpowered configuration. These effects can be explained by a combination of factors: The angle of incidence of the propeller with respect to the wing chord, which means the propeller blowing induces an effective angle of attack on the wing. This angle increases with lower advance ratios. The maximum lift behaviour will also be affected by the trajectory of the slipstream. As wing circulation increases (e.g., due to flap deflection) the slipstream is deflected towards the wing suction side, which may result in the flap no longer being immersed in the slipstream at high angles of attack. In chapter 4 we traced several important interactions to this effect. For multi-element wings, the maximum lift may not be dictated by flow separation, but by the interaction between the main element and the flap [37].

It should be noted that the polars in Figs. 5.1 through 5.3 are based on local pressure measurements, which may be influenced by local aerodynamic phenomena and not represent the entire wing condition. The clean wing configuration suffered from stall cells occurring at high angles of attack (see Appendix A) and the propeller blowing is an inherently three-dimensional flowfield.
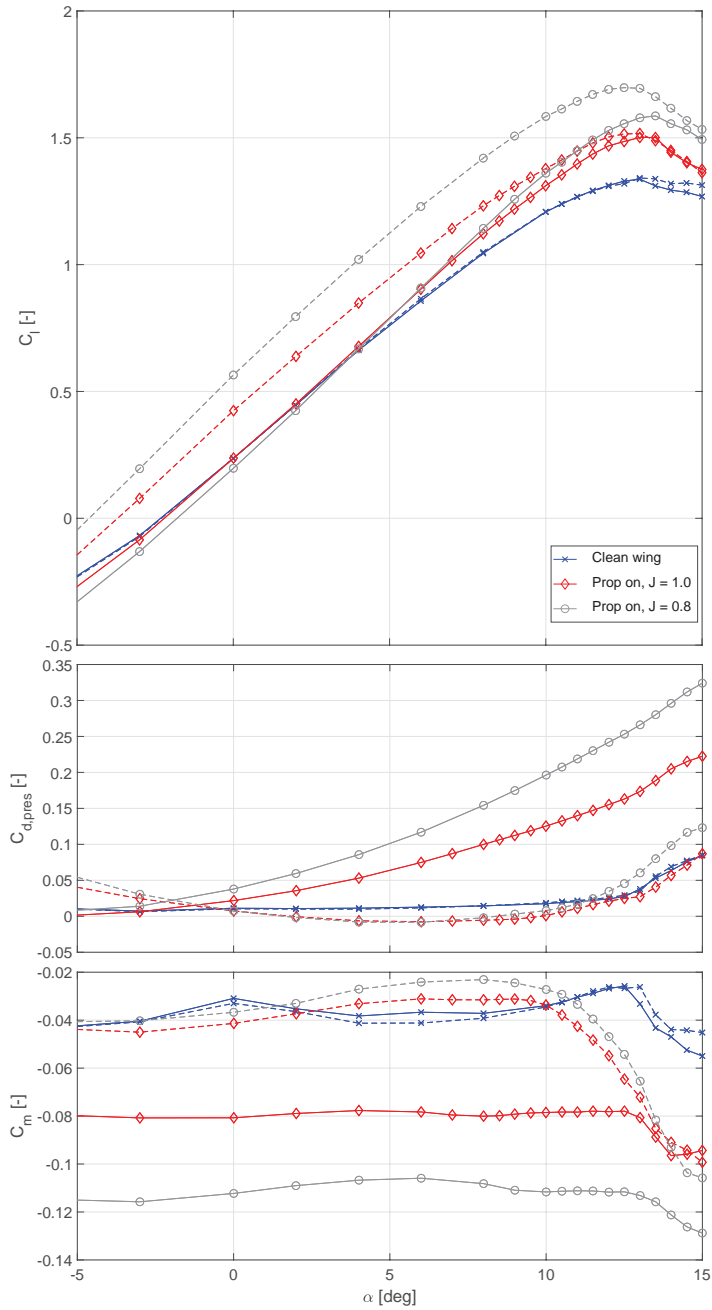
Figure 5.1: Polars of local aerodynamic coefficients for wing with flap nested, comparing clean wing and propeller on configurations. Solid and dashed lines represent respectively down- and upgoing blade sides. Uncorrected wind tunnel data.
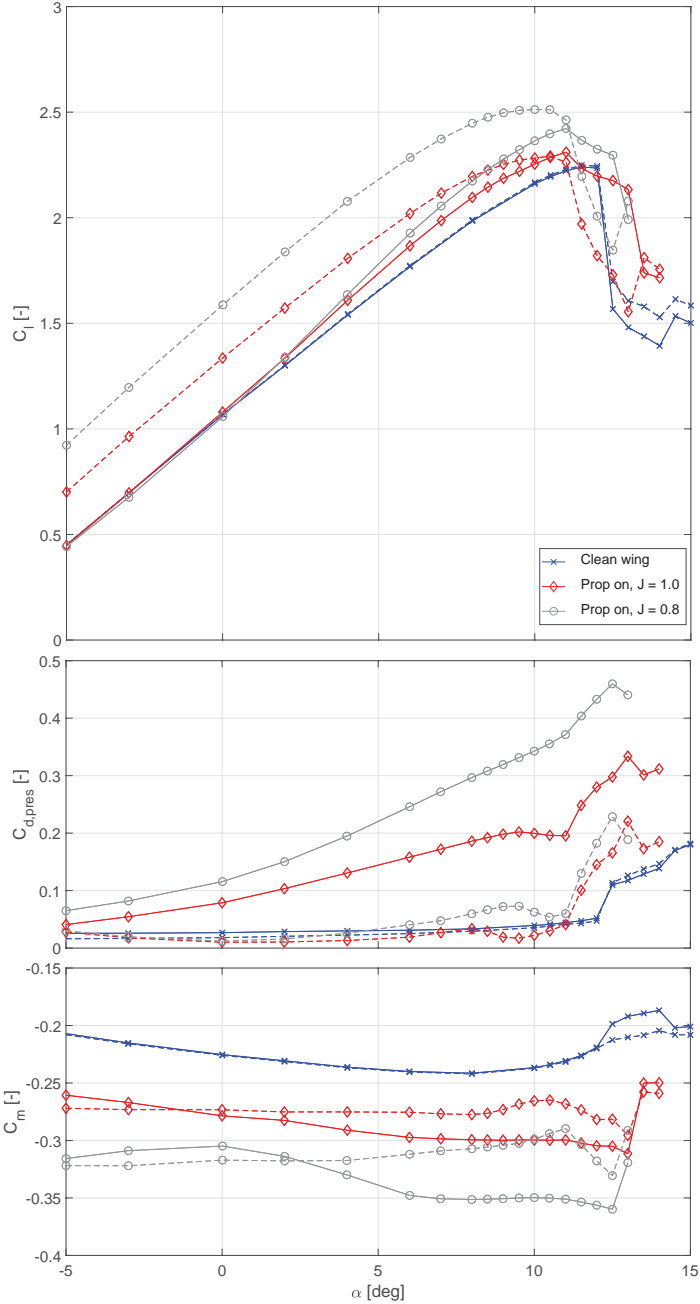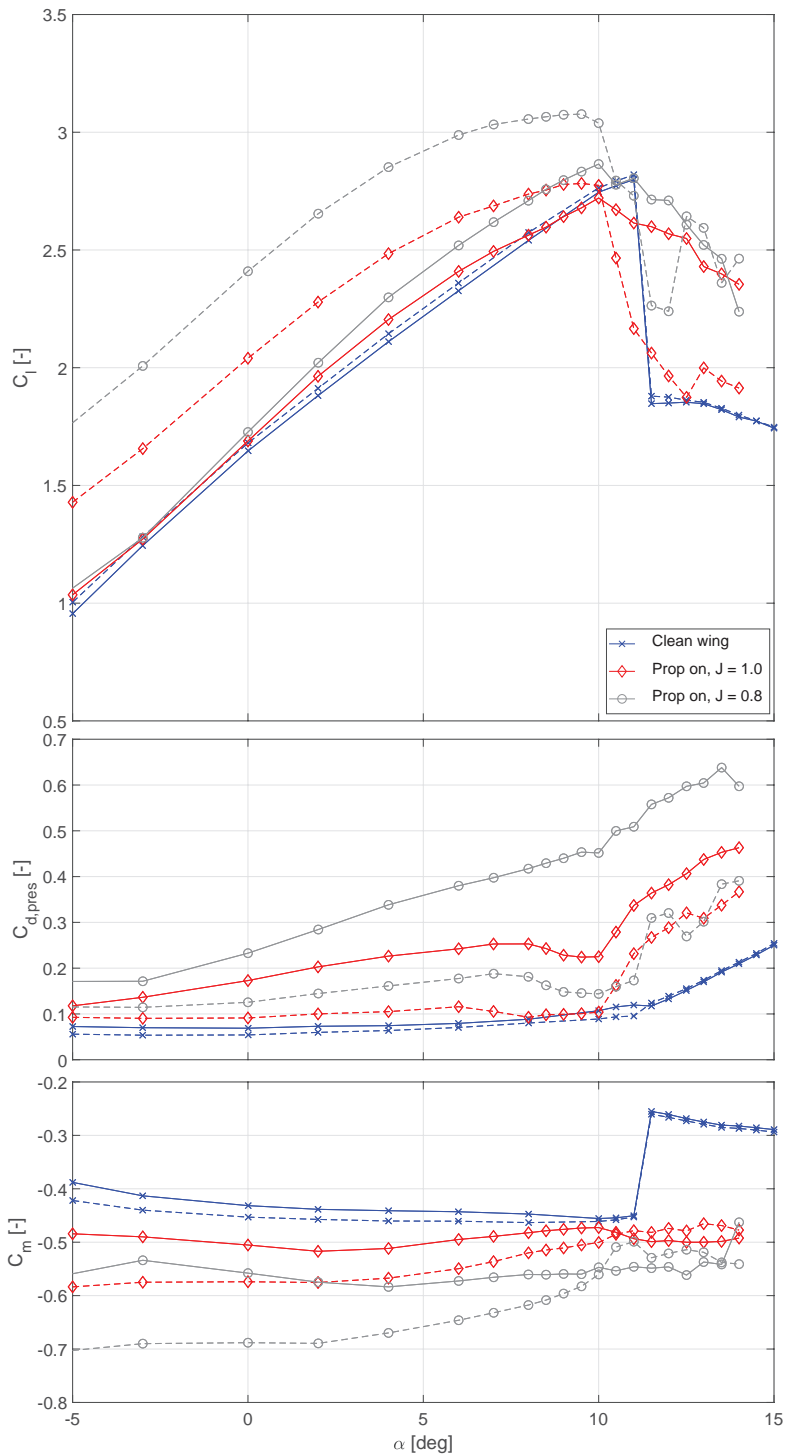
Figure 5.2: Polars of local aerodynamic coefficients for wing with flap deployed ($\delta_f$ = 15 deg, d$x$ = 8%, d$s$ = 2%), comparing clean wing and propeller on configurations. Solid and dashed lines represent respectively down- and upgoing blade sides. Uncorrected wind tunnel data.

Figure 5.3: Polars of local aerodynamic coefficients for wing with flap deployed ($\delta_f = 30$ deg, d$x = 0\%$, d$s = 3\%$), comparing clean wing and propeller on configurations. Solid and dashed lines represent respectively down- and upgoing blade sides. Uncorrected wind tunnel data.

### 5.1.1. Aerodynamic interaction phenomena with flap nested

Oil flow visualizations of the wing in powered conditions gives more insight into the overall aerodynamic phenomena that occur on the wing in the powered cases. Figure 5.4 shows the powered flap nested configuration at $J = 0.8$ for three angles of attack. It clearly shows the area affected by the propeller slipstream, the edge of which moves spanwise towards the down-going blade side as it passes the wing (I). The down-going blade side shows most deformation in the first 20% of the chord, while the up-going blade side shows most deformation towards the rear 50% chord. The latter seems to decrease as angle of attack increases, though this cannot be verified based on the oil flow images. Within the slipstream boundaries, the flow expands as it moves over the wing (II), opposite to the main swirl direction. This expansion increases with increasing angle of attack. On the nacelle, flow in opposite direction to the main swirl component is also present (III). It is likely that this is a result of the root vortex system, which moves over the wing slightly above the surface. This reveals a pitfall of oil flow visualization for slipstream interaction, as the off-the-surface flow characteristics may be dominant for the wing performance but cannot be visualized.

As angle of attack increases, areas of separated flow start to form on the outside of the slipstream affected area. These are believed to be caused by local increases in angle of attack induced by vorticity shed into the wake due to the disturbance of the spanwise lift distribution caused by the slipstream [31]. At $\alpha = 13$ deg, the separated areas displace the boundaries of the slipstream (at least on-the-surface) causing a significant reduction in affected area of the wing. At $\alpha = 0$ deg, some interference can be observed on the separation line at the trailing edge (V), which seems to originate from the nacelle and induces slight trailing edge separation. This area moves spanwise as the expansion of on-the-surface flow within the streamline increases with angle of attack. At $\alpha = 13$ deg, this area of separated flow seems to have merged with the larger separated area on the outside boundary of the slipstream.



(a) $\alpha = 0$ deg          (b) $\alpha = 10$ deg          (c) $\alpha = 13$ deg
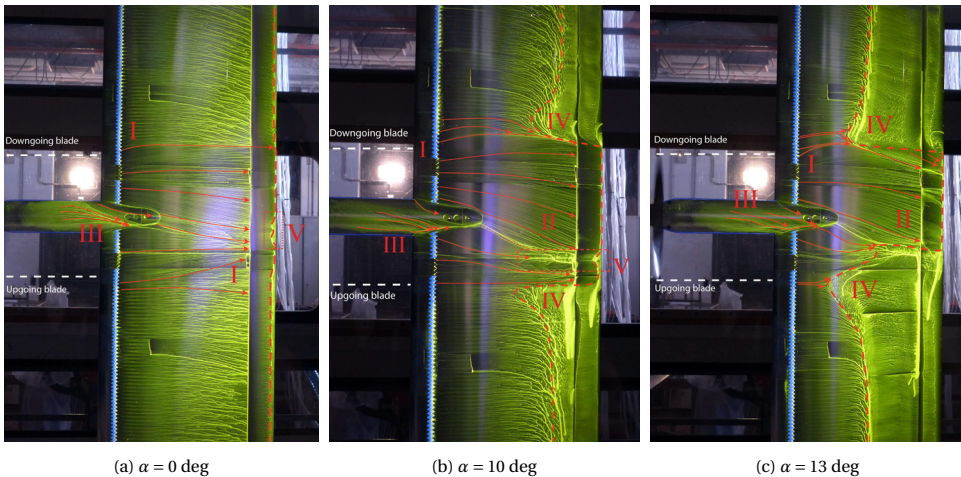
Figure 5.4: Oil flow visualization images of the wing with flap nested and propeller ($J = 0.8$) at various angles of attack.

Overall, the oil flow images illustrate the complexity of the propeller-wing interactive flowfield. Local deformation of streamlines within the slipstream are highly variable, and slipstream deformation shows to be highly dependent on spanwise loading. Furthermore, the importance of volumetric / off-the-surface flow visualization is underlined, as on-the-surface flows seem to move in opposite direction to the swirl in the main body of the slipstream. Finally, the importance of spanwise resolution is exemplified, as the flow is highly three-dimensional. Although the pressure taps on the downgoing blade side (identifiable by the taped off region on either side of the nacelle) seems to be positioned in a streamwise-oriented part of the slipstream, the port-side pressure taps see crossflow components, making any interpretation of the measurements as a two-dimensional wing section impossible.

### 5.1.2. Aerodynamic interaction phenomena with flap deflected

Oil flow images of the wing with flaps deflected show some important additional phenomena compared to the flap nested configuration. Figure 5.5 shows the oil flow images of both the pressure and suction side of the powered case with 30 deg flap at $J = 0.8$ and $\alpha = 8$ deg. On the main element, we see most of the same structures (I, II, III, and IV) as described for the flap nested cases in Section 5.1.1. On the upper surface of the flap, however, we can identify a laminar separation bubble on portions of the span. Since the propeller slipstream trips the boundary layer (in a time-averaged sense, see [86]), the part of the flap that is washed by the slipstream can be identified by the lack of separation bubble (VII). This should not be confused with the effects of the flap brackets, which also



(a) Suction side                                         (b) Pressure side
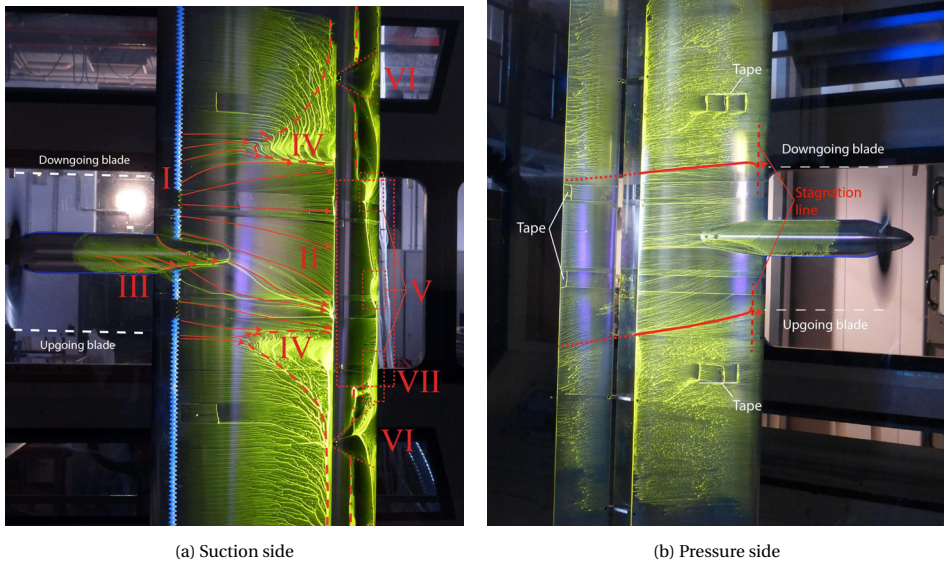
Figure 5.5: Oil flow visualization of both sides of the wing for the powered configuration with $\delta_f = 30$ deg, $J = 0.8$, $\alpha = 8$ deg, showing the deformation of the slipstream and impingement of the pressure side slipstream half on the flap.

locally cause a turbulent boundary layer on the flap (VI). The washed area of the flap shows several vortical structures (V), likely due to root and tip vortex interactions. More critically, the washed area of the flap is much wider than, and offset from, the washed area on the main element. Figure 5.5b shows that the offset from the main element is because the flap is immersed in the flow coming off of the pressure side of the main element, which undergoes significant deformation before it reaches the flap. The impact of the slipstream on the wing flow thus differs in spanwise direction from the impact on the flap flow. The wing and flap, in turn, directly affect each other through the typical multi-element airfoil aerodynamic principles.

The performance of the wing under influence of the propeller slipstream is thus the results of a highly complex interaction, with spanwise variations beyond the area directly behind the propeller. This performance is highly dependent on the deformation of the slipstream as it passes the wing. Simplified numerical analyses such as streamtube models [87, 88] will thus be invalid for high-lift configurations, as they will not accurately represent the area of the flap being immersed in the slipstream, nor the concentrations of dynamic pressure that will result from the slipstream deformation over the main element. Furthermore, this insight is of importance to distributed propulsion application of propeller-blown lift augmentation, as it indicates that interactions between slipstreams of closely spaced propellers is inevitable in an installed condition. Some notion of this can already be found in recent numerical simulations of distributed propulsion flows, such as Keller [11]. Although distributed propeller configurations are beyond the primary scope of this dissertation, an exploration of these interactions is provided in Chapter 7.

### 5.1.3. SLIPSTREAM SHAPE IN THE WAKE

To further investigate the slipstream deformation, we use measurements of total pressure coefficient $C_{p,t}$. Figure 5.6 shows measurements of $C_{p,t}$ in the $zy$-plane at $x/c = -2$ (meaning one chord behind the trailing edge of the airfoil with flap nested at $\alpha = 0$ deg), showing how much the slipstream has deformed after it passed the wing. Since the propeller adds total pressure to the flow, we can identify the slipstream shape from contour lines of $C_{p,t} > 1$. Note that viscous losses in the wing boundary layer and wake will locally invalidate this definition of the slipstream edge. Nonetheless, the overall slipstream deformation is still represented accurately.

For the flap nested configuration at $\alpha = 0$ deg (Fig. 5.6a), the slipstream undergoes spanwise shear known from literature [31]. A central region of pressure loss, likely tied to the nacelle wake and root vorticity, can be clearly identified in each half of the slipstream. At higher angles of attack, the slipstream deforms completely from its initial circular shape. From Fig. 5.6, we can derive that the upper slipstream half stretches into a vertical *stem*, while the lower slipstream half elongates into a horizontal *base*. The central pressure losses are displaced towards the upper-right quadrant as the two halves merge. At $\alpha = 0$ deg but with flaps deflected (Figs. 5.6d and 5.6g), we see a mixture of the deformation typical for low-lift and high-lift conditions. The deformation of the upper half of the slipstream remains similar to the low-lift case (Fig. 5.6a), while the lower half is elongated horizontally.
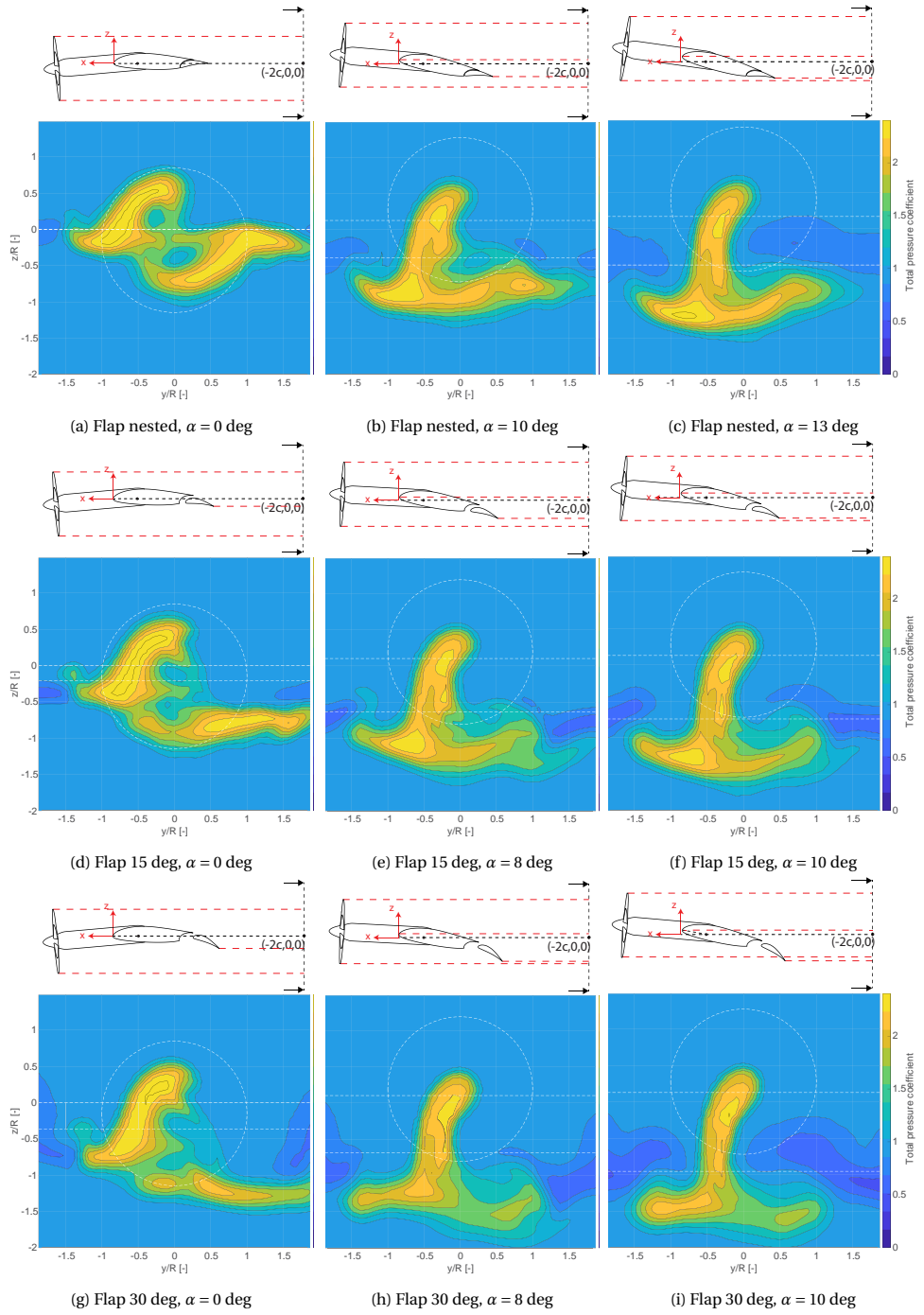
(a) Flap nested, $\alpha = 0$ deg

(b) Flap nested, $\alpha = 10$ deg

(c) Flap nested, $\alpha = 13$ deg

(d) Flap 15 deg, $\alpha = 0$ deg

(e) Flap 15 deg, $\alpha = 8$ deg

(f) Flap 15 deg, $\alpha = 10$ deg

(g) Flap 30 deg, $\alpha = 0$ deg

(h) Flap 30 deg, $\alpha = 8$ deg

(i) Flap 30 deg, $\alpha = 10$ deg

Figure 5.6: Total pressure in the yz-plane at $x/c = -2$ for various powered configurations at $J = 0.8$. View in streamwise direction. Dashed lines indicate projections of the propeller, leading- and trailing edge on the yz-plane. Pressure taps are located at $y/R = \pm 0.7$.

### 5.1.4. IMPACT OF DEFORMATION ON LIFT PERFORMANCE

Clearly the deformation of the slipstream is a complex aerodynamic process, that directly affects the flow conditions of the flap. Although the results from Section 5.1 show that the deformation greatly impacts the washed area of the flap, these results do not provide any insight into the resulting aerodynamic performance of the wing. Moreover, we note the downside of surface-based flow analysis for propeller-wing-flap interaction specifically. Some analysis of the impact of slipstream deformation on the wing performance is thus warranted. To this end we utilize the high-fidelity numerical results available from LBM simulations. These have been validated against the experimental data (see Chapter 3) and for the remainder of this chapter we consider them to be an extension of the experiment that Section 5.1 is based on. For more details on the simulations and the validation with experimental data, see Sections 2.2.3 and 3.2 of this dissertation, respectively. In the remainder of this chapter, the presented results are based on the LBM simulations, unless specified otherwise.

    Figure 5.7 shows the spanwise distribution of sectional lift coefficients for the main and flap elements. Vertical, dashed lines mark the locations of the nacelle body and the propeller radius. Horizontal dashed lines represent the sectional lift coefficient of the clean wing, estimated by taking the average of the lift coefficient between $y/R = -6$ and $-4$. The distributions are calculated from numerical simulations by integrating the force over finite spanwise sections of the main wing and flap element surfaces. Since the nacelle is blended into the wing, their individual contributions cannot be properly separated. The lift distributions in Fig. 5.7 therefore include the nacelle contribution. As a result, the sectional lift coefficients in the nacelle region are not representative for the



(a) Main element. Dotted lines indicate nacelle region.          (b) Flap element
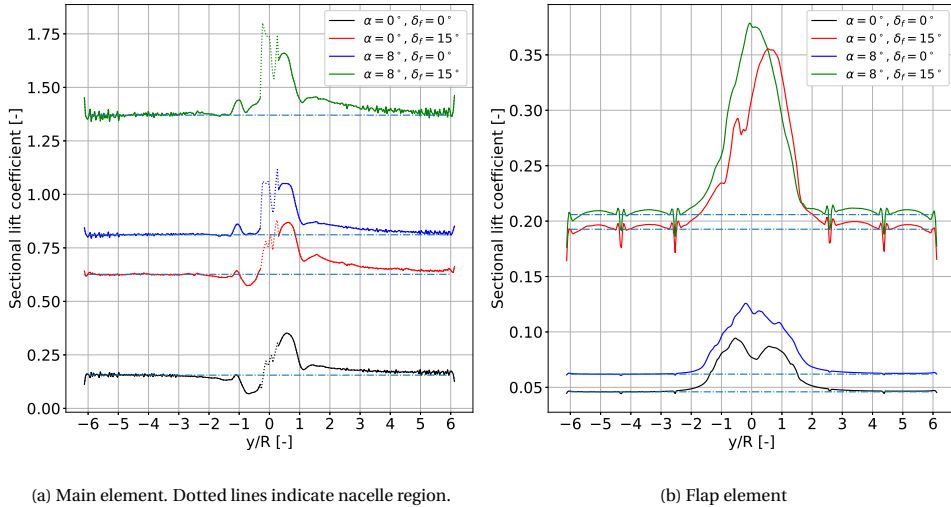
Figure 5.7: Spanwise lift distributions for the main and flap elements, extracted from the numerical simulations. Horizontal dash-dotted lines indicate the sectional wing lift without influence of the propeller.

wing performance and are therefore reported with dotted lines.

The results in Fig. 5.7 show distinct differences in how the main and flap elements are affected by the slipstream, as a result of its deformation. Under the influence of the propeller slipstream, the lift distribution on the wing changes. On the main element most of this change is located within the area directly behind the propeller. The distribution is asymmetric around the wing centre axis due to the effects of swirl, and the strongest gradient is found on the upgoing blade side. The gradients in spanwise lift cause shedding of trailing vorticity, which induces increased wing lift on the upgoing blade side. This effect extends beyond the wing area directly behind the propeller. These effects all follow standard propeller-wing interaction theory known from, e.g., Veldhuis [31].

The flap lift distribution, however, shows some very distinct differences. The augmentation of the lift coefficient is much stronger on the flap than it is on the main element. Furthermore, the distribution is no longer strongly asymmetric, suggesting the flap does not experience a swirling flow, which would induce spanwise variation of apparent angle of attack. This is confirmed in Section 5.3.3. The lift augmentation on the flap is also shifted towards the upgoing blade side to varying deg. This can be attributed to the deformation of the slipstream on the lower surface of the main element.

It should be noted that the lift of multi-element wings is the result a fully coupled aerodynamic system, meaning the lift distributions of main and flap element cannot be truly analysed separately. For example, the augmentation of the flap lift will induce additional circulation on the main element as well [35]. Nevertheless, understanding the aerodynamic phenomena by which the slipstream interacts with the wing and flap, and especially how these interactions differ from each other, can assist in optimizing the overall wing performance.

## 5.2. Slipstream deformation in literature

In the previous sections, we identified several key phenomena of propeller-wing-flap interaction on the wing surface flow, including leading-edge expansion, cross-flow behind the nacelle and separation outboard of the slipstream edge. We also discussed the deformation of the slipstream, that this affects the flap specifically and shown that the deformation is much more extensive in high-lift conditions. We have furthermore established that the deformation has a measurable impact on the performance characteristics of the wing as well. Clearly, it is necessary to understand the mechanisms of the slipstream deformation in detail.

In existing literature on propeller-wing interaction, several of these phenomena have already been discussed. Slipstream deformation also occurs in low-lift conditions, albeit to a much lesser extent, as documented by Samuelsson [30] and Veldhuis [31]. More recently, it has been discussed by Sinnige [89] in the context of tip-mounted propellers and van Arnhem for multi-engined transport aircraft [53]. However, as is the case with earlier literature, the main focus of these treatises is low-lift conditions and the importance of the deformation on the flow of slotted flaps is not recognized. Roosenboom [90, 91, 92] sheds light on the internal structure of the slipstream as it passes the wing in a high-lift transport aircraft configuration. However, their analysis does not extend to the flap flow and focuses on streamwise slices of the slipstream, which do not fully visualize the slipstream deformation. Moreover, the mechanisms of slipstream deformation are not

fully understood. Although some hypotheses are put forth in the aforementioned works, no definitive conclusion is reached.

While the mechanisms of slipstream deformation have not been fully studied in aeronautical literature, substantial work has been done in the related field of propeller-rudder interaction. Felli et al. [94] and Felli and Falchi [93] performed extensive experimental measurements of a propeller-rudder configuration using Particle Image Velocimetry (PIV) and Laser Doppler Velocimetry (LDV). They discuss the dynamics of the tip and hub vortices of a propeller slipstream as they encounter a downstream rudder, showing that the tip vortices wrap around the rudder (or wing) leading edge and maintain connection between the tip vortices on both sides of the wing until they leave the trailing edge. They also propose the main mechanisms of slipstream deformation to be a combination of vortex image effects and spanwise pressure gradients displacing the tip vortices at the edge of the slipstream, shown in Fig. 5.8. Felli and Falchi [93] furthermore show that the hub vortex has a profound interaction with the boundary layer when it impinges on the wing directly, and experiences a spanwise shift opposite to that of the tip vortices. Felli et al. [94] report no such interaction, as their propeller is offset from the wing and the hub vortex passes the wing away from the surface.

The dynamics of the tip and hub vortices is further investigated by Muscari et al. [95]
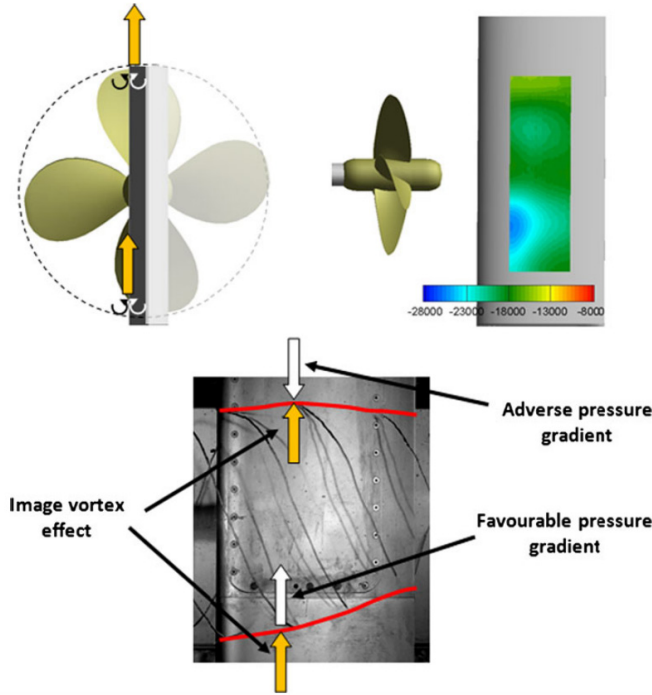


Figure 5.8: Mechanisms of spanwise displacement of tip vortices in propeller-wing interaction, consisting of image vortex effects (top-left) and pressure gradient effects (top right), resulting in asymmetric spanwise displacement of the tip vortices on the wing. From [93].

using detached eddy simulation. They note that the interaction cannot be treated as separate mechanisms of tip and hub vortex impingement, as they strongly affect each other as well. Additionally, they stress the importance of the exchange of vorticity between the slipstream and the wing boundary layer. Felli [33] continues on the work of Felli and Falchi [93], and Muscari et al. [95], providing a very thorough overview of the dynamics of the slipstream vortex system as it interacts with a rudder, based on another extensive experimental campaign. Posa et al. [96] perform Large Eddy Simulations (LES) of the configuration tested by Felli and Falchi [93], and are able to characterize the slipstream deformation in additional detail, confirming the mechanisms described by Felli and Falchi [93] and Muscaria et al. [95]. Posa and Broglia [97, 98] later extend the state-of-the-art with simulations of a propeller-rudder configuration with a rudder at incidence, providing extensive descriptions of the flowfield, although they do not analyse the vortex dynamics and mechanisms to the extent that Felli [33] does for the zero incidence case.

Despite the extensive work on the dynamics of the vortex system in propeller-rudder interaction, there are several important differences with a typical aeronautical application that require addressing, before a direct translation of the results can be made. Firstly, all of the works on propeller-rudder interaction discussed thus far share the same propeller and model topology. Additionally, most of the works consider a non-lifting wing, which is not the operating condition of interest for aeronautical applications. The studies by Posa and Broglia [97, 98] are an exception, as they address the impact of a rudder at incidence. However, the angle of attack is only applied to the wing, while the propeller keeps the same orientation. This is not representative of an installed tractor propeller on an aircraft, for two reasons: it effectively changes the position of the propeller relative to the airfoil, and it avoids a substantial part of the non-uniform inflow field that the propeller will experience when it is tilted together with the wing. Furthermore, the propeller in propeller-rudder interactions is always detached, which leads to a much more concentrated hub vortex that is likely to interact with the wing differently than in the case of an attached nacelle. The nacelle-wing junction will also affect the propeller-wing interaction in aeronautical applications, as it induced local suction peaks on the wing leading edge [99] and may result in local separation bubbles [53]. Finally, a slotted flap element has never been considered before, which also limits the levels of wing circulation that has been included in literature thus far. It is therefore worthwhile to characterize the slipstream of a given propeller-wing-flap configuration, study its development from the initial circular shape and compare this to established literature on similar propeller-wing interactions.

## 5.3. Characterization of the slipstream development

In this section we characterize the slipstream deformation in the propeller-wing-flap interaction. We will discuss the development of the slipstream in streamwise direction, and reflect on the mechanisms of slipstream deformation discussed in Section 5.2. Furthermore, we visualize the deformation at various chordwise stations of the wing, which is particularly important to understand the impact of the slipstream deformation on a deployed flap element.

### 5.3.1. Regions of Deformation

To analyse the development of the deformation, we define three regions, shown in Fig. 5.9. Note that the first region is aligned with the propeller axis, while the other two regions are aligned with the wing chord. For any of these regions, the flow is a result of the coupled interaction between propeller and wing. The slipstream affects the local wing aerodynamics, while the wing affects the slipstream trajectory and the propeller performance, which in turn affects the distribution of total pressure in the slipstream. This can never be treated as anything but the complete sum of its parts. In the next sections, we discuss the different phenomena that deform the slipstream sequentially in streamwise direction, knowing we are describing the complete end result only.

The regions are based on different stages of deformation, identified from the development of the slipstream shape shown in Fig. 5.10. It shows the outline of the slipstream by means of the contour line of $C_{p,t} \geq 1.05$. This value is chosen to get a clearer visualization of the slipstream edge. Due to measurement noise and viscous effects that diffuse the slipstream edge, the contour line at $C_{p,t} = 1$ becomes irregular. Since the gradient in total pressure at the slipstream boundary is very steep, $C_{p,t} = 1.05$ is still a good representation of the position of the slipstream edge and provides an effective visualization of the slipstream shape. Figure 5.10 shows the slipstream shape at various streamwise locations: upstream of the wing, at the main element leading-edge, at the main element cove, and in the wing wake, for the case with $\alpha = 8$ deg and $\delta_f = 15$ deg. Figure 5.10f visualizes the locations of the slices. From Fig. 5.10, it becomes clear that significant slipstream deformation occurs not only when the slipstream physically intersects with the wing surface, but also upstream of the wing. Additionally, significant deformation is present between the flap trailing edge and the wake position.
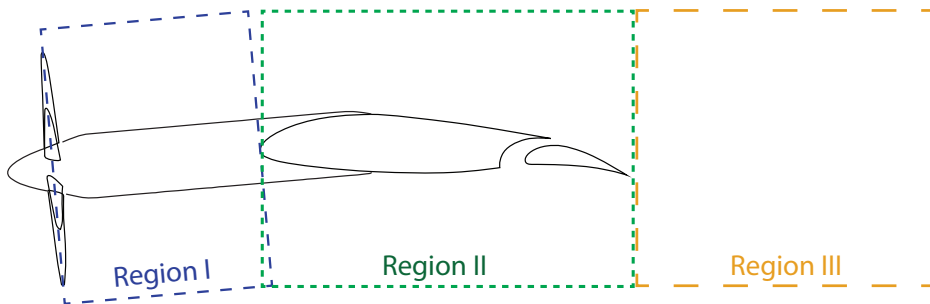


Figure 5.9: Definition of slipstream deformation analysis regions.
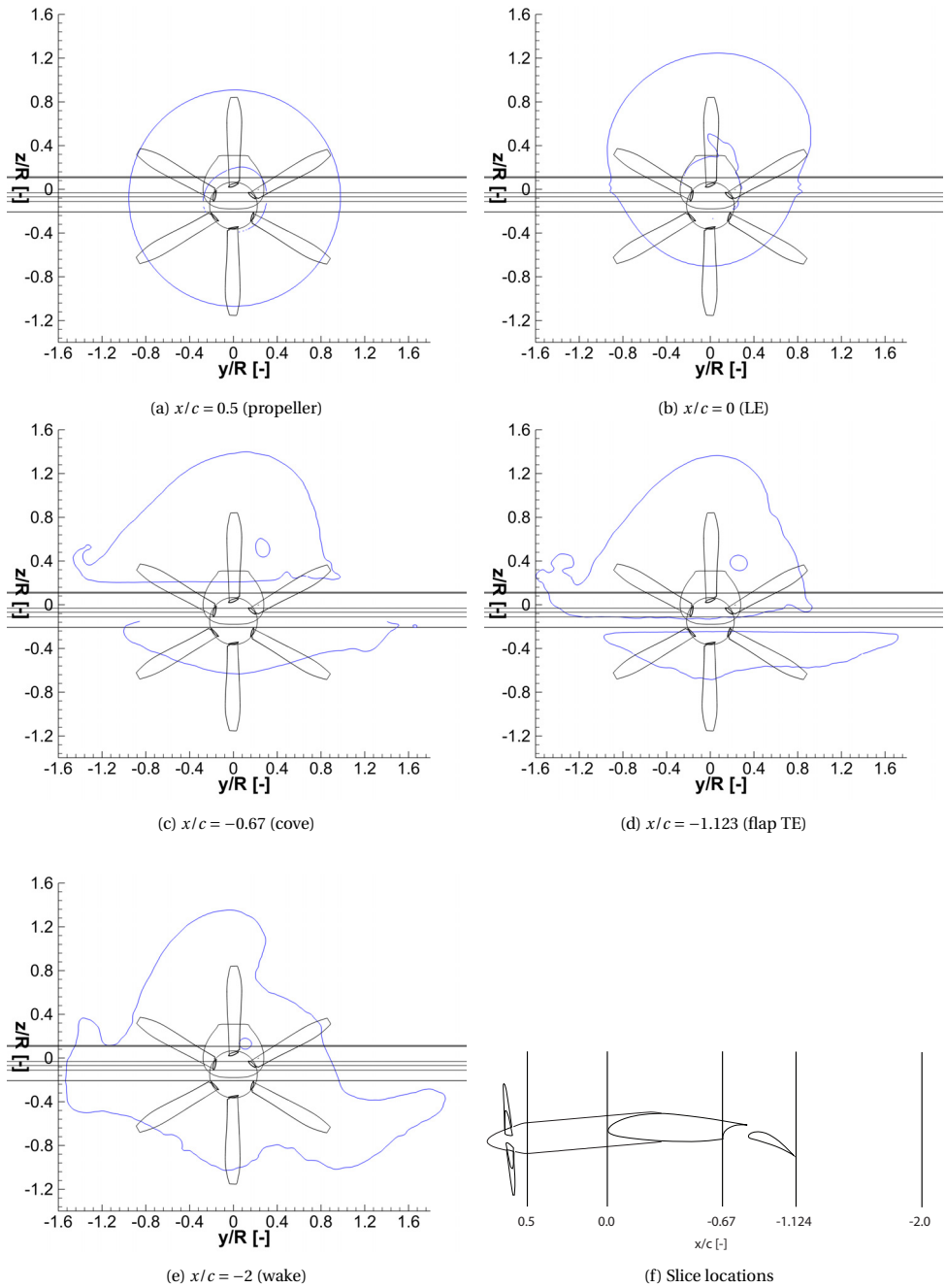
(a) $x/c = 0.5$ (propeller)

(b) $x/c = 0$ (LE)

(c) $x/c = -0.67$ (cove)

(d) $x/c = -1.123$ (flap TE)

(e) $x/c = -2$ (wake)

(f) Slice locations

Figure 5.10: Contour lines of $C_{p,t} = 1.05$ at various downstream stations illustrating overall slipstream deformation.

### 5.3.2. REGION I — PROPELLER TO WING

Figure 5.11 shows contours of total pressure coefficient in a plane just behind the propeller, combined with the in-plane components of the velocity vectors (hereinafter referred to as the *in-plane velocity vectors*). At this position, the slipstream is in its initial state. We define this region in propeller frame, with the yz-plane parallel to the plane of rotation, to best visualize the deformation from the initial circular shape.

The initial state of the slipstream is inherently a function of both the angle of attack and the wing upwash. At $\alpha = 0$ deg and no flap deflection, the propeller sees a slight negative angle of inflow, as the wing-induced upwash is insufficient to offset the negative geometric angle of the propeller with respect to the wing chord. Deflecting the flap to 15 deg increases the wing circulation enough to counteract the geometric installation angle and the propeller operates nearly in uniform flow conditions. The propeller thus experiences significant effect of the wing upwash, even at $\alpha = 0$ deg. Also note that this configuration has a relatively long nacelle and thus less wing-induced upwash at the propeller plane than a typical configuration.

For higher angles of attack, the propeller operates at a positive relative inflow angle. This means the blade sees an in-plane component of the inflow velocity, which moves against the downgoing blade and with the upgoing blade. We can denote these sides as the advancing and retreating blade sides, respectively. As a result of the in-plane velocity component, the maximum pressure rise shifts to the downgoing (advancing) blade side. These effects are all well described by the classic works on propeller-wing interaction (e.g., Veldhuis [31]) and further investigated by Stokkermans [85] and van Arnhem [53]. The gaps in the contours near the nacelle (e.g., in Fig. 5.11d) are not local deformation, but local pressure losses. These are the result of separation on the blade root due to the in-plane velocity component.

Despite the clearly demonstrated impact of the wing-induced upwash on the propeller inflow at $\alpha = 0$ deg and $\delta_f = 15$ deg, the in-plane velocity vectors in the $\alpha = 0$ deg configurations (Figs. 5.11a and 5.11b) are dominated by the swirl of the propeller. At higher angles of attack (Figs. 5.11c and 5.11d), the swirl is still clearly present, but of the same order of magnitude as the vertical component of the freestream and the wing upwash. At the nacelle, this causes the flow on the downgoing blade side to flow against the swirl direction. This has a significant impact on the development of a pair of vortices originating from the nacelle region, and will be discussed further in Section 5.3.3.

Close behind the propeller, the impact of the wing upwash and freestream incidence angle is mostly seen in the shifting of the disk loading and the local swirl. The same flow components convect the slipstream towards the wing upper surface as it moves closer to the wing. For configurations at low angle of attack (and low-lift) this displacement is insignificant, but at higher angles of attack (and high-lift) this causes significant slipstream deformation, as shown in Fig. 5.12. This occurs even before the slipstream interacts with the wing physically. We also see the root losses on the upgoing blade side convected toward the upper side of the nacelle, due to swirl and flow around the nacelle.
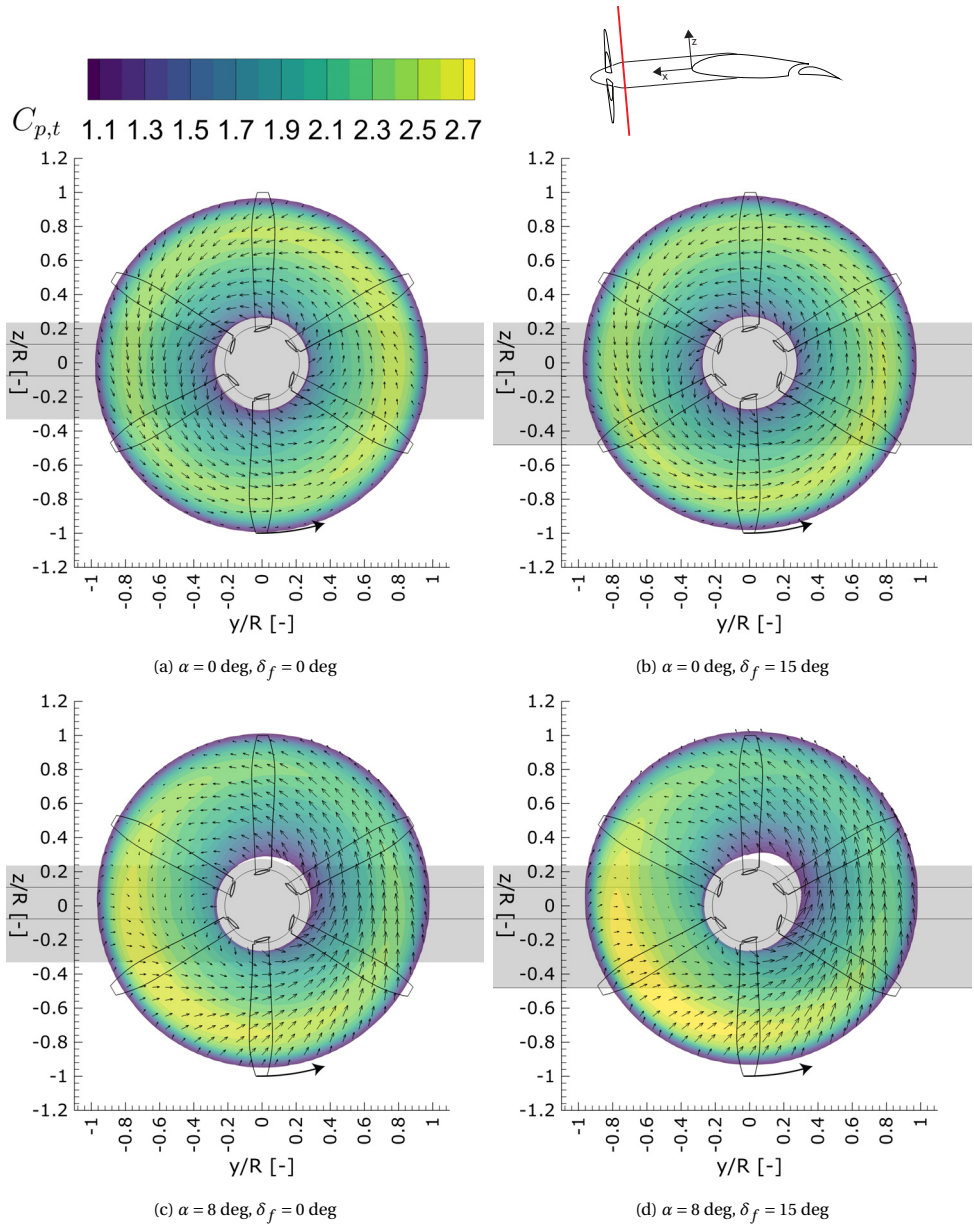
(a) $\alpha = 0$ deg, $\delta_f = 0$ deg

(b) $\alpha = 0$ deg, $\delta_f = 15$ deg

(c) $\alpha = 8$ deg, $\delta_f = 0$ deg

(d) $\alpha = 8$ deg, $\delta_f = 15$ deg

Figure 5.11: Slipstream slices in yz-plane at $x/c = 0.5$ (propeller frame), showing in-plane velocity vectors and the distribution of $C_{p,t}$. Slice perpendicular to propeller axis.
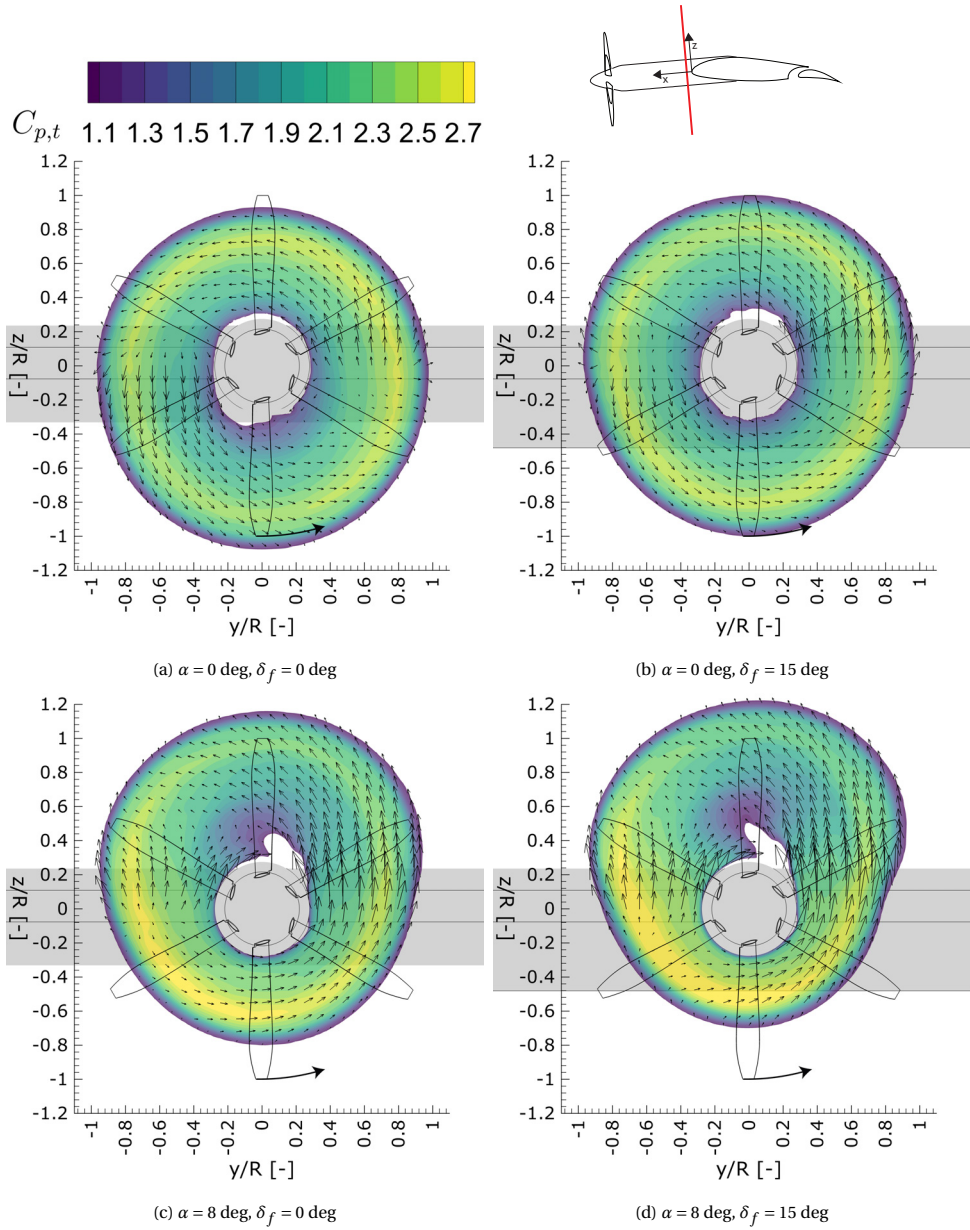
(a) $\alpha = 0$ deg, $\delta_f = 0$ deg

(b) $\alpha = 0$ deg, $\delta_f = 15$ deg

(c) $\alpha = 8$ deg, $\delta_f = 0$ deg

(d) $\alpha = 8$ deg, $\delta_f = 15$ deg

Figure 5.12: Slipstream slices in yz-plane at $x/c = 0.02$ (just upstream of the leading edge), showing in-plane velocity vectors and the distribution of $C_{p,t}$. Slice perpendicular to propeller axis.

This deformation can be attributed to the region of flow acceleration around the wing leading edge. In that region, the slipstream is convected vertically much more than in the surrounding flow. The relative position of the slipstream with respect to the wing leading edge can then have a large impact on the slipstream deformation. Furthermore, the orientation and magnitude of the local velocity vectors at the wing leading edge can vary strongly between cases. For low $\alpha$, the stagnation point of the wing is on the upper surface on the downgoing blade side and the local velocity accelerates towards the lower surface. In the high $\alpha$ cases, the flow always accelerates from the lower to the upper surface and the local velocity magnitude is much higher.

These effects are all highly dependent on the particular wing configuration. A different vertical installation position of the propeller, or a different distance between propeller and wing leading edge, will change how the slipstream will displace before it reaches the wing and therefore how it interacts with the wing itself. In literature on propeller-wing interaction the importance of the horizontal propeller distance is often considered negligible with respect to the vertical position (e.g., Cui et al. [43]). Veldhuis [31] discusses the intersection of the wing with the velocity distribution in the slipstream. Clearly, in high-lift configurations these considerations change, as not only the loading distribution of the propeller and position of the slipstream are affected, but also its shape of the slipstream.

### 5.3.3. Region II — Over the wing

At the start of Region II, the slipstream physically interacts with the wing and splits in parts that move on both sides of the wing. We have already established that the vertical position of the slipstream just ahead of the wing leading edge is dependent on the freestream angle of incidence and the wing upwash. The impact of the vertical shifting position becomes evident from Fig. 5.13, showing slices of the slipstream at 5% chord downstream of the leading edge. Overall, the slipstream shape is still very close to that presented in Fig. 5.12, but for the low $\alpha$ cases the majority of the slipstream moves along the wing lower surface, while for high $\alpha$ it is the opposite.

Besides splitting the slipstream, the main effect of the interaction at the leading edge as seen in Fig. 5.13 is the spanwise displacement of the slipstream close to the wing surface. We have already discussed that, among others, Felli [33] explains the displacement of the slipstream edge (or rather, the tip vortices) as a combination of two effects: image vortex effects and a pressure gradient effects. Felli [33] considers two main vortex image effects, namely that of the streamwise component of vorticity in the overall wing surface, and that of the vertical component of vorticity in the wing leading edge. These two effects are illustrated in Fig. 5.14. The initial expansion of the slipstream away from the propeller axis (hereinafter referred to as *outboard* direction) is attributed to the latter of the two image vortex effects. Felli [33] does not emphasize, however, that the deformation of the tip vortices has a significant impact on the image vortex effects. The outboard displacement of the tip vortices does not only occur on the tip vortices upstream of the leading edge, but also on the tip vortices that are wrapping around the leading edge. The wrapping of the tip vortices around the wing leading edge is well established by, among others, Felli [33] himself, and is also clear from the isosurfaces of $\lambda_2$ in the numerical simulation results in Fig. 5.15. As the tip vortices wrap around the leading edge, the entire wrapped
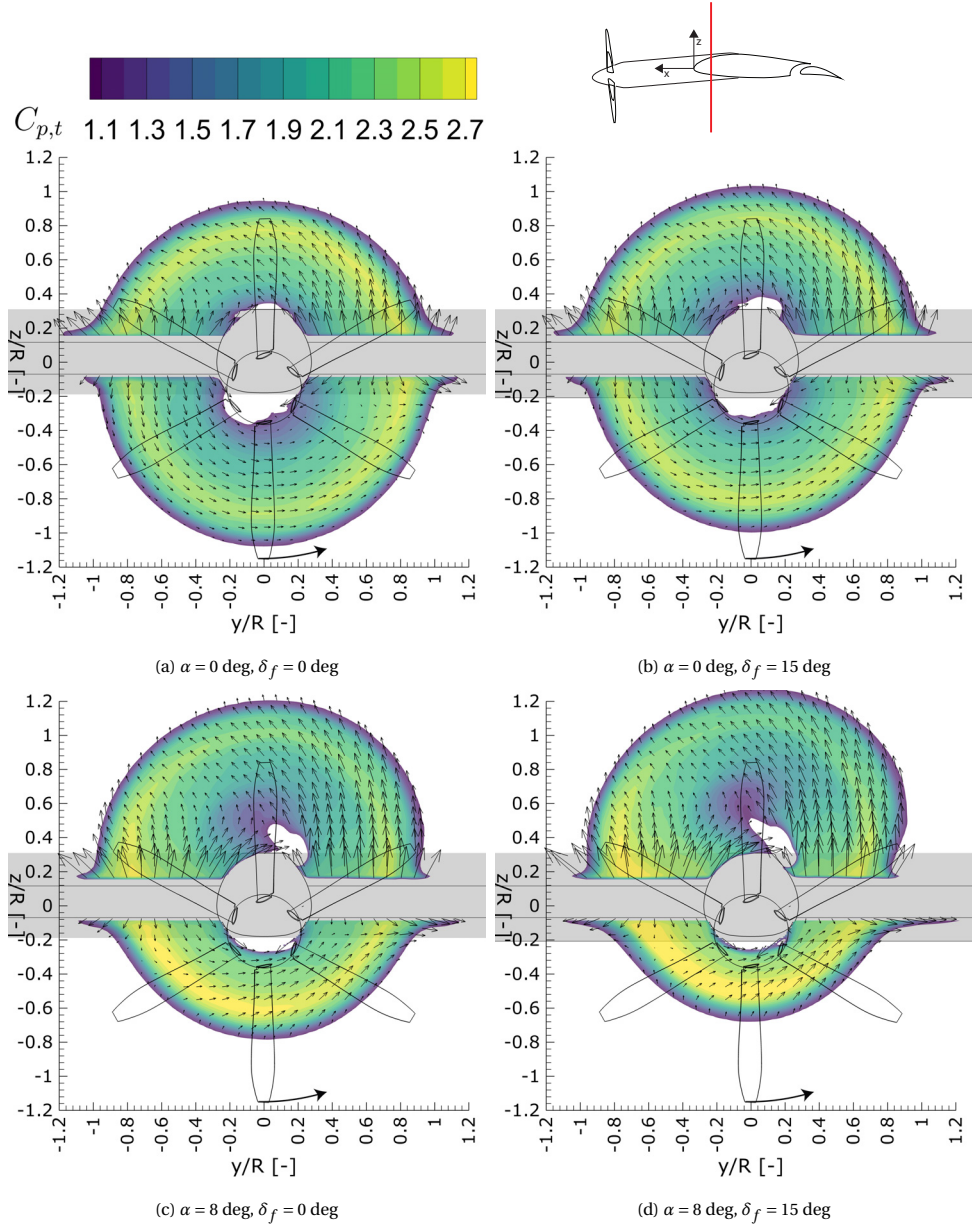
Figure 5.13: Slipstream slices in yz-plane at $x/c = -0.05$ (just downstream of the leading edge), showing in-plane velocity vectors and the distribution of $C_{p,t}$. Slice perpendicular to flap nested wing chord.
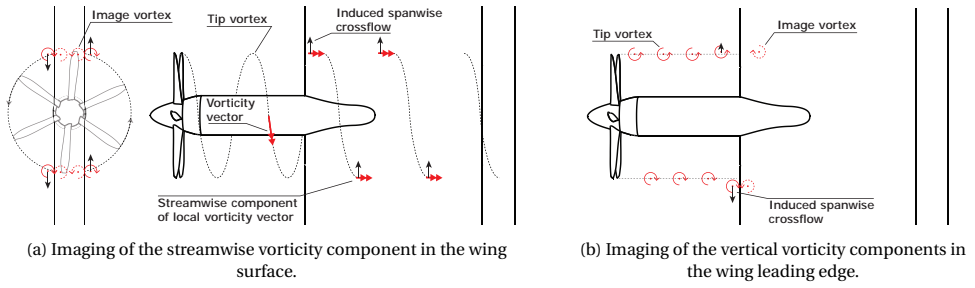
(a) Imaging of the streamwise vorticity component in the wing surface.

(b) Imaging of the vertical vorticity components in the wing leading edge.

Figure 5.14: Schematic illustration of the image vortex effects of the slipstream vorticity in the wing leading edge and over the surface.

filament experiences self-induction in the outboard direction through the image vortex effect. This is better illustrated in Fig. 5.16. As the wrapped filaments are, naturally, very close to the wing surface, the image vortex effect is particularly substantial, since it scales inversely with distance to the surface. As the filaments stretch further around the wing surface, they will lose strength and thus the effect diminishes.

Moreover, the interaction with the leading edge deforms the entire tip vortex near the wing, as seen in the isosurfaces of $\lambda_2$ from the numerical simulation results in Fig. 5.15. This means that, near the wing surface, most of the vorticity in the tip vortices on the upgoing blade side is oriented in upstream direction, rather than downstream direction as is the case for the undisturbed tip vortices. The principle is schematically illustrated in Fig. 5.17. This has a direct impact on the first vortex image effect (Fig. 5.14a). Again, as the vortex image effect scales inversely with distance from the wing surface, this will substantially change the local contribution of the image vortex effect on the slipstream
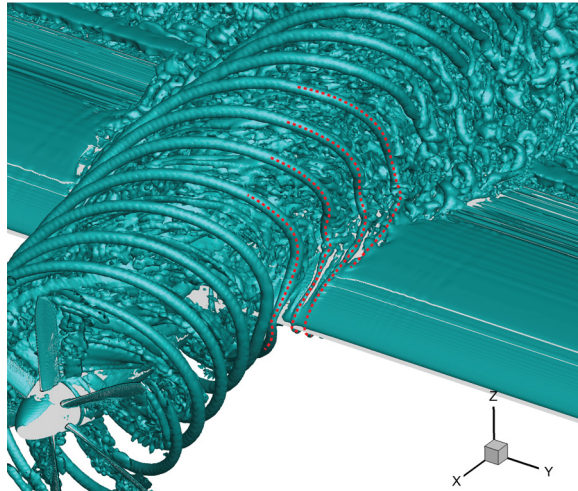


Figure 5.15: Isosurfaces of $\lambda_2 = -5V_\infty^2/c^2$ showing the tip vortices wrapping around the leading edge and displacing outboard (indicated by dashed red lines). $\alpha = 8$ deg, $\delta_f = 15$ deg.
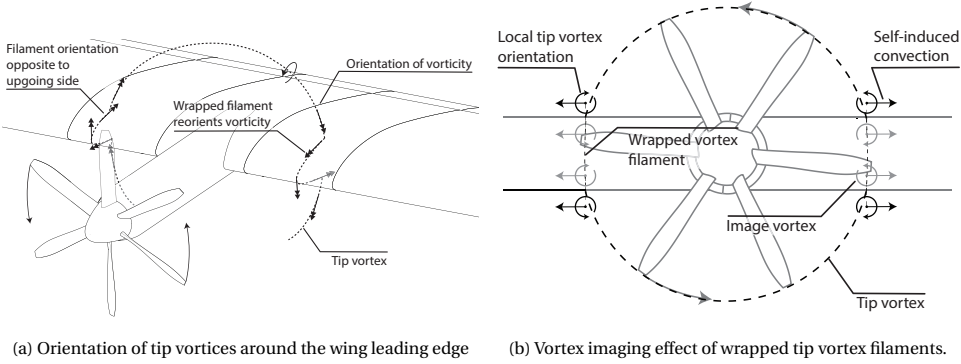
(a) Orientation of tip vortices around the wing leading edge

(b) Vortex imaging effect of wrapped tip vortex filaments.

Figure 5.16: Schematic illustration of the tip vortex wrapping and imaging effect in the wing surface.

deformation. At this point, we cannot say whether this difference with the analysis by Felli [33] (and preceding works like [100] and [95]) is due to the differences in configuration or can be generalized. The deformation of the tip vortex is a function of the ratio between vortex core size and wing leading edge radius [101, 102, 103], which is likely significantly different between our setup and that of the various propeller-rudder studies we discussed previously, which all share the same geometries.

In addition to the image vortex effects, the slipstream edge is also displaced by the local spanwise pressure gradients [33]. For a symmetrical, non-lifting wing, we can identify three main contributions: scaling of the local pressure due to increased dynamic pressure in the slipstream, the angle of attack induced by the tangential velocities in the slipstream, and the local static pressure field behind the propeller. For a lifting wing, however, the pressure distribution around the wing changes both inside and outside the propeller slipstream. The various contributions are illustrated in Fig. 5.18. Note that the impact of angle of attack also changes sign of the effect of dynamic pressure scaling. The direction of the induced crossflow due to the spanwise pressure gradients can thus completely change for a lifting wing, particularly in high-lift conditions.

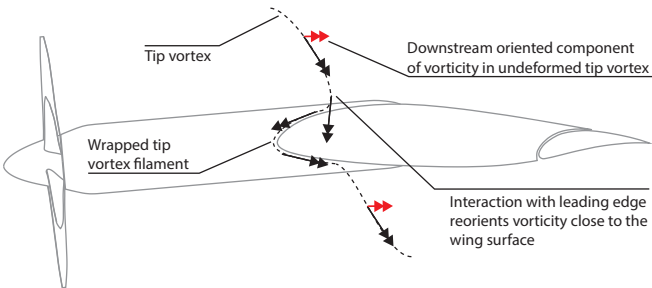It is worth noting that the vortex imaging effects and the pressure gradients are not



Figure 5.17: Schematic illustration of the reorientation of vorticity in the tip vortices on the upgoing blade side due to the interaction with the wing leading edge.

(a) Dynamic pressure

(b) Tangential velocities
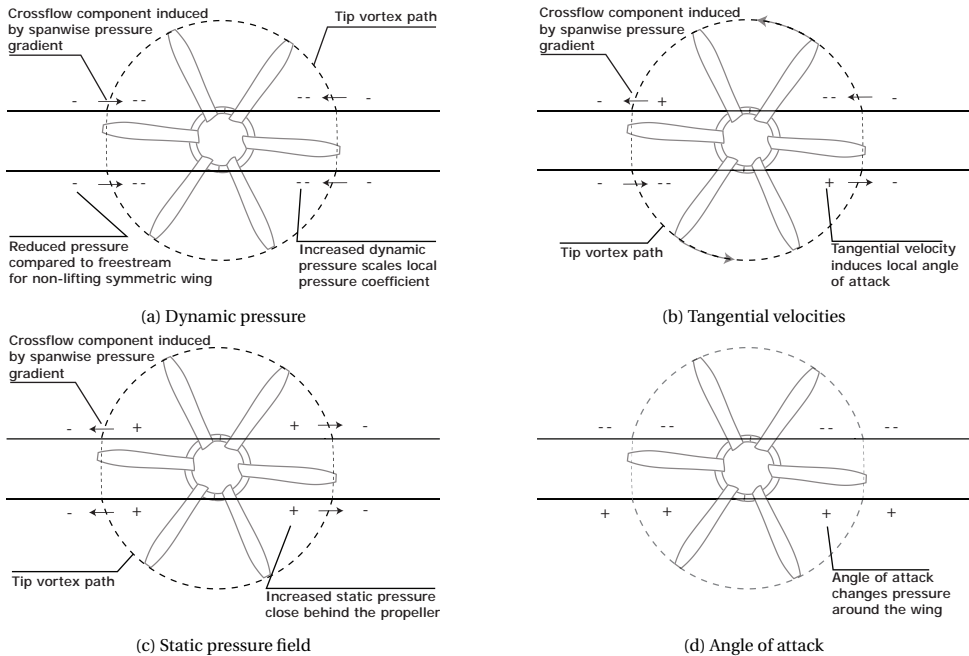
(c) Static pressure field

(d) Angle of attack

Figure 5.18: Schematic illustration of the four main contributions to the spanwise pressure gradients induced by propeller-wing interaction on a lifting wing. Front view.

fully decoupled features of the flow. Rather, the image vortex effects have a direct impact on the local pressure field. However, this impact is very small compared to the global effects of freestream, slipstream flow and wing shape on the pressure field. We therefore treat the image vortex effects as independent of the pressure gradient effects.

The strength and direction of the spanwise pressure gradient effects is thus dependent on the relative balance between the contributions illustrated in Fig. 5.18 and will therefore differ with configuration and operating condition. Figure 5.19 shows the spanwise distribution of static pressure coefficient $C_p$ on the wing surface at $x/c = -0.05$ for two different configurations. The arrows indicate the direction of local convection imposed by the pressure gradient on the tip vortices. For $\alpha = 0$ deg and $\delta_f = 0$ deg (Figs. 5.19a and 5.19c), the pressure gradients emphasize the outboard displacement at the upper left and bottom right quadrants, while they oppose the image vortex effect on the upper right and bottom left quadrants. For $\alpha = 8$ deg and $\delta_f = 15$ deg (Figs. 5.19b and 5.19d), however, the pressure gradients cause outboard movement on the wing lower surface and inboard movement on the wing upper surface.

Reviewing the slipstream shapes in Fig. 5.13, we clearly see the various contributions at play. In Fig. 5.13a, the most elongation is found at the upper left and lower right quadrants, where both vortex image effects and pressure gradient effects work in the same direction. The deformation at the lower left and upper right quadrants is smaller, as the pressure gradients oppose the image vortex effects. In Figs. 5.13c and 5.13d the deformation on the wing lower surface is much larger than on the wing upper surface, as

(a) $\alpha = 0$ deg, $\delta_f = 0$ deg, upper surface

(b) $\alpha = 8$ deg, $\delta_f = 15$ deg, upper surface

(c) $\alpha = 0$ deg, $\delta_f = 0$ deg, lower surface

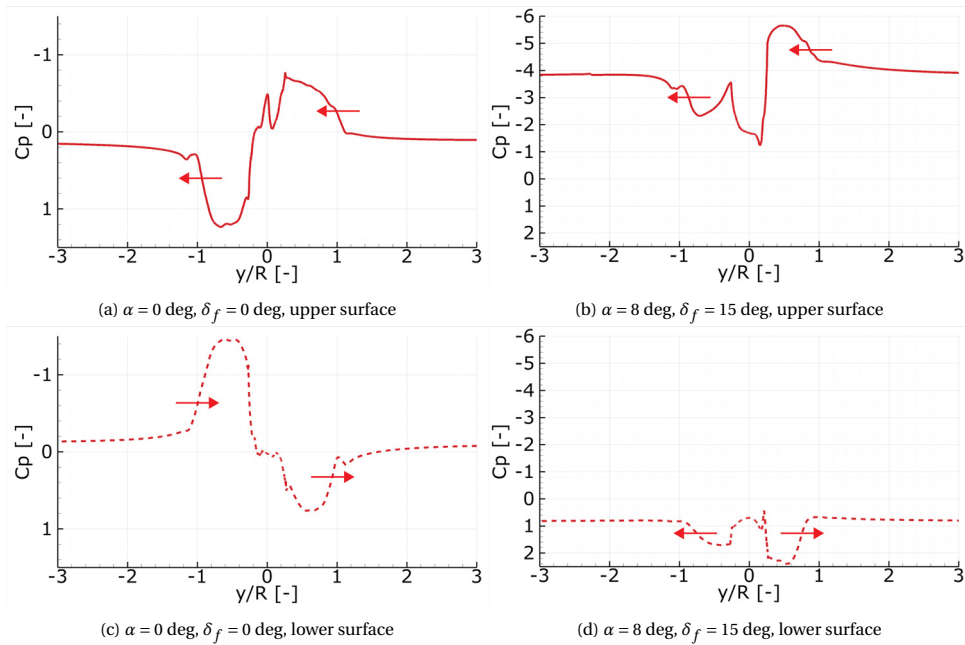(d) $\alpha = 8$ deg, $\delta_f = 15$ deg, lower surface

Figure 5.19: Spanwise pressure distributions at $x/c = -0.02$ on the upper (solid) and lower (dashed) surface. Arrows indicate the direction of the crossflow component induced by the pressure gradient at the slipstream edge.

the pressure gradients work in the same direction as the vortex image effects. Furthermore, the pressure gradients in the high $\alpha$ cases are much larger than in the low $\alpha$ cases, increasing their impact on the deformation.

Similar to the vortex imaging effects, the impact of the spanwise pressure gradients is concentrated near the wing surface and the leading edge. The pressure gradients are strongest close to the wing surface and diminish quickly when moving away from the surface, as shown in Fig. 5.20a. Similarly, the pressure gradients are strongest close to the wing leading edge and diminish quickly further downstream (although they do not disappear completely), as shown in Fig. 5.20b.

The slipstream deforming much more close to the surface than away from it, at least initially when it physically interacts with the wing, also means that surface flow alone does not adequately represent the state of flow around the wing in propeller-wing(-flap) configurations. Not all portions of the wing where the surface is washed by the slipstream are equally immersed. Particularly on the wing lower surface in the high $\alpha$ cases, the leading edge deformation effects cause a significant expansion of the slipstream area on the wing surface, while the overall shape and distribution of the slipstream have not changed much. This means for certain regions on the wing the boundary layer is affected by the slipstream, but shortly off-the-surface there is no slipstream and thus no rise in total pressure.

As the tip vortex elements that are wrapped around the leading edge displace, they

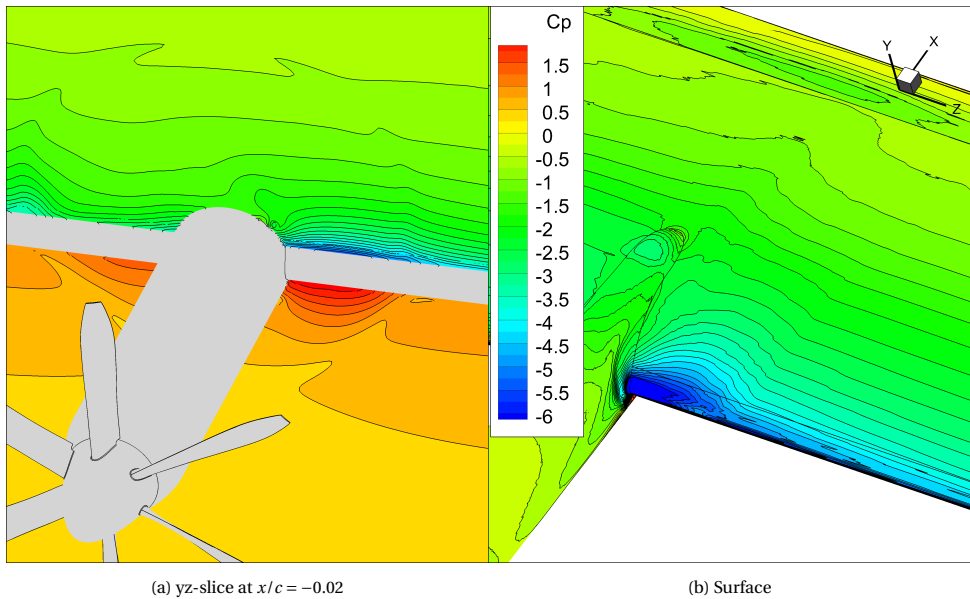(a) yz-slice at $x/c = -0.02$                    (b) Surface

Figure 5.20: Contours of static pressure coefficient in a volume slice near the leading edge and on the wing surface. Note how the gradients quickly diminish when moving away from the wing surface and along the chord line. $\alpha = 8$ deg, $\delta_f = 15$ deg.

pull and stretch parts of the slipstream that are further away from the wing surface. By the time the slipstream reaches the main element cove area, it has deviated significantly from its initial circular shape, as shown in Fig. 5.21. In particular, the edges of the slipstream that are close to the wing surface have expanded and diffused.

This expansion and diffusion is a result of interactions between the various tip vortex filaments that become aligned with the wing surface at the edge of the slipstream. Felli [33] showed that these filaments remain connected to the main tip vortex along the entire chord of the wing. Between these filaments, secondary vortices of opposite sign are induced in the wing boundary layer, as shown in Fig. 5.22. The secondary vortices wrap around the tip vortex filaments, as do the filaments themselves. The latter is visible more clearly in Fig. 5.22b. Overall, the slipstream boundary becomes diffused due to the various vortex-vortex and vortex-boundary layer interactions, leading to a loss of the tip vortex helical structure.

The strength of the vortex that rolls up from the stretched tip vortex filaments varies at each edge of the slipstream. It depends on the alignment between the deformation of the tip vortex filament and the overall orientation of the undeformed helical vortex system of the slipstream. The mechanism is illustrated in Fig. 5.23. On the upper surface downgoing blade side, the deformation of the tip vortex as it wraps around the wing leading edge emphasizes the orientation of the undeformed tip vortex. In this case, a significant portion of the tip vortex wraps up into the vortex at the slipstream edge. On the wing upper surface upgoing blade side, the deformation is opposite to the undeformed orientation of the tip vortices. As a result, only the deformed filaments align along the
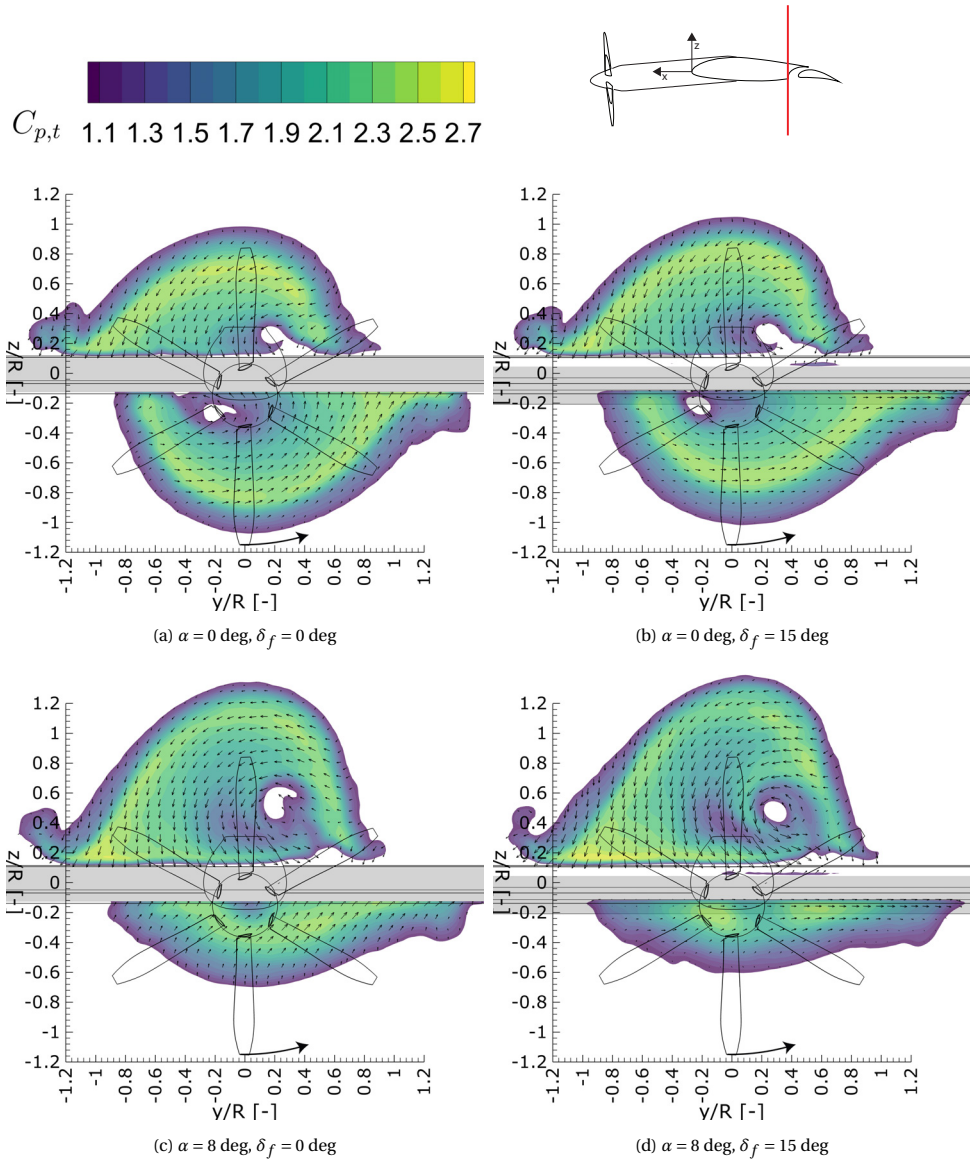
(a) $\alpha = 0$ deg, $\delta_f = 0$ deg

(b) $\alpha = 0$ deg, $\delta_f = 15$ deg

(c) $\alpha = 8$ deg, $\delta_f = 0$ deg

(d) $\alpha = 8$ deg, $\delta_f = 15$ deg

Figure 5.21: Slipstream slices in yz-plane at $x/c = -0.67$ (at the main element cove), showing in-plane velocity vectors and the distribution of $C_{p,t}$. Slice perpendicular to flap nested wing chord.

wing surface and roll up into a much weaker vortex. On the wing lower surface, the same occurs but on mirrored sides.

This mechanism is strengthened by the wing circulation, which induces a rotation on the tip vortex helix. Figure 5.24 shows a schematic illustration of this mechanism on each side of the propeller. On the upgoing blade side, the tip vortices are rotated to be

(a) $\alpha = 0$ deg, $\delta_f = 0$ deg

(b) $\alpha = 8$ deg, $\delta_f = 15$ deg
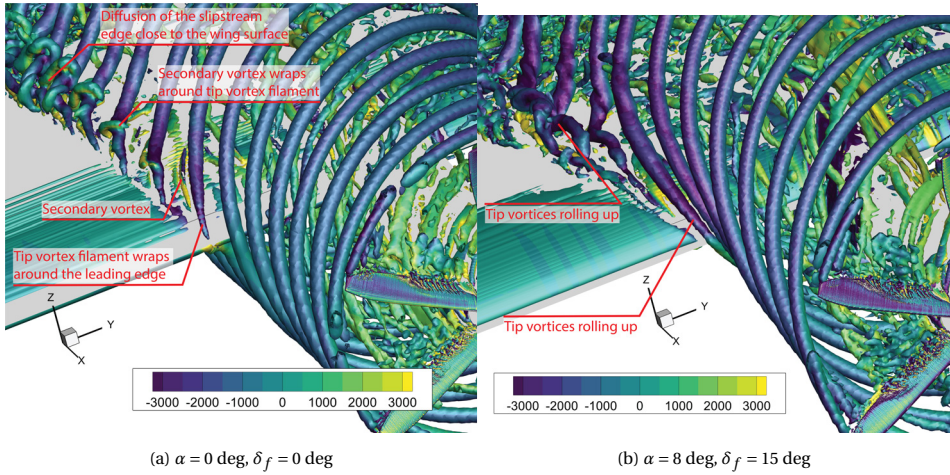
Figure 5.22: Isosurfaces of $\lambda_2 = -100 V_\infty^2/c^2$, showing the alignment and roll-up of the stretched tip vortex filaments on the wing surface. Coloured by vorticity component parallel to the wing chord.

more perpendicular to the wing chord. On the downgoing blade side, however, the tip vortices become more parallel to the wing chord. This reorients the local vorticity to align more with the wing chord, causing a larger portion of the tip vortex to roll into the surface interaction. For high angles of attack, the asymmetric disk loading increases the tip vortex strength on the downgoing blade side, leading to a stronger tip vortex roll-up on that side.

These observations yield several valuable insights to be investigated further. The relation between deformation and helix angle suggests that deformation may be mitigated to a degree by designing for lower advance ratios. This may prove particularly interesting for distributed propeller cases, where deformation will increase interactions between adjacent slipstreams.

From the slices of $C_{p,t}$ in Fig. 5.21, we can also identify concentrated region of total pressure loss at the centre of the slipstream. This is the viscous core of a vortex that rolls up at the nacelle on both sides of the wing. Figure 5.25 visualizes these *nacelle-root vortices* by



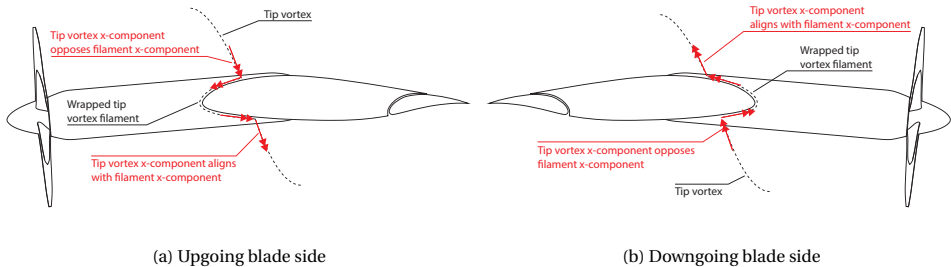(a) Upgoing blade side

(b) Downgoing blade side

Figure 5.23: Illustration of the alignment of the slipstream helix angle with the local deformation of the tip vortices, contributing to the vortex roll-up at the slipstream edge on the wing surface.

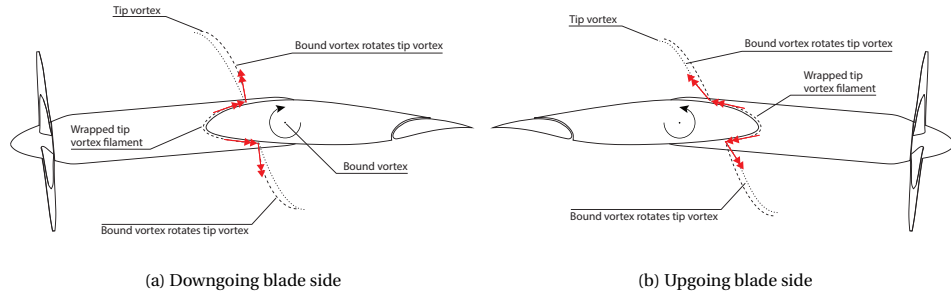(a) Downgoing blade side                    (b) Upgoing blade side

Figure 5.24: Illustration of the bound circulation of the wing rotating the slipstream helix, affecting the alignment of tip vortices that roll up near the wing surface.

isosurfaces of the x-component of vorticity (in wing frame). Vorticity distributed around the nacelle body rolls into a pair of concentrated vortices near the wing leading edge. These vortices are hereinafter referred to as the *nacelle/root vortices,* since they consist of vorticity on the nacelle surface and the propeller blade root vorticity. For low angles of attack, these vortices are of comparable strength on both sides of the wing and reach far into the wake region. For higher angles of attack, the vortex on the upper side is much stronger. We can still see a vortex on the lower side, but this breaks down before it reaches the cove. The residual momentum loss from the vortex core of this vortex later impinges on the flap.

   The formation of the nacelle/root vortices is based on vortex convection and stretching, similar to the tip vortices wrapping around the leading edge. The sources of vorticity
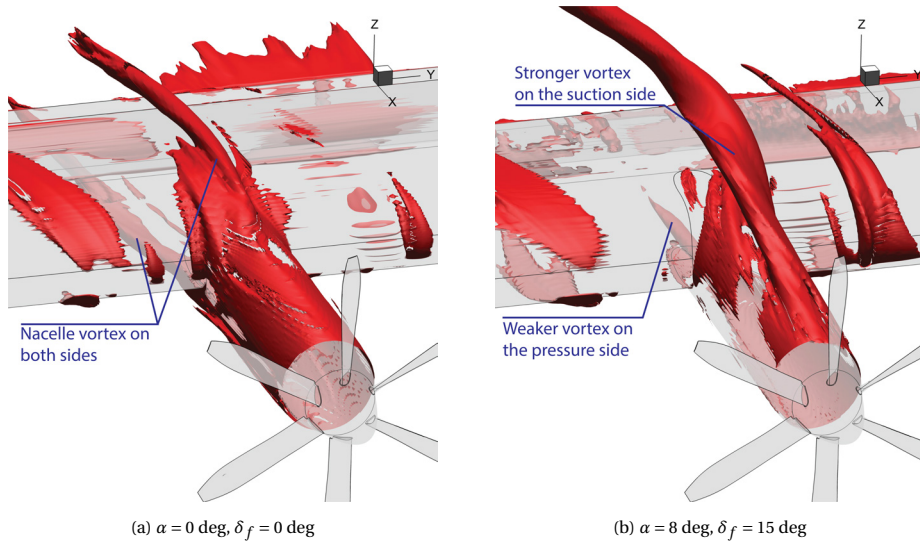


(a) $\alpha = 0$ deg, $\delta_f = 0$ deg                    (b) $\alpha = 8$ deg, $\delta_f = 15$ deg

Figure 5.25: Isosurface of the x-component of vorticity (in wing frame) at $\omega = -3000\,s^{-1}$, showing the formation of a vortex on both sides of the wing from vorticity around the nacelle.

for the formation of the nacelle/root vortex are the vorticity in the nacelle boundary layer and the propeller blade root vortex. The former will be relatively small compared to the latter, particularly at low angles of attack. The propeller root vorticity can be decomposed into longitudinal (or streamwise) and azimuthally oriented vorticity, as is common in slipstream tube models. Figure 5.26 illustrates how these two parts of the vortex system will interact with the wing leading edge to form the nacelle/root vortex. The vortex lines are all positively oriented and will wrap into a concentrated vortex when they are convected into each other by flow around the nacelle and wing leading edge. The vortex rings will fold around the nacelle and wing leading edge, reorienting into a vortex pair on each side of the wing. The positive-oriented part of the deformed vortex rings will wrap into the same vortex as the deformed vortex lines, leaving the negative-oriented part of the deformed vortex rings to form a much weaker, negative-oriented nacelle/root vortex. The illustrations of Fig. 5.26 thus predicts a vortex pair on each side of the wing, with the positive-oriented vortex stronger than the negative-oriented vortex. This vortex pair will self-induce a velocity component away from the surface of the wing. Furthermore, the vortex on the upper surface will be stronger than on the lower surface, particularly for high-lift conditions.

The mechanism illustrated in Fig. 5.26 is supported by looking at slices of vorticity along the nacelle and wing. Figure 5.27a shows the component of vorticity aligned with the wing chord, which roughly equates to the local flow direction. Along the nacelle, the vorticity is mostly evenly distributed and fully positive. As we get closer to the leading edge, we can see the orientation flip. The upper right and lower left quadrants become negative as the root vorticity wraps around the leading edge. Further downstream on the wing we see a distinct vortex pair. The negative-oriented vortex is weaker and dissipates, leaving only the positive vortex to move further down the wing.

For higher angles of attack, the described mechanism no longer seems to hold, as shown in Fig. 5.27b. However, when visualizing the vortex structures in the time-accurate results (Fig. 5.28), it can in fact still be observed. Because the angular velocity of the blade is much lower at the root than at the tip, the root vorticity is already strongly aligned with the flow. This causes a large portion of the root vortices to directly roll into the



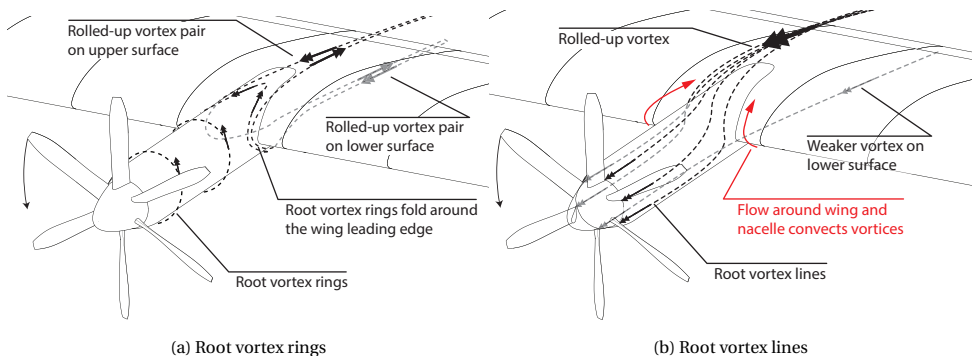(a) Root vortex rings  (b) Root vortex lines

Figure 5.26: Illustration of the root vorticity rolling up into the nacelle/root vortex at the wing leading edge, based on vortex ring and vortex lines decomposition.
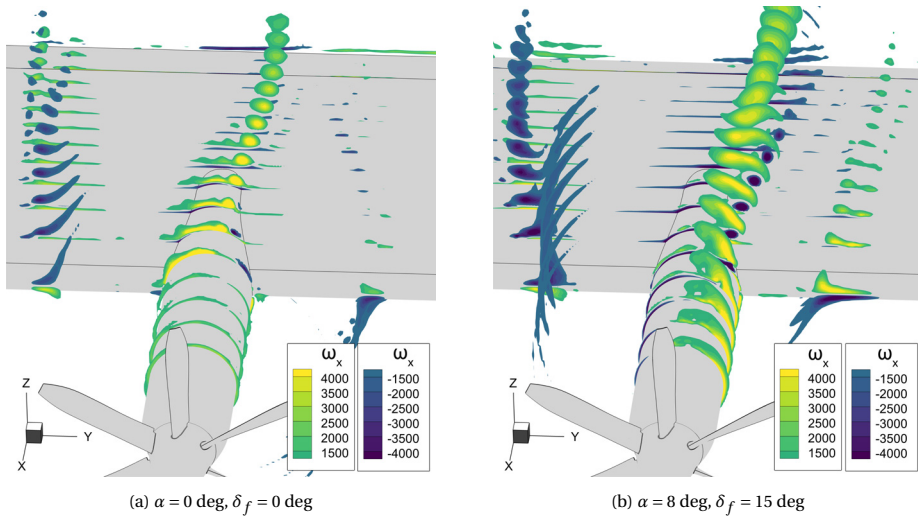
(a) $\alpha = 0$ deg, $\delta_f = 0$ deg          (b) $\alpha = 8$ deg, $\delta_f = 15$ deg

Figure 5.27: Slices of the x-component of vorticity (in wing frame) where $|\omega| > 1500\ s^{-1}$.

nacelle/root vortex. Residual root vortices still wrap around the leading edge and a small portion rolls into the nacelle/root vortex on the wing lower surface. Additionally, due to the positive angle of incidence of the nacelle, local flow around the nacelle also induces vorticity in the nacelle boundary layer. On the downgoing blade side, this opposes the root vorticity.

Revisiting Fig. 5.21, we can see the nacelle vortices dominate the in-plane velocities near the wing surface downstream of the nacelle, inducing a strong spanwise velocity component on the wing surface. The latter drives flow from the downgoing blade side into the upgoing blade side, creating a shear layer at their interface. This shear layer is illustrated in Fig. 5.29 by slices of $C_{p,t} < 1$. From oil flow visualization (see Fig. 5.30), we have seen this shear layer causing local flow separation and confluencing with separation regions outside the slipstream at very high angles of attack. The effects of the nacelle/root vortex may thus limit the wing performance in the maximum lift regime.

A different position of the nacelle could greatly change the interaction of the nacelle/-root vortex with the wing surface flow. A nacelle under the wing, for instance, would mean all the root vorticity convects along the lower surface. This would mitigate the crossflows on the upper surface and thus the shear layer shown in Fig. 5.29 and associated flow separation. However, such a nacelle position would also result in more of the nacelle vorticity impinging on the flap, which may affect it negatively. Furthermore, the nacelle position has a direct impact on the propeller-wing interaction, depending on the propeller diameter. Nonetheless, the role of the nacelle/root vortex in the wing surface flow development further emphasizes that the nacelle integration is a critical aspect of propeller-wing interaction, particularly in high-lift conditions.

Overall, the slipstream deformation on the main element is evidently dominated by the tip and root vortices wrapping around the leading edge. The resulting nacelle/root vortex dominates the flow phenomena that occur within the boundaries of the slipstream,

(a) Upgoing blade side

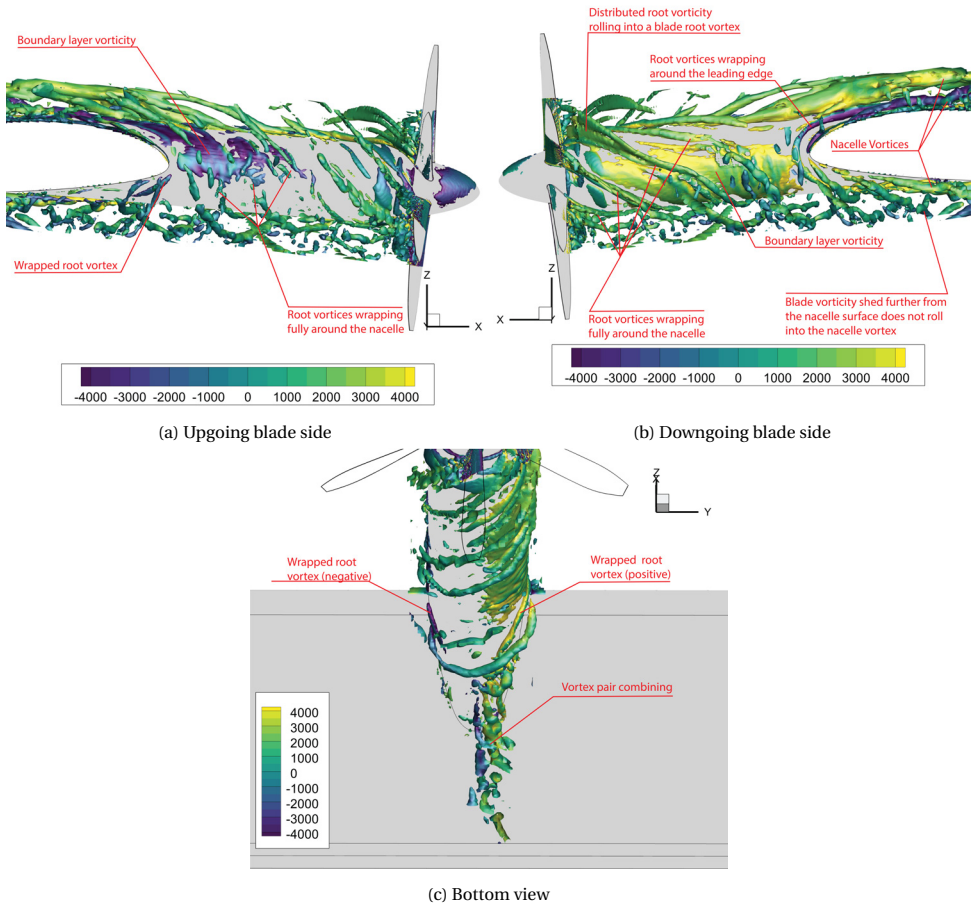(b) Downgoing blade side

(c) Bottom view

Figure 5.28: Isosurfaces of $\lambda_2 = -10V_\infty^2/c^2$, showing the root vorticity roll-up around the nacelle. Tip vortex values blanked to reveal the nacelle flow. Isosurface coloured by the x-component of vorticity in the wing frame.

while the deformation of the slipstream boundaries is determined by the tip vortex filaments that align and gather at the slipstream edges.

The interaction of the slipstream with the flap differs significantly from the main element interactions. The flap has no nacelle, and root vorticity has readily formed into concentrated vortices aligned with the flow. Furthermore, the flap is immersed in the part of the slipstream that travels along the wing lower surface. Only a small portion of the flow moves through the gap and, due to the deformation, no concentrated tip vortices wrap around the flap.

The rotation of the helical vortex system due to the wing circulation (see Fig. 5.24), as well as the pressure field around the flap, affect the spacing of the tip vortices on both sides of the wing. On the wing upper surface, they are spaced further apart, delaying vortex-vortex interactions and breakdown of the helical vortex system. On the wing lower
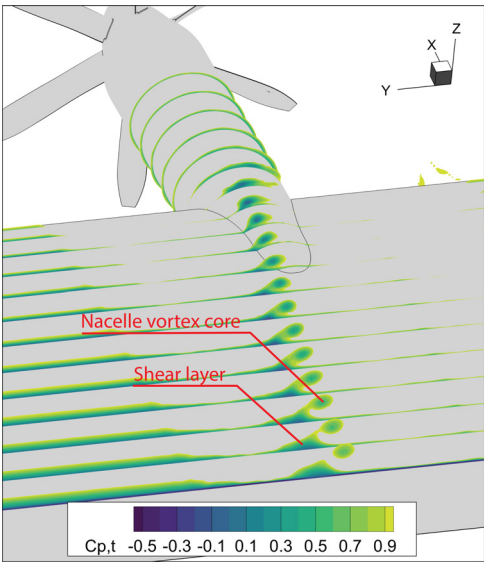
Figure 5.29: Slices of total pressure coefficient, limited to $C_{p,t} < 1$, showing the shear layer and nacelle/root vortex.

surface, however, it is the opposite. The tip vortices are pushed into each other, forcing them to interact. This causes them to leapfrog and combine into larger vortical structures that eventually break down, as visualized in Fig. 5.31. The figure shows that this process, which we will denote as *vortex system instability*, occurs much earlier along the wing chord for configurations with stronger bound circulation.

Resulting from this interaction, the flow that immerses the flap is fairly uniform in the high-lift cases. As illustrated by the in-plane velocity vectors in Fig. 5.21, the high-lift cases show little asymmetry due to swirl effects. For lower lift cases, the swirl — and nacelle/root



(a) $\alpha = 10$ deg

(b) $\alpha = 13$ deg
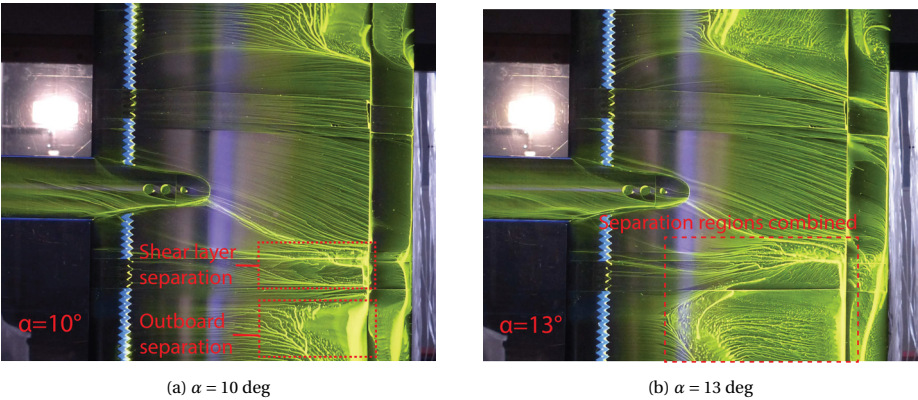
Figure 5.30: Oil flow images showing flow separation on the upper surface. Flap nested.

vortex effects — is still dominant. Overall, the flap lift is augmented due to the increase in dynamic pressure and the resulting lift distribution is relatively symmetrical, as discussed previously in section 5.1.4.

Over the flap itself, the majority of deformation occurs on the upgoing blade side. Figure 5.32 shows the slipstream shape at the flap trailing edge. For clarity, the slipstream shape at the main element cove (Fig. 5.21) is shown using a single contour line of $C_{p,t} = 1.05$. Note that at the flap trailing edge, the upper half of the slipstream no longer interacts physically with any surface as it has left the main element and is separated from the flap element by the gap flow. The lower part of the slipstream impinges upon the flap surface, causing some spanwise expansion. Since it has been established that the slipstream no longer consists of a concentrated helical vortex system when it reaches the flap, no distinct vortices wrap around its leading edge and no dominant vortex imaging effects take place. The deformation of the slipstream on the flap will then be dominated by the pressure gradient effects.
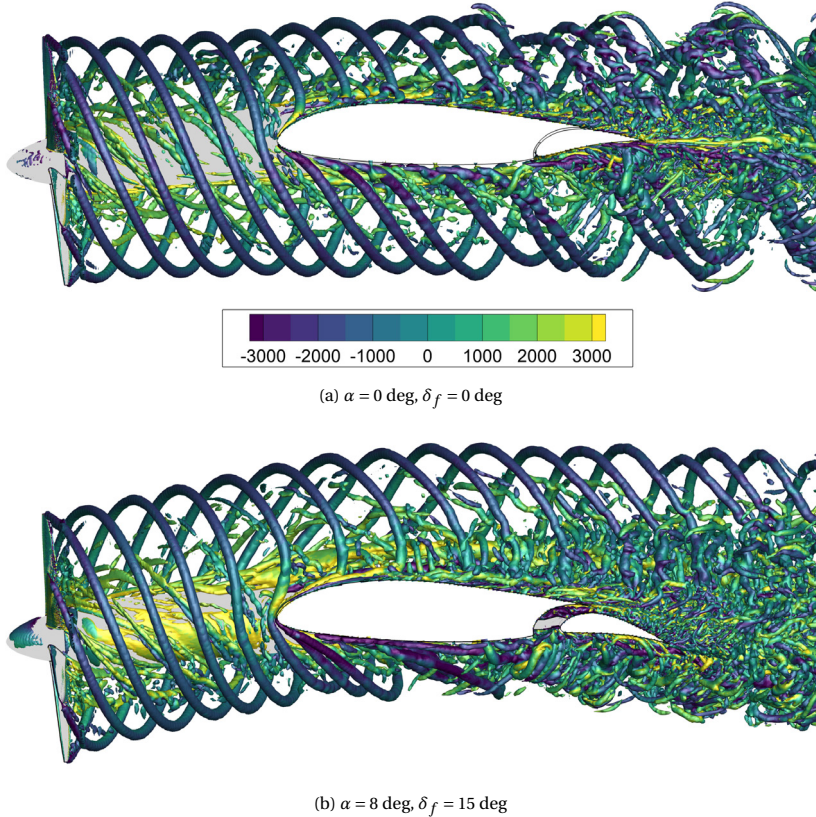
**5**



(a) $\alpha = 0$ deg, $\delta_f = 0$ deg



(b) $\alpha = 8$ deg, $\delta_f = 15$ deg

Figure 5.31: Isosurfaces of $\lambda_2 = -100 U_\infty^2/c^2$, showing the breakdown of the helical tip vortex structure for different configurations. Coloured by x-component of vorticity.
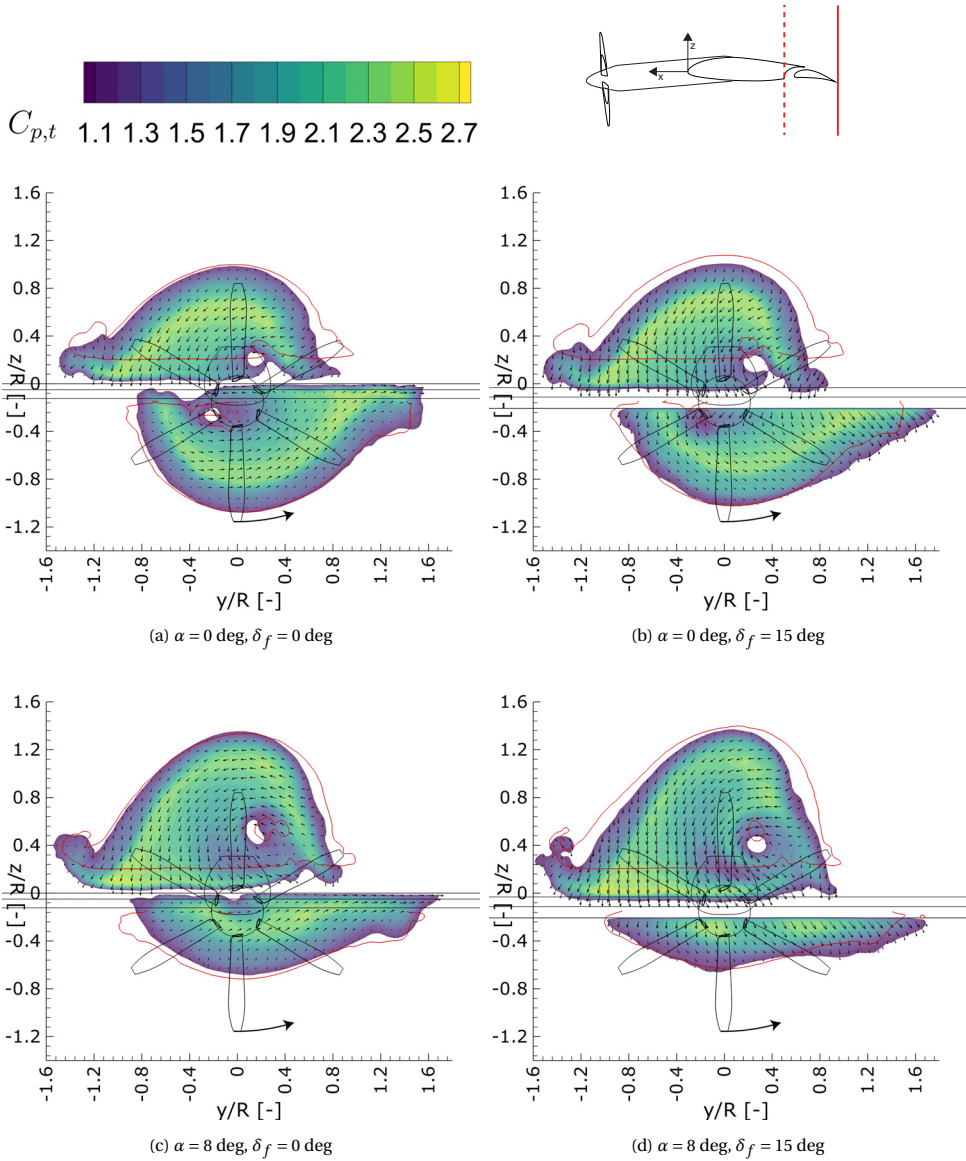
Figure 5.32: Slipstream slices in yz-plane at the flap trailing edge, showing in-plane velocity vectors and the distribution of $C_{p,t}$. Slice perpendicular to flap nested wing chord. Red contour lines indicate the slipstream shape at the main element cove position for comparison.

### 5.3.4. REGION III — WING WAKE

The final stage of deformation occurs in the wake of the wing, after the slipstream has left the flap trailing edge. Figure 5.33 shows the slipstream distribution and in-plane velocity vectors in the wake of the wing, at $x/c = -2$. At this stage, the slipstream has combined into a single structure again, although the two halves of the slipstream can still be clearly identified for the configurations at $\alpha = 0$ deg. The slipstream has clearly dissipated significantly compared to the flap trailing edge position (Fig. 5.32), owing to the breakdown of the vortex system and mixing with the wing and flap wakes. It should be noted that at this point, numerical dissipation and diffusion in the simulations will also have a significant impact on the distributions.

Regardless of the contribution of numerical dissipation to the gradients of the slipstream distribution in the wake, we can see that significant deformation and redistribution occurs after the slipstream leaves the wing trailing edge. The in-plane velocity vectors are dominated by the (remainders of the) nacelle/root vortex, particularly for the high $\alpha$ configurations. For configurations with flaps deployed, the lower right quadrant is dominated by the downwash rather than the nacelle/root vortex. Overall, this causes the slipstream to rotate around the nacelle/root vortex and continue to stretch towards the upgoing blade side.

These observations have two major implications. Firstly, the state of the slipstream in the wake of the wing cannot be used in a straightforward manner to judge the deformation of the slipstream on the wing. Despite the significant deformation that takes place on the wing up to the flap trailing edge, the slipstream maintains much more of its circular shape than the wake images would lead us to believe. Particularly the extent of shearing of the slipstream on the wing may be overestimated from the wake measurements alone.

Secondly, the deformation of the slipstream in the wake may be critical to the aerodynamic performance of the empennage and flight stability in typical tube-and-wing aircraft configurations. Slipstream effects on the empennage are generally modelled using straightforward slipstream tube models (e.g., the method proposed by Obert [104], recently applied by Bouquet and Vos [105]). While this may prove sufficient in low-lift conditions to a certain degree, it is clear from the distributions shown in Fig. 5.33 that this assumption will not hold for high-lift configurations, particularly when flaps are deployed. Considering the deformation that takes place in the wake within a single chord distance, the impact of the slipstream on the empennage (or any other downstream surface) cannot be predicted accurately with standard slipstream modelling methods.
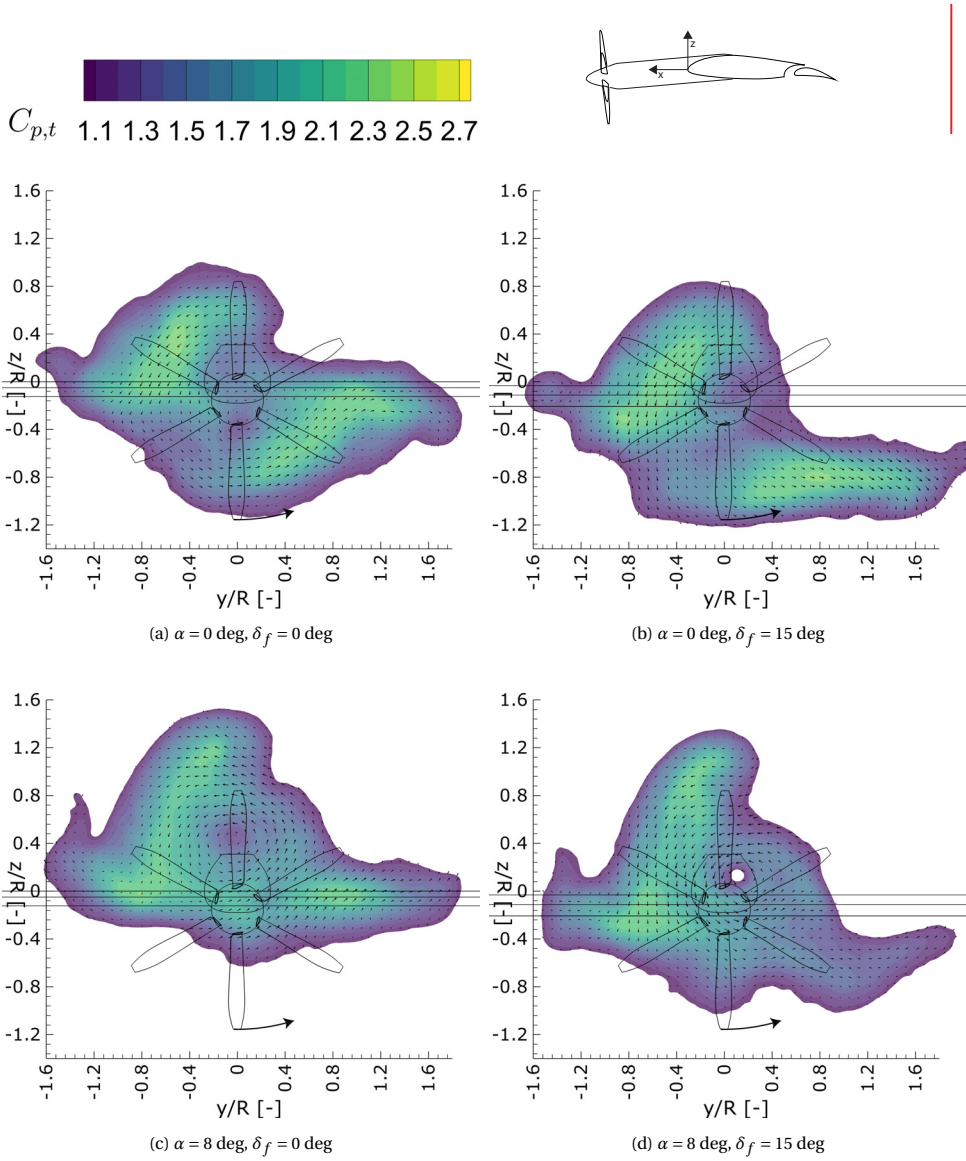
**5**

(a) $\alpha = 0$ deg, $\delta_f = 0$ deg

(b) $\alpha = 0$ deg, $\delta_f = 15$ deg

(c) $\alpha = 8$ deg, $\delta_f = 0$ deg

(d) $\alpha = 8$ deg, $\delta_f = 15$ deg

Figure 5.33: Slipstream slices in yz-plane at $x/c = -2$ (in the wake), showing in-plane velocity vectors and the distribution of $C_{p,t}$. Slice perpendicular to flap nested wing chord.

## 5.4. Key Findings

In this chapter, we investigated the aerodynamic performance of the propeller-wing-flap model, identified the main aerodynamic phenomena that occur in various combinations of angle of attack and flap deflection, and characterized the slipstream deformation and its dominant mechanisms. The analyses of this chapter lead to the following key findings:

- The propeller slipstream induces flow separation on the upper surface of the main element in high-lift conditions.

- The flap flow is dominated by the part of the slipstream that passes the lower surface of the main element. The flap sees much less effect of tangential velocities in the slipstream compared to the main element. It therefore experiences a more uniformly distributed lift augmentation, without the anti-symmetry that is characteristic for the main element.

- The maximum augmentation of lift coefficient due to the slipstream is notably larger on the flap than on the main element.

- Slipstream deformation is an important aspect of the propeller-wing-flap interaction, particularly in high-lift conditions. It has a direct effect on the part of the flap that is immersed in the slipstream, and thus on the flap spanwise lift distribution. This in turn affects the main element lift distribution and thus the whole system aerodynamic performance.

- Substantial slipstream deformation can already occur upstream of the wing leading edge in high-lift conditions. The vertical position of the slipstream with respect to the wing is critical for this part of the deformation.

- The observed deformations of the slipstream on the main element follow the principle mechanisms described by Felli [33], even in high-lift conditions with flap deployed. However, the orientation of the image vortex effects and pressure gradient effects are very different compared to a symmetric, non-lifting wing.

- The slipstream deformation is dominated by the interactions of the tip and root vortex systems with the wing.

- The crossflow on the wing surface downstream of the nacelle are a direct effect of the nacelle/root vortex. The nacelle position and integration is thus critical to the slipstream deformation and propeller-wing-flap aerodynamic interaction.

- Due to the nacelle-wing integration, a part of the root vortex system passes the lower surface of the wing, even at high angles of attack and high levels of wing circulation. This is likely very different from the same case with a detached nacelle, where the entire root vortex system can be convected over the upper surface of the wing.

- Slipstream deformation may be controlled by optimizing advance ratio and propeller thrust and torque. This is further explored in Chapter 6.

- The stability of the helical vortex system is directly affected by the wing circulation, as it reduces spacing between tip vortices on the lower surface, expediting their interaction and breakdown. On the upper surface, the tip vortices are spaced further apart by the wing circulation, delaying their interaction and subsequent breakdown.

- Slipstream deformation in the wake is dominated by the velocities induced by the nacelle/root vortex.

**5**

# 6

# SLIPSTREAM DEFORMATION WITH VARYING PROPELLER OPERATING CONDITIONS

*In the previous chapter, we discussed the importance of slipstream deformation for the aerodynamic performance of propeller-wing-flap configurations, particularly in high-lift conditions. The aerodynamic mechanisms that dominate the slipstream deformation follow those proposed by recent literature. In this chapter, we continue the study of these mechanisms by analysing the relation between integral performance characteristics of the propeller and the resulting slipstream deformation, based on the results of the second experiment. Specifically, we study how the longitudinal and azimuthal vorticity added to the flow by the propeller affects the slipstream deformation. An overview of how these components of vorticity are related to propeller performance characteristics and how they are controlled in the experiment is given in Section 6.1. In Section 6.3 we analyse the measurements in the propeller plane (see Chapter 2) to verify the propeller's operating conditions, and thus the slipstream characteristics. We then continue with the analysis of the slipstream deformation for each of the tested propeller conditions. This analysis is performed for low-lift configuration ($\alpha = 0$ deg, flap nested) in Section 6.4 and high-lift configuration ($\alpha = 8$ deg, $\delta_f = 15$ deg) in Section 6.5.*

---

## 6.1. Controlling slipstream characteristics

In Chapter 5 we have shown how the propeller-wing-flap interaction and the resulting slipstream deformation are a result of the following main concepts:

- the physical obstruction of the helical vortex system by the wing,

- the image vortex system of the slipstream in the wing surface,

- the wing circulation convecting the helical vortex system,

- the helical vortex system inducing velocities around the wing, causing spanwise lift gradients,

- the helical vortex system interacting with itself, often incited by the convections of the above effects.

We have also seen how the orientation of the vortices in the helical vortex system with respect to the wing surface affect the resulting deformation. Deformations of vortices, both due to physical interaction with the wing surface and due to circulation-induced convective components, that opposed the initial orientation of the vortex system resulted in much weaker interactions than when the vortex system was locally aligned with the deformation. A different helix angle will then result in a different deformation. Similarly, as vortex image effects are directly related to vortex strength, a change in vortex concentration would change the deformation resulting from the propeller-wing-flap interaction. Clearly, the slipstream characteristics (i.e., helix angle, individual vortex strength and total vorticity) as induced by the propeller are a critical aspect of the subsequent interaction with the wing. We may thus be able to impose some control on the propeller-wing-flap interaction by controlling the propeller operating conditions. In this chapter, we investigate how the slipstream deformation is affected by the slipstream characteristics, and by extension the propeller performance coefficients.

By decomposing the helical vortex system of the slipstream into longitudinally and azimuthally oriented vorticity, or vortex lines and vortex rings, we can see that the helix angle depends on the ratio between the longitudinal and azimuthal parts. This approach, illustrated in Fig. 6.1, is the same that we used to understand the mechanisms behind the nacelle-root vortex roll-up in Chapter 5. By modifying the amount of longitudinal
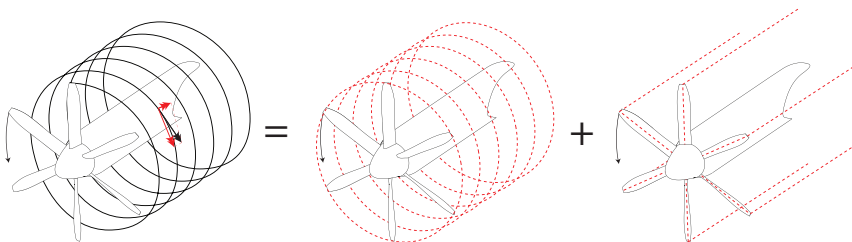


Figure 6.1: Decomposition of the helical vortex system of the slipstream into longitudinally and azimuthally oriented vorticity.

or azimuthal vorticity introduced into the flow by the propeller, we can control the helix angle of the helical vortex system. The individual tip vortex strength changes if the same total vorticity in the slipstream is achieved with fewer blades, or if the helix angle remains the same, but the total vorticity in the slipstream is reduced. In wind tunnel experiments, the only control we have to vary these quantities for a given propeller is by varying the advance ratio, blade pitch and number of blades. If we assume that longitudinal vorticity in the slipstream scales directly with the torque coefficient $Q_c = \frac{Q}{\rho V^2 D^3}$, while azimuthal vorticity scales with thrust coefficient $T_c = \frac{T}{\rho V^2 D^2}$, we can control the balance between them by controlling the ratio of $T_c$ and $Q_c$. This can be achieved by selecting appropriate combinations of blade pitch angle $\beta_{0.7R}$ and advance ratio $J$. Changing the number of blades, while maintaining equal $Q_c$ and $T_c$ leads to a direct change in the strength of each individual tip vortex, but equal total vorticity in the slipstream. Similarly, an equal ratio of $T_c$ and $Q_c$ at different magnitudes would result in equal helix angle but varying total vorticity (and individual vortex strength).

## 6.2. Determining propeller conditions

Unfortunately, not enough experimental data were available of the propeller performance to determine these conditions. We therefore simulated the performance for various blade pitch settings and number of blades, across a wide range of advance ratios, using a Blade Element Momentum (BEM) model [106]. Installed on the wing, the propeller operates in a non-uniform inflow field resulting from the bound circulation on the wing. To verify this will not change the operating conditions of the propeller to an extent that will invalidate the goal of the experiment, we applied the method by van Arnhem [64] to predict the propeller performance at an inflow angle. These simulations were run at an inflow angle of 5 designing, as this is the highest angle that the method was validated at. The results are summarized in Fig. 6.2. It shows calculated $Q_c - T_c$ curves for the 6-bladed (solid) and 3-bladed (dashed) propeller at specific blade pitches. Black curves represent the performance in isolated conditions, while the red curves signify the curves for the propeller with an inflow angle of 5 deg.

The curves in Fig. 6.2 show very little difference between the isolated and installed performance. We attribute this to the limited advance ratios that are achievable in the experimental setup, due to torque limitations of the electric motors. At lower advance ratios, the calculated curves deviate more between isolated and installed conditions, but within the range achievable in the experiment there is little difference. It should be noted that apparent angle of incidence for the propeller during the experiment is likely to exceed 5 deg, particularly in high-lift configuration. However, based on Fig. 6.2, they are unlikely to shift to such a degree that they invalidate the main objective of the selected operating conditions, which is focused on primarily changing $T_c$ and $Q_c$ one factor at a time.

The performance curves from Fig. 6.2 can then be used to select specific operating conditions that allow us to discretely vary $T_c$ and $Q_c$. The selected conditions are summarized in Table 6.1. The 6-bladed propeller with $\beta_{0.7R} = 30$ deg at $J = 0.8$ serves as the baseline, and represents the maximum $Q_c$ that could be achieved by the electric motors used in the experiment. This propeller condition matches what was analysed in Chapter 5. The same propeller with $\beta_{0.7R} = 45$ deg at $J = 1.195$ produces significantly lower $T_c$, but
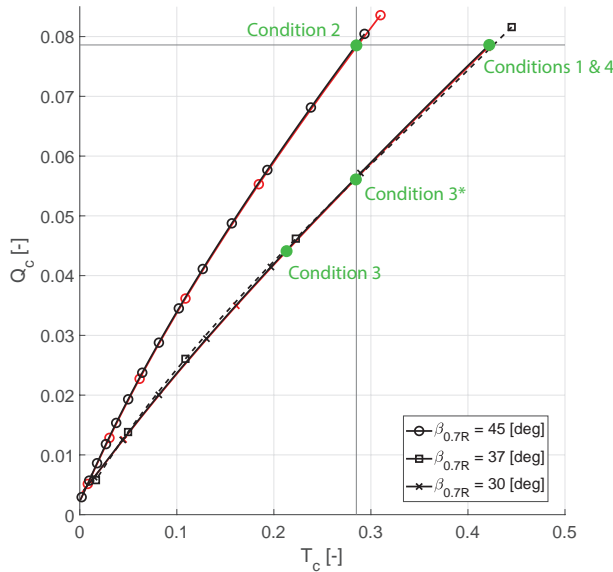
Figure 6.2: Calculated performance curves for the TUD-XPROP-S with six blades (solid) and three blades (dashed). Performance curves are shown for isolated conditions (black) and installed conditions (red). Chosen operating conditions marked in green.

the same $Q_c$, leading to our second condition. We then find the condition for the propeller with $\beta_{0.7R} = 30$ deg that matches this lower $T_c$ to arrive at the third condition. Finally, we add the three-bladed propeller with $\beta_{0.7R} = 37$ deg at $J = 0.717$, which is predicted to produce the same $T_c$ and $Q_c$ as the first condition. This enables us to compare the effect of the same total vorticity concentrated in fewer, stronger tip vortices. Unfortunately, due to an oversight the third condition was performed at $J = 0.984$, rather than $J = 0.904$, during the experiment. This means the thrust coefficients do not match exactly between condition 2 and 3.

Table 6.1: Summary of numerical predictions of propeller performance for operating conditions used in the experiment. Configurations will be referred to by their handle.

| Condition | Handle | $N_b$ [-] | $\beta_{0.7R}$ [deg] | $J$ [-] | $T_c$ [-] | $Q_c$ [-] |
|---|---|---|---|---|---|---|
| 1 | High $T_c$/High $Q_c$ | 6 | 30 | 0.800 | 0.422 | 0.079 |
| 2 | Low $T_c$/High $Q_c$ | 6 | 45 | 1.195 | 0.284 | 0.079 |
| 3* (target) | - | 6 | 30 | 0.904 | 0.284 | 0.056 |
| 3 (actual) | Low $T_c$/Low $Q_c$ | 6 | 30 | 0.984 | 0.210 | 0.044 |
| 4 | Three-bladed | 3 | 37 | 0.717 | 0.284 | 0.079 |

## 6.3. THRUST AND TORQUE COEFFICIENT VERIFICATION

Since the design points are determined from numerical simulation, it is worth verifying that the propeller is operating roughly at the desired condition. To this end, we analyse the measurements of total pressure coefficient $C_{p,t} = \frac{p_t - p_{s,\infty}}{q_\infty}$ in the propeller plane (Fig. 2.13a). Figure 6.3 shows the distributions of $C_{p,t}$ in that plane for the various conditions. The missing parts of the distribution were obscured by the nacelle during the experiment and could therefore not be measured. Since the propeller increases the total pressure of the flow, the slipstream can be defined by $C_{p,t} > 1$. Note the step-like artefacts at the outer border of the slipstream. These are artefacts of interpolation caused by the limited resolution in spanwise direction and the very strong gradient in total pressure at the

**6**



(a) Condition 1: $\beta_{0.7R} = 30\,deg$, $J = 0.8$, $N_b = 6$

(b) Condition 2: $\beta_{0.7R} = 45\,deg$, $J = 1.195$, $N_b = 6$

(c) Condition 3: $\beta_{0.7R} = 30\,deg$, $J = 0.984$, $N_b = 6$

(d) Condition 4: $\beta_{0.7R} = 37\,deg$, $J = 0.717$, $N_b = 3$
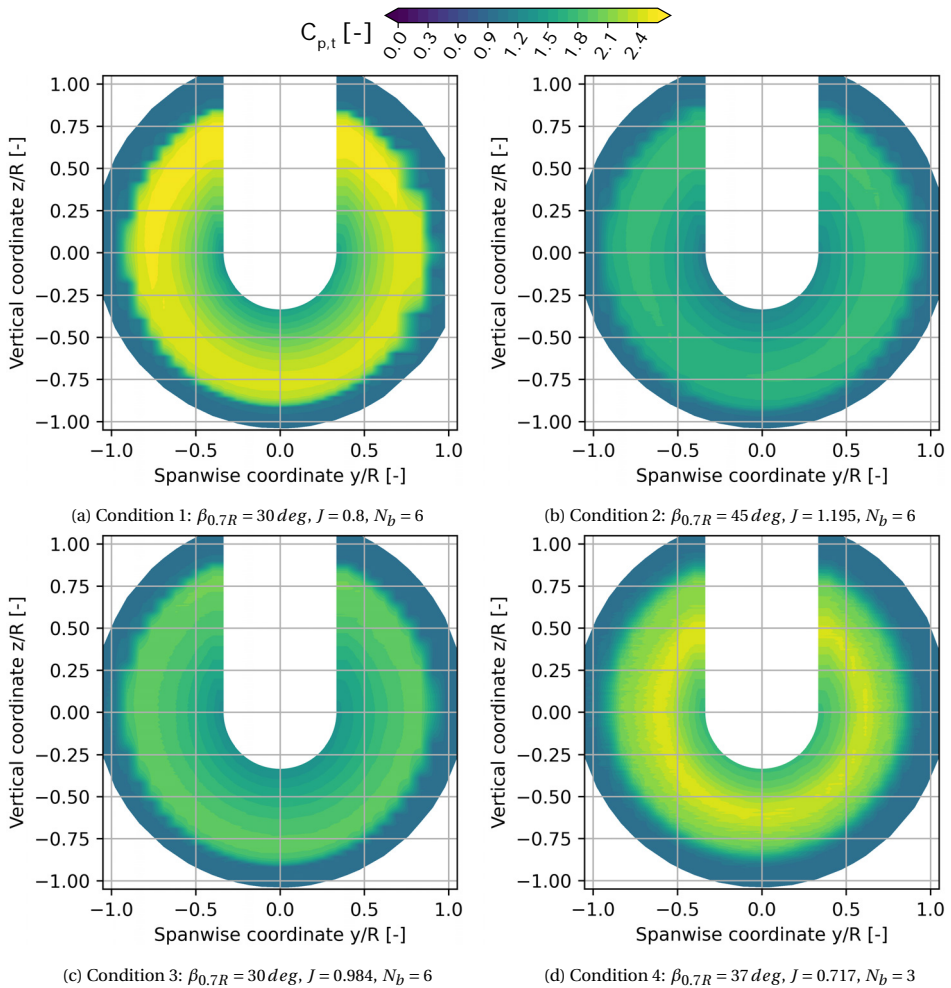
Figure 6.3: Distributions of total pressure coefficient $C_{p,t}$ in the plane behind the propeller. Missing area was obscured by the nacelle.

slipstream edge. This gradient is nearly discontinuous and could not be accurately fitted with typical interpolation methods. [1]

As expected, it shows that the case for $\beta_{0.7R} = 30\,deg$ at $J = 0.8$ gives the highest total pressure coefficients, as it produces the most thrust. The 3-bladed configuration ($\beta_{0.7R} = 37\,deg$ at $J = 0.717$) was designed to produce the same thrust coefficient, however the distribution (Fig. 6.3d) shows much lower values of $C_{p,t}$ and a very different distribution. Particularly at the edge of the slipstream, much less total pressure is added to the flow. This indicates that the tips of the three bladed propellers were separated during operation.

We can integrate the distributions of Fig. 6.3 to calculate an equivalent thrust coefficient $T_C^* = \int \frac{(C_{p,t}-1)}{2D^2}\,dA$, given for each condition in Table 6.2. As a part of the distribution is missing, this value cannot be compared to the design thrust coefficient $T_c$. Nonetheless, it gives an indication of the relative difference in loading between the different propeller conditions, and whether this aligns with the design aim of each condition.

In a similar fashion, we compare the different conditions in terms of swirl in the slipstream to determine whether they operate at comparable torque coefficients. We compare the various cases based on the tangential velocity component induced at $\psi = 270\,deg$ ($y/R = 0$). At this location, the y-component of the velocity vector is exclusively dependent on the local torque and not affected by the wing upwash component. The radial distributions of the y-component of velocity are shown in Fig. 6.4. It shows that Condition 1 ($\beta_{0.7R} = 30\,deg$, $J = 0.8$) and Condition 2 ($\beta_{0.7R} = 45\,deg$, $J = 1.195$) yield very similar tangential velocity distributions. Additionally, Condition 4 ($\beta_{0.7R} = 37\,deg$, $J = 0.717$, $N_b = 3$) induces tangential velocity of comparable order of magnitude and distribution, despite the separation of the blade tips. Assuming the distributions of Fig. 6.4 as representative for the entire disk, we can calculate an equivalent torque coefficient

---

[1]The results in this chapter have all been generated in python with *matplotlib.pyplot.tricontourf.*
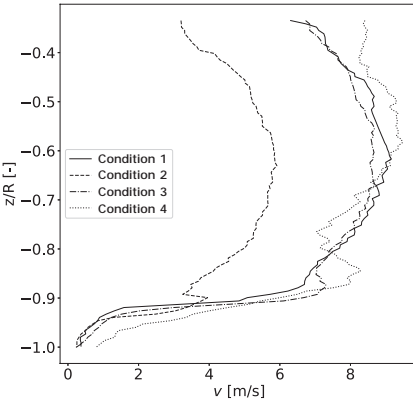


Figure 6.4: Radial distribution of the y-component of velocity at $\psi = 270\,deg$.

Table 6.2: Summary of equivalent thrust and torque coefficients of the tested propeller conditions.

|  | 1 | 2 | 3 | 4 |
|---|---|---|---|---|
| Condition | 1 | 2 | 3 | 4 |
| $N_b$ [-] | 6 | 6 | 6 | 3 |
| $\beta_{0.7R}$ [deg] | 30 | 45 | 30 | 37 |
| $J$ [-] | 0.800 | 1.195 | 0.984 | 0.717 |
| $T_c^*$ [-] | 0.2747 | 0.1781 | 0.1428 | 0.2320 |
| $Q_c^*$ [-] | 0.0724 | 0.0664 | 0.0402 | 0.0749 |
| $T_c^*/Q_c^*$ [-] | 3.79 | 3.00 | 3.55 | 3.10 |

$Q_c^* = \int \int \frac{u \Delta v r^2}{V_\infty^2 D^2} \, dr \, d\psi$ [107]. The equivalent torque and thrust coefficients are reported in Table 6.2.

From Table 6.2 it is clear that conditions 1 and 2 indeed operate at comparable $Q_c$, but different $T_c$. Conditions 3 and 4 do not satisfy their original design points, as condition 3 was operated at the wrong advance ratio and condition 4 suffered blade tip separation that was not predicted. We therefore do not have a direct comparison where only $Q_c$ is varied at constant $T_c$. However, condition 3 happens to operate at a $T_c/Q_c$ ratio that is near to condition 1, meaning the slipstream helix angle is comparable but with a lower total vorticity. Furthermore, the change in $Q_c$ between conditions 2 and 3 is still much larger than the change in $T_c$. This still allows for the analysis of the relative dominance of $T_c$ and $Q_c$ for the slipstream deformation. In fact, in the remainder of this section we will show that thrust coefficient has very little impact on the slipstream deformation, meaning we can still use condition 3 to show the impact of the torque coefficient. Additionally, while condition 4 suffers from separation on the blade tips, it still operates at a $Q_c$ close to condition 1, meaning it can offer an additional comparison for the comparable torque cases.

## 6.4. SLIPSTREAM DEFORMATION IN LOW-LIFT CONFIGURATION

As a result of the propeller-wing aerodynamic interaction, the propeller slipstream deforms from its initial, circular shape. In the low-lift condition, this deformation mostly occurs in the form of a shearing effect of the two halves of the slipstream that pass the wing on each side of the wing, and spanwise elongation near the wing surface. This is shown for each of the propeller conditions in Fig. 6.5 by means of the distributions of $C_{p,t}$ in the wake plane. The effect of the tested propeller conditions on the slipstream deformation is relatively limited in low-lift condition. Figure 6.5 shows that comparable torque coefficients (Figs. 6.5a and 6.5b) result in nearly identical deformation, while varying both torque and thrust coefficient (Fig. 6.5c) results in a clear reduction of the deformation. For the latter condition, the slipstream remains closer to its initial, circular shape, with less elongation of the upper-left and lower-right regions of the slipstream and less inboard movement of the lower-left and upper-right regions. The three-bladed propeller condition (Fig. 6.5d) shows comparable deformation of the slipstream to Figs. 6.5a and 6.5b, with the major difference that the gradient of total pressure coefficient at the edge of the slipstream is much more gradual, due to the blade tip separation.

The difference in deformation is visualized more clearly in Fig. 6.6, which compares the slipstream shape of the high $T_c$/high $Q_c$ condition with the other conditions by use of the contour line for $C_{p,t} = 1.05$. As the slipstream can be identified by the addition of total pressure in the flow, this contour yields the outer boundary and therefore shape of the slipstream. Note that we take $C_{p,t} = 1.05$ instead of $C_{p,t} = 1.00$ to mitigate effects of noise and uncertainty on the pressure measurements and achieve a clear image of the outer border of the slipstream. Since the gradient at this border is very strong, $C_{p,t} = 1.05$ is still an accurate representation of the slipstream edge.

Figure 6.6a shows that the low $T_c$/high $Q_c$ condition has slightly larger regions of pressure loss near the wing surface, while the low $T_c$/low $Q_c$ condition (Fig. 6.6b) particularly has larger pressure loss areas near the slipstream centre. The former will be discussed
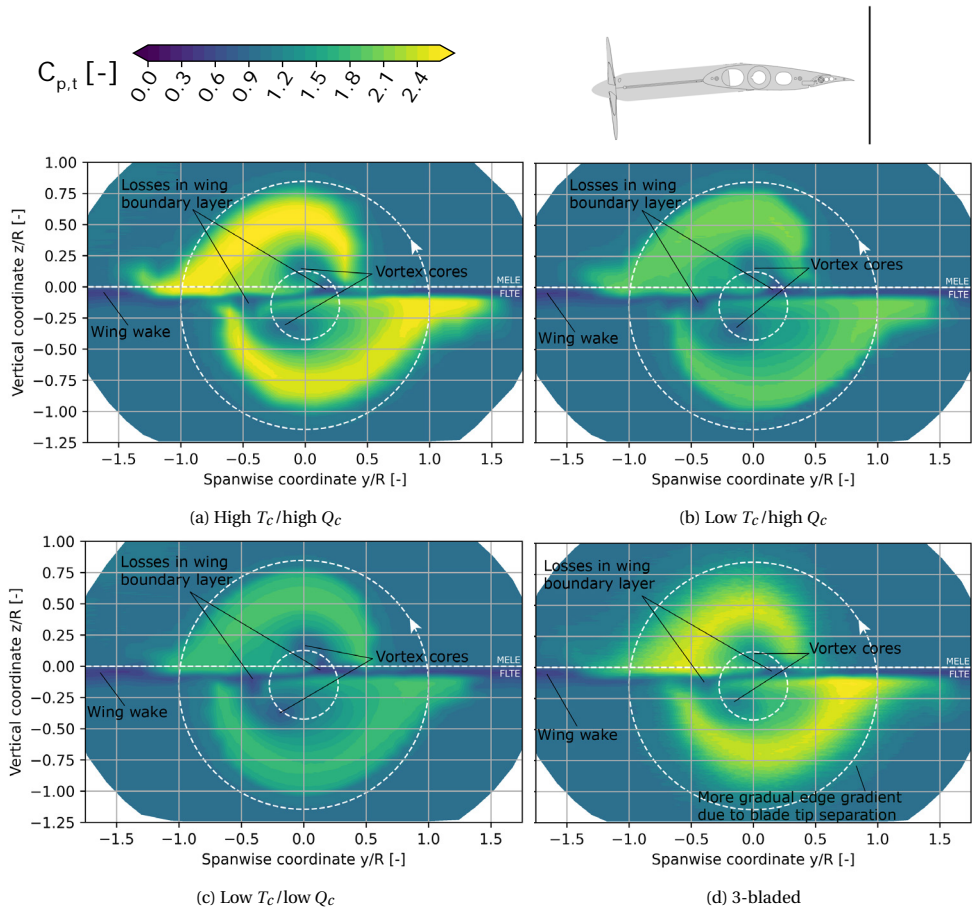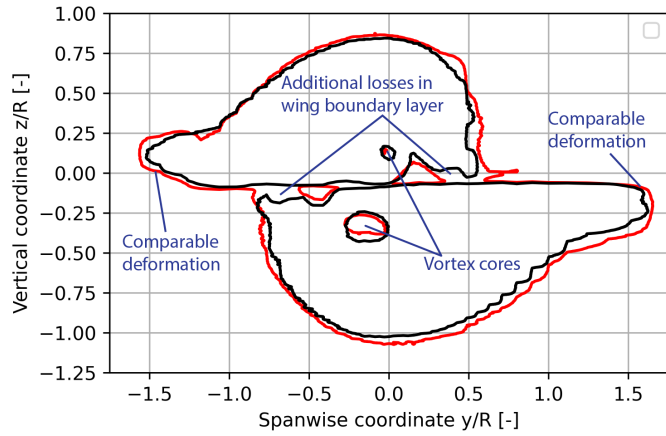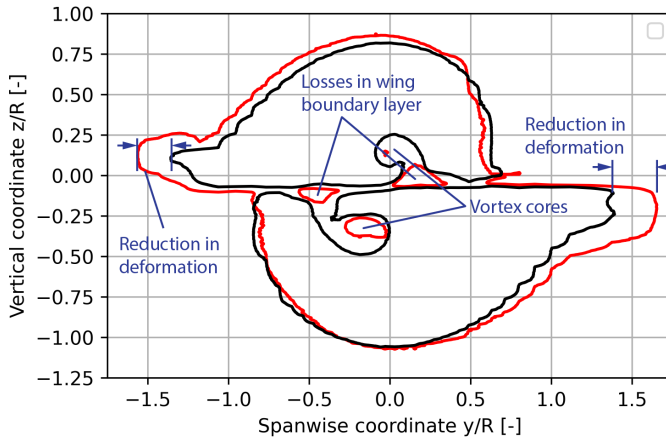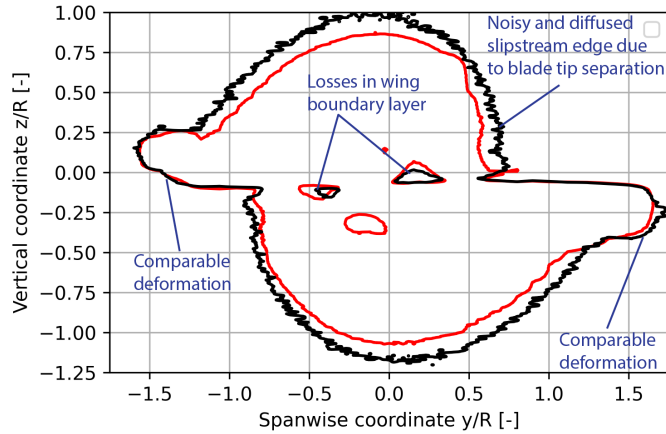
Figure 6.5: Distributions of scaled total pressure coefficient just behind the flap trailing edge for each propeller condition, visualizing the total deformation of the slipstream over the wing. $\alpha = 0$ deg, $\delta_f = 0$ deg. Dashed lines indicate projections of propeller tip and root, and wing leading edge (MELE) and flap trailing edge (FLTE).

in more detail in the treatment of the high-lift configuration in Section 6.5. The latter are associated with vortices as seen from the in-plane velocity vectors shown in Fig. 6.7. Since the low $T_c$/low $Q_c$ condition adds significantly less total pressure coefficient to the slipstream, pressure losses in the viscous cores of these vortices show up more clearly on the contour line of Fig. 6.6b.

As the viscous losses in the wing boundary layer reduce the total pressure coefficient, it is difficult to determine the exact area of the wing that is washed by the slipstream (here-inafter referred to as *washed area*) from the total pressure measurements alone. Figures 6.8 and 6.9 therefore visualize the surface flow (upper and lower surface, respectively) using the oil flow visualization images. It shows the extracted oil flow highlights, over-lapping the high $T_c$/high $Q_c$ condition (in black) with high $T_c$/low $Q_c$ (blue), low $T_c$/low $Q_c$ (red) and the three-bladed propeller (green). It should be noted that the shearlines

(a) High $T_c$/high $Q_c$ (red) versus low $T_c$/high $Q_c$ (black)



(b) High $T_c$/high $Q_c$ (red) versus low $T_c$/low $Q_c$ (black)



(c) Six-bladed (red) versus three-bladed (black)

Figure 6.6: Contour lines of $C_{p,t} = 1.05$ just behind the flap trailing edge, comparing each propeller condition with the high $T_c$/high $Q_c$ baseline, visualizing the total deformation of the slipstream over the wing. $\alpha = 0$ deg, $\delta_f = 0$ deg.
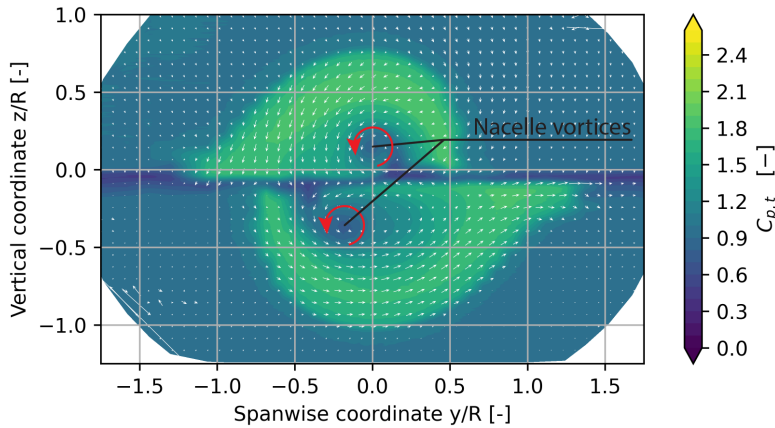
Figure 6.7: Vector plot of the in-plane velocities, overlaid on the distribution of (unscaled) total pressure distribution. Low $T_c$/low $Q_c$ condition, $\alpha = 0$ deg, $\delta_f = 0$ deg.

visualized by the oil flow are not direct streamlines and are affected by many factors such as gravity and oil thickness. Slight changes in the oil lines are therefore not always directly analogous to changes in flow condition, and require careful interpretation.

Similar to the overall slipstream deformation, the surface flow is nearly identical for comparable $Q_c$. Figure 6.8a shows a small spanwise shift in the flow structure on the upper surface trailing edge. For low $T_c$/low $Q_c$, the oil flow lines near the slipstream edge clearly show less spanwise convection compared to the baseline (see Fig. 6.8b and 6.9b). The difference is largest at the locations where the blade moves towards the wing surface (i.e., the upgoing blade side on the lower surface, and the downgoing blade side on the upper surface). Additionally, the region behind the nacelle in Fig. 6.9b shows less spanwise shift for the low $T_c$/low $Q_c$ condition, indicating a smaller crossflow component. The three-bladed case surface flow patterns are nearly identical to the six-bladed baseline, with some deviations at the outer boundaries of the slipstream. Again, this can be attributed to the outer edge of the slipstream being diffused due to the separation on the blade tips. The significant shift in the separation bubble in Fig. 6.9c is best explained by the turbulence around the slipstream edge resulting from the blade tip separation, as the shear lines in the oil flow otherwise indicate no significant shift in slipstream edge trajectory. For all conditions, however, the exact slipstream edge is difficult to identify and on the upgoing blade side of the upper surface, no clear flow structures can be compared.

In an attempt to clearly identify the slipstream edge and quantify the change in deformation, we used both the thermography measurements and the oil flow image extracts to determine the edges of the washed area for the various conditions. The results are shown in Fig. 6.10a for the upper surface and Fig. 6.10b for the lower surface. Figure 2.15 in Section 2.1.2 showed how these images are constructed. Note that the slipstream edge in Fig. 6.10b is only traced up to the main element cove area, as it was not possible to accurately estimate the position of the slipstream edge beyond that. Furthermore, the three-bladed propeller condition is not included, since the blade tip separation diffuses the slipstream edge and can have unexpected impact on the transition of the
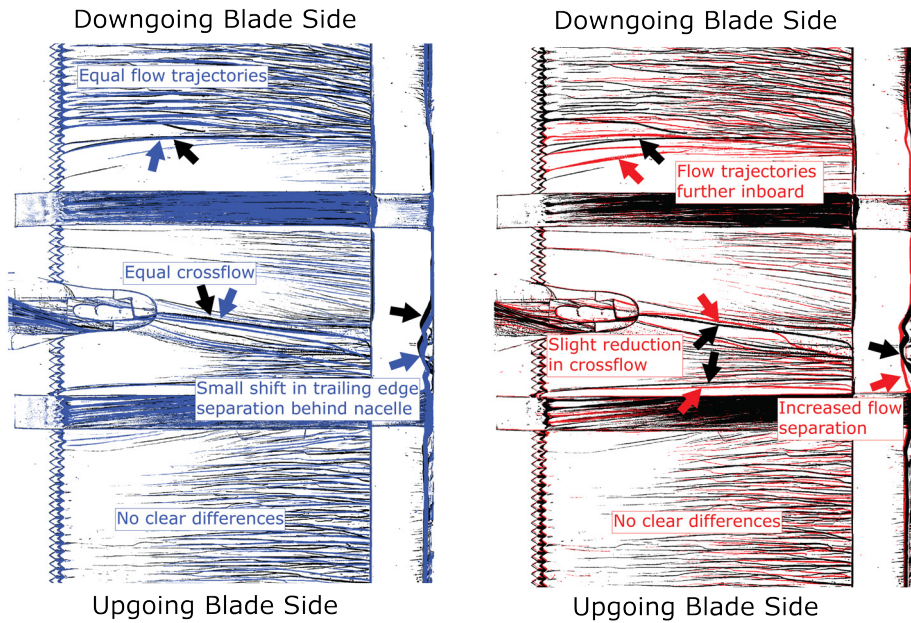
(a) High $T_c$/high $Q_c$ (black) versus low $T_c$/high $Q_c$ (blue)



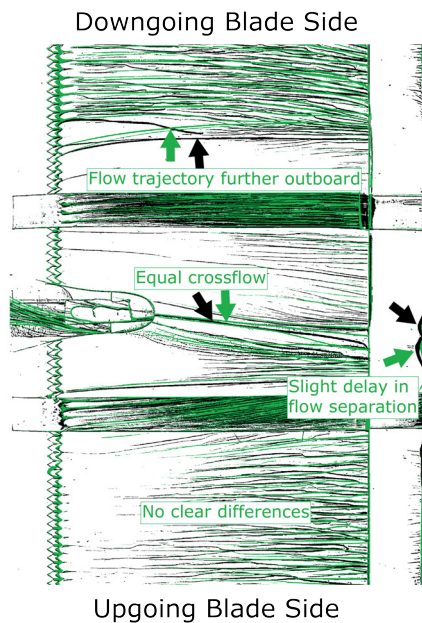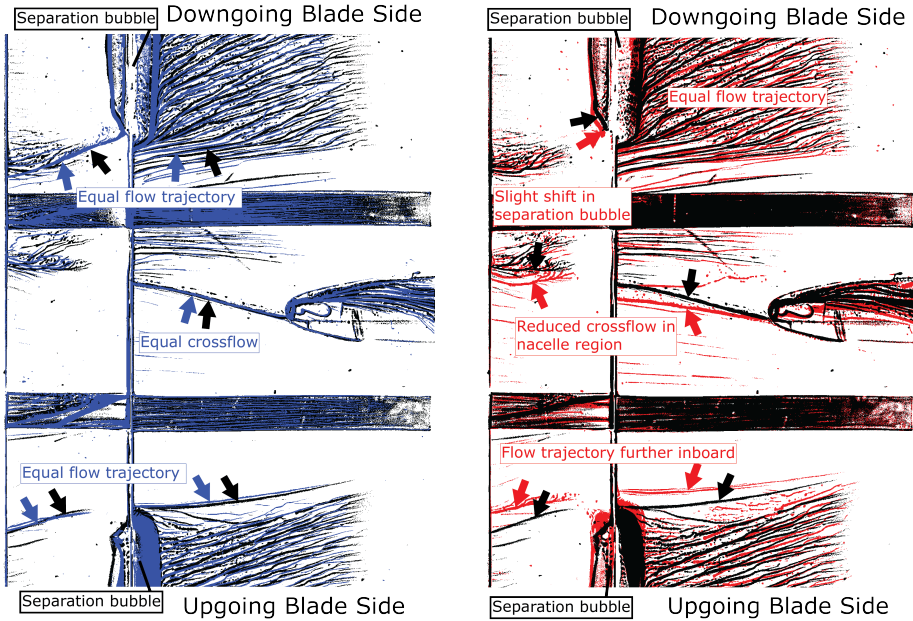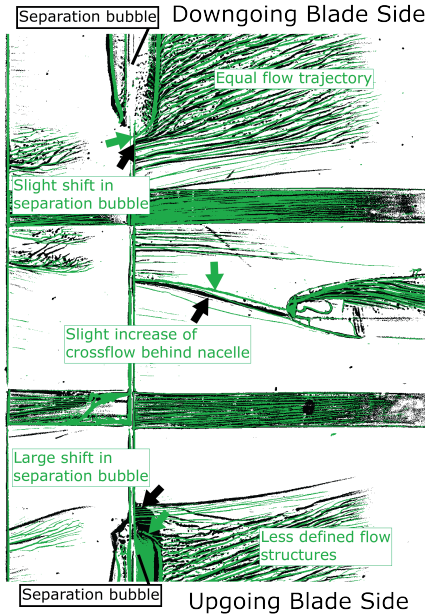(b) High $T_c$/high $Q_c$ (black) versus low $T_c$/low $Q_c$ (red)



(c) High $T_c$/high $Q_c$ (black) versus three-bladed (green) propeller

Figure 6.8: Overlays of (zoomed in) oil flow images, filtered for highest intensity features, comparing the flow on the wing upper surface for high $T_c$/high $Q_c$ with each of the other propeller conditions. $\alpha = 0$ deg, $\delta_f = 0$ deg. Freestream direction from left to right.

(a) High $T_c$/high $Q_c$ (black) versus low $T_c$/high $Q_c$ (blue)

(b) High $T_c$/high $Q_c$ (black) versus low $T_c$/low $Q_c$ (red)

(c) High $T_c$/high $Q_c$ (black) versus three-bladed (green) propeller

Figure 6.9: Overlays of (zoomed in) oil flow images, filtered for highest intensity features, comparing the flow on the wing lower surface for high $T_c$/high $Q_c$ with each of the other propeller conditions. $\alpha = 0$ deg, $\delta_f = 0$ deg. Freestream direction from right to left.

(a) Upper Surface. Freestream from left to right.



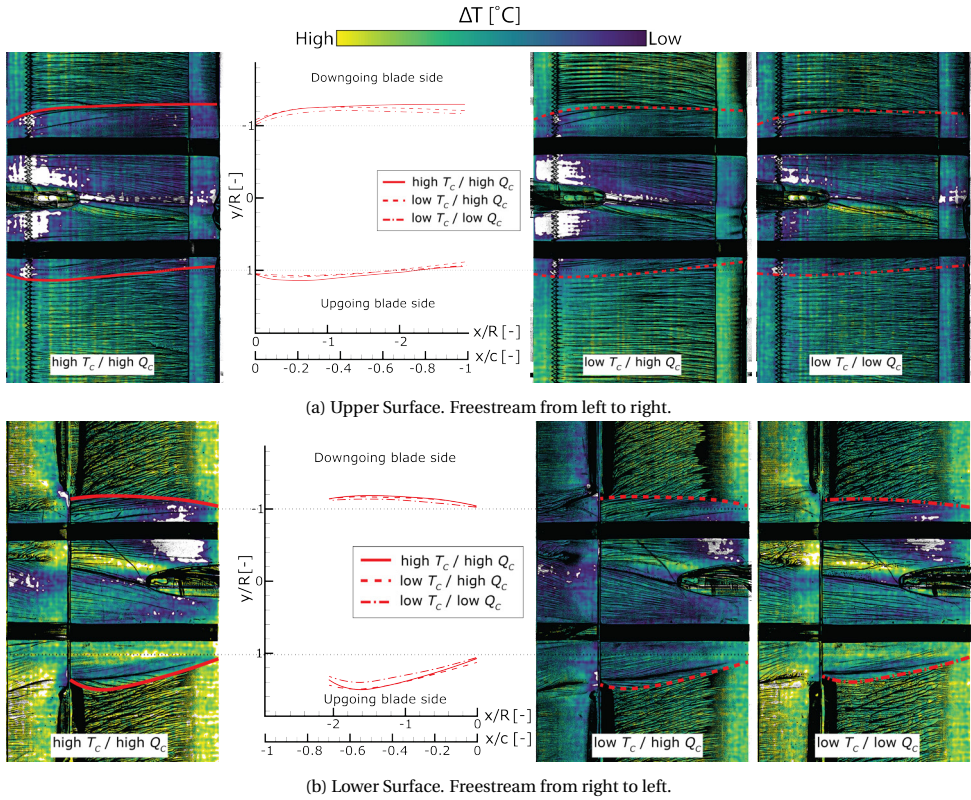(b) Lower Surface. Freestream from right to left.

Figure 6.10: Comparisons of the paths of the slipstream on the wing surface for the various propeller conditions, estimated from thermography and oil flow images. $\alpha = 0$ deg, $\delta_f = 0$. Colour gradients represent local change in temperature.

wing boundary layer, on which the thermography is strongly dependent.

Figure 6.10 clearly visualizes that the change in deformation is largest on the upper surface downgoing blade side and the lower surface upgoing blade side. The maximum difference in spanwise displacement between the high $T_c$/high $Q_c$, and the low $T_c$/low $Q_c$ case is $0.1R$ on the lower surface upgoing blade side, which is roughly 20% of the total displacement of the high $T_c$/high $Q_c$ case. On the upper surface downgoing blade side the difference between the high $T_c$/high $Q_c$ and the low $T_c$/low $Q_c$ is again around $0.1R$, roughly 40% of the total displacement for the high $T_c$/high $Q_c$ case at that edge. The change in displacement is thus equivalent in both cases, but is significantly more impactful on the upper surface. It should be noted that these values are extracted from qualitative measurements and are therefore subject to some uncertainty, but they do show a coherent trend where the washed area of the wing is significantly affected by the propeller condition.

Between $T_c$ and $Q_c$, the torque coefficient is dominant for the slipstream deformation, where a lower torque coefficient results in less spanwise displacement of the slipstream

edge on the wing surface and less redistribution of the total pressure in the slipstream from its initial, circular shape. In Fig. 6.10, the conditions with comparable $Q_c$ show nearly the same trajectory of the slipstream edge regardless of $T_c$ setting. From the mechanisms proposed by Felli [33] (see Chapter 5), it could be expected that a significant change in $T_c$ would particularly affect the leading edge deformation, as the azimuthal vorticity will directly impact the vortex imaging effect. Figure 6.10 only shows small changes at the wing leading edge for the different loading conditions, however. This may be explained by the change in spanwise pressure gradients at the leading edge, imposed by the change in thrust coefficient, opposing the vortex imaging effects. Unfortunately, we cannot definitively draw this conclusion, as the current experiment does not yield enough data in this region and the quantification of the slipstream path has some uncertainty. Although the thermography does visualize the slipstream path near the leading edge fairly well (particularly on the upper surface), it is insufficient to investigate the relative contributions of the vortex image and spanwise pressure gradient effects to the total deformation. Time-accurate (or phase-accurate) measurements or simulations that resolve the tip vortices near the leading edge will prove crucial in further investigating the relative balance between these effects.

## 6.5. SLIPSTREAM DEFORMATION IN HIGH-LIFT CONFIGURATION

In the high-lift configuration, the impact of the propeller condition on the slipstream deformation is much more significant than in the low-lift configuration. Figure 6.11 shows the distribution of total pressure coefficient just behind the flap trailing edge for the various propeller conditions, while Fig. 6.12 again visualizes the slipstream shape by means of the $C_{p,t} = 1.05$ contour lines. Overall, the conditions with comparable $Q_c$ (Figs. 6.11a and 6.11b) again show comparable deformation (visualized well in Fig. 6.12a), but with a clear deviation on the upgoing blade side of the upper slipstream part. There is an apparent gap in the slipstream of the low $T_c$/high $Q_c$ condition (Fig. 6.12a), which also occurs in the low $T_c$/low $Q_c$ condition (Fig. 6.12b). Figures 6.11b and 6.11c show regions of low total pressure coefficient here. These are secondary vortex structures, as illustrated by the in-plane velocity vectors for the low $T_c$/low $Q_c$ condition in Fig. 6.13. Furthermore, the low $T_c$/low $Q_c$ condition has significantly more pressure losses inside the slipstream, as evident from Fig. 6.12b. These phenomena will be discussed further at a later stage in this section.

Beyond the differences in the distribution of total pressure for the internal parts of the slipstream, the differences in slipstream deformation follow the same patterns as in the low-lift conditions. The low $T_c$/high $Q_c$ condition (Fig. 6.12a) is largely comparable to the baseline, while the low $T_c$/low $Q_c$ condition (Fig. 6.12b) has significantly less deformation on both the upgoing and downgoing blade sides. The low $T_c$/high $Q_c$ condition does show a reduction in slipstream deformation on the upgoing blade side of the lower part of the slipstream (see Fig. 6.12a). From the measurements it is not entirely clear whether this is a reduction in slipstream deformation or just a result of dissipation of the total pressure at the slipstream edge. The oil flow visualizations (discussed below) do not show a clear deviation in slipstream deformation, however. The three-bladed propeller condition (Fig. 6.12c), finally, shows comparable deformation compared to the high $T_c$/high $Q_c$ baseline, but with a more diffuse boundary. A region of lower total pressure seems to be present
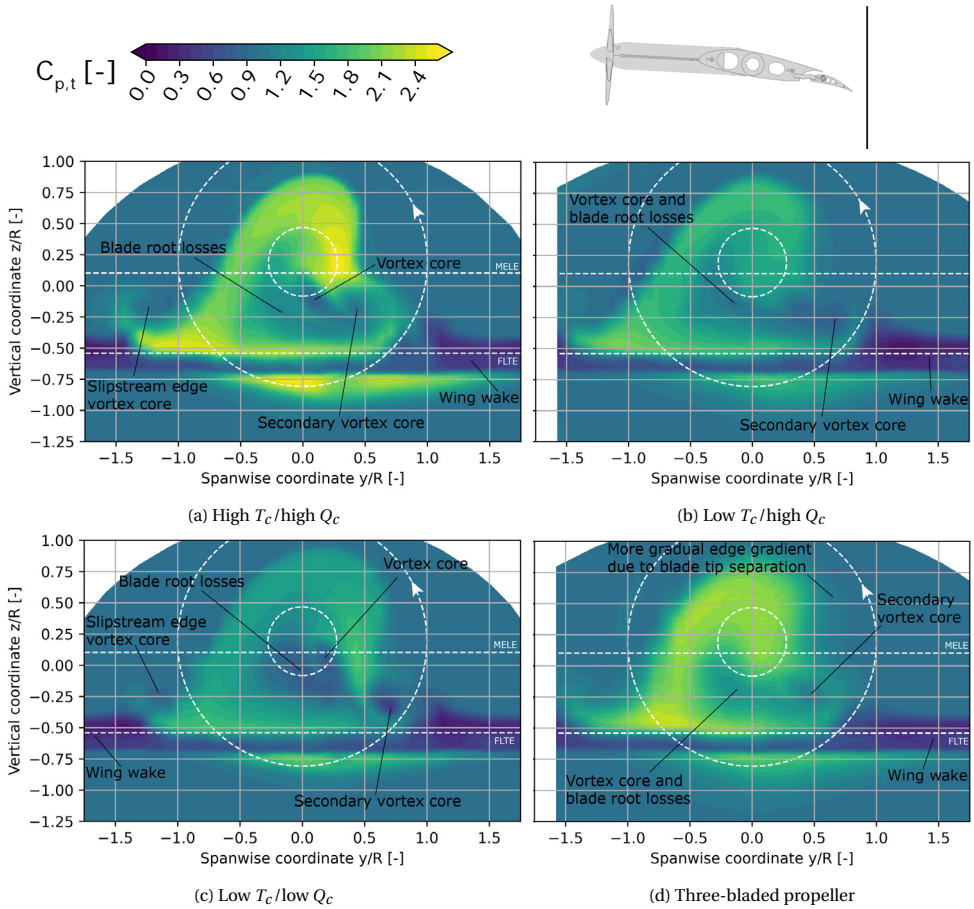
Figure 6.11: Distributions of total pressure coefficient just behind the flap trailing edge for each propeller condition, visualizing the total deformation of the slipstream over the wing. $\alpha = 8$ deg, $\delta_f = 15$ deg. Dashed lines indicate projections of propeller tip and root, and wing leading edge (MELE) and flap trailing edge (FLTE).

here like for the low $T_c$/high $Q_c$ and low $T_c$/low $Q_c$ conditions, but it does not show in the contour line of Fig. 6.12c. This can likely be attributed to the diffuse slipstream boundary resulting from the separation on the blade tips.

In general, the comparisons of shear lines extracted from the oil flow visualizations (Figs. 6.14 and 6.15) show similar results to the low-lift configuration, albeit with much more emphasized deviations. The low $T_c$/high $Q_c$ condition is nearly identical to the baseline on the upper surface (Fig. 6.14a), with small deviations developing towards the aft section of the main element on the downgoing blade side. These deviations can also be seen in the contour line comparison of Fig. 6.12a, which reveals these deviations to be only local. The flow trajectories on the upgoing blade side of the lower surface (Fig. 6.15a) show a more significant change in deformation, which we are unable to explain based on current data. Apart from the extension on the lower surface upgoing blade side, however,
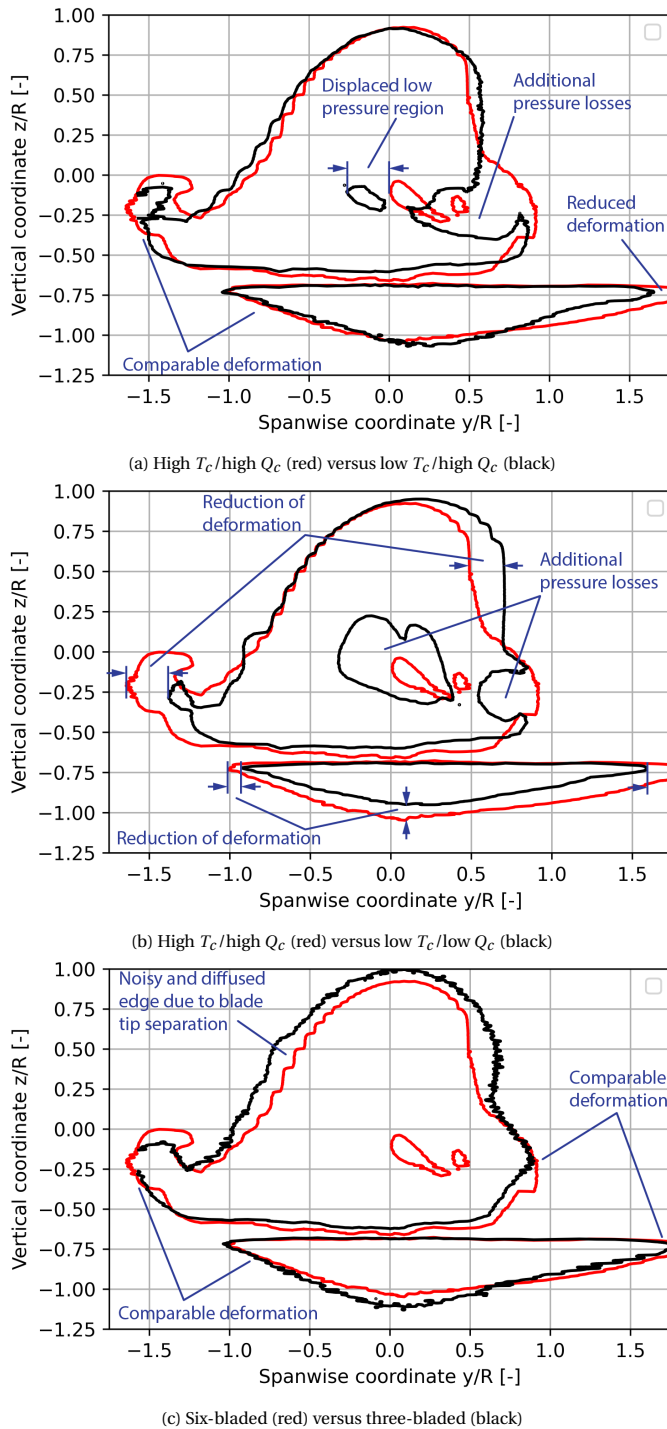
(a) High $T_c$/high $Q_c$ (red) versus low $T_c$/high $Q_c$ (black)

(b) High $T_c$/high $Q_c$ (red) versus low $T_c$/low $Q_c$ (black)

(c) Six-bladed (red) versus three-bladed (black)

Figure 6.12: Contour lines of $C_{p,t} = 1.05$ just behind the flap trailing edge, comparing each propeller condition with the high $T_c$/high $Q_c$ baseline, visualizing the total deformation of the slipstream over the wing. $\alpha = 8$ deg, $\delta_f = 15$ deg.
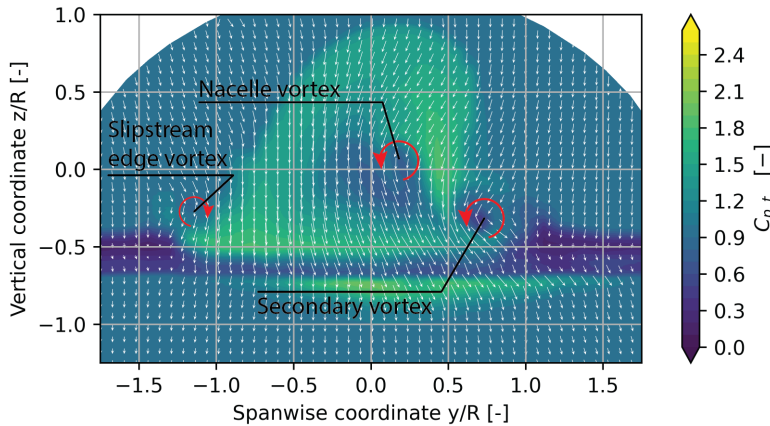
Figure 6.13: Vector plot of the in-plane velocities, overlaid on the distribution of (unscaled) total pressure distribution. Low $T_c$/low $Q_c$ condition, $\alpha = 8$ deg, $\delta_f = 15$ deg.

the slipstream shape is still highly comparable to the high $T_c$/high $Q_c$ condition. The low $T_c$/low $Q_c$ condition (Fig. 6.14b) shows less outboard displacement at the edges and less crossflow behind the nacelle. The three-bladed condition (Figs. 6.14c) again yields nearly identical flow trajectories on the upper surface, with more diffuse outer boundaries and some small differences in crossflow trajectories behind the nacelle.

On the lower surface, all conditions show nearly identical flow trajectories behind the nacelle. The trajectories are almost fully aligned in chordwise direction, indicating little to no crossflow. In the high-lift configuration, very little of the slipstream passes the lower surface, as the freestream and wing upwash convect most of the slipstream over the upper surface. As a result, the nacelle-root vortex on the lower surface is very weak and there is little locally induced crossflow. This is strongly dependent on the configuration and particularly prominent for the wing model used in this experiment, due to the relatively large distance between the propeller and wing leading edge.

As with the low-lift configuration, quantifying the slipstream edge trajectory from the oil flow images alone is difficult and prone to error. Figure 6.16 therefore shows the overlays of thermography and oil flow highlights to improve the estimation of the slipstream edge.[2] The majority of the change in deformation again occurs on the upper surface downgoing blade side and lower surface upgoing blade side. The low $T_c$/low $Q_c$ condition shows less spanwise displacement than the other conditions, with a reduction of roughly $0.15R$ on each of the aforementioned edges. The high $T_c$/high $Q_c$ and low $T_c$/high $Q_c$ conditions result in very comparable slipstream paths, again suggesting that torque coefficient (or longitudinal vorticity in the slipstream) is the dominant parameter for slipstream deformation. Even near the leading edge, the trajectories are nearly equal, indicating that even the leading edge expansion of the slipstream is hardly affected by $T_c$ (or, rather, azimuthal vorticity in the slipstream).

---

[2]Note that for the upper surface at low $T_c$/high $Q_c$ condition, only the oil flow image is shown, as there was no thermography measurement available.

(a) High $T_c$/high $Q_c$ (black) versus low $T_c$/high $Q_c$ (blue)

(b) High $T_c$/high $Q_c$ (black) versus low $T_c$/low $Q_c$ (red)



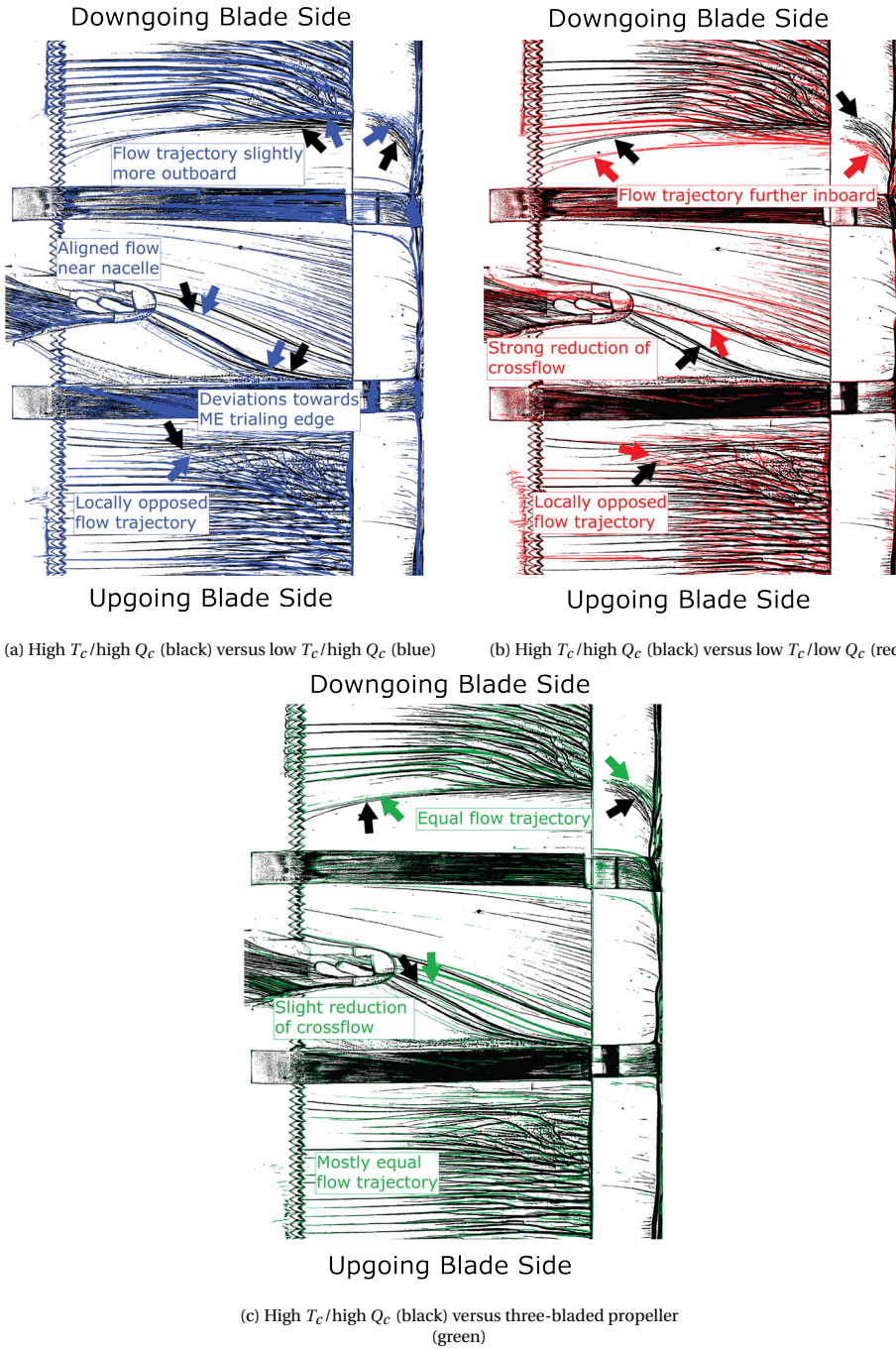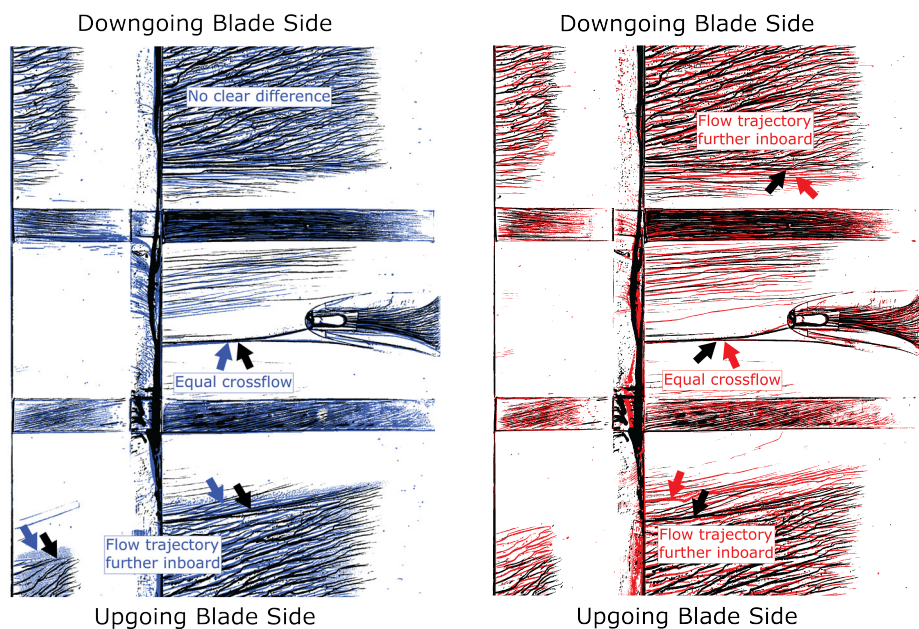(c) High $T_c$/high $Q_c$ (black) versus three-bladed propeller (green)

Figure 6.14: Overlays of (zoomed in) oil flow images, filtered for highest intensity features, comparing the flow on the wing upper surface for high $T_c$/high $Q_c$ with each of the other propeller conditions. $\alpha = 8$ deg, $\delta_f = 15$ deg. Freestream direction from left to right.

(a) High $T_c$/high $Q_c$ (black) versus low $T_c$/high $Q_c$ (blue),

(b) High $T_c$/high $Q_c$ (black) versus low $T_c$/low $Q_c$ (red),

(c) High $T_c$/high $Q_c$, (black) versus three-bladed prop (green)

Figure 6.15: Overlays of (zoomed in) oil flow images, filtered for highest intensity features, comparing the flow on the wing lower surface for high $T_c$/high $Q_c$ with each of the other propeller conditions. $\alpha = 8$ deg, $\delta_f = 15$ deg. Freestream direction from right to left.

(a) Wing upper surface. Oil flow image only. Freestream left to right.



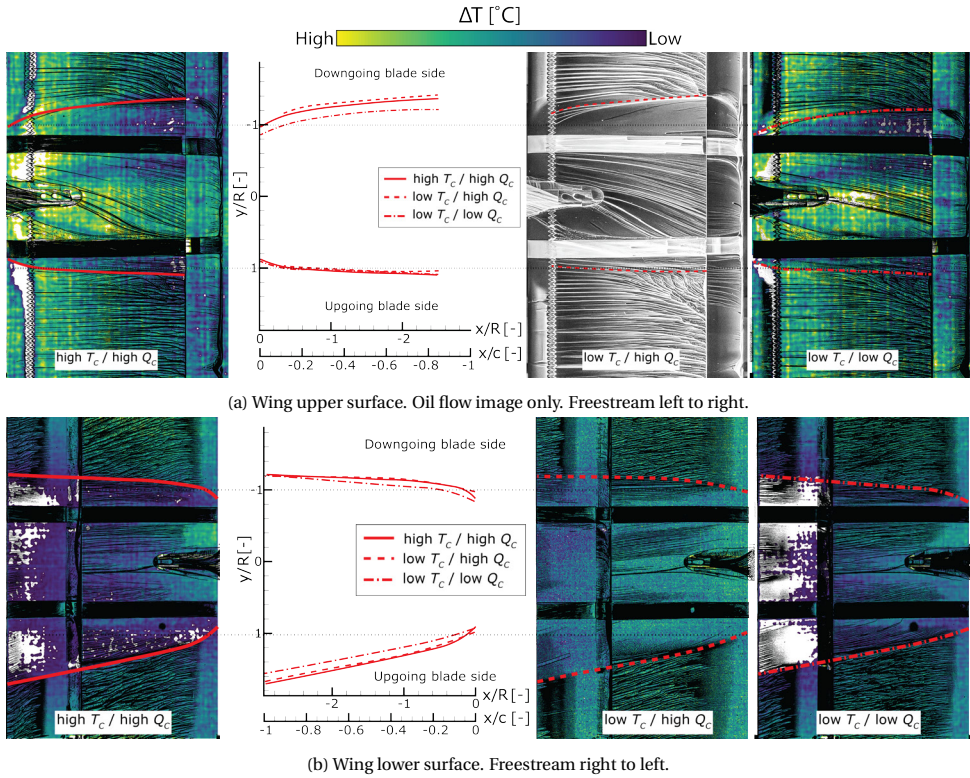(b) Wing lower surface. Freestream right to left.

Figure 6.16: Comparisons of the paths of the slipstream on the wing surface for the various propeller conditions, estimated from thermography and oil flow images. $\alpha = 8$ deg, $\delta_f = 15$ deg. Colour gradients represent local change in temperature.

To further investigate the changes to the internal distribution of total pressure in the slipstream, we combine the various measurement planes of the pressure probe in Fig. 6.17. It visualizes the development of the various regions of pressure losses. For the high $T_c$/high $Q_c$ condition (Fig. 6.17a), the regions of total pressure loss are concentrated around a set of vortices. From the LBM simulations of the same configuration (see Chapter 5), we know that the central region of total pressure losses is a combination of the viscous core of a nacelle vortex and separation on the blade root at the upgoing blade side. The latter occurs due to the angle of inflow into the propeller, resulting from both geometric angle with respect to the freestream and the upwash induced by the wing circulation [31, 85, 53]. The separated blade root wakes wrap around the rolled up nacelle vortex. This is consistent with the internal distribution of total pressure coefficient in Fig. 6.17a.

However, as identified earlier in this section, the various conditions show very different internal distributions of total pressure coefficient. The low $T_c$/high $Q_c$ condition (Fig. 6.17b) shows no clear vortex cores, despite its similarity in deformation to the high $T_c$/high $Q_c$ condition. Rather, it shows a wide region of lower pressure in the slipstream that stretches along the wing surface. It also lacks the concentration of total pressure at the upgoing blade side that is present in the high $T_c$/high $Q_c$ condition. The low $T_c$/low

$Q_c$ condition (Fig. 6.17c) yields a total pressure distribution is more comparable to the high $T_c$/high $Q_c$ condition (Fig. 6.17a) than to the low $T_c$/high $Q_c$ condition (Fig. 6.17c), while the deformation of the slipstream is much reduced. There is a clear central pressure loss region that originates directly from the nacelle region, and a secondary region of total pressure loss, indicating a secondary vortex core, which seems to originate from the wing boundary layer or the nacelle junction. The region of pressure loss around the nacelle vortex, which we attributed to separation on the upgoing side blade root, is much increased, however.

The inconsistencies of the internal slipstream distribution between the three conditions, and its connection to separation on the upgoing side blade root, leads us to conclude that it is not directly related to the values of $T_c$ and $Q_c$, but rather to advance



(a) High $T_c$/high $Q_c$
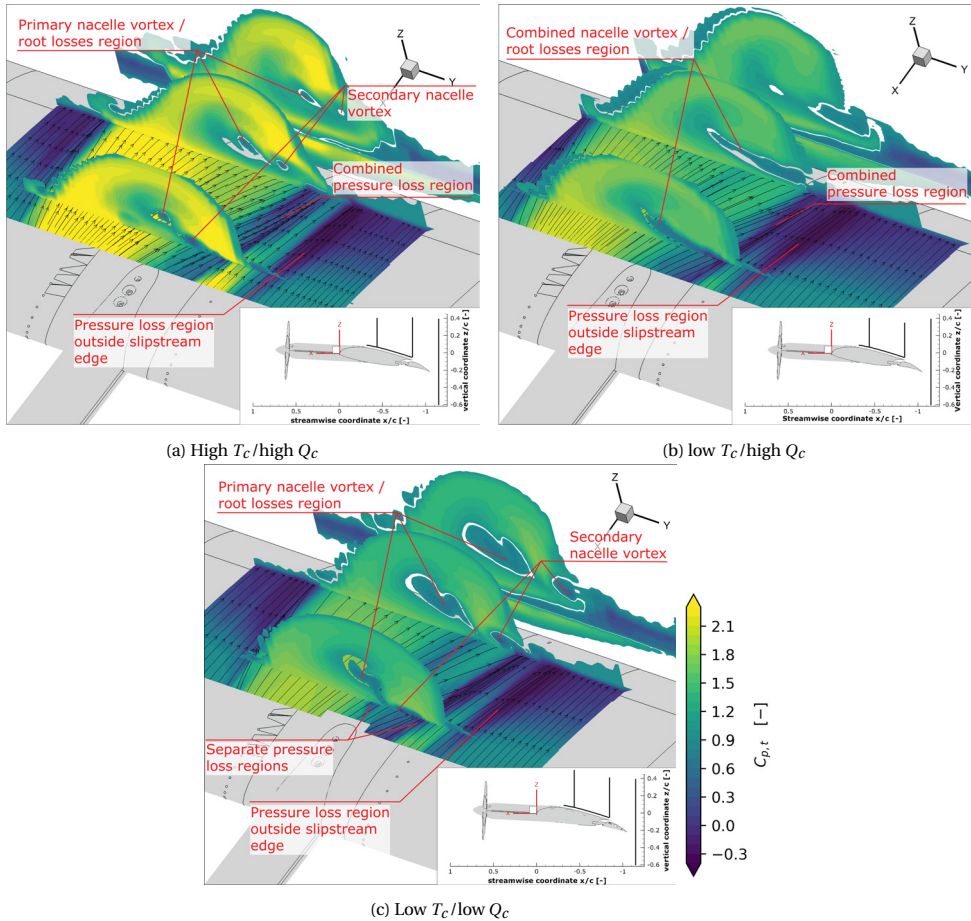
(b) low $T_c$/high $Q_c$

(c) Low $T_c$/low $Q_c$

Figure 6.17: Contours of total pressure coefficient at various chordwise slices, together with the plane at $4\,mm$ from the surface, showing the development of the nacelle vortex and pressure loss regions inside the slipstream. $\alpha = 8$ deg, $\delta_f = 15$ deg.

ratio. The low $T_c$/low $Q_c$ condition operates at a much higher advance ratio than the high $T_c$/high $Q_c$ condition, and the low $T_c$/high $Q_c$ condition at a higher advance ratio still (see Table 6.1). This means that the non-axial component of inflow imposed on the propeller due to the high-lift condition and angle of attack with respect to the freestream, is higher relative to the rotational speed of the propeller. This will induce more separation on the blade root than a lower advance ratio condition, but has limited impact on torque and thrust coefficient since it only involves the blade root, where the loading is relatively small. The manner in which the blade root wakes distribute around the slipstream and the wing is highly dependent on the nacelle vortex however, which is dependent on $T_c$ and $Q_c$. This results in different internal distributions for each of the tested conditions.

Figure 6.17 also shows that the various conditions yield different regions of total pressure loss on the wing surface, within the boundaries of the slipstream. These regions are not to be confused with the boundary layer thickening that occurs just outside the slipstream, which leads to local separation at high angles of attack (see Chapter 5). The different areas are more clearly shown in Fig. 6.18, which combines the pressure measurements near the wing surface with the oil flow images. Note that the pressure measurements are positioned at $4\,mm$ from the wing surface, and not all streamlines match exactly with the oil flow visualization. The conditions with high $Q_c$ show a single region of total pressure loss on the upgoing blade side within the wing washed area. In the high $T_c$/high $Q_c$ condition (Fig. 6.18a), this region is separated from the thick wing boundary layer outside the slipstream by a small portion of higher total pressure slipstream flow. In case of the low $T_c$/high $Q_c$ condition (Fig. 6.18b), this region merges with the wing boundary layer outside the slipstream near the main element trailing edge. For the low $T_c$/low $Q_c$ condition (Fig. 6.18c), however, two distinct regions of pressure loss can be identified within the washed area. This likely indicates that for the high $Q_c$ conditions, these two regions have combined due to the higher crossflow component on the wing surface behind the nacelle.

Oil flow visualizations in Chapter 5 showed that near maximum lift, the region of pressure loss within the washed area can cause local separation and even merge with flow separation zones outside the slipstream. Figure 6.18 clearly shows that the regions of pressure losses originate from the nacelle region. For the low $T_c$/low $Q_c$ condition (Fig. 6.18c), the two regions can be traced to the nacelle-wing junction on either side of the nacelle. At these junctions, separation bubbles can occur as the rapidly accelerating flow around the leading edge meets the flow passing along the nacelle (see Chapter 5 and the results by van Arnhem [53]). These bubbles are strongest at the upgoing blade side, where the acceleration around the leading edge is largest as a result of the increased angle of attack induced by the local tangential velocities in the slipstream. This may be directly related to the observed pressure regions, of which the region originating from the upgoing blade side junction has most significant total pressure losses, as well as the secondary vortex observed in Fig. 6.17c. The nacelle integration clearly has an important role in the propeller-wing interaction in high-lift configurations.
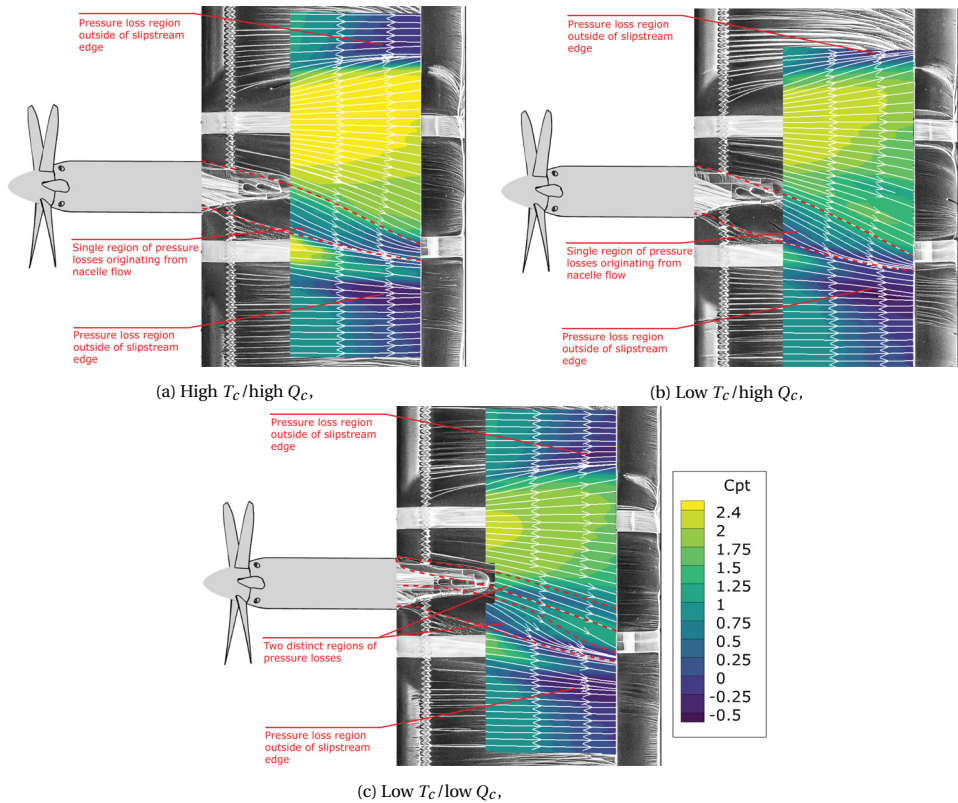
(a) High $T_c$/high $Q_c$,



(b) Low $T_c$/high $Q_c$,



(c) Low $T_c$/low $Q_c$,

Figure 6.18: Contours of total pressure coefficient at $4\,mm$ from the surface, on top of oil flow visualization on the wing surface, showing the origin of pressure loss regions inside the slipstream. $\alpha = 8$ deg, $\delta_f = 15$ deg.

## 6.6. KEY FINDINGS

In this chapter, we have shown how the deformation of the slipstream due to wing interaction is related to the characteristics of the helical vortex system, directly related to the thrust and torque coefficients of the propeller, leading to the following conclusions:

- Torque coefficient, or longitudinal vorticity in the slipstream, is the dominant parameter for the slipstream deformation.

- A lower torque coefficient leads to significantly lower crossflow components on the wing surface directly behind the nacelle, and also results in less spanwise displacement of the slipstream edge on the wing surface.

- Thrust coefficient, or azimuthal vorticity in the slipstream, has negligible impact on the deformation of the slipstream.

- The impact of propeller condition on the slipstream deformation and development is much larger in high-lift configuration than in low-lift configuration. Whereas in low-lift the propeller condition mostly impacts the displacement near the wing

surface, in high-lift it affects both the internal distribution of total pressure and the slipstream shape further away from the wing surface.

- The nacelle integration has a major impact on the internal distribution of total pressure in the slipstream, as well as on local pressure loss regions on the wing surface.

Further research is required to understand the deformation of the slipstream at the leading edge in high-lift configuration, which seems to be dominating the downstream development. The data obtained in this region during the experiments in this dissertation are limited. This will likely require instantaneous flow measurements that can identify the individual tip vortices, or high-fidelity numerical simulations.

**6**

# 7

# SLIPSTREAM DEFORMATION IN DISTRIBUTED PROPELLER CONFIGURATION

*In Chapters 5 and 6 we have defined the main aerodynamic phenomena of propeller-wing-flap interaction and described by which aerodynamic mechanisms they occur. The deformation of the slipstream has been a central theme in the interaction and it is extensive and complex, particularly in high lift conditions. As established in Chapter 1, the additional propellers in a distributed propeller configuration add new interaction modes to the system due to interactions between propellers and their slipstreams. The extent of slipstream deformation we have seen so far in single propeller configurations leave no room for adjacent slipstreams without interaction between them. In this chapter, we explore the differences in the slipstream deformation between a propeller-wing configuration (flap deflections are not included) with a single propeller compared to a distributed propeller system, based on wake rake measurements of total pressure. This is done in Section 7.1. Section 7.2 further explores slipstream deformation in the distributed propeller configuration, by showing the impact of synchrophasing between propellers on the resulting slipstream deformation. The contents of this chapter are based on the first and third experiment described in Chapter 2.*

---

A version of this chapter has been published in Ref. [58].

## 7.1. Single vs Multi-propeller slipstream

The deformation of the slipstream after interaction with the wing is, particularly in high-lift conditions, not symmetric and extends in spanwise direction far beyond the radius of the propeller. Consequently, the slipstreams of additional propellers in a distributed propeller configuration will, depending on their spacing along the wing, have to interact. This section explores how the slipstream deformation is affected by the presence of additional propellers, based on experimental measurements of total pressure coefficient in the wake of a propeller-wing-flap model. The measurements highlight four primary differences: a reduction in slipstream deformation behind the central propeller, a shift in the nacelle vortex position, suppression of slipstream induced separation, and clear dependency of deformation on the position of the propeller in the array.

Figure 7.1 shows the total pressure coefficient $C_{p,t}$ in the wake for both the single propeller (left) and distributed propeller (right) configurations at various angles of attack. The maximum concentrations of $C_{p,t}$ in Fig. 7.1 are slightly higher in the distributed propeller configuration compared to the single propeller, but do not constitute a superposition of each propeller's contribution. Instead, the $C_{p,t}$ distribution remains more uniformly distributed and closer to its initial circular shape. At higher angles of attack (Figs. 7.1c through 7.1f), the reduction of slipstream deformation is even more pronounced. Particularly the upper half of the slipstream is much less concentrated on the downgoing blade side and the $C_{p,t}$ contours are overall more uniformly distributed.

Pressure distributions on the wing suggest that the wing itself is also more uniformly immersed in the slipstream. Figure 7.2 presents the pressure distributions of the single and distributed propeller configurations. The reader will notice fewer data points around $x/c = 0.7$ for the distributed propulsion case, as these were taped off together with the flap gap. Dashed lines represent the upgoing blade side, while the solid lines are the downgoing blade side[1]. The distribution of total pressure coefficient on the upgoing blade side closely match between the single and distributed propeller cases. On the downgoing blade side, however, suction on the upper surface is increased in the distributed propeller configuration for $\alpha = 10$ and $\alpha = 13$ deg. This suggests an overall reduction of slipstream deformation compared to the single propeller configuration.

The reduction of deformation also aligns with the theory of propeller-wing interaction mechanisms proposed by Felli [33] (see also the discussions in Sections 5.2 and 5.3.3), who attributes the deformation to the combination of vortex imaging effects and the spanwise pressure gradients. The presence of the adjacent slipstreams reduces the spanwise pressure gradient, thereby greatly reducing the spanwise deformation. Additionally, the vortex imaging effects of adjacent slipstreams will oppose each other at their interface, limiting the spanwise displacement.

The extent to which the slipstream deformation is reduced in distributed propeller configurations compared to the single propeller case warrants further investigation. The pressure distributions presented in Fig. 7.2 are local, and the wing experiences strong spanwise variations under influence of the slipstream (see Chapter 5). The distribution of total pressure in the wing wake shown in Fig. 7.1 may be dominated by deformation downstream of the wing, while on the wing itself the slipstream shape may be similar between

---

[1]In the context of the distributed propeller case, we will always refer to upgoing and downgoing blade sides relative to the central propeller, ensuring consistency with the single propeller configuration.
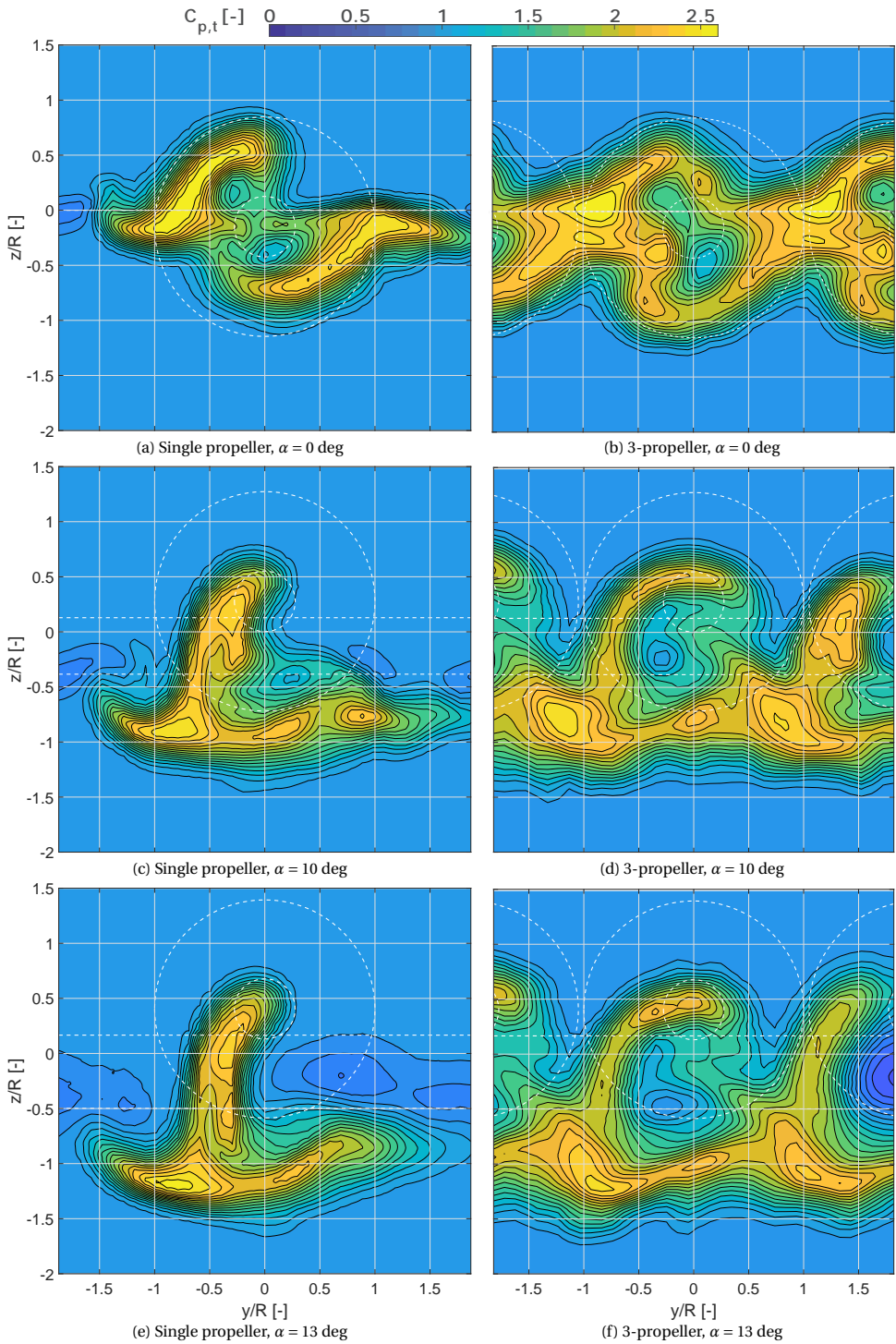
Figure 7.1: Contours of $C_{p,t}$ in the wake of a wing with single and distributed propellers. View in streamwise direction. Dashed lines are projections of the propeller(s), leading- and trailing-edges. $J = 0.8$, propellers out of phase.

the distributed and single propeller configurations. The results presented here suggest, however, that a distributed propeller configuration would experience fewer effects of propeller-wing interaction in high-lift condition than the single propeller configuration.

Figure 7.1 also reveals a low-pressure region at the centre of the slipstream in the distributed propeller configuration, attributed to the nacelle vortex core. This low-pressure region is not as clearly defined in the single propeller measurements, except for a small area (around $y/R = 0.25$ and $z/R = -0.4$) in Figure 7.1c. The limited spanwise resolution of the measurements and the relatively small size of the nacelle vortex core likely contribute

**7**



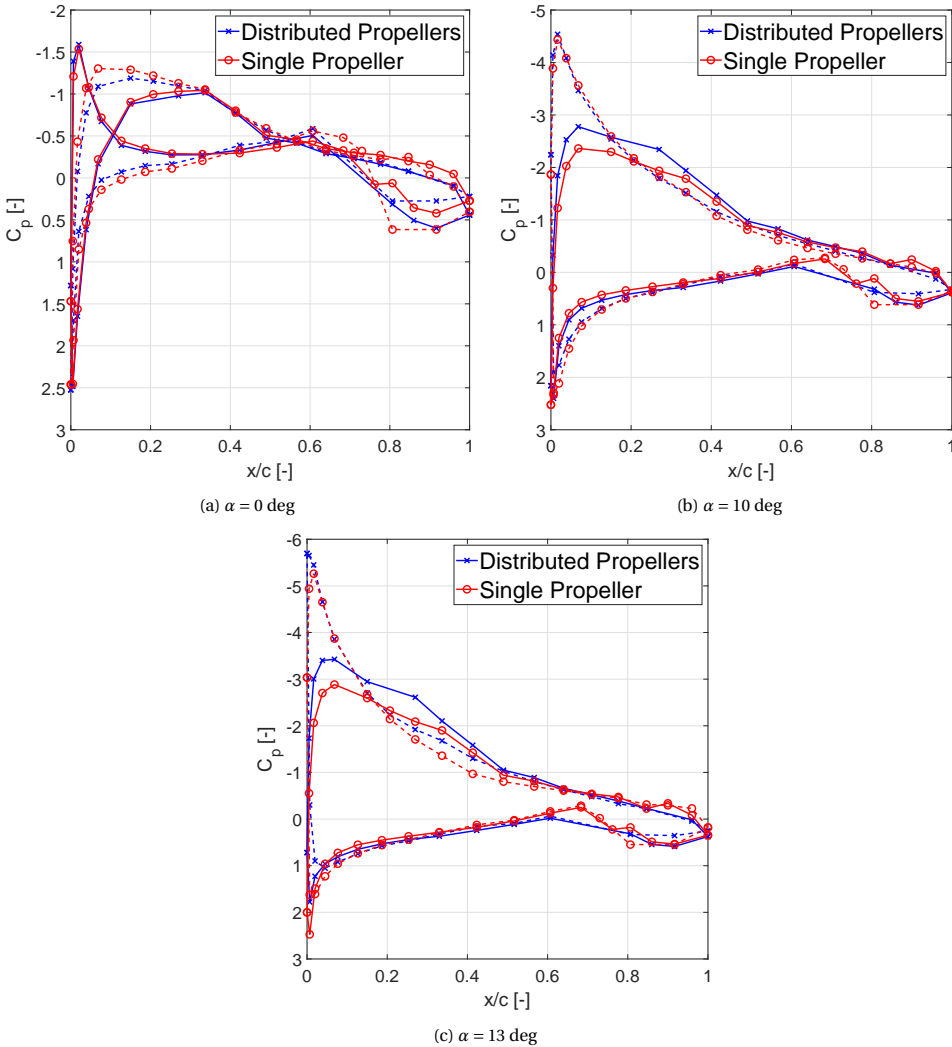(a) $\alpha = 0$ deg

(b) $\alpha = 10$ deg

(c) $\alpha = 13$ deg

Figure 7.2: Pressure distributions comparing single propeller with distributed propeller configuration for various angles of attack. Solid and dashed lines represent down-going and up-going blades sides, respectively.

to this discrepancy. However, numerical results for the single propeller configuration in Chapter 5, confirmed the presence of this region in the single propeller configuration, where it shifts spanwise to the upgoing blade side. In contrast, the distributed propeller measurements show the low-pressure region concentrated on the downgoing blade side. These observations indicate that distributed propeller configurations influence nacelle vortex development and spanwise displacement, warranting further investigation in future research.

For a single propeller configuration at high angles of attack, the interaction of the propeller slipstream induces local areas of flow separation on the wing just outside the slipstream (see Section 5.1.1). In Figs. 7.1c and 7.1e, these can be seen as pockets of lower total pressure coefficient near the edge of the slipstream. For the distributed propeller configuration, these regions of separation are suppressed by the presence of adjacent slipstreams. This suppression is dependent on the propeller spacing, as shown by Bongen et al. [45] in a similar experiment.

In Fig. 7.1f, however, we observe a large region of separation next to the right-most slipstream. This region has a much lower total pressure coefficient than the separation regions measured in the single propeller configuration. This suggests that the separation induced by the slipstream-wing interaction may be stronger in the distributed propeller case, which would be critical to distributed propeller arrays that do not cover the entire wing. Whether this is the case, however, requires further investigation. In the experiments and simulations performed by Bongen et al. [45], similar separation regions occurred as a result of interactions with the wall junctions. Unfortunately, junction flows were not monitored in the distributed propeller experiment.

We expect, however, that the increase in separation is a result of the slipstream-wing interaction and not just a wall-junction effect. In the single propeller experiment, wall junctions effects were monitored and found to be small and of negligible effect on the flow at the centre of the wing. Local regions of separation outside the slipstream also occurred in that experiment, as a result of the slipstream-wing interaction. Furthermore, the spacing between the outer propellers and the wind tunnel walls in this experiment are much larger than in the experiment by Bongen et al. [45], making is less likely that the horseshoe vortex at the wall junction would induce the additional separation at the slipstream edge.

The measurements of the distributed propeller configuration, finally, show a clear difference in slipstream deformation for the outboard propellers. Although the individual slipstreams of the propellers are difficult to distinguish, it is evident that the slipstream of the right-most propeller experiences a different deformation than the central propeller's slipstream. In fact, the shape of the slipstream behind the right-most propeller in the distributed configuration is still reminiscent of the single propeller slipstream. This is illustrated in Fig. 7.3 by overlapping and aligning the single propeller contour lines on the distributed propeller measurements for $\alpha = 10$ deg. Compared to the single propeller configuration, however, it is not located directly behind the propeller but rather displaced significantly towards the centre propeller.

Interestingly, the left-most propeller slipstream shows much more similarity to the centre propeller. It is hard to fully judge based on the measurements of the present experiment, as the measurement area does not cover the propellers completely. Nonetheless,
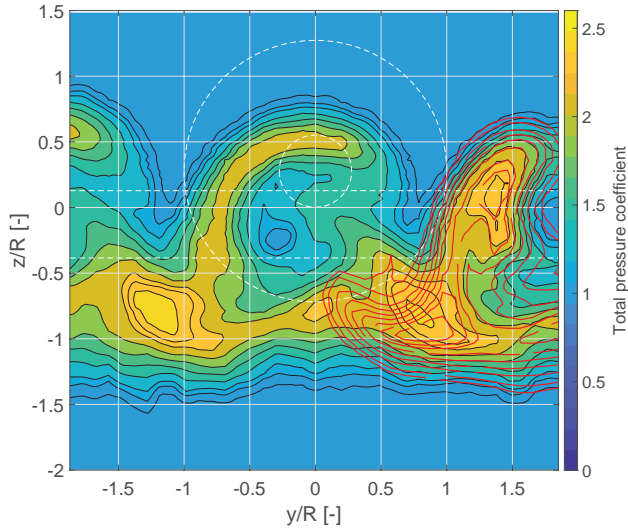
Figure 7.3: Illustration of the similarity between the shape of the slipstream at the right-most propeller in the distributed propeller configuration and that of the single propeller case.

this could mean that rotation direction of the outermost propellers of a finite distributed propeller array could have a critical role in the interaction with the wing.

The difference in slipstream deformation between the right-most and centre propeller signifies that the configuration is not representative of an infinite wing with an infinite array of propellers. This is an important consideration for experimental and numerical work on distributed propeller-wing interactions. Experiments in the field of distributed propellers are often conducted with a three-propeller setup (e.g., [108], [45]), while many numerical investigations apply a periodic boundary condition to a single propeller configuration (e.g., [47]). Crucially, although flow on the wing surface may look similar, the off-the-surface flow can behave significantly different.

## 7.2. Impact of phase control

Phase control is a recognized technique in literature as a potential method for reducing propeller noise [16], but how it may affect the flowfield around the wing has not been studied much in literature. In experiments of an isolated distributed propeller setup (i.e., without the wing) with three TUD-XPROP-S propellers, de Vries et al. [109] showed that the relative blade phase angle of the propellers has an effect on the interaction of the adjacent slipstreams at their interface. In the isolated case, this effect remained small and was ultimately insignificant. However, when these slipstreams interact with a lifting wing, the small deviations due to blade phase interactions could lead to significant differences in the slipstream deformation. We therefore measured the wake of the distributed propeller configuration for several relative blade phase angles $\Delta\phi$. The results are shown in Figures 7.4 and 7.5, for $\alpha = 0$ and $\alpha = 8$ deg respectively.

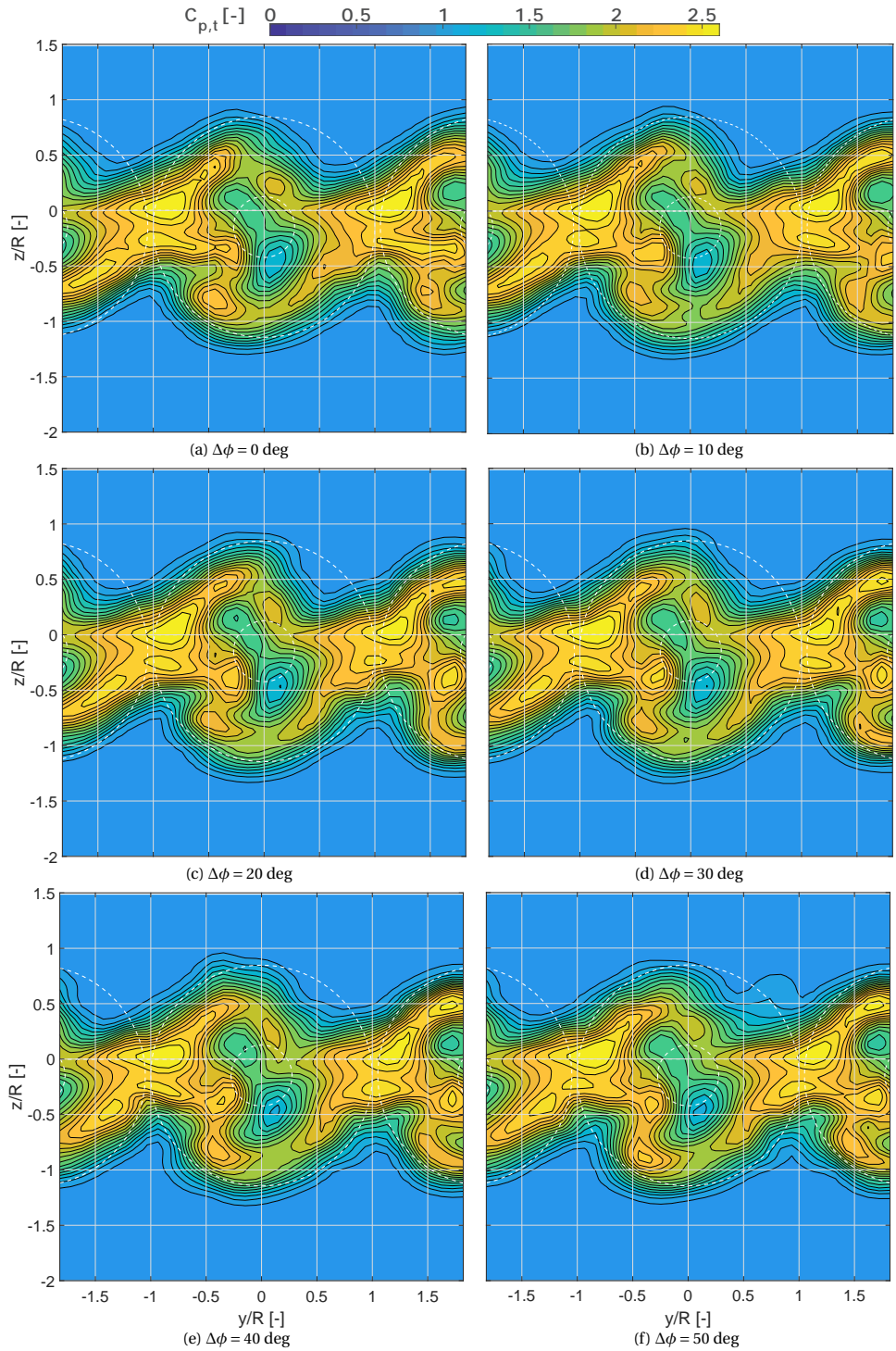For low angle of attack, the impact of the blade phase angle remains small. Some

Figure 7.4: Contours of $C_{p,t}$ for distributed propellers at varying $\Delta\phi$. $J = 0.8$, $\alpha = 0$ deg. View in streamwise direction. Dashed lines are projections of the propeller(s), leading- and trailing-edges.
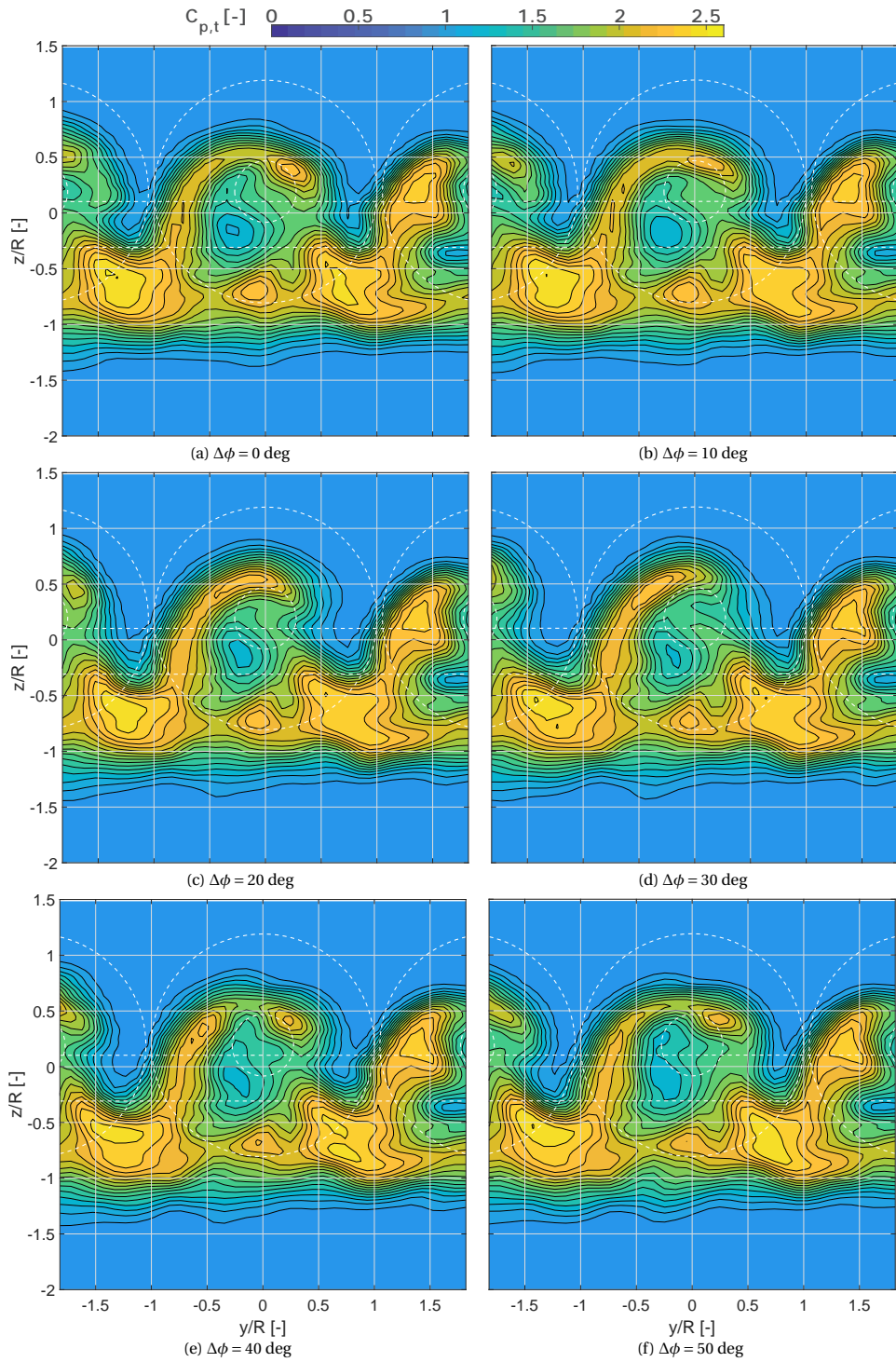
Figure 7.5: Contours of $C_{p,t}$ for distributed propellers at varying $\Delta\phi$. $J = 0.8$, $\alpha = 8$ deg. View in streamwise direction. Dashed lines are projections of the propeller(s), leading- and trailing-edges.

variations occur on the upper right and lower left portions of the distributions. For $\alpha = 8$ deg, the impact of $\Delta\phi$ is more significant. As $\Delta\phi$ increases, the total pressure distributions in the central portion of the slipstream (around $y/R = 0$) gradually change shape and become more concentrated. Past $\Delta\phi \approx 30$ deg, the changes revert gradually. Considering the propellers have six blades, the effects of $\Delta\phi$ will repeat every 60 deg and the relative distance between tip vortices of adjacent propellers is mirrored around $\Delta\phi = 30$ deg. Figures 7.4 and 7.5 do show this periodic behaviour. It is not mirrored about $\Delta\phi = 30$ deg exactly, which is to be expected since the configuration is not symmetric.

At low angle of attack, $\Delta\phi$ mostly affects the distribution at the slipstream interfaces, while for higher angles this extends to the central portion of the slipstream. This is better visualized in Fig. 7.6. It shows a contour map of the maximum deviation from the mean across all measured values of $\Delta\phi$ for the data presented in Figures 7.4 and 7.5. For $\alpha = 0$ deg, deviations are concentrated around the edge of the slipstream. They mostly remain within 10-15% of the mean value, with some local outlier regions. For $\alpha = 8$ deg, however, deviations are clearly concentrated on the upper half of the slipstream, on the upgoing blade side. The $\Delta\phi$ clearly affects the development of that part of the slipstream for high angles of attack. Interestingly, the slipstream behind the right-most propeller is hardly affected by changes to $\Delta\phi$, as illustrated by Fig. 7.5. This is not the case for the low angle of attack results.

The pressures on the wing at the locations of the pressure taps are virtually unaffected by the changes in $\Delta\phi$, as shown by Fig. 7.7. It shows the deviation from the mean pressure distribution as a result of $\Delta\phi$. Since the pressure taps are located relatively far from the location where the slipstreams interact, additional measurements are required to draw definitive conclusions regarding the variation of local pressures at the interaction location. However, it is evident that the change in $\Delta\phi$ does not have a significant impact on the global loading distribution of the wing, as this would show in Fig. 7.7.
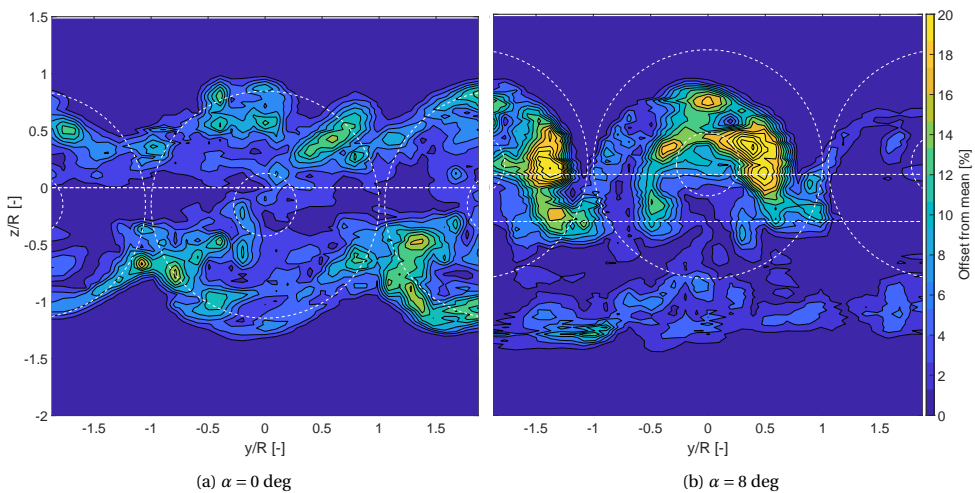


(a) $\alpha = 0$ deg

(b) $\alpha = 8$ deg

Figure 7.6: Contour plots showing the maximum deviation from the mean $C_{p,t}$ as a result of changing blade phase angle.

(a) $\alpha$ = 0 deg
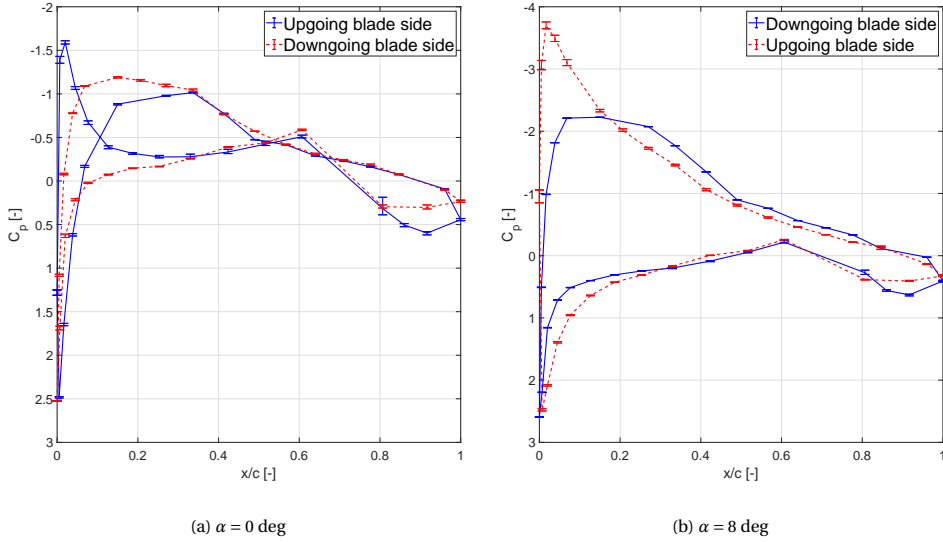
(b) $\alpha$ = 8 deg

Figure 7.7: Pressure distributions on the wing with variability due to variations in blade phase angle shown as error bars.

## 7.3. Key Findings

In this chapter, we have identified several key differences between single and distributed installed propeller configurations in terms of propeller-wing aerodynamic interaction, based on experimentally measured distributions of total pressure coefficient. Furthermore, we assessed the impact of relative phase control between propellers on the slipstream development of a distributed propeller configuration. Together, these lead to various phenomena in distributed propeller-wing interaction that warrant further investigation:

- Compared to the single propeller configuration, the slipstream remains more uniformly distributed, indicating more uniform immersion of the wing in the slipstream. This may be particularly significant for multi-element wings and lead to better high-lift performance compared to single propeller configurations.

- Phase control has a clear effect on the slipstream deformation in the wake at higher angles of attack, specifically on the upgoing blade side. Further study is required to determine whether the local wing performance is equally affected, which would be a critical consideration when utilizing phase control to suppress propeller noise.

- The separation induced by a single propeller slipstream at high angles of attack is suppressed by adjacent propeller slipstreams. However, the induced separation at the end of a distributed propeller array may be stronger as a result.

- The wake of the distributed propeller configuration shows very different deformations for the centre propeller and the right-most propeller, meaning the centre

propeller performance does not represent a propeller operating in an infinite propeller array. This needs to be considered when setting up experiments to provide experimental validation data for numerical simulations of installed distributed propeller systems.

# 8

# NACELLE INTERFERENCE EFFECTS

*In Chapters 5 and 6 we have treated the nacelle as an inherent part of the propeller system. We have discussed how the nacelle geometry and integration play an integral role in the roll-up of the nacelle-root system vortex, which induces local crossflow on the wing surface and dominates the slipstream deformation in the wake of the wing. However, the nacelle also has direct interaction modes with the wing and flap. In this chapter, we explore the effects of nacelle integration on the wing flow, both with and without flaps deflected, when not dominated by the propeller slipstream. The scope of this exploration is limited to the specific nacelle integration design that is described in Chapter 2. We start by providing some background on the study of nacelle effects in literature in Section 8.1. Subsequently, we investigate the effects of the installed nacelle without a propeller, to understand how the nacelle integration affects the wing flow and why this differs from the case with a blowing propeller. This is presented in Section 8.2 and is based on results from the first experiment (see Chapter 2). Section 8.3 then considers low thrust conditions, when the propeller slipstream affects the wing flow but does not dominate the whole flowfield, based on results from the second experiment. In Section 8.3.1 we synthesize the results and form some hypotheses on how the nacelle interference effects are affected by the propeller slipstream.*

---

Parts of this chapter have been published in Ref. [54]

## **8.1.** BACKGROUND ON NACELLE INTERFERENCE EFFECTS

Whereas the aerodynamic interactions between propellers and wing has been of interest for decades, the effects of the nacelle integration have received much less attention. Many studies in the field of propeller-wing aerodynamic interactions feature simplification of the nacelle-wing integration, such as detached nacelles (e.g., Oldeweme et al. [48]) or the removal of the nacelle entirely (usually in numerical studies with actuator disk methods, such as Beckers [46] and Schollenberger [12]). This is often done to simplify the positioning of the propeller relative to the wing. However, the nacelle design and its integration with the wing has complex aerodynamic interactions with both the wing and the propeller [110, 111, 112].

Several early studies on propeller-wing interaction include installed nacelles, and even investigate variations in nacelle design. Notable examples include Eggleston [113] and Samuelsson [30]. Eggleston [113] reports on results of wind tunnel experiments for the Havilland Dash 8, investigating several common turboprop nacelle designs (see Fig. 8.1). They note that long nacelles extending beyond the wing trailing edge yielded significant benefits to aircraft performance.[1] Samuelsson [30] includes several nacelle designs in their study on propeller-wing interactions, showing that the nacelle geometry has a significant impact on the flowfields around the wing.
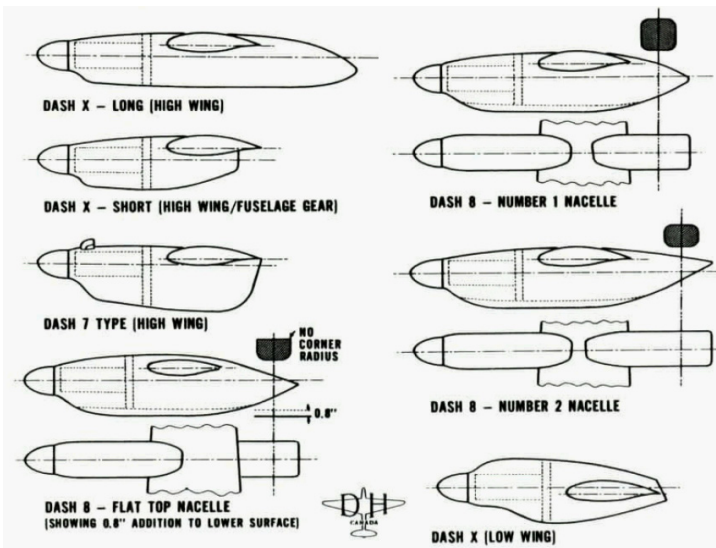


Figure 8.1: Nacelle designs tested for the Havilland Dash 8, from [113].

Neither of these studies, however, investigate the nacelle effects in low or unpowered conditions, nor do they focus on high angles of attack. More recent studies indicate that this interference effect can be particularly strong in high-lift conditions. Radespiel et al. [114] show that, without propeller blowing, the nacelle of a typical turboprop aircraft induces strong nacelle vortices at high angles of attack. These vortices travel close to

---

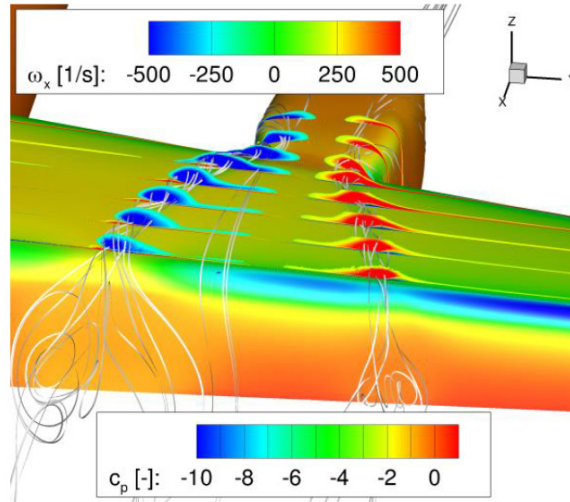[1]Note, however, that all of the designs in Fig. 8.1 cover the wing leading edge.

Figure 8.2: Nacelle vortices bursting over a blown flap, from [114].

the wing surface and may burst when moving over the flap (see Fig. 8.2). It should be noted, however, that Radespiel et al. study a configuration with internally blown flaps. Qiu et al. [99] investigate the impact of nacelle integration on the wing flow in high-lift conditions without a propeller for a typical turboprop configuration. They define four main unfavourable effects that affect the wing flow in a coupled manner: a wedge-like flow pattern behind the nacelle caused by spanwise pressure gradients, boundary layer accumulation on the wedge border that leads to separation, local angle of attack increase due to the nacelle blockage, and an increased wall friction at the nacelle-wing junction. The first three effects are summarized in Fig. 8.3. The last effect causes local separation bubbles at the nacelle-wing junction, a phenomenon that was also noted by van Arnhem [53].

In the context of modern distributed propeller aircraft, the importance of the effects described by Qiu et al. [99] is greatly increased, as a much larger portion of the wing span will be affected by any flow interference from the nacelle. However, to the knowledge of the authors, these aerodynamic phenomena are not explored in further detail in literature. We could find no further studies on these effects, nor on the potential of these effects to prevail in powered conditions. In previous chapters in this dissertation (specifically Chapters 5 and 6) we have seen the influence of the nacelle in powered conditions. It is involved in the formation of the nacelle-root vortex system, which is a dominant factor in crossflows on the wing surface and in the slipstream deformation in the wake. However, these effects can be interpreted as nacelle-slipstream interference, more so than nacelle-wing interference[2]. In all cases of nacelle effects described in Chapters 5 and 6, the nacelle

[2]We specifically mention *interference* here, rather than *interaction*, mostly because we can only investigate a single nacelle configuration. Additionally, although the flow around the nacelle is definitely affected by the wing performance, the nacelle is mostly a passive element in the system. In the conditions investigated in this chapter, we therefore mostly consider it to *interfere* with the wing and flap flow.
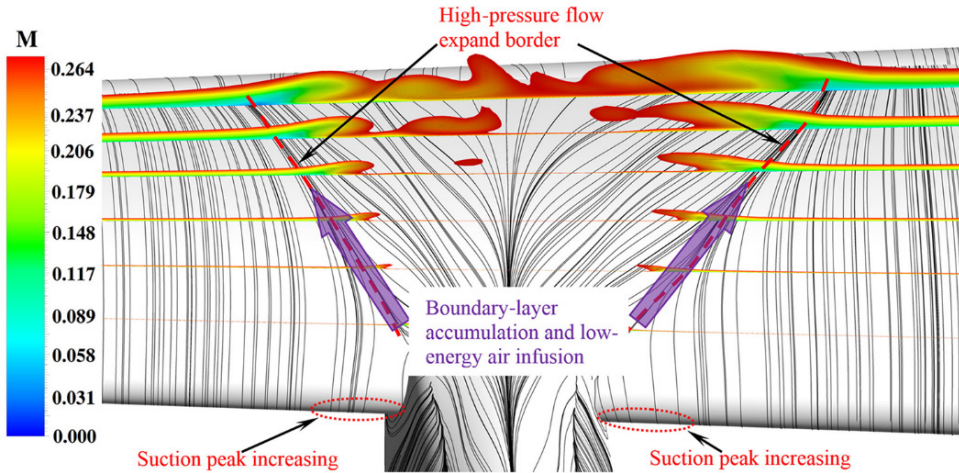
Figure 8.3: Wedge-like flow pattern on the wing surface due to nacelle interference, from [99].

affects the helical vortex system of the slipstream, which in turn affects the rest of the flow.

One may question the relevance of the nacelle integration effects, if from chapters 5 and 6 the effects described by Qiu et al. [99] appear to be mostly suppressed in the presence of a moderately to highly loaded propeller. However, for conventional aircraft (that do not rely on propeller blowing for lift augmentation) the propeller loading is very low during landing, while high-lift devices are deployed to maximum deflections. In flow, and it is unclear from literature whether in these situations the nacelle interference effects reappear.

For common turboprop aircraft, such as the ATR-72 and Dash-8, the nacelle integration effects may not be of primary concern[3]. The area of the wing that is affected by these effects is, to some extent, limited. For multi-engined designs, in particular modern distributed propeller concepts, the situation changes. If these concepts utilize leading-edge mounted distributed propeller systems without significant blowing in landing conditions, the nacelle integration effects may drastically diminish the high-lift performance. Even when such an aircraft does utilize propeller blowing for high-lift augmentation, the effects described in this chapter would mean that in case of engine failure, the aircraft does not only lose the lift augmentation of the propeller blowing but could experience sudden flow separation. The nacelle placement and integration will then become critical design choices.

In the context of propeller-airframe integration, the nacelle-wing effects currently represent purely a loss mechanism. However, as with other interaction effects that are leveraged by closely-coupled propeller-airframe integration and design, this poses an opportunity for optimization or even additional benefit. The nacelle integration clearly deserves more attention than it has received thus far in literature, both for its role in

---

[3]Or simply severely underappreciated.

propeller-wing(-flap) interaction and slipstream deformation, as for its effect on the wing flow in low thrust conditions.

In this chapter, we therefore expand on the current knowledge of nacelle-wing interference effects by investigating the aerodynamic phenomena that occur in zero and low-powered conditions. The scope of this investigation is limited to the specific nacelle integration design of the wing used in the experiments (see Chapter 2). Note that this nacelle is minimal compared to typical turboprop nacelles, meaning that observed interference effects will likely be more substantial in scenarios with more conventional nacelle designs. Although the shape and relative length of the nacelle differs strongly from the boxy and more traditional turboprop nacelle designs features in the works of Radespiel et al. [114] and Qiu et al. [99], it shares the fact that it covers the wing leading edge. We will show that, despite the differences in nacelle design, the nacelle-wing interference results in flow phenomena that are very similar to those observed in literature. Additionally, we will discuss how these phenomena differ from the powered cases discussed in previous chapters.

## 8.2. Nacelle Interference Effects on the Unblown Wing

We first investigate the impact of the nacelle integration the wing without the presence of a propeller slipstream. Since the nacelle covers the leading edge of our wing, we should expect a high-pressure region behind the nacelle, based on the results by Qiu et al. [99]. At higher angles of attack, a wedge-like flow pattern may develop on the wing upper surface as a result. The results of the first experiment do not feature pressure measurements in the region directly behind the nacelle, but do include oil flow visualizations that show the various aerodynamic flow phenomena that occur. In section 8.2.1 we discuss the flow patterns of the wing with flap nested, while in section 8.2.2 we discuss the flow patterns of the wing with flaps deployed. In section 8.2.3 we shortly discuss the impact of the nacelle on the local aerodynamic coefficients of the wing.

### 8.2.1. Interaction phenomena with flaps nested

Oil flow visualizations of the wing surface flow with flap nested, presented in Fig. 8.4, show clearly how the wing surface flow is affected by the presence of the nacelle. At $\alpha = 0$ deg (Fig. 8.4a), the nacelle has little impact on the wing flow. A small region of flow disturbance is present directly behind the nacelle; the wing surface flow is otherwise undisturbed. At higher angles of attack, however, several aerodynamic phenomena occur. A wedge-shaped flow pattern is present behind the nacelle (I), which remains attached up to the trailing edge (the thick dashed line indicates the approximate location of the separation line). This is consistent with the results by Qiu et al. [99].

At the edge of the wedge-shaped flow pattern, early flow separation is induced (II). The oil flow traces these regions back to the nacelle-wing junction (III). This again is qualitatively consistent with the study by Qiu et al. [99], where boundary layer accumulation at the boundary of the wedge-shaped flow region results in early onset of separation. Clearly, the wing flow is affected significantly by the presence of the nacelle in the high-lift regime, even with flap nested. At the trailing edge, small disturbances in the flow can be observed (IV), possibly from nacelle vortices.

8

(a) $\alpha = 0°$



(b) $\alpha = 10°$
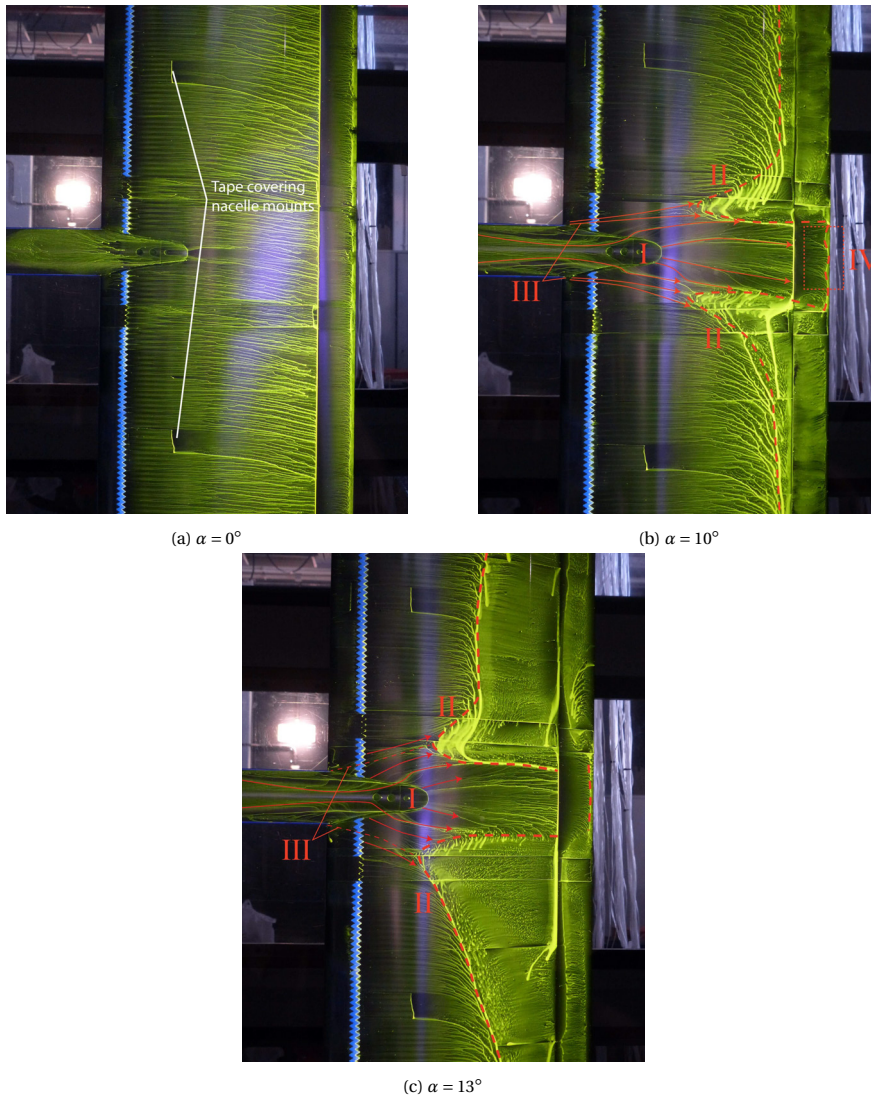


(c) $\alpha = 13°$

Figure 8.4: Oil flow visualization of the wing with nacelle, showing attached flow directly behind the nacelle and induced separation near nacelle. Dashed line indicates the approximate separation line. $\delta_f = 0$ deg.

## 8.2.2. INTERACTION PHENOMENA WITH FLAPS DEPLOYED

When flaps are deployed, the wedge flow behind the nacelle widens significantly as a result of a steeper spanwise pressure gradient between the region directly behind the nacelle and the suction peak on the wing leading edge. Figure 8.5 shows oil flow visualization of the wing with deployed flap at $\alpha = 10$ deg. Again, the thick dashed line approximates the separation line across the wing. In both cases, flow separation induced by the nacelle increases significantly compared to the flap nested configuration at the same angle of

attack. The boundary layer accumulation becomes visible as diffuse regions (I) in the oil flow and results in flow separation that dominates the wake. Figure 8.6 displays the total pressure coefficient in the wake of the wing at $\alpha = 8$ deg and $\delta_f = 15$ deg, showing large pressure loss regions resulting from the nacelle interference. The wake directly behind the nacelle is thinner than wing wake, as there is no adverse pressure gradient and thus the boundary layer does not grow significantly.

The aforementioned pressure gradients between the nacelle region and the wing leading edge become so large, that it induces flow reversal on the wing near the nacelle-wing junction. The wing leading edge at the nacelle-wing junction shows reversed flow (II) ahead of the zigzag tape and vortex structures (III) can be observed in the nacelle-wing junction where flow coming off of the nacelle circulates into the reversed flow region. Notably, the oil flow shows clear shearlines in the reversed flow region, suggesting that there is still significant surface shear. This does not follow typical separated flow, where the surface shear is strongly reduced in the separated region.

To better understand the flow structures around the nacelle-wing junction, we can use the work by Plijter [115]. They performed RANS simulations of the same model geometry. These simulations are performed at a higher Reynolds number and a slightly different angle of attack, but can still help with a phenomenological explanation of the nacelle interference effects. Figure 8.7 shows how the pressure loss regions of Fig. 8.6



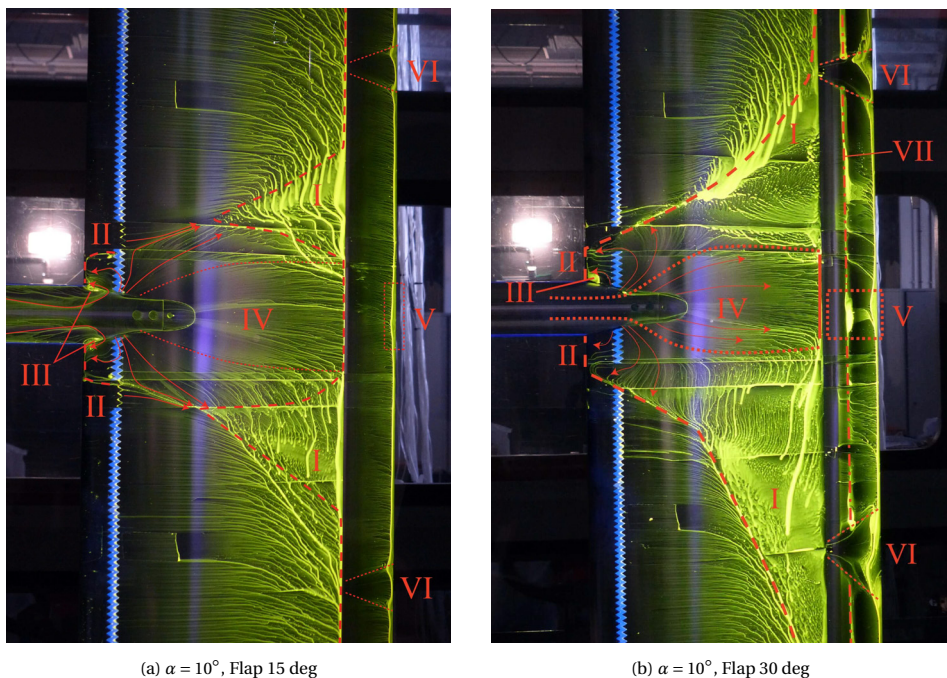(a) $\alpha = 10°$, Flap 15 deg          (b) $\alpha = 10°$, Flap 30 deg

Figure 8.5: Oil flow visualization images of the wing with nacelle mounted at different flap settings, showing the development of the flow expansion behind the nacelle with increasing flap deflection. Dashed line indicates the approximate separation line, dash-dotted line shows a laminar separation bubble.
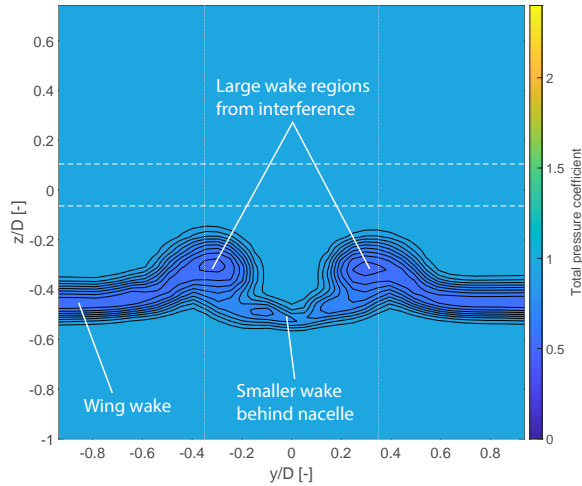
Figure 8.6: Total pressure coefficient in the wake. $\alpha = 8$ deg, $\delta_f = 15$ deg. Experimental measurements.

clearly develop from the edge of the wedge flow and the nacelle-wing junction. Figure 8.8 furthermore shows how the flow around the nacelle-wing junction is an intricate combination of various flow structures. The wake regions of Fig. 8.7 consist of boundary layer thickening from the edge of the wedge flow region, as well as the viscous cores of vortices originating from the nacelle-wing junction. These vortices can burst when they move into the low pressure region of the flap, as was observed by Radespiel et al.
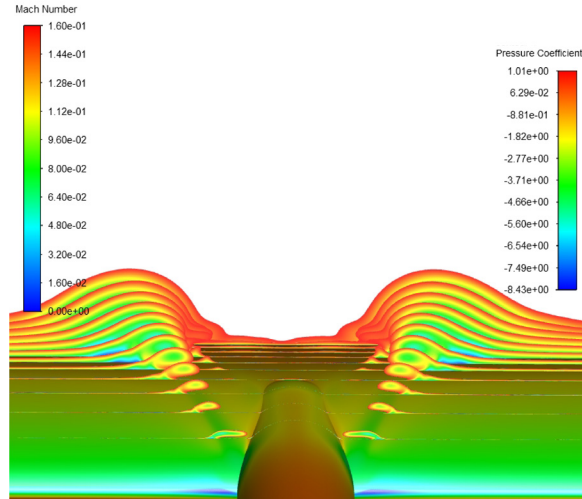


Figure 8.7: Development of wake regions visualized by slices of Mach contours. $\alpha = 8.3$ deg, $\delta_f = 15$ deg. RANS simulations from [115].
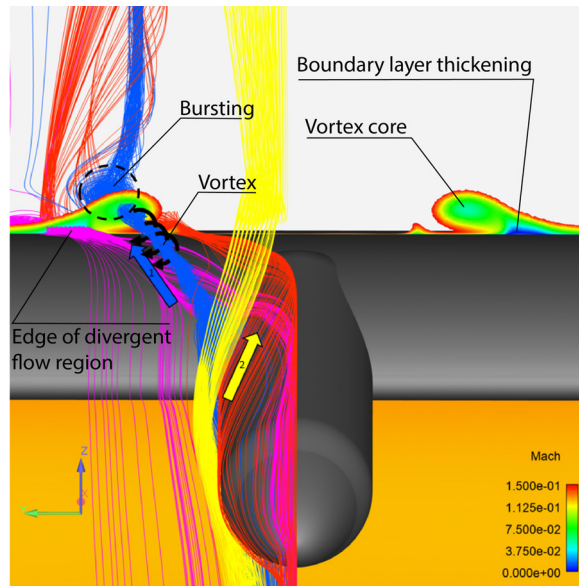
Figure 8.8: Various flow structures involved in nacelle wake development. $\alpha = 8.3$ deg, $\delta_f = 15$ deg. RANS simulations from [115].

[114]. This vortex bursting is thus not exclusive to very highly lifting Coandă flaps. While Qiu et al. [99] also report strong vortices from the nacelle interference, they are not so clearly connected to the nacelle-wing junction. Overall, though the nacelle interference phenomena are shared between the various geometries, the relative strength of these phenomena clearly differs between designs.

### 8.2.3. IMPACT ON LOCAL WING PERFORMANCE
To get a sense of the impact of nacelle interference effects on the wing performance, we can look at local aerodynamic coefficients calculated from the pressure taps on the wing. Figure 8.9 shows polars of these coefficients for the clean wing and the wing with nacelle mounted, at each of the flap deflections. Note that these are very local measurements, while the oil flow images have shown the nacelle interference effects to be highly three-dimensional.

For the flap nested cases, the $C_l - \alpha$ curves remain nearly identical up to the maximum lift angle. With flaps deployed, both the maximum lift coefficient and the angle at which it is reached change drastically for the nacelle-mounted case. Furthermore, the stall behaviour is changed completely. Whereas the clean wing shows a sharp drop-off in lift coefficient beyond the maximum lift angle, the curve is more gradual for the nacelle-mounted cases. This is a result of the wedge-like flow pattern becoming wider as the angle of attack increases, effectively emulating trailing edge stall behaviour.

In the region of $\alpha = 5$ to $10$ deg, both flapped cases show a negative slope in the pressure drag with the nacelles mounted. This is likely related to the suction peak at the leading edge of the main element due to the blockage of the nacelle [99]. The relative
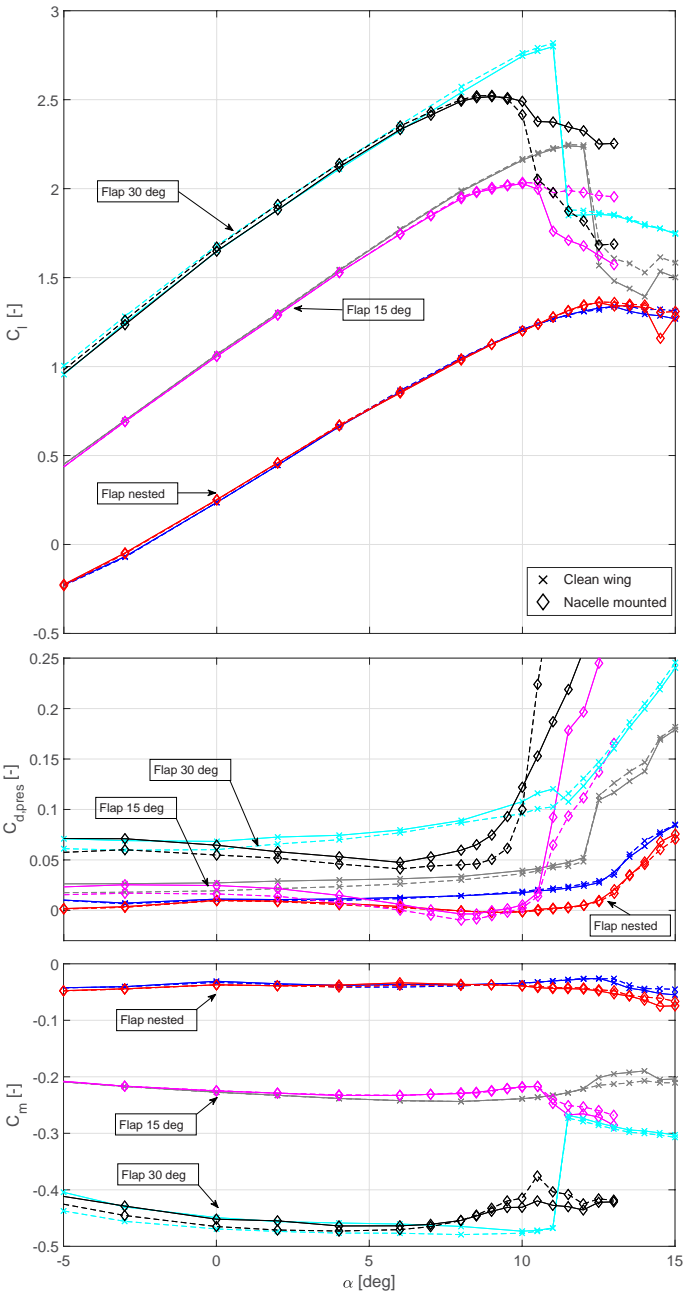
Figure 8.9: Polars of local aerodynamic coefficients for the clean wing and nacelle mounted configurations of each flap deflection. Dashed and solid lines represent respectively starboard- and port-side pressure tap locations. Uncorrected wind tunnel data.

contribution to pressure drag by the main element and the flap in these cases supports this conclusion, as the main element has negative drag contributions at low angles of attack. The case with $\delta_f = 30$ deg and nacelle mounted no longer displays the jump in moment coefficient that is observed on the clean wing around $\alpha = 11$ deg, which was caused by complete separation of the flap flow.

Based on the oil flow visualizations in Section 8.2.2, the flap flow seems to have little interference from the nacelle effects. The $\delta_f = 15$ deg case shows no interaction besides separation induced on the outer part of the flap due to interference with the flap brackets (VI). A slight induction of trailing edge separation can be observed downstream of the nacelle (V), which is likely related to the lack of pressure recovery region in the wake of the main element, inducing slight trailing edge separation on the flap. A similar structure is observed for $\delta_f = 30$ deg. Note also the major effect of the flap brackets on the flow for $\delta_f = 30$ deg, which induces early separation and removes the laminar separation bubble, marked by the dash-dotted line (VII).

Local pressure distributions (Fig. 8.10) confirm that the flap loading at $\delta_f = 15$ deg is
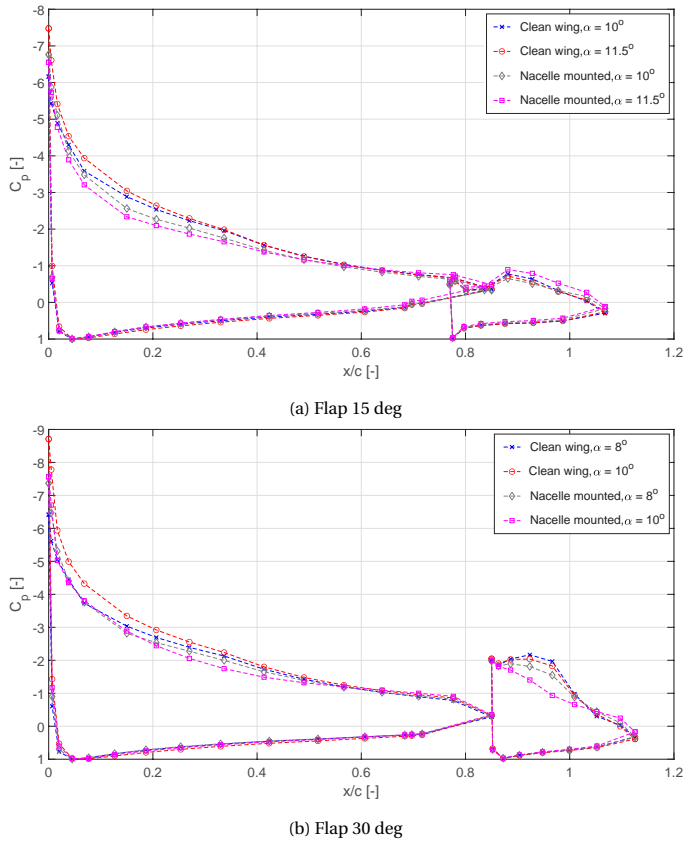


(a) Flap 15 deg



(b) Flap 30 deg

Figure 8.10: Comparison of pressure distributions on the upgoing blade side for clean wing and nacelle mounted with flap deflected near the maximum lift angle.

hardly affected by the nacelle interference on the main element, but for $\delta_f = 30$ deg shows a loss of suction on the flap at $\alpha = 10°$. This is likely caused by the separated wake of the main element induced by the nacelle effects, which significantly alters the off-the-surface flow characteristics above the flap.

## 8.3. NACELLE INTERFERENCE IN LOW-THRUST CONDITIONS

Clearly, the nacelle imposes critical flow effects on the wing in high-lift conditions when no propeller slipstream is present. However, we have not observed the same phenomena in the results of Chapters 5 and 6, where the wing was blown by a highly loaded propeller. This raises the question if the nacelle-wing interactions become more significant at lower propeller loading, where the dominance of the slipstream on the flow around the wing is reduced. To explore the potential nacelle-wing effects in low thrust conditions, we performed oil flow visualization on the wing surface and pressure probe measurements in the flow, as part of the second experiment described in Chapter 2. Measurements were taken at a *low thrust* condition ($J = 1.98$, $T_c = 0.05$, $Q_c = 0.019$) representative of propeller loading in landing configuration, as well as at a *zero power* condition ($J = 2.42$, $T_c < 0.005$, $Q_c < 0.005$) where almost no power was supplied to the electric motor driving the propeller. For all measurements, the flap was deflected to $\delta_f = 15$ deg and the angle of attack was $\alpha = 8$ or 10 deg.

Figure 8.11 shows a comparison of oil flow visualizations of the wing surface flow at $\alpha = 8$ deg for the nacelle configuration without propeller, with propeller in low thrust condition and with propeller in zero power condition. Without a propeller, the oil flow shows the effects discussed in Section 8.2: wedge flow in the region behind the nacelle and reverse flow regions on both sides of the nacelle resulting from the interface between nacelle flow and wing leading edge flow. In the low thrust and zero power conditions, some of these effects are still clearly visible.

However, there is still a clear presence of the propeller slipstream, even at zero power, which affects some of the nacelle-wing interference phenomena. The wedge flow behind the nacelle is less pronounced and no longer symmetrical around the nacelle centreline. The reverse flow regions at the wedge flow boundary are suppressed. While for zero power separation still occurs, for the low thrust conditions only low shear regions are present. These low shear regions indicate that thick boundary layers are present, however they have not led to flow separation. We can also still clearly identify a slipstream edge on the downgoing blade side, including outboard flow separation (see also Section 5.1) At the downgoing blade side, also some local interference of the flap flow is present.

The suppression of the reverse flow regions is most likely caused by a combination of turbulence introduced by the propeller blades and the higher momentum flow in the slipstream. Although the propeller operates at very low thrust, there is still a significant increase in total pressure, particularly on the downgoing blade side. This is evident from total pressure measurements just behind the trailing edge, shown in Fig. 8.12. The concentration of total pressure on the downgoing blade side is caused by the non-uniform inflow of the propeller due to the geometric angle of incidence and the wing upwash effect. It is offset by total pressure losses from root separation on the upgoing blade side. This also explains why a clear slipstream edge is present on the downgoing blade side in Figs. 8.11b and 8.11c, but not on the upgoing blade side. Even in the zero power condition,

(a) No prop, $\alpha = 8$ deg

(b) Low thrust, $\alpha = 8$ deg
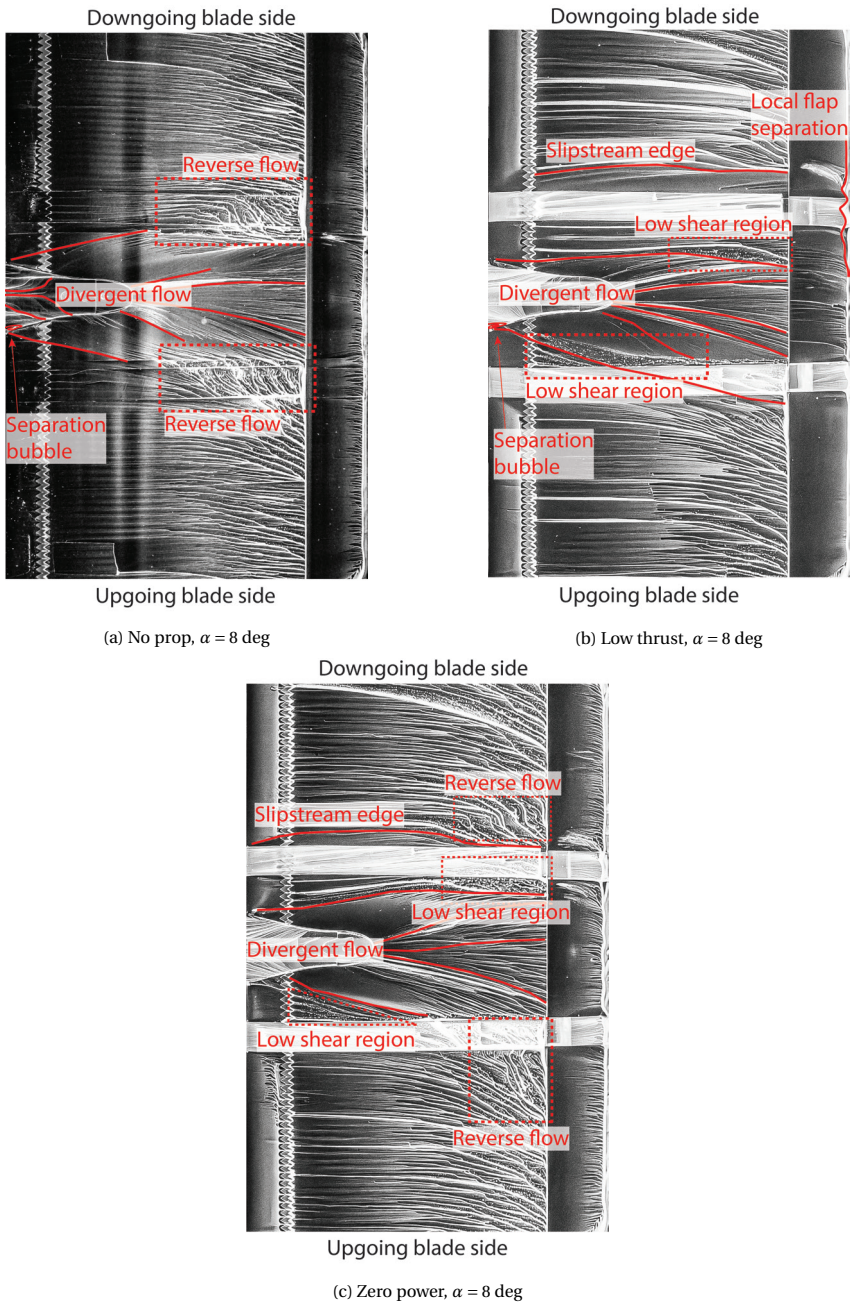
(c) Zero power, $\alpha = 8$ deg

Figure 8.11: Surface oil flow on the upper surface of the wing, comparing the pure nacelle effects with low thrust propeller conditions. $\alpha = 8$ deg, $\delta_f = 15$ deg.

(a) Low thrust, $\alpha = 8$ deg
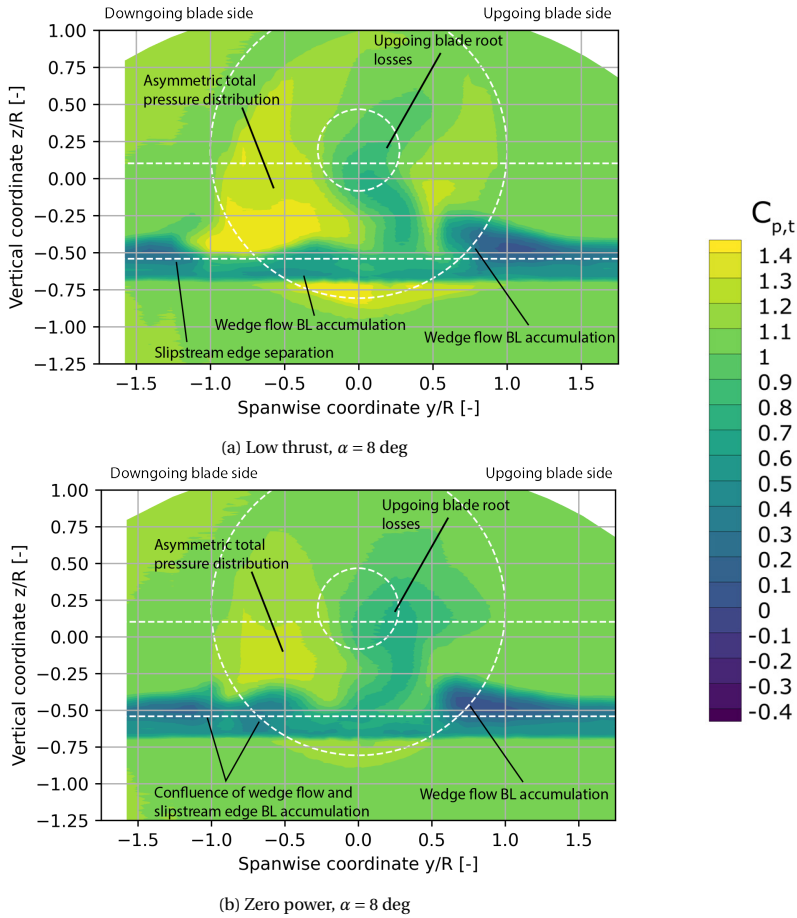


(b) Zero power, $\alpha = 8$ deg

Figure 8.12: Total pressure coefficient just behind the flap trailing edge. $\delta_f = 15$ deg. Dashed white lines indicate locations of the propeller disk, nacelle, and wing leading and trailing edges.

some total pressure is still being introduced into the flow on the downgoing blade side (see Fig. 8.12b).

In the low thrust and zero power conditions, both the nacelle and propeller slipstream effects induce thickening of the wing boundary layer. Figure 8.13 shows contours of $1.05 < C_{p,t} < 0.95$ at various chordwise stations over the wing, visualizing the development of pressure loss regions over the wing. On the downgoing blade side, we can clearly see two regions of pressure losses developing, one at the slipstream edge and the other from the nacelle-junction, likely at the wedge flow boundary. While for the low thrust condition these regions remain mostly separate, for the zero power condition they merge towards the main element trailing edge. On the upgoing blade sides, both conditions only show signs of a single region of boundary layer accumulation, consistent with the wedge flow boundary.

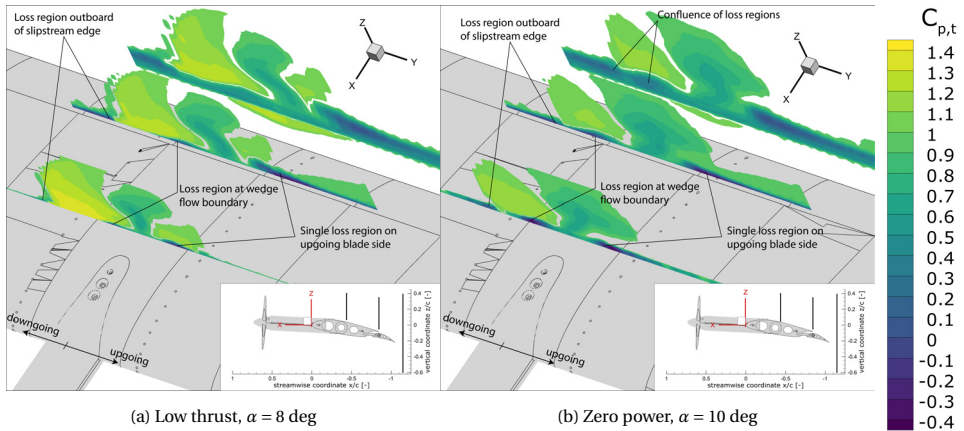(a) Low thrust, $\alpha = 8$ deg          (b) Zero power, $\alpha = 10$ deg

Figure 8.13: Slices of total pressure coefficient at various chordwise stations of the wing upper surface, visualizing the development of the nacelle induced losses over the wing. $\delta_f = 15$ deg.

At higher angle of attack, the nacelle integration effects become more dominant. Figure 8.14 shows the same comparison of oil flow images as Fig. 8.11 but at $\alpha = 10$ deg. Effects of the slipstream are still present in both the low power and zero power conditions. Divergence of the flow behind the nacelle is still reduced compared to the configuration without propeller. Although separation bubbles occur for both the low thrust and zero power conditions at the nacelle-wing junction, this is a clear reduction from the reverse flow regions near the junction for the case without propeller. Flow separation occurs on both the downgoing and upgoing blade sides for the low thrust condition as well as the zero power condition. However, the flow separation on the downgoing blade side seems to occur outboard of the slipstream rather than at the boundary of the wedge flow in both conditions. On the upgoing blade side, the slipstream seems to have no clear impact and the reverse flow region is similar between all three conditions of Fig. 8.14.

Contours of total pressure coefficient just behind the flap trailing edge (Fig. 8.15) show much the same features for $\alpha = 10$ deg as for $\alpha = 8$ deg. Total pressure is increased on the downgoing blade side and for the low thrust case, two regions of pressure losses can be seen. For the zero power condition, these regions have clearly merged, as discussed before (see Fig. 8.13). On the upgoing blade side, a single large region of pressure loss is present in both conditions, consistent with the observations from the oil flow visualizations of Fig. 8.14.

(a) No prop, $\alpha = 10$ deg



(b) Low thrust, $\alpha = 10$ deg
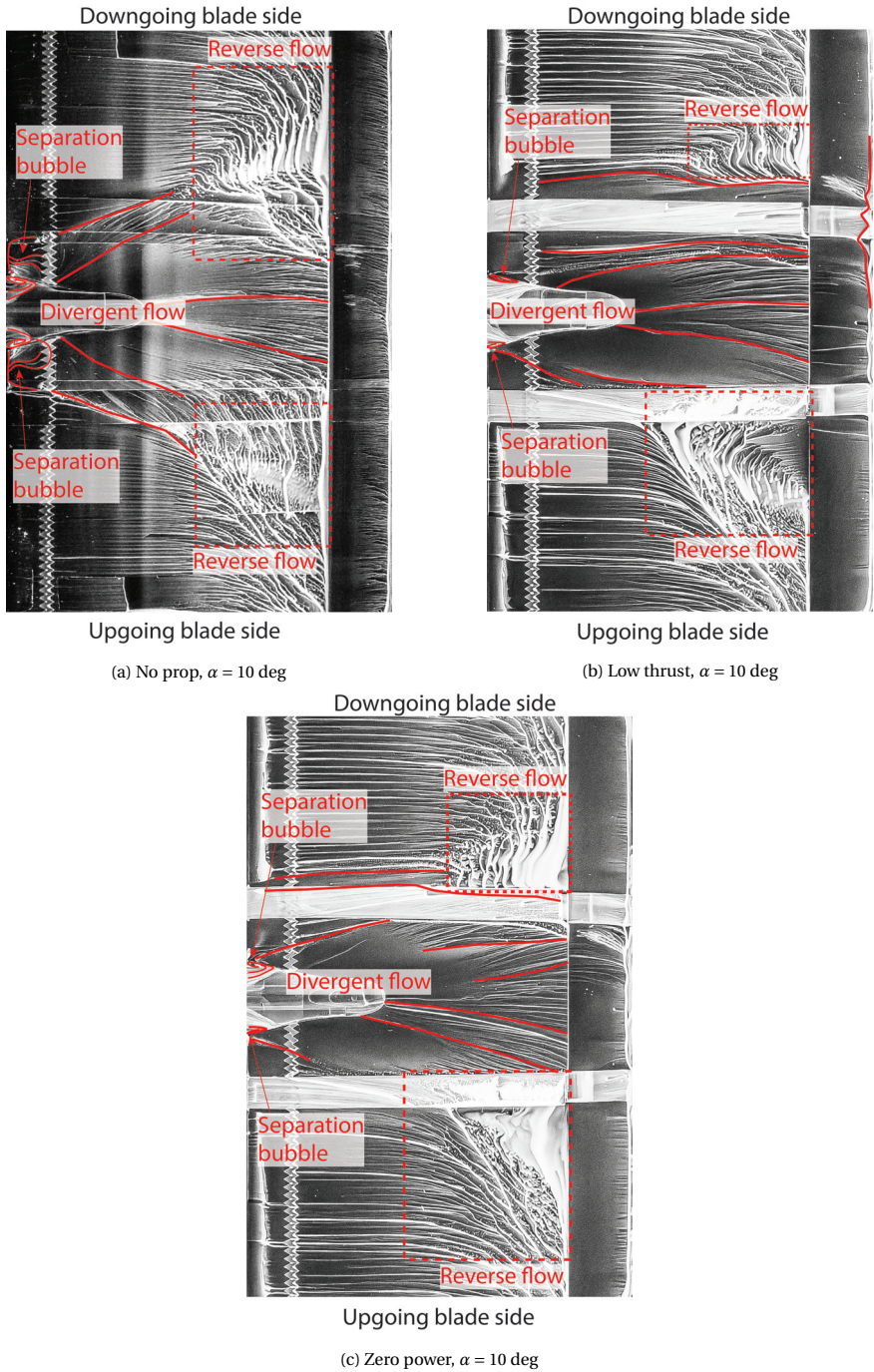


(c) Zero power, $\alpha = 10$ deg

Figure 8.14: Surface oil flow on the upper surface of the wing, comparing the pure nacelle effects with low thrust propeller conditions. $\alpha = 10$ deg, $\delta_f = 15$ deg.
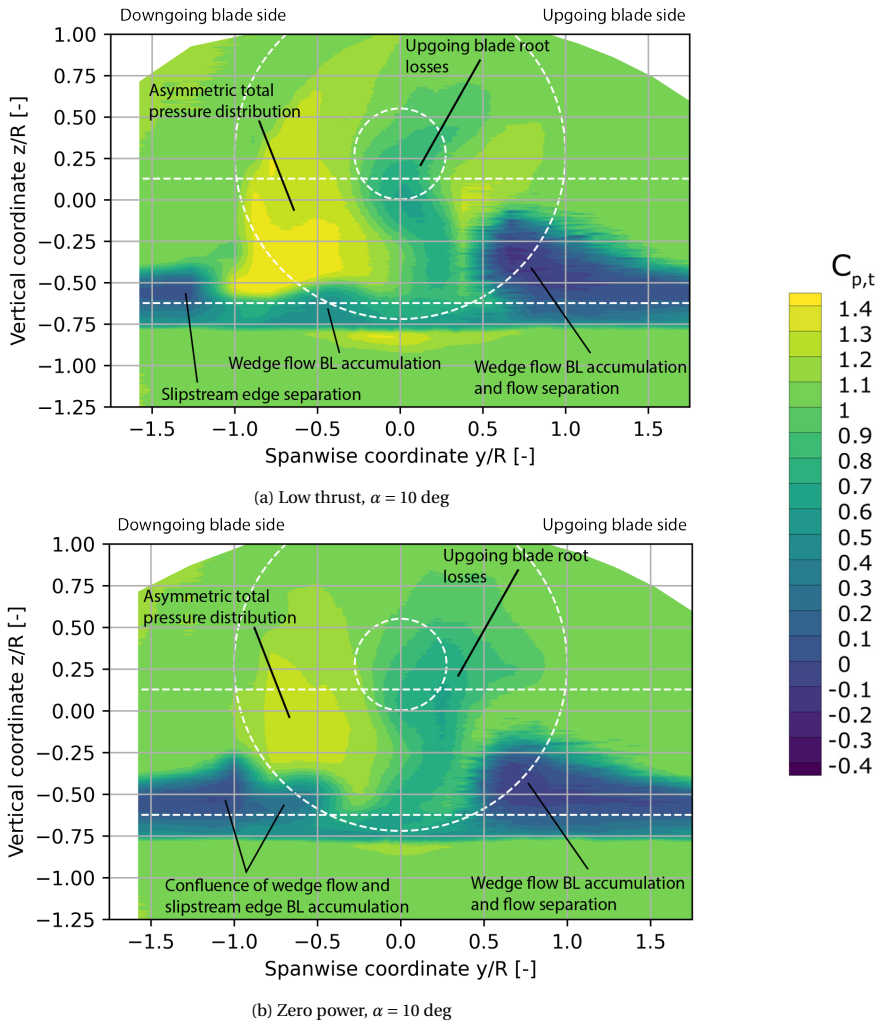
(a) Low thrust, $\alpha = 10$ deg



(b) Zero power, $\alpha = 10$ deg

Figure 8.15: Total pressure coefficient just behind the flap trailing edge. $\delta_f = 15$ deg.

## 8.3.1. ON THE MECHANISMS OF THE NACELLE INTERFERENCE

Combining the results from this chapter with observations of the nacelle flow in previous chapters (specifically, chapters 5 and 6) we can form some hypotheses about the evolution of the nacelle interference effects in high-lift conditions, in both powered and unpowered configurations. For the unpowered condition, these mostly overlap with the observations by Qiu et al. [99], but add some insights into the relation to wing circulation.

Figure 8.16 shows illustrations of the evolution of the wedge flow for increasing wing lift. At low lift, the nacelle interference effects are minimal. Although the high pressure region and wedge flow behind the nacelle already occur, the spanwise pressure gradients are not sufficient to cause significant flow divergence or boundary layer accumulation. At
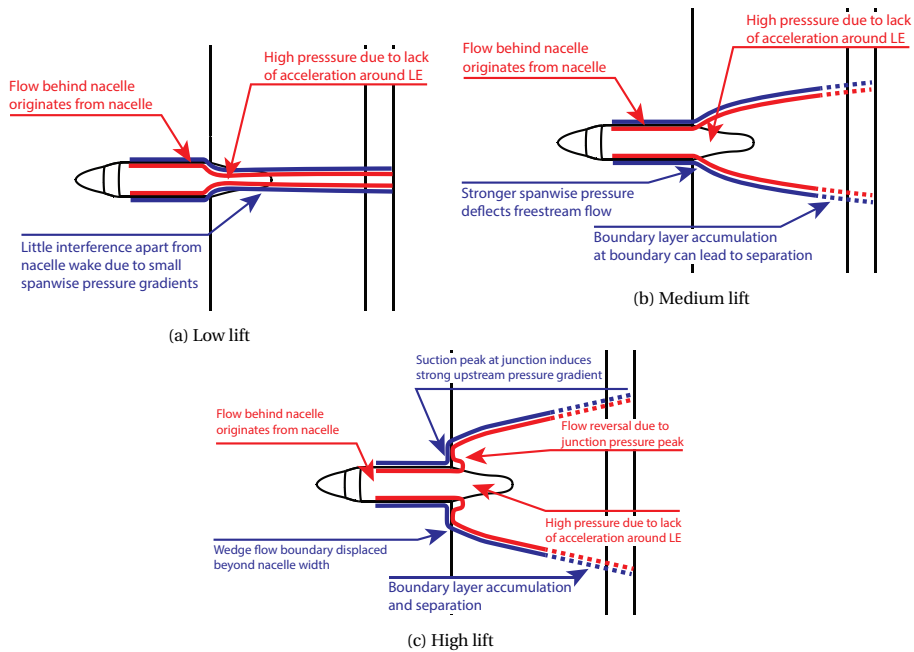
(a) Low lift

(b) Medium lift

(c) High lift

Figure 8.16: Illustrations of the envisioned evolution of the wedge flow pattern induced by the nacelle interference in unpowered conditions for increasing levels of wing lift.

medium lift, the spanwise pressure gradient increases as the suction peak on the wing leading edge increases, leading significant wedge flow. At the boundary of the wedge flow, boundary layer accumulation occurs, potentially leading to flow separation. For high lift, the suction peak at the wing leading edge is further increased by the blockage around the nacelle, which induces an additional angle of attack at the nacelle-wing junction [99]. This creates an upstream pressure gradient from the nacelle high-pressure region, leading to flow reversal near the nacelle-wing junction. The wedge flow is expanded beyond the width of the nacelle, affecting a large portion of the wing span. Note that this is not traditional boundary layer separation in an adverse pressure gradient, since the oil flow showed clear shear lines, while typical flow separation leads to low shear regions.

It should be stressed that the descriptions and illustrations given here are not exhaustive of nacelle interference effects. We forego the complexity of the flow around the nacelle-wing junction, or the role of the junction vortices. Comparison with literature in this chapter, as well as the design optimization attempts by Qui et al. [99], have already shown that the relative strength of the various flow structures around the nacelle-wing junction can differ significantly between designs. It is not yet clear what the role of the junction vortices is in the boundary layer accumulation at the wedge flow boundary, or in the wedge flow itself. This requires further study.

In powered conditions, the slipstream and nacelle interference effects affect the wing flow simultaneously. We limit our discussion here to high-lift conditions, where the nacelle interference effects are most pronounced. Figure 8.17 illustrates the evolution of

(a) Low thrust

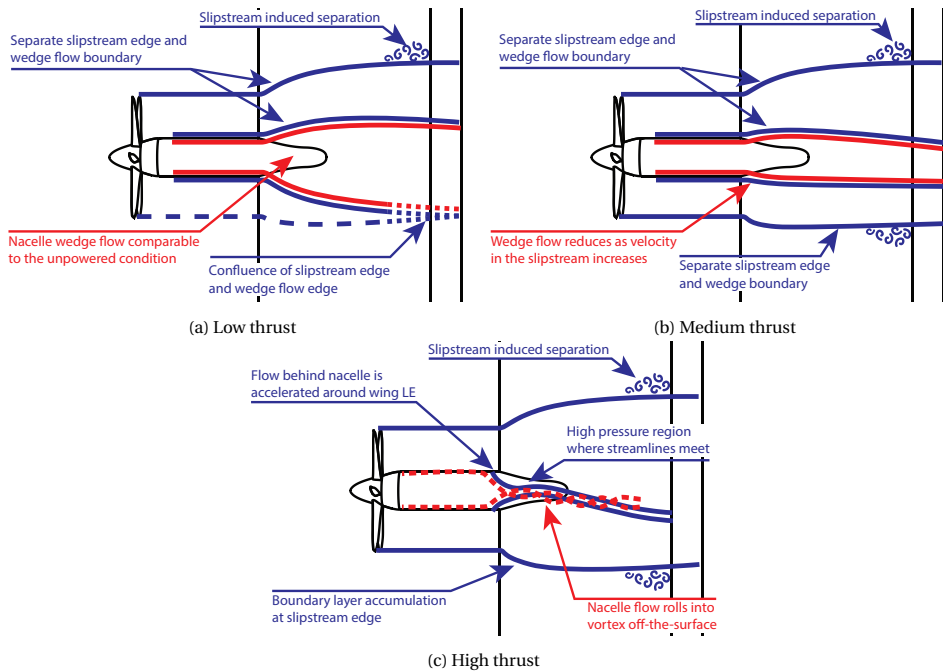(b) Medium thrust

(c) High thrust

Figure 8.17: Illustrations of the envisioned evolution of the slipstream and nacelle interference effects in powered conditions for increasing levels of propeller thrust in a high-lift configuration.

the slipstream and nacelle interference effects for increasing thrust settings. At low thrust, the slipstream is concentrated on the downgoing blade side due to the non-uniform inflow at the propeller disk location. On the upgoing blade side, there is little to no total pressure added, leading to confluence of the slipstream edge and the wedge flow boundary. This results in effects very similar to the unpowered condition. On the upgoing blade side, there is a separate slipstream edge and wedge flow boundary. [4] Although the higher momentum of the slipstream flow will reduce the boundary layer accumulation at the wedge flow boundary, the slipstream edge may induce outboard flow separation. The asymmetric distribution of total pressure in the slipstream also shifts the wedge flow such that it is no longer symmetrical around the nacelle centreline.

For medium thrust conditions, the additional slipstream velocity will likely reduce the wedge flow behind the nacelle and separate the slipstream edge from the wedge flow boundary on both sides of the nacelle. Note that we did not observe this condition in the current study, rather this is based on observations of the differences between low and high thrust settings. As separate slipstream edges present on both sides of the nacelle, slipstream induced flow separation is also likely to occur on both sides. Further increasing thrust will eventually converge the wedge flow and the nacelle flow will be dominated by the root vorticity, rolling into the nacelle-root vortex discussed in Chapter 5. As the

---

[4]The zero power condition showed confluence of the slipstream edge and wedge flow boundary even on the downgoing blade side, but this will likely only occur at extremely low thrust settings.

flow directly behind the nacelle no longer originates from the nacelle itself, but rather from flow that has accelerated around the leading edge, the principal mechanism of the wedge flow pattern is no longer present. Although pressure contours in Chapter 5 still show a higher pressure directly behind the nacelle (see for instance Fig. 5.20b), this will be caused by the interface of accelerated flow from the upgoing and downgoing blade sides, not by the lack of acceleration around the leading edge.

Again, the illustrations of Fig. 8.17 only serve as a simplification of the flow mechanisms, and to achieve a first intuition regarding the critical difference in mechanisms between low and high thrust conditions. It foregoes the role of swirl, which will typically increase along with thrust settings, and various other complications of the propeller-wing interaction. Figure 8.17b is also not directly based on observations and the development of the flow features from the low thrust condition to the high thrust condition should be investigated in detail. Studying this development may provide guidelines on minimum thrust settings to mitigate nacelle interference effects on the wing flow, which may be particularly important for the operation of distributed propeller aircraft.

## 8.4. KEY FINDINGS

From the results presented in this chapter, we can distil various key findings regarding nacelle interference effects:

- Flow interference of a leading-edge mounted nacelle can induce significant flow separation on the wing in high-lift conditions. The affected wing area can extend far beyond the nacelle width.

- Despite the differences in nacelle design, similar interference effects are observed as in literature. The integration with the wing therefore seems more critical than the nacelle design itself.

- The flow around the nacelle-wing junction is highly three-dimensional and very complex. Strong vortices can be shed from this junction. The role of these vortices in the nacelle interference effects requires further study.

- The slipstream of a highly loaded propeller suppresses the nacelle interference effects, likely because the root vorticity dominates the nacelle flow and rolls into the nacelle-root vortex, rather than flowing over the wing surface.

- At low propeller thrust, the wing surface experiences a combination of slipstream effects and nacelle interference effects. The slipstream effects reduce the wedge flow behind the nacelle, but the nacelle interference effects are still present, while the slipstream also induces outboard flow separation. The asymmetric distribution of total pressure in the slipstream due to the non-uniform inflow condition at the propeller disk in high-lift configuration is an important factor in this interaction.

# III

## CONCLUSIONS AND RECOMMENDATIONS

# 9

## CONCLUSIONS

*This dissertation has discussed the aerodynamic interaction of propeller-wing-flap systems, based on both numerical and experimental studies, with the objective to* **characterize the phenomena and mechanisms that dominate the propeller-wing-flap aerodynamic interaction**. *We have done so by discussing how the aerodynamic interactions of multi-element airfoils are affected by the non-uniform inflow caused by a propeller slipstream, as well as how classic propeller-wing aerodynamic interaction is affected by the addition of a slotted flap. We defined the dominant factors and interactions of a multi-element airfoil in a slipstream, revealed several aerodynamic phenomena that are specific to the propeller-wing(-flap) interaction in high-lift conditions and discussed the importance of slipstream deformation to the resulting performance of the wing, and the flap in particular. This was followed by a characterization of how the slipstream deforms in different stages due to the interaction with the wing and how this depends on characteristics of the helical vortex system. Finally, we explored how the slipstream deformation for a single propeller differs from a distributed propeller system, and how the nacelle integration interferes with the wing flow in conditions where the propeller slipstream is not dominant. As we conclude this dissertation, we synthesize the research findings into a concise summary of these phenomena and mechanisms. This chapter aims to encapsulate the essence of the research, offering a comprehensive overview of the conclusions reached throughout the dissertation, and reflect on the research questions.*

## 9.1. Aerodynamic Interactions of a Multi-Element Airfoil immersed in a Jet

By neglecting three-dimensional effects of the propeller slipstream, such as swirl, we can reduce the propeller-wing-flap system effectively to a multi-element airfoil immersed in a jet of high dynamic pressure. Although the aerodynamic mechanisms of the interaction between airfoil elements is well described in literature, these might change when it is immersed in a non-uniform flowfield. In Chapter 4, we performed a sensitivity study of a two-element airfoil immersed in a jet of constant velocity distribution, evaluating a total of nine design factors and their interactions. These include angle of attack, flap deflection, gap and overlap, jet velocity ratio, size and vertical position, Reynolds number and Mach number. We evaluated the dominant factors and interactions using regression analysis of a second order model augmented with three-factor interactions.

At first observation, the governing design parameter sensitivities of the aerodynamic performance of multi-element airfoils do not change significantly when immersed in a jet. When comparing the aerodynamic performance of a two-element airfoil in uniform flow conditions with a fixed jet flow, the same design factors and interactions between these factors were found to be dominant. Angle of attack and flap deflection are by far dominant for lift and drag responses, while moment coefficient is dominated by angle of attack and flap overlap. Interactions between factors have little to no contribution to the lift, drag, and moment responses.

The additional dynamic pressure in the jet may, however, locally cause critical Mach numbers to be reached on the main element suction side. In these cases, the aerodynamic performance of the airfoil is drastically changed, in particular the drag response. Additionally, flap deflection is no longer the dominant factor and is replaced by Mach number. Interactions between the Mach number and both angle of attack and flap deflection become critical for the drag response.

When considering models that allow various jet sizes, positions and velocity ratios, we found that the velocity ratio is by far the most dominant factor for all aerodynamic responses. However, it did not show strong interactions with any other factors. This further emphasizes that the principle aerodynamic mechanisms and dependencies of a multi-element airfoil are not affected by the jet immersion (although the absolute values of aerodynamic forces on the wing are obviously affected by the jet).

**Research question 1**

How are typical multi-element airfoil aerodynamic interactions affected by an upstream jet of increased total pressure?

- - - - - - - - - - - - - - - - - - - - - - - - - - - - - - - - - - - - - - - - -

The non-uniform flowfield from a jet of higher total pressure does not change the dominant factors for the aerodynamic interaction of multi-element airfoils, except for the potential induction of transonic flow on the main element resulting from the increase in dynamic pressure within the jet.

Significant interactions were observed between jet size, jet position and angle of attack. We established that these interactions influence the jet alignment with the airfoil and how

much the flap is immersed in the flow. The optimal position of the jet with respect to the airfoil is found to change between smaller jets, which benefit from lower positions, and larger jets, which generally favour higher positions. Separating the factor analysis per wing element, we found that the impact of jet size, jet position, angle of attack and their interactions stems mostly from their influence on the flap lift.

Particularly in terms of lift augmentation (the ratio of lift coefficient generated by the airfoil immersed in a jet compared to in uniform flow) flap immersion is critical. Jet velocity ratio is still by far the most dominant factor, which is to be expected since the lift force scales with the square of velocity. All other significant factors and interactions, however, relate to the position, size, and trajectory of the jet. The highest lift augmentation required the flap to be fully immersed in the jet.

## 9.2. Aerodynamic Characteristics of Propeller-Wing-Flap Interaction

Similar to how we can view the propeller-wing-flap system as a multi-element airfoil in non-uniform flow, we also investigated how the classic propeller-wing interaction is affected by the addition of a flap element. Several of the aerodynamic phenomena that occur have been described in literature, such as the two-way interaction between propeller and wing aerodynamic performance and the spanwise shearing of the slipstream. However, the addition of the flap to the system increases the impact of known phenomena, and adds new phenomena that are not usually observed in literature on propeller-wing interaction.

### 9.2.1. High-lift propeller-wing-flap interaction phenomena

In high-lift conditions, various phenomena occur in the flow that are not present in low-lift conditions. The propeller slipstream suppresses flow separation where it washes the wing, but expedites flow separation just outboard of the washed area. Crossflows on the wing upper surface become more significant in high-lift and can result in local flow separation within the boundaries of the slipstream.

The propeller experiences a substantial non-uniform inflow as a result of the geometric angle of attack with the freestream and the upwash induced by the wing. The latter is particularly significant, despite the relatively long nacelle of this particular configuration. The non-uniform inflow causes an asymmetric loading on the propeller disk, which is characterized by a higher total pressure on the downgoing blade side. This also means that the tip vortices and their interactions are stronger on the downgoing blade side.

A deployed flap is washed by the part of the slipstream that passes on the pressure side of the main element. As a result, the flap is strongly affected by the slipstream deformation that occurs on the pressure side of the main element. This deformation is very different from the suction side of the main element, and is characterized by a general expansion and a shift to the upgoing blade side. The flap also further deforms the slipstream, but primarily affects the part of the slipstream that passes the lower surface of the main element. This part is elongated in spanwise direction, similar to the effect of increasing the angle of attack of a single element wing.

9

> **Research question 2**
>
> How does the aerodynamic interaction between the propeller and main element affect the flap flow?
>
> - - - - - - - - - - - - - - - - - - - - - - - - - - - - - - - - - - - - - - - - - - - -
>
> The flow over the flap is highly dependent on the upstream aerodynamic inter-actions. The flap is immersed in the part of the slipstream that travels along the lower surface of the main element, which displaces and deforms as it passes the main element. This slipstream deformation dictates which part of the flap is affected by the slipstream. As wing circulation increases, more of the slipstream is deflected to the upper surface of the wing and less of the slipstream immerses the flap. This can strongly reduce lift augmentation on the flap.

> **Research question 3**
>
> How does the slotted flap affect the slipstream deformation?
>
> - - - - - - - - - - - - - - - - - - - - - - - - - - - - - - - - - - - - - - - - - - - -
>
> Flap deployment has a similar impact on slipstream deformation as increasing the angle of attack of a single element wing, where the part of the slipstream that passes the pressure side of the main element elongates in spanwise direction. However, the flap deflection mostly affects this part of the slipstream and has much less impact on the part of the slipstream that passes the suction side of the main element.

The effect of the slipstream deformation on the lift distribution is significant, particularly for the flap. While the main element mainly experiences augmentation of the lift distribution within the area directly behind the propeller, the part of the flap that experiences lift augmentation due to the slipstream interaction is off-centre and wider than a propeller diameter. Furthermore, it lacks the characteristic asymmetry imposed by swirl that is observed on the main element. This poses restrictions on which slipstream models are accurate for use in simulating propeller-wing-flap interactions. Since the main and flap element aerodynamic performance is inherently coupled by multi-element wing aerodynamics, the shift in flap lift augmentation affects the main element lift as well.

**9**

### 9.2.2. CHARACTERIZING THE SLIPSTREAM DEFORMATION

As the slipstream interacts with the wing, deformation of the slipstream occurs in various stages. Upstream of the wing, significant deformation of the slipstream takes place depending on the position of intersection with the wing. This deformation is a result of vertical transport of the slipstream due to the local flow angle, as well as the interaction with the flow acceleration around the wing leading edge.

As the slipstream impinges on the wing, the tip vortices are stretched around the wing leading edge. The tip vortices transport outwards strongly at the wing leading edge due to self-induced convection resulting from image vortex systems in the wing surface. This effect is opposed or increased by the local spanwise pressure gradient that results from the propeller-wing(-flap) interaction. The observed deformations agree with the

mechanisms described in literature, although we found the direction in which each of the deformation mechanisms act to be different from their description in literature.

The stretched tip vortex filaments align at the slipstream edge and roll into larger vortex systems. This effect is strongest on the downgoing blade side upper surface, where the tip vortices are already aligned more with the wing surface, further aided by wing circulation effects. These rolled-up vortex systems may contribute to the flow separation outboard of the slipstream, but cannot fully explain it as the strongest rolled-up vortex occurs on the downgoing blade side, while the flow separation is most significant on the upgoing blade side. This requires further research.

The nacelle and root vorticity rolls into two vortex systems, one on each side of the wing. For higher wing circulation, more vorticity is convected to the upper surface of the wing and the vortex on that side grows stronger. The mechanism by which this occurs depends on the physical interaction of the root vortices with the wing leading edge, similar to the tip vortex filament roll-up. The root vortices wrap around the wing leading edge on both sides of the nacelle, while they can convect freely on the upper and lower surfaces of the wing. This results in a vortex pair of opposite sign on the top and bottom of the nacelle, which is dominated by the general orientation of vorticity in the undisturbed root vortex system (opposite to the propeller rotation direction).

The rolled up root vortex induces a strong crossflow component on the wing surface within the boundaries of the slipstream. This crossflow drives flow from the downgoing blade side into the upgoing blade side. At the interface, a shear layer develops that can locally separate at high angles of attack, possibly interacting with other local separation regions and limiting maximum lift.

The interaction of the slipstream with the flap differs significantly from the main element interactions. The flap is immersed in the part of the slipstream that travels along the wing lower surface and only a small portion moves through the flap gap. Unlike the main element, no concentrated vortices wrap around the flap leading edge. The interaction with the wing upstream of the flap affects the stability of the helical vortex system. Tip vortices are pushed into each other on the lower surface, causing them to leapfrog and combine into a larger vortical structure. As a result, the flow affecting the flap is uniform and lacks swirl, and thus does not impose asymmetrical loading such as is experienced by the main element.

**Research question 4**

How does the aerodynamic interaction between the propeller and the flap differ from the interaction between the propeller and wing?

Unlike the main element, the flap does not experience tip and root vortices wrapping around its surface. Due to the deformation of the tip vortices around the main element, the interaction with the wing boundary layer and vortex-vortex interactions in the slipstream helix, concentrated vortical structured break down before reaching the flap. The flap therefore does not experience the same asymmetrical loading as the main element, and the slipstream deformation is more uniform and lacks swirl.

**9**

> **Research question 5**
>
> How are classical propeller-wing aerodynamic interactions affected by the inclusion of a slotted flap?
>
> - - - - - - - - - - - - - - - - - - - - - - - - - - - - - - - - - - - - - - - -
>
> Deploying the flap greatly increases the wing circulation, which increases the non-uniform inflow experienced by the propeller and thus the asymmetrical distribution of total pressure in the slipstream. Additionally, the slipstream is displaced towards the wing upper surface, which inherently reduces the lift augmentation of the flap, which is mostly affected by the part of the slipstream which travels along the lower surface of the main element. This creates a complex interaction of wing circulation and slipstream position. The vertical displacement of the slipstream can also cause substantial deformation of the slipstream upstream of the wing, depending on the vertical position of the slipstream with respect to the wing.

Downstream of the wing, the deformation is dominated by the nacelle-root vortex, which imposes a dominant rotational component on the slipstream. Significant deformation takes place in the wake. At the flap trailing edge, the part of the slipstream that passes the upper surface of the wing still holds much more resemblance to its circular shape. This means immersion of the wing is not well represented by the slipstream shape in the wake. Additionally, the slipstream deformation clearly cannot be overlooked in the aerodynamic performance of downstream surfaces, such as the empennage. Particularly when flaps are deployed, the slipstream that reaches these downstream stations will not resemble a typical slipstream tube whatsoever.

> **Research question 6**
>
> How does the primary aerodynamic interaction between the propeller and wing in high-lift conditions differ from low-lift conditions?
>
> - - - - - - - - - - - - - - - - - - - - - - - - - - - - - - - - - - - - - - - -
>
> In high-lift conditions, the propeller sees a significant non-uniform inflow, which causes an asymmetric loading on the disk. Although the mechanisms of interaction between the slipstream and the wing are similar to the low-lift condition, the slipstream induces flow separation on the wing just outside the washed area. The wing circulation affects the stability of the helical vortex system of the slipstream, causing early breakdown of tip vortices on the pressure side, while delaying breakdown on the suction side. The slipstream deformation is significantly increased compared to the low-lift condition and spans a much larger part of the wing.

## **9.3.** Slipstream Deformation with varying Propeller Operating Conditions

From the mechanisms of the deformation of the helical vortex system, it can be understood that the orientation of the helix with respect to the wing surface will impact the

resulting deformation. In chapter 2, we showed how this can be related to the operating condition of the propeller, specifically the thrust and torque coefficients. The thrust coefficient can be directly related to the amount of azimuthally oriented vorticity introduced into the flow, while the torque coefficient relates to the longitudinally oriented vorticity introduced into the flow.

We found that between these two, the torque coefficient was dominant for the slipstream deformation. A lower torque coefficient leads to significantly lower crossflow components on the wing surface directly behind the nacelle. Furthermore, it results in less spanwise displacement of the slipstream edge on the wing surface. The thrust coefficient, however, has negligible impact on the slipstream deformation (within the tested range).

> **Research question 7**
>
> How does the slipstream deformation depend on the propeller operating conditions?
>
> - - - - - - - - - - - - - - - - - - - - - - - - - - - - - - - - - - - - - - -
>
> The deformation of the slipstream is dominated by the streamwise vorticity in the slipstream, which scales with the torque coefficient. The impact of azimuthal vorticity, which scales with the thrust coefficient, is much smaller in comparison.

The impact of the propeller condition (or the slipstream characteristics) on the slipstream deformation is much larger in high-lift conditions than in low-lift conditions. Furthermore, the distribution of total pressure internal to the slipstream varies strongly between propeller conditions. This is likely related to the particular combination of advance ratio and local inflow angles, leading to root losses on the blade, rather than the thrust and torque coefficients and the resulting deformation.

The nacelle integration has a major impact on the internal distribution of the total pressure in the slipstream, as well as on the local pressure losses on the wing surface. These pressure losses may result in local flow separation in high-lift conditions, or even lead to large scale flow separation when interfacing with the separation induced at the slipstream edge. For the low thrust and torque condition, two distinct pressure loss regions on the wing wake were observed, which could be directly traced to the nacelle-wing junctions.

Overall, the slipstream deformation can be reduced to a certain extent by designing for a helical vortex system that is more perpendicular to the wing chord. This corresponds to a high thrust-to-torque ratio, or high propeller efficiency, which thus aligns with typical design practices for propeller performance.

## 9.4. SLIPSTREAM DEFORMATION IN DISTRIBUTED PROPELLER CONFIGURATIONS

The extent of slipstream deformation in a single propeller-wing-flap system in high-lift conditions is such that in a distributed propeller configuration, adjacent slipstreams would be forced to interface and interact. By measuring total pressure in the wake of a wing with a single and distributed propeller system, we showed that in the distributed

configuration the slipstream remains more uniformly distributed than for a single propeller. This indicates more uniform immersion of the wing in the slipstream. A more uniform immersion may be particularly significant for multi-element wings and lead to more consistent high-lift performance of distributed propeller-wing-flap systems, as per the findings of chapter 4.

Phase control has a clear effect on the slipstream deformation in the wake at higher angles of attack, specifically on the upgoing blade side. Further study is required to determine whether the local wing performance is equally affected, which would be a critical consideration when utilizing phase control to suppress propeller noise.

The separation induced by a single propeller slipstream at high angles of attack is suppressed by adjacent propeller slipstreams. However, we observed separation regions at the end of a distributed propeller array that were stronger than expected from the single propeller case, which warrants further investigation.

The wake of the distributed propeller configuration shows very different deformations for the centre propeller and the right-most propeller, meaning the centre propeller performance does not represent an infinite propeller array. This needs to be considered when setting up experiments to provide experimental validation data for numerical simulations of installed distributed propeller systems.

> **Research question 8**
>
> How does the aerodynamic interaction between a distributed propeller system and a wing differ from a single propeller-wing setup?
>
> - - - - - - - - - - - - - - - - - - - - - - - - - - - - - - - - - - - - - - - - - -
>
> The adjacent propellers in the distributed propeller configuration reduce the slipstream deformation, resulting in a more uniform distribution of total pressure in the wake. The wing is likely more uniformly immersed in the slipstream, leading to a better high-lift performance compared to a single propeller configuration. Additionally, the flow separation on the wing induced by the slipstream as found in the single propeller configuration is suppressed in the distributed propeller configuration.

## **9.5.** NACELLE INTERFERENCE EFFECTS

While the nacelle plays an important role in the development of the slipstream in highly loaded propeller conditions, it also has substantial interference effects on the wing flow. We specifically investigated these interference effects at in high-lift conditions (high angle of attack and flaps deployed), both in absence of a propeller and at low thrust coefficients, representative of a landing condition.

In the absence of a propeller slipstream, flow interference of a leading-edge mounted nacelle can induce significant flow separation on the wing in high-lift conditions. As angle of attack increases, the affected wing area can extend far beyond the nacelle width. The main mechanisms of this interference follow those observed in the (limited) literature on the subject, despite differences in nacelle design. The relative importance of the various flow phenomena did vary however, suggesting the integration with the wing is more critical than the nacelle design itself.

The flow around the nacelle-wing junction is highly three-dimensional and very complex. Strong vortices can be shed from this junction. The role of these vortices in the nacelle interference effects requires further study.

At low propeller thrust, the wing surface experiences a combination of slipstream effects and nacelle interference effects. The slipstream effects reduce the wedge flow behind the nacelle, but the nacelle interference effects are still present, while the slipstream also induces outboard flow separation. The asymmetric distribution of total pressure in the slipstream due to the non-uniform inflow condition at the propeller disk in high-lift configuration is an important factor in this interaction.

The slipstream of a highly loaded propeller suppresses the nacelle interference effects, likely because the root vorticity dominates the nacelle flow and rolls into the nacelle-root vortex, rather than flowing over the wing surface. Further study of the propeller loading required to suppress nacelle interference effects could be a critical topic for the implementation and operation of distributed propeller systems on future aircraft, as they are likely to suffer more from the nacelle interference than twin-engine configurations.

> **Research question 9**
>
> How does the nacelle design and integration affect the propeller-(nacelle-)wing-flap aerodynamic interaction?
>
> - - - - - - - - - - - - - - - - - - - - - - - - - - - - - - - - - - - - - - - -
>
> In the absence of a propeller, the nacelle induces significant changes to the wing loading distribution. As a result, at higher angles of attack, significant flow separation will occur that is different from the clean-wing condition. In the presence of the propeller, both nacelle interference effects and slipstream interactions occur on the wing surface. For a highly loaded propeller, however, the propeller root vorticity dominates the nacelle flow, which rolls into the nacelle-root vortex and thereby suppresses the nacelle interference effects.

**9**

# 10

## RECOMMENDATIONS

*Due to the complexity of propeller-wing-flap aerodynamics, there remain many topics of interest for future research, which fell outside the scope of this dissertation. In this chapter, we discuss several opportunities for future research based on the findings and limitations of this dissertation. These include the extension of the validation dataset with time-accurate measurements, the exploration of slipstream-induced flow separation, the performance of flaps in distributed propeller configurations, and optimizing the nacelle integration to mitigate interference. The latter may be extended to innovative nacelle designs that could leverage synergistic aerodynamic interactions.*

## 10.1. TIME-ACCURATE EXTENSION TO THE DATASET

This dissertation is accompanied by a validation dataset, based on the first and second experiments (see Chapter 2). While this dataset is already quite extensive and will hopefully prove useful for future research, it is limited by the steady-state nature of the measurements. The dataset includes no time-accurate or phase-resolved measurements, which limits its usefulness for high-fidelity unsteady numerical simulations. An extension of the dataset with time-accurate data, for instance using Particle Image Velocimetry (PIV), would therefore be very much of interest.

## 10.2. EXPLORATION OF SLIPSTREAM-INDUCED FLOW SEPARATION

The research presented in this dissertation still leaves questions regarding the flow separation that is induced at the edge of the slipstream. Although the alignment of deformed vortex filaments at the edge is certainly a contributor, the exact manner by which these filaments affect the local wing boundary layer is not fully understood. This will be a balance of several factors of the interaction that affect the boundary layer growth and eventual separation, such as local adverse pressure gradients, Reynolds number and the strength of the slipstream edge vortex. The latter is strongest on the downgoing blade side of the upper surface, while both in the experimental and numerical results the separation is most significant on the upgoing blade side. The adverse pressure gradient on the upper surface is strongest on the upgoing blade side, which might explain the separation location. However, the exact interplay of these factors is not yet fully understood and requires further investigation.

## 10.3. SLIPSTREAM DEFORMATION IN DISTRIBUTED PROPELLER CONFIGURATIONS

In chapter 7, we have shown that the slipstream deformation of an installed distributed propeller configuration differs significantly from that of a single propeller and wing. The deformation is, to some extent, mitigated compared to the single propeller-wing configuration and the total pressure in the slipstream is more uniformly distributed. We expect this to result in a better high-lift performance for wings with distributed propellers than for single propellers. However, the measurements of the third experiment, on which Chapter 7 is based, are very limited and provide little insight into the local flow phenomena that occur on the wing at the interface of adjacent slipstreams. Further experiments are required, both to further investigate the phenomena that occur, and to provide much needed validation data for numerical simulations. Numerical simulations of the same setup would also be of interest, to investigate the flow phenomena described in Chapter 7 in more detail and also to have a direct numerical comparison for the single propeller case.

Furthermore, the implications of having partial-span distributed propeller systems in high-lift conditions are of interest. In chapter 7, we discuss the occurrence of major flow separation at the edge of the propeller array. This may simply be related to interaction with the wind tunnel walls, as was observed in similar experiments by Bongen et al. [45].

However, considering the significantly larger distance between the wind tunnel walls and the outermost propeller, this may also be related to the interaction between adjacent slipstreams. As the wing lift augmentation due to a propeller slipstream depends on the diameter-to-chord ratio [27, 77, 116], the loading gradient at the edge of a propeller array may be stronger than for a single propeller. This may lead to increased flow separation outside the washed area of the wing.

## 10.4. OPTIMIZING NACELLE INTEGRATION

The importance of nacelle integration for the flowfield of propeller-wing-flap systems has been stressed throughout this dissertation. The specific nacelle integration analysed in this dissertation was shown to have dominant effects on the flow, particularly in high-lift conditions, in both powered (see Chapter 5) and unpowered (see Chapter 6) configurations. The interference effects would likely pose limiting constraints on the performance of distributed propeller configurations. Due to the number of nacelles on the wing, a larger portion of the span would be affected by nacelle interference than for typical turboprop configurations. However, the conclusions presented in this dissertation regarding the nacelle effects are limited by the specificity of the configuration. Even though we do show that the observed aerodynamic phenomena are largely shared between our configuration and those in literature, the implication of different nacelle designs and integration strategies are not known and warrant further study.

The challenges posed by the nacelle interference effects also put forth opportunities for optimization. By designing nacelles and nacelle-wing junction to reduce the negative impact of nacelle interference, we may be able to mitigate the limitations posed on the high-lift performance. Qui et al. [99] already attempted to improve the flow features surrounding the nacelle integration by lowering the nacelle position such that it no longer fully covers the wing leading edge. They found this to be ineffective, particularly due to its cruise performance, while a higher position that increased the strength of the nacelle junction vortices was found to be more beneficial. This also overlaps with findings by Eshelby [34], who finds that the higher and longer nacelle positions for the Dash-8 aircraft generally improved the high-lift performance.

However, the configurations discussed by both Qiu et al. and Eshelby consider typical turboprop designs, which feature propellers with a large propeller diameter to wing chord ratio. In chapter 4 of this dissertation, we discuss a relation between this ratio and the optimal vertical position of the (in the case of Chapter 4) jet. Smaller relative propeller diameters may benefit more from lower positions, as the flap immersion is more critical than the increased dynamic pressure over the main element upper surface. This conclusion overlaps with the consensus in literature (see, for instance, []) that lower positions are generally favourable in high-lift propeller applications, which usually feature diameter-to-chord ratios of less than 1. The observations by Eshelby [34] regarding the nacelle position therefore may not hold for smaller relative propeller diameters.

An under-wing position of the nacelle, where the integration point lies behind the wing stagnation point, may mostly solve the nacelle interference effects that limit the high-lift performance in unpowered conditions. Based on the findings in Chapter 8, we expect that a nacelle position where the junction is positioned behind the main element stagnation point is likely to drastically change the nacelle interference effects, as it is likely

to avoid the wedge-like flow features on the upper surface. Furthermore, a lower nacelle position may also benefit the powered conditions. It would mean that the nacelle-root system vortex in powered conditions would pass fully on the lower surface, which would reduce crossflow on the upper surface. This crossflow was connected to local boundary layer accumulation and flow separation in Chapter 5. Such configurations are, of course, associated with their own potential drawback, most notably the drag penalties in cruise conditions associated with a lower nacelle position and increased wetted area. It should also be noted that the propeller position, and therefore that of the nacelle, plays a role in many aerodynamic interactions that have been studied extensively in literature (e.g., [40, 31, 43, 47, 48]), but have not been discussed in this section. Nonetheless, the impact of nacelle position and the wing integration, both in powered and unpowered conditions, is a topic that warrants further investigation.

Finally, the impact of the nacelle interference should motivate the investigation of novel integration concepts. Tiltable nacelles may be a solution to some problems of the high-lift performance, while maintaining optimal drag characteristics during cruise. While this is difficult to implement on the large engines of a typical turboprop aircraft, this may be easier for distributed propeller configurations with smaller electric motors and nacelles. A variable nacelle angle can also have benefits for propeller performance, by mitigating non-uniform inflow conditions, and for powered high-lift performance, by controlling the intersection between the propeller slipstream and the wing for varying wing circulation and angle of attack. Nacelle-root vortex system ingestion may be another interesting concept. Ingesting the nacelle-root vortex system into, for instance, a cooling inlet around the nacelle, could reduce the impact of nacelle effects on the wing flow while also providing necessary cooling for electric motors.

**10**

# A

## PERFORMANCE CHARACTERISTICS OF THE TUD-PWF MODEL IN CLEAN CONFIGURATION

This appendix includes the general performance characteristics of the Delft University of Technology Propeller-Wing-Flap (TUD-PWF) wind tunnel model (see Chapter 2.1.1) in clean wing configuration, meaning without propeller or nacelle mounted. The presented results were obtained during the first experiment, detailed in Chapter 2.1.3. This appendix includes a comparison of the baseline measurements with original documentation on the airfoil design by Boermans and Rutten [62]. It furthermore details issues with stall cells at high angles of attack, the boundary layer suction system used and the sensitivity of the wing to the method of boundary layer tripping.

### A.1. BASELINE MEASUREMENTS

Figure A.1 shows the aerodynamic coefficients obtained from the pressure tap measurements during the experiment, in comparison with data obtained by Boermans and Rutten [62] in reference experiments using the same airfoil. It should be noted that the 30 degrees flap case by Boermans features 0.5% overlap rather than 0% as in the present experiments. Both the present (LTT) and data from Boermans and Rutten (Boermans) have been corrected for windtunnel boundary effects using the method by Allen and Vincenti [117], however, for the present experiments the wake blockage correction is only based on pressure drag. Whereas Boermans and Rutten report total drag extracted from wake rake measurements, no such data was available for the LTT experiments. The wake blockage correction for the LTT data is therefore slightly undervalued, though this is expected to be within 1% of the respective coefficient values as the model chord of 0.3 m is small compared to the wind tunnel width of 1.8 m (since the model is mounted vertically).

---

The contents of this appendix were previously published in Ref. [54].
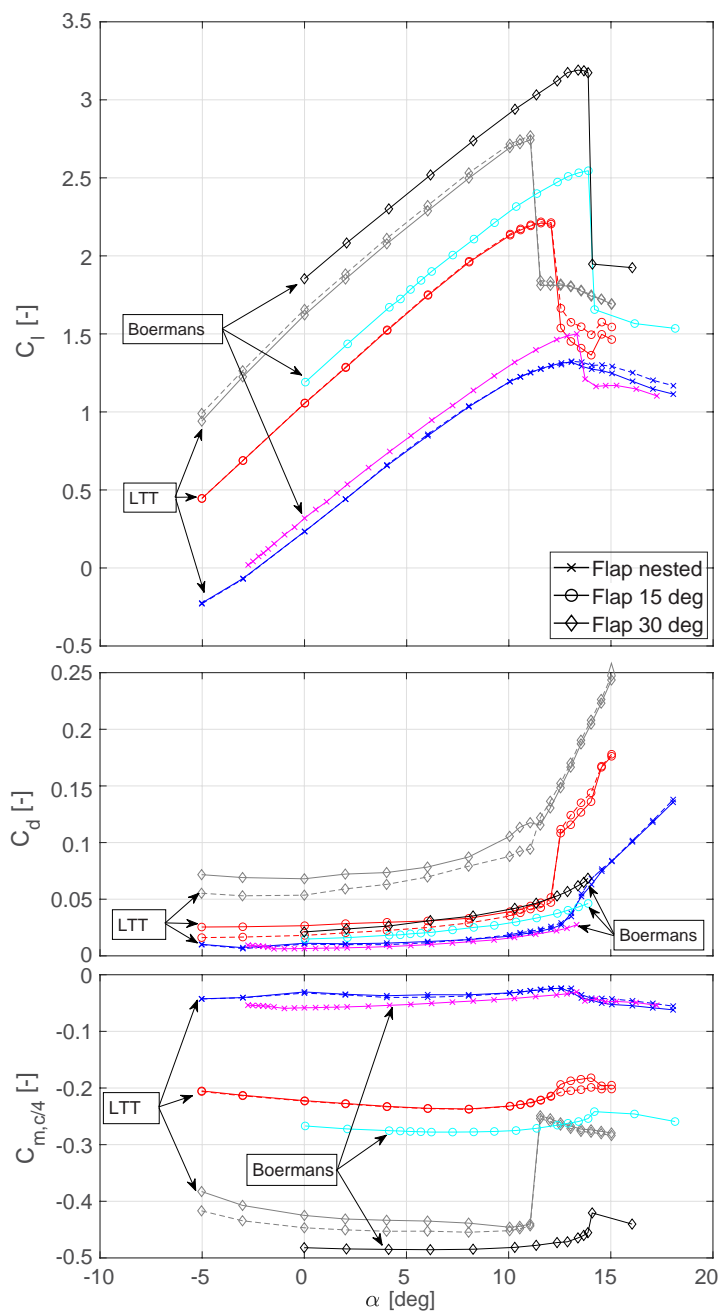
Figure A.1: Polars of local aerodynamic coefficients for clean wing configurations in the first experiment (LTT) versus reference (Boermans) [62]. Solid and dashed lines of LTT data represent respectively down- and upgoing blade side pressure tap locations. Corrected wind tunnel data.

The results obtained by Boermans and Rutten [62] are different from the results obtained in the presently described experiment, as can be seen from Fig. A.1. The lift coefficient with flap nested is consistently higher in the Boermans data than in the present experiment and it shows leading edge stall characteristics, while the present experiment shows signs of more gradual trailing edge stall. The discrepancy between Boermans and LTT data increases when a flap is deployed, showing significantly higher flap effectiveness in the Boermans experiments, with more lift generated across the polar and a higher angle of maximum lift. The moment coefficients fall closer together for both experiments, with the major discrepancy found in the 30 degrees flap case, which shows a large jump post-stall due to complete flow separation on the flap. The Boermans data shows flow on the flap to remain attached despite the main element stalling and thus shows a much smaller change in moment coefficient.

### A.1.1. Reynolds and Mach Number Effects

At least a part of the observed differences between the LTT and Boermans results can be attributed to Reynolds number effects. The Boermans experiments were performed at $Re = 3E6$ for the flap nested case, $Re = 2E6$ for the 15 degrees flap and $Re = 1.7E6$ for the 30 degrees flap, while the LTT experiments were all performed at approximately $Re = 6E5$. This meant that laminar separation bubbles could occur, which were observed with the 30 degree flap case. Increases in angle of maximum lift are in line with what would be expected of Reynolds number effects in this critical range [61]. Mach number effects may also play a role, particularly for the flapped cases. Though these effects have not been investigated specifically, they are expected to be small. The LTT experiments were performed at $M = 0.088$ for all configurations, while the Boermans data were captured at $M \approx 0.23$, $M \approx 0.15$ and $M \approx 0.12$ for flap nested, flap 15 degrees and flap 30 degrees cases, respectively.

### A.1.2. Spanwise variations

During baseline measurements of the clean wing at high angles of attack, low-frequency unsteady behaviour of pressure measurements was noticed along with the existence of spanwise variation of flow separation on the wing. The latter are visualized using tufts in Fig. A.2. The observations are consistent with observations made on other quasi-2D windtunnel setups, such as by Winkelmann and Barlow [61], Yon and Katz [118] and more recently Broeren and Bragg [119]. Broeren and Bragg [119] specifically describe the existence of two types of post-stall behaviours, namely stall cells as three-dimensional structures and low-frequency unsteady oscillations.

Addition of the zigzag tape improved two-dimensionality of the flow, resulting in less divergence between starboard- and port-side pressure tap measurements, but spanwise variation was not fully eliminated. The model with nacelle mounted no longer showed clear stall cells, but still exhibited spanwise asymmetry at higher angles of attack. This is consistent with observations by Winkelmann and Barlow [120] and Yon and Katz [118], who note a correlation between the wing aspect ratio and the number of stall cells that form. Considering the nacelle to effectively slice the wing into two low aspect ratio parts, this would eliminate the possibility for a full stall cell to develop but would not solve the spanwise asymmetry. For the interpretation of the pressure measurements, this means
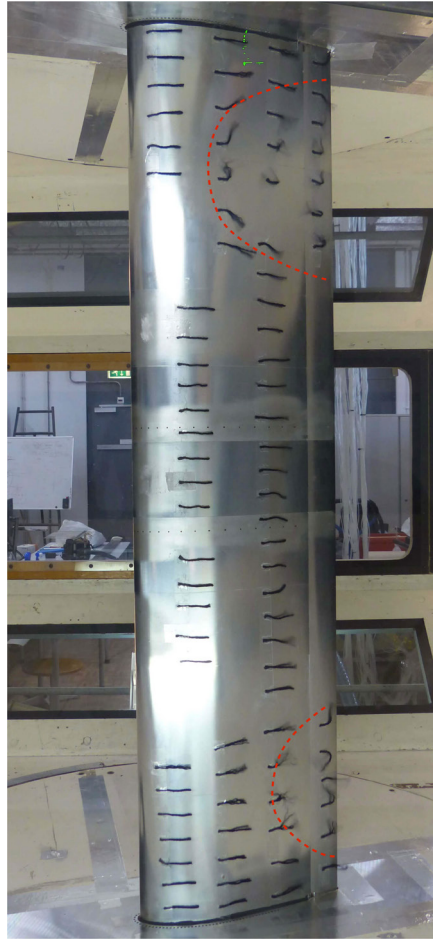
Figure A.2: Stall cells occurring on the clean wing with flap nested at $\alpha = 13^o$ visualized by tufts.

that they should always be treated as local measurements only and cannot represent the complete wing, even in clean wing configuration.

## A.2. Boundary Layer Suction System

In experiments with the same model in a different wind tunnel by de Vries et al. [121], strong junction flows were observed at the wing-wall boundary that induced early onset of separation. In order to mitigate these effects, a wall boundary layer suction (BLS) system was applied, based on the system applied in the original reports of the NLF-Mod22(B) profile by Boermans and Rutten [62]. Figure A.3 shows the row of holes in the wall end plate, present at both sides of the model, which were externally connected to a suction pump. Because the flap was to be moved throughout the experiment, suction holes were only applied around the main element. The interaction between the wing and the wall

boundary layer of the wind tunnel in the presently described experiments was found to lead to no appreciable affect of the BLS on any of the measurements taken. The results presented in this dissertation were therefore all captured without application of BLS.



Figure A.3: Holes in the side plate around the main element of the wing for the suction system.

## A.3. SENSITIVITY TO TRIPPING METHOD

In an attempt to provide a fixed boundary layer tripping point for numerical validation purposes, as well as to mitigate three-dimensional flow characteristics at high angles of attack, several trip strips were tested on the wing, all placed at 10% chord on the suction side only. Originally, the intention was to apply carborundum to the wing as a tripping mechanism, following the calculation procedure from Braslow [122]. Unfortunately, although spanwise flow variation seemed to be mitigated, this induced strong decambering and reduction of maximum lift coefficient of the wing, as can be seen in Fig. A.4. The decambering effect was attributed to the method of application, as the carborundum was placed on a thin layer of adhesive tape which was in turn applied to the wing. This may have caused unintended boundary layer growth.

Application of zigzag-strips yielded better results. A strip of 0.255 mm height and 12 mm width was applied, resulting in a lift polar much closer to the untripped case, while mitigating spanwise variation as shown in Fig. A.4 by the reduced discrepancy between port and starboard measurements compared to the untripped case. Attempts to further reduce the decambering effect by applying zigzag strips of smaller width and lower heights did not prove fruitful, as all deviations from the 0.255/12 mm strip resulted in a higher discrepancy with the untripped measurements. The 0.255/12 mm zigzag-strip was therefore determined to be the best option and was applied at 10% of the chord for all of the measurements described in the present document.
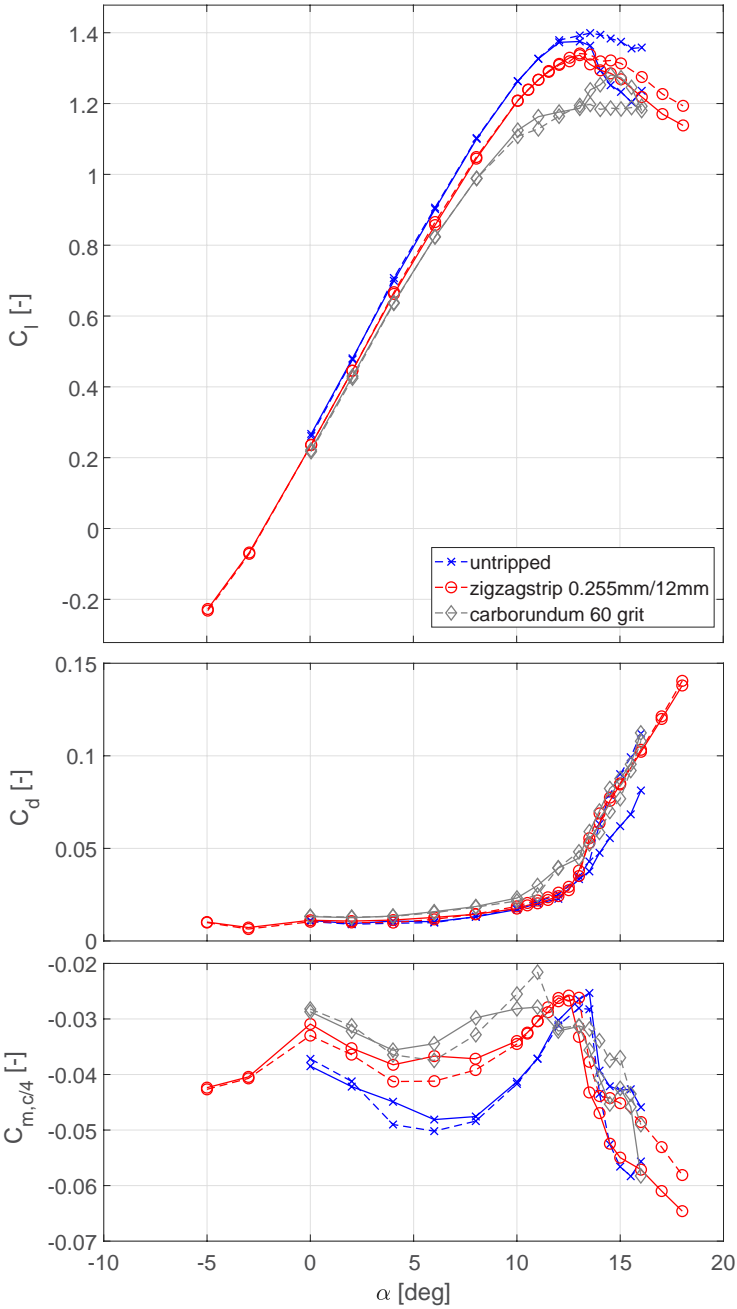
Figure A.4: Integrated local pressure measurements versus angle of attack for various methods of boundary layer tripping, showing significant decambering compared to the untripped lift polar.

# B

# 2D RANS GRID CONVERGENCE STUDY

This appendix contains details on the grid convergence study performed for the 2D RANS simulations described in Chapter 2, which were used for the verification of MSES in Chapter 3.

For each of the verification points used to verify the modified MSES solver in Chapter 3, we carried out a grid convergence study following the approach outlined by Eça and Hoekstra [123] to estimate the discretization error. This approach uses least-squares based Richardson Extrapolation to deal with the inherent scatter present in simulations on unstructured meshes, and incorporate this in the error estimation. Table B.1 summarizes the number of cells and relative average cell size in each grid for each run. The various mesh refinements were achieved by reducing the main airfoil element size by 1.2, which results in consistently increasing refinement for each consecutive grid due to the dependency on the main airfoil discretization. Only the initial layer height and number of inflation layers remain constant between each refinement, to satisfy the observation by Roache [124] that grid convergence should be performed from the edge of the wall layer out. The total number of cells varies between verification points due to differences in the inflation layers, which are Reynolds number dependent, and different jet positions.

Table B.1: Overview of number of cells and relative cell sizes for each configuration

| | VP1 (Max L/D) | | VP2 (Min $C_d$) | | VP3 (Max $C_l$) | | VP4 (Max $C_d$) | | VP5 (Min L/D) | |
|---|---|---|---|---|---|---|---|---|---|---|
| | $N_{cells}$ | $h_i/h_1$ | $N_{cells}$ | $h_i/h_1$ | $N_{cells}$ | $h_i/h_1$ | $N_{cells}$ | $h_i/h_1$ | $N_{cells}$ | $h_i/h_1$ |
| Grid 1 | 4.14e6 | 2.01 | 3.28e6 | 1.99 | - | - | - | - | - | - |
| Grid 2 | 5.85e6 | 1.69 | 4.60e6 | 1.68 | 6.03e6 | 1.69 | 5.79e6 | 1.69 | 3.59e6 | 1.67 |
| Grid 3 | 8.26e6 | 1.42 | 6.47e6 | 1.41 | 8.57e6 | 1.42 | 8.25e6 | 1.42 | 5.04e6 | 1.41 |
| Grid 4 | 1.17e7 | 1.19 | 9.14e6 | 1.19 | 1.21e7 | 1.19 | 1.17e7 | 1.19 | 7.10e6 | 1.19 |
| Grid 5 | 1.67e7 | 1.00 | 1.29e7 | 1.00 | 1.72e7 | 1.00 | 1.66e7 | 1.00 | 1.00e7 | 1.00 |

[1]The contents of this appendix were previously published in Ref. [56].

B

Table B.2 shows the discretization error of the finest grid of each verification point resulting from the grid convergence study. Verification points 3 through 5 were not properly converged for the coarsest grids, so the convergence for these points is only based on the four finest grids. The resulting discretization error is below 5% for all coefficients, except for the moment coefficient of verification point 5. We attribute this to the grids not being in the asymptotic region, resulting in unpredictable behaviour of the least-squares Richardson extrapolation as shown in Fig. B.1. The maximum difference in $C_m$ between all grids of VP5 are within 2% of each other, which we deem sufficient for a comparison with MSES. Comparisons in Chapter 3 are all based on the finest grids of the convergence study.

Table B.2: Discretization error for the finest grid of each verification point.

|  | VP1 (Max. $L/D$) | VP2 (Min. $C_d$) | VP3 (Max. $C_l$) | VP4 (Max. $C_d$) | VP5 (Min. $L/D$) |
|---|---|---|---|---|---|
| $N_{grids}$ | 5 | 5 | 4 | 4 | 4 |
| $C_l$ | 0.36% | 0.37% | 1.33% | 0.24% | 0.43% |
| $C_d$ | 3.07% | 1.81% | 1.55% | 1.84% | 4.49% |
| $C_m$ | 0.18% | 0.38% | 1.45% | 2.54% | 6.02% |

(a) $C_l$ response

(b) $C_d$ response

(c) $C_m$ response
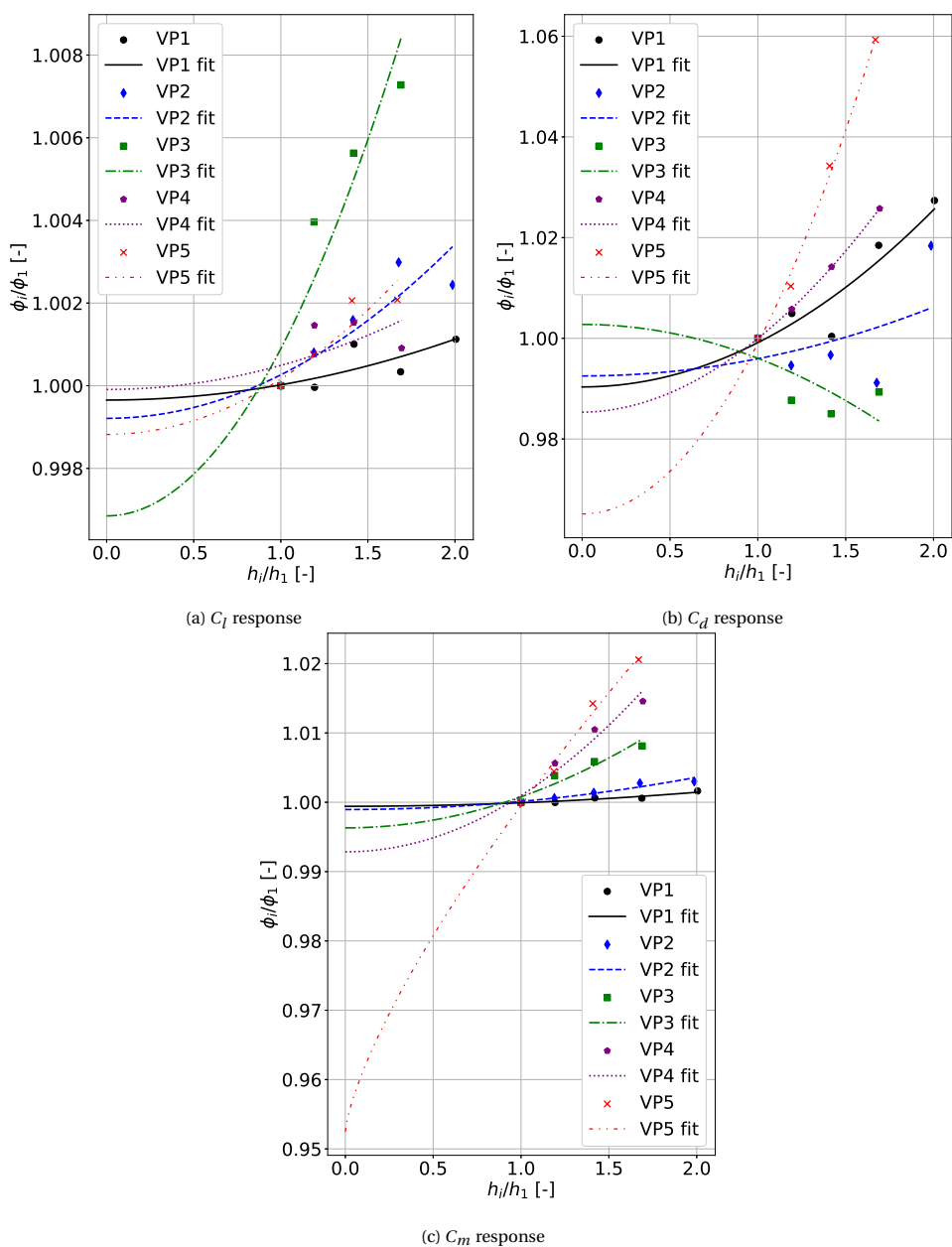
Figure B.1: Grid convergence trends for lift, drag, and moment coefficients of the airfoil for each of the verification runs.

# REFERENCES

[1] Epstein, A. H., "Aeropropulsion for Commercial Aviation in the Twenty-First Century and Research Directions Needed," *AIAA Journal*, Vol. 52, No. 5, 2014, pp. 901–911. DOI: 10.2514/1.J052713.

[2] Rudnik, R., Rossow, C.-C., and Frhr. v. Geyr, H., "Numerical simulation of engine/airframe integration for high-bypass engines," *Aerospace Science and Technology*, Vol. 6, No. 1, 2002, pp. 31–42. DOI: 10.1016/S1270-9638(01)01139-7.

[3] Dron, S., "Toward ACARE 2020: Innovative engine architectures to achieve the environmental goals?" *26th Congress of International Council of the Aeronautical Sciences 2008*, International Council of the Aeronautical Sciences, Anchorage, Alaska, USA, 2008, p. 10.

[4] CFM International, "CFM RISE program," White paper, CFM, 2021.

[5] Magliozzi, B., Hanson, D. B., and Amiet, R. K., "Propeller and propfan noise," *Aeroacoustics of Flight Vehicles: Theory and Practice. Volume 1: Noise Sources*, Vol. 1, 1991, pp. 1–64.

[6] Nicolai, L. M., and Carichner, G., "Chapter 17: Propeller Propulsion Systems," *Fundamentals of Aircraft and Airship Design. Volume 1 - Aircraft Design*, American Institute of Aeronautics and Astronautics, 2010, Chap. 17, 1$^{st}$ ed., pp. 435–466.

[7] Thijssen, R., Proesmans, P., and Vos, R., "Propeller Aircraft Design Optimization for Climate Impact Reduction," *33rd Congress of the International Council of the Aeronautical Sciences*, International Council of the Aeronautical Sciences, Stockholm, Sweden, 2022, p. 23.

[8] Moore, M. D., and Fredericks, B., "Misconceptions of Electric Aircraft and their Emerging Aviation Markets," *52nd Aerospace Sciences Meeting*, American Institute of Aeronautics and Astronautics, Reston, Virginia, 2014, pp. 1–17. DOI: 10.2514/6.2014-0535.

[9] Stoll, A. M., Bevirt, J., Moore, M. D., Fredericks, W. J., and Borer, N. K., "Drag Reduction Through Distributed Electric Propulsion," *14th AIAA Aviation Technology, Integration, and Operations Conference*, American Institute of Aeronautics and Astronautics, Reston, Virginia, 2014, pp. 16–20. DOI: 10.2514/6.2014-2851.

[10] Sinnige, T., "Aerodynamic and Aeroacoustic Interaction Effects for Tip-Mounted Propellers - An Experimental Study," Phd dissertation, Delft University of Technology, 2018. DOI: 10.4233/uuid:214e1e9a-c53e-47c7-a12c-b1eb3ec8293b.

**B**

[11] Keller, D., "Towards higher aerodynamic efficiency of propeller-driven aircraft with distributed propulsion," *CEAS Aeronautical Journal*, Vol. 12, No. 4, 2021, pp. 777–791. DOI: 10.1007/s13272-021-00535-5.

[12] Schollenberger, M., Kirsch, B., Lutz, T., Krämer, E., and Friedrichs, J., "Aerodynamic interactions between distributed propellers and the wing of an electric commuter aircraft at cruise conditions," *CEAS Aeronautical Journal*, 2024. DOI: 10.1007/s13272-023-00706-6.

[13] Smith, L. H., "Wake ingestion propulsion benefit," *Journal of Propulsion and Power*, Vol. 9, No. 1, 1993, pp. 74–82. DOI: 10.2514/3.11487.

[14] de Vries, R., "Hybrid-Electric Aircraft with Over-the-Wing Distributed Propulsion Aerodynamic Performance and Conceptual Design," Phd dissertation, Delft University of Technology, 2022. DOI: 10.4233/uuid:ef87dc11-e7b2-4726-a41f-28588d64c58d.

[15] Paula Costa, F., Tomita, J. T., Silva, V. T., Andersson, N., Grönstedt, T., and Bringhenti, C., "Aerodynamic Analysis of Conventional and Boundary Layer Ingesting Propellers," *Journal of Engineering for Gas Turbines and Power*, Vol. 145, No. 1, 2023, pp. 1–20. DOI: 10.1115/1.4055014.

[16] Pascioni, K. A., Rizzi, S. A., and Schiller, N., "Noise Reduction Potential of Phase Control for Distributed Propulsion Vehicles," *AIAA Scitech 2019 Forum*, American Institute of Aeronautics and Astronautics, Reston, Virginia, 2019, pp. 1–16. DOI: 10.2514/6.2019-1069.

[17] Patterson, M. D., "Conceptual Design of High-Lift Propeller Systems for Small Electric Aircraft Coceptual Design of High-Lift Propeller," Phd dissertation, Georgia Institute of Technology, 2016.

[18] Borer, N. K., Patterson, M. D., Viken, J. K., Moore, M. D., Bevirt, J., Stoll, A. M., and Gibson, A. R., "Design and Performance of the NASA SCEPTOR Distributed Electric Propulsion Flight Demonstrator," *16th AIAA Aviation Technology, Integration, and Operations Conference*, American Institute of Aeronautics and Astronautics, Reston, Virginia, 2016, pp. 1–20. DOI: 10.2514/6.2016-3920.

[19] Viken, J. K., Viken, S., Deere, K. A., and Carter, M., "Design of the Cruise and Flap Airfoil for the X-57 Maxwell Distributed Electric Propulsion Aircraft," *35th AIAA Applied Aerodynamics Conference*, American Institute of Aeronautics and Astronautics, Reston, Virginia, 2017, pp. 1–41. DOI: 10.2514/6.2017-3922.

[20] Torenbeek, E., *Synthesis of Subsonic Airplane Design*, Springer Netherlands, Dordrecht, 1982. DOI: 10.1007/978-94-017-3202-4.

[21] Rudolph, P. K. C., "High-Lift Systems on Commercial Subsonic Airliners," NASA Contractor Report 4746, National Aeronautics and Space Administration, Seattle, Washington, USA, 1996.

[22] Kuhn, R. E., and Draper, J. W., "Investigation of Effectiveness of Large-Chord Slotted Flaps in Deflecting Propeller Slipstreams Downward for Vertical Take-Off and Low-Speed Flight," NACA Technical Note 3364, National Advisory Committee for Aeronautics, 1955.

[23] AGARD, "Aerodynamics of V/STOL Aircraft," AGARDograph 126, Advisory Group for Aerospace Reserach and Development, 1968.

[24] Moebs, N., Eisenhut, D., Bergmann, D., and Strohmayer, A., "Selecting figures of merit for a hybrid-electric 50-seat regional aircraft," *IOP Conference Series: Materials Science and Engineering*, Vol. 1024, No. 1, 2021, p. 012071. DOI: 10.1088/1757-899X/1024/1/012071.

[25] "NASA Urban Air Mobility (UAM) Reference Vehicles," https://sacd.larc.nasa.gov/uam-refs/, 2024.

[26] Prandtl, L., "Mutual Influence of Wings and Propeller," NACA Technical Notes 74, National Advisory Committee for Aeronautics, 1921.

[27] Jameson, A., "The Analysis of Propeller-Wing Flow Interaction," *NASA SP-228: Analytic Methods in Aircraft Aerodynamics*, National Aeronautics and Space Administration, 1970, pp. 721–742.

[28] Kroo, I., "Propeller-Wing Integration for Minimum Induced Loss." *Journal of Aircraft*, Vol. 23, No. 7, 1986, pp. 561–565. DOI: 10.2514/3.45344.

[29] Witkowski, D. P., Lee, A. K., and Sullivan, J. P., "Aerodynamic interaction between propellers and wings," *Journal of Aircraft*, Vol. 26, No. 9, 1989, pp. 829–836. DOI: 10.2514/3.45848.

[30] Samuelsson, I., "Experimental Investigation of Low Speed Model Propeller Slipstream Aerodynamic Characteristics Including Flow Field Surveys and Nacelle/Wing Static Pressure Measurements," *17th Congress of the International Council of the Aeronautical Sciences*, International Council of the Aeronautical Sciences, Stockholm, Sweden, 1990, pp. 17–84.

[31] Veldhuis, L., "Propeller wing aerodynamic interference," Phd dissertation, Delft University of Technology, 2005. URL https://resolver.tudelft.nl/uuid:8ffbde9c-b483-40de-90e0-97095202fbe3.

[32] Aljabri, A., and Hughes, A., "Wind Tunnel Investigation of the Interaction of Propeller Slipstream with Nacelle/Wing/Flap Combinations," Paper 21 21, Advisory Group for Aerospace Research & Development, 1984.

[33] Felli, M., "Underlying mechanisms of propeller wake interaction with a wing," *Journal of Fluid Mechanics*, Vol. 908, 2021, p. A10. DOI: 10.1017/jfm.2020.792.

[34] Eshelby, M. E., "On the Aerodynamics of Installed Propellers," Paper 8 AGARD CP-366, Advisory Group for Aerospace Research and Development, 1984.

**B**

[35] Smith, A. M. O., "High-Lift Aerodynamics," *Journal of Aircraft*, Vol. 12, No. 6, 1975, pp. 501–530. DOI: 10.2514/3.59830.

[36] Wild, J., "Experimental investigation of Mach- and Reynolds-number dependencies of the stall behavior of 2-element and 3-element high-lift wing sections," *50th AIAA Aerospace Sciences Meeting including the New Horizons Forum and Aerospace Exposition*, American Institute of Aeronautics and Astronautics, Reston, Virigina, 2012, pp. 1–22. DOI: 10.2514/6.2012-108.

[37] Rumsey, C. L., and Ying, S. X., "Prediction of high lift: review of present CFD capability," *Progress in Aerospace Sciences*, Vol. 38, No. 2, 2002, pp. 145–180. DOI: 10.1016/S0376-0421(02)00003-9.

[38] Kuhn, R. E., and Draper, J. W., "An Investigation of a Wing-Propeller Configuration Employing Large-Chord Plain Flaps and Large-Diameter Propellers for Low-Speed Flight and Vertical Take-Off," NACA Technical Note 3307, National Advisory Committee for Aeronautics, 1954.

[39] Kuhn, R. E., and Hayes, Jr., W. C., "Wind-Tunnel Investigation of Effect of Propeller Slipstreams on Aerodynamic Characteristics of a Wing Equipped with a 50-Percent-Chord Sliding Flap and a 30-Percent-Chord Slotted Flap," NACA Technical Note 3918, National Advisory Committee for Aeronautics, 1957.

[40] Hayes, Jr., W. C., Kuhn, R. E., and Sherman, I. R., "Effects of Propeller Position and Overlap on the Slipstream Deflection Characteristics of a Wing-Propeller Configuration Equipped with a Sliding and Fowler Flap," NACA Technical Note 4404, National Advisory Committee for Aeronautics, 1958.

[41] Newsom, Jr., W. A., "Effect of Propeller Location and Flap Deflection on the Aerodynamic Characteristics of a Wing-Propeller Combination for Angles of Attack from 0 degrees to 80 degrees," NACA Technical Note 3917, National Advisory Committee for Aeronautics, 1957.

[42] Bertelsen, W. D., and Bertelsen, W. R., "History of Deflected Slipstream VTOL Aircraft," *American Helicopter Society 61st Annual Forum*, American Helicopter Society International, Grapevine, TX, 2005, pp. 1–18.

[43] Cui, G.-P., Feng, L.-H., and Wang, W.-J., "Aerodynamic characteristic of deflected slipstream aimed at vertical takeoff and landing," *Journal of Aircraft*, Vol. 56, No. 4, 2019, pp. 1418–1426. DOI: 10.2514/1.C035047.

[44] Long, T., Drela, M., Hansman, J., and Courtin, C., "Parametric Design Study for a Blown Flapped Wing," *AIAA AVIATION 2021 FORUM*, American Institute of Aeronautics and Astronautics, Reston, Virginia, 2021, pp. 1–26. DOI: 10.2514/6.2021-2871.

[45] Bongen, D., Firnhaber Beckers, M., Schollenberger, M., Bergmann, D. P., Lutz, T., Gothow, A., Saeed, M., Weiss, J., Bardenhagen, A., and Radespiel, R., "Simulation of a Distributed Propulsion System in a Wind Tunnel," *AIAA AVIATION 2022 Forum*,

**B**

American Institute of Aeronautics and Astronautics, Chicago, Illinois, 2022, pp. 1–18. DOI: 10.2514/6.2022-3818.

[46] Beckers, M. F., Schollenberger, M., Lutz, T., Bongen, D., Radespiel, R., Florenciano, J. L., and Funes-Sebastian, D. E., "Numerical Investigation of High-Lift Propeller Positions for a Distributed Propulsion System," *Journal of Aircraft*, Vol. 60, No. 4, 2023, pp. 995–1006. DOI: 10.2514/1.C037248.

[47] Firnhaber Beckers, M., Schollenberger, M., Lutz, T., Bongen, D., Radespiel, R., Florenciano, J. L., and Funes-Sebastian, D. E., "CFD Investigation of High-Lift Propeller Positions for a Distributed Propulsion System," *AIAA AVIATION 2022 Forum*, American Institute of Aeronautics and Astronautics, Reston, Virginia, 2022, pp. 1–18. DOI: 10.2514/6.2022-3217.

[48] Oldeweme, J., Lindner, T. K., Scholz, P., and Friedrichs, J., "Experimental Propeller Performance Analysis of Distributed, Single and Isolated configurations," *Journal of Physics: Conference Series*, Vol. 2716, No. 1, 2024, p. 012004. DOI: 10.1088/1742-6596/2716/1/012004.

[49] de Vries, R., van Arnhem, N., Sinnige, T., Vos, R., and Veldhuis, L. L., "Aerodynamic interaction between propellers of a distributed-propulsion system in forward flight," *Aerospace Science and Technology*, Vol. 118, 2021, p. 107009. DOI: 10.1016/j.ast.2021.107009.

[50] van Dam, C., "The Aerodynamic Design of Multi-Element High-Lift Systems of Transport Airplanes," *Progress in Aerospace Sciences*, Vol. 38, No. 2, 2002, pp. 101–144.

[51] Wild, J., "Recent research topics in high-lift aerodynamics," *CEAS Aeronautical Journal*, Vol. 7, No. 3, 2016, pp. 345–355. DOI: 10.1007/s13272-016-0206-3.

[52] Rumsey, C. L., Slotnick, J. P., and Sclafani, A. J., "Overview and Summary of the Third AIAA High Lift Prediction Workshop," *Journal of Aircraft*, Vol. 56, No. 2, 2019, pp. 621–644. DOI: 10.2514/1.C034940.

[53] van Arnhem, N., "Unconventional Propeller-Airframe Integration for Transport Aircraft Configurations," Phd dissertation, Delft University of Technology, 2022. DOI: 10.4233/uuid:4d47b0db-1e6a-4f38-af95-aafd33c29402.

[54] Duivenvoorden, R. R., Suard, N., Sinnige, T., and Veldhuis, L. L., "Experimental Investigation of Aerodynamic Interactions of a Wing with Deployed Fowler Flap under Influence of a Propeller Slipstream," *AIAA AVIATION 2022 Forum*, American Institute of Aeronautics and Astronautics, Reston, Virginia, 2022, pp. 1–19. DOI: 10.2514/6.2022-3216.

[55] Ribeiro, A. F., Duivenvoorden, R. R., and Martins, D., "High-Fidelity Simulations of Propeller-Wing Interactions in High-Lift Conditions," *AIAA AVIATION 2023 Forum*, American Institute of Aeronautics and Astronautics, San Diego, CA, 2023, pp. 1–16. DOI: 10.2514/6.2023-3541.

[56] Duivenvoorden, R. R., Sinnige, T., Veldhuis, L. L. M., and Friedrichs, J., "Multi-Element Airfoil in Jet Flows: Identifying Dominant Factors and Interactions," *Journal of Aircraft*, 2024, pp. 1–19. DOI: 10.2514/1.C037741.

[57] Duivenvoorden, R. R., Ribeiro, A. F. P., Sinnige, T., and Veldhuis, L. L. M., "Slipstream Deformation in Propeller-Wing-Flap Aerodynamic Interaction," *in review*, 2024, pp. 1–36.

[58] Duivenvoorden, R. R., Monteiro, F. d., and Sinnige, T., "Experimental Measurements of Slipstream Deformation for an Installed Distributed Propeller Configuration," *34th Congress of the International Council of the Aeronautical Sciences*, International Council of the Aeronautical Sciences, Florence, Italy, 2024, pp. 1–12.

[59] Dobbinga, E., and van Ghesel Grothe, J. A., "De Lage-Snelheids Windtunnel van de Sub-Afdeling Vliegtuig Bouwkunde der Technische Hogeschool," Technical Report 77, Delft University of Technology, 1955. URL https://resolver.tudelft.nl/uuid:dbf0b1e4-f765-439f-9acd-309de527d2c7.

[60] Serpieri, J., "Cross-Flow Instability: Flow diagnostics and control of swept wing boundary layers," Phd dissertation, Delft University of Technology, 2018. DOI: 10.4233/uuid:3dac1e78-fcc3-437f-9579-048b74439f55, URL https://resolver.tudelft.nl/uuid:3dac1e78-fcc3-437f-9579-048b74439f55.

[61] Barlow, J. B., Rae, W. H., and Pope, A., *Low-Speed Wind Tunnel Testing*, 3rd ed., John Wiley & Sons, Inc., 1999.

[62] Boermans, L., and Rutten, P., "Two-dimensional aerodynamic characteristics of airfoil NLF-MOD22 with fowler flap," Tech. rep., Delft University of Technology, Delft, 1995.

[63] van Arnhem, N., de Vries, R., Sinnnige, T., and Veldhuis, L. L., "XPROP-S propeller geometry," Zenodo, 2022. DOI: 10.5281/zenodo.6355670.

[64] van Arnhem, N., de Vries, R., Sinnige, T., Vos, R., Eitelberg, G., and Veldhuis, L. L. M., "Engineering Method to Estimate the Blade Loading of Propellers in Nonuniform Flow," *AIAA Journal*, Vol. 58, No. 12, 2020, pp. 5332–5346. DOI: 10.2514/1.J059485.

[65] Duivenvoorden, R. R., Sinnige, T., and Veldhuis, L. L., "TU Delft Propeller-Wing-Flap (TUD-PWF) wind tunnel model geometry," Zenodo, 2025. DOI: 10.5281/zenodo.13344026.

[66] Duivenvoorden, R. R., Sinnige, T., and Veldhuis, L. L. M., "Experimental dataset of wind tunnel campaigns with a propeller-wing-flap model," 4TU.ResearchData, 2025. DOI: 10.4121/3161b813-ad38-4f9c-bb9d-333b895f46bc.

[67] Savitzky, A., and Golay, M. J. E., "Smoothing and Differentiation of Data by Simplified Least Squares Procedures." *Analytical Chemistry*, Vol. 36, No. 8, 1964, pp. 1627–1639. DOI: 10.1021/ac60214a047.

[68] Shaw-ward, S., Titchmarsh, A., and Birch, D. M., "Calibration and Use of n -Hole Velocity Probes," *AIAA Journal*, Vol. 53, No. 2, 2015, pp. 336–346. DOI: 10.2514/1.J053130.

[69] Zuccher, S., and Saric, W. S., "Infrared thermography investigations in transitional supersonic boundary layers," *Experiments in Fluids*, Vol. 44, No. 1, 2007, pp. 145–157. DOI: 10.1007/s00348-007-0384-1.

[70] Simon, B., Filius, A., Tropea, C., and Grundmann, S., "IR thermography for dynamic detection of laminar-turbulent transition," *Experiments in Fluids*, Vol. 57, No. 5, 2016, p. 93. DOI: 10.1007/s00348-016-2178-9.

[71] Monteiro, F. d., Duivenvoorden, R. R., Ragni, D., Avallone, F., and Sinnige, T., "Experimental Analysis of Synchrophasing Impact on Noise of Distributed Propeller Systems in Tractor Configuration," *30th AIAA/CEAS Aeroacoustics Conference (2024)*, American Institute of Aeronautics and Astronautics, Reston, Virginia, 2024, pp. 1–10. DOI: 10.2514/6.2024-3421.

[72] Drela, M., "Newton solution of coupled viscous/inviscid multielement airfoil flows," *AIAA 21st Fluid Dynamics, Plasma Dynamics and Lasers Conference, 1990*, 1990. DOI: 10.2514/6.1990-1470.

[73] Drela, M., "Design and optimization method for multi-element airfoils," *AIAA/AHS/ASEE Aerospace Design Conference, 1993*, 1993. DOI: 10.2514/6.1993-969.

[74] Drela, M., "A User's Guide to MSES 3.05," Tech. Rep. July 2007, 2007.

[75] van den Berg, B., and Oskam, B., "Boundary Layer Measurements on a Two-Dimensional Wing with Flap and a Comparison with Calculations," Report NLR MP 79034 U, National Aerospace Laboratory (NLR), The Hague, The Netherlands, 1979.

[76] Montgomery, D. C., *Design and Analysis of Experiments*, 8th ed., John Wiley & Sons, Inc., 2013.

[77] Ting, L., Liu, C. H., and Kleinstein, G., "Interference of wing and multipropellers," *AIAA Journal*, Vol. 10, No. 7, 1972, pp. 906–914. DOI: 10.2514/3.50244.

[78] Patterson, M. D., Derlaga, J. M., and Borer, N. K., "High-Lift Propeller System Configuration Selection for NASA's SCEPTOR Distributed Electric Propulsion Flight Demonstrator," *16th AIAA Aviation Technology, Integration, and Operations Conference*, American Institute of Aeronautics and Astronautics, Reston, Virginia, 2016, pp. 1–19. DOI: 10.2514/6.2016-3922.

[79] Landman, D., Simpson, J., Vicroy, D., and Parker, P., "Efficient methods for complex aircraft configuration aerodynamic characterization using response surface methodologies," *Collection of Technical Papers - 44th AIAA Aerospace Sciences Meeting*, Vol. 15, No. January, 2006, pp. 11032–11043. DOI: 10.2514/6.2006-922.

B

[80] O'Brien, R. M., "A caution regarding rules of thumb for variance inflation factors," *Quality and Quantity*, Vol. 41, No. 5, 2007, pp. 673–690. DOI: 10.1007/s11135-006-9018-6.

[81] Daoud, J. I., "Multicollinearity and Regression Analysis," *Journal of Physics: Conference Series*, Vol. 949, No. 1, 2018. DOI: 10.1088/1742-6596/949/1/012009.

[82] Duda, B. M., Fares, E., Kotapati, R., Li, Y., Staroselsky, I., Zhang, R., and Chen, H., "Capturing Laminar to Turbulent Transition within the LBM based CFD solver PowerFLOW," *AIAA Scitech 2019 Forum*, American Institute of Aeronautics and Astronautics, Reston, Virginia, 2019, pp. 1–11. DOI: 10.2514/6.2019-1832.

[83] Casalino, D., Romani, G., Zhang, R., and Chen, H., "Lattice-Boltzmann calculations of rotor aeroacoustics in transitional boundary layer regime," *Aerospace Science and Technology*, Vol. 130, 2022, p. 107953. DOI: 10.1016/j.ast.2022.107953.

[84] Carnes, J., and Coder, J. G., "Benchmarking the Langtry-Menter Transition Model Using OVERFLOW for the AIAA Transition Modeling Workshop," *AIAA AVIATION 2022 Forum*, American Institute of Aeronautics and Astronautics, Reston, Virginia, 2022, pp. 1–26. DOI: 10.2514/6.2022-3680.

[85] Stokkermans, T. C. A., and Veldhuis, L. L. M., "Propeller Performance at Large Angle of Attack Applicable to Compound Helicopters," *AIAA Journal*, Vol. 59, No. 6, 2021, pp. 2183–2199. DOI: 10.2514/1.j059509.

[86] Miley, S. J., Howard, R. M., and Holmes, B. J., "Wing laminar boundary layer in the presence of a propeller slipstream," *Journal of Aircraft*, Vol. 25, No. 7, 1988, pp. 606–611. DOI: 10.2514/3.45630.

[87] Lötstedt, P., "A Propeller Slipstream Model in Subsonic Linearized Potential Flow," ICAS-90-5.4.4 ICAS-90-5.4.4, International Council of the Aeronautical Sciences, 1990.

[88] van Beek, C. M., Piers, W. J., and Oskam, B., "Aerodynamic Engine / Airframe Integration for High Performance Aircraft and Missiles," AGARD-CP-498 AGARD-CP-498, Advisory Group for Aerospace Research & Development, 1992.

[89] Sinnige, T., Ragni, D., Malgoezar, A. M., Eitelberg, G., and Veldhuis, L. L., "APIAN-INF: an aerodynamic and aeroacoustic investigation of pylon-interaction effects for pusher propellers," *CEAS Aeronautical Journal*, Vol. 9, No. 2, 2018, pp. 291–306. DOI: 10.1007/s13272-017-0247-2.

[90] Roosenboom, E. W., Heider, A., and Schröder, A., "Investigation of the propeller slipstream with particle image velocimetry," *Journal of Aircraft*, Vol. 46, No. 2, 2009, pp. 442–449. DOI: 10.2514/1.33917.

[91] Roosenboom, E. W., Stürmer, A., and Schröder, A., "Advanced experimental and numerical validation and analysis of propeller slipstream flows," *Journal of Aircraft*, Vol. 47, No. 1, 2010, pp. 284–291. DOI: 10.2514/1.45961.

[92] Roosenboom, E. W. M., "Image based measurement techniques for aircraft propeller flow diagnostics," Phd dissertation, Delft University of Technology, 2011.

[93] Felli, M., and Falchi, M., "Propeller tip and hub vortex dynamics in the interaction with a rudder," *Experiments in Fluids*, Vol. 51, No. 5, 2011, pp. 1385–1402. DOI: 10.1007/s00348-011-1162-7.

[94] Felli, M., Roberto, C., and Guj, G., "Experimental analysis of the flow field around a propeller–rudder configuration," *Experiments in Fluids*, Vol. 46, No. 1, 2009, pp. 147–164. DOI: 10.1007/s00348-008-0550-0.

[95] Muscari, R., Dubbioso, G., and Di Mascio, A., "Analysis of the flow field around a rudder in the wake of a simplified marine propeller," *Journal of Fluid Mechanics*, Vol. 814, 2017, pp. 547–569. DOI: 10.1017/jfm.2017.43.

[96] Posa, A., Broglia, R., and Balaras, E., "The wake structure of a propeller operating upstream of a hydrofoil," *Journal of Fluid Mechanics*, Vol. 904, No. A12, 2020, pp. 1–35. DOI: 10.1017/jfm.2020.680.

[97] Posa, A., and Broglia, R., "Flow over a hydrofoil at incidence immersed within the wake of a propeller," *Physics of Fluids*, Vol. 33, No. 12, 2021. DOI: 10.1063/5.0075231.

[98] Posa, A., and Broglia, R., "Development of the wake shed by a system composed of a propeller and a rudder at incidence," *International Journal of Heat and Fluid Flow*, Vol. 94, No. September 2021, 2022, p. 108919. DOI: 10.1016/j.ijheatfluidflow.2021.108919.

[99] Qiu, Y., Bai, J., and Qiao, L., "Aerodynamic Effects of Wing-Mounted Engine Nacelle on High-Lift Configuration of Turboprop Airliner," *Journal of Aircraft*, Vol. 55, No. 3, 2018, pp. 1082–1089. DOI: 10.2514/1.C034529.

[100] Felli, M., Camussi, R., and Di Felice, F., "Mechanisms of evolution of the propeller wake in the transition and far fields," *Journal of Fluid Mechanics*, Vol. 682, 2011, pp. 5–53. DOI: 10.1017/jfm.2011.150.

[101] Marshall, J. S., and Yalamanchili, R., "Vortex cutting by a blade. II - Computations of vortex response," *AIAA Journal*, Vol. 32, No. 7, 1994, pp. 1428–1436. DOI: 10.2514/3.12212.

[102] Marshall, J. S., "Vortex cutting by a blade. I - General theory and a simple solution," *AIAA Journal*, Vol. 32, No. 6, 1994, pp. 1145–1150. DOI: 10.2514/3.12113.

[103] Marshall, J. S., and Grant, J. R., "Penetration of a blade into a vortex core: vorticity response and unsteady blade forces," *Journal of Fluid Mechanics*, Vol. 306, 1996, pp. 83–109. DOI: 10.1017/S0022112096001243.

[104] Obert, E., "A Method for the Determination of the Effect of Propeller Slipstream on the Static Longitudinal Stability and Control of Multi-Engined Aircraft," Report LR-761, Delft University of Technology, 1994. URL https://repository.tudelft.nl/record/uuid:547ca83f-5b6b-4234-b580-b3cb82177294.

**B**

[105] Bouquet, T., and Vos, R., "Modeling the Propeller Slipstream Effect on Lift and Pitching Moment," *55th AIAA Aerospace Sciences Meeting*, American Institute of Aeronautics and Astronautics, Reston, Virginia, 2017. DOI: 10.2514/6.2017-0236.

[106] Barara, D., Sluis, M. V., and Sinnige, T., "Impact of Installation Effects on Optimal Propeller Design : Application to a Boundary-Layer-Ingesting Propeller," *AIAA Aviation Forum and ASCEND co-located Conference Proceedings*, American Institute of Aeronautics and Astronautics, Las Vega, NV, 2024, pp. 1–15. DOI: 10.2514/6.2024-3522.

[107] Öhman, L. H., "Torque and Thrust from Five-Hole Pressure Probe Measurements in the Near Slipstream of a Propeller in Compressible Flow," NRC report IAR-AN-81, National Research Council Canada, Ottawa, Canada, 1995.

[108] Agrawal, D. R., Asad, F., Berk, B., Long, T., Lubin, J., Courtin, C., Drela, M., Hansman, R. J., and Thomas, J., "Wind Tunnel Testing of a Blown Flap Wing," *AIAA Aviation Forum*, American Institute of Aeronautics and Astronautics, Dallas, Texas, 2019, pp. 1–20. DOI: 10.2514/6.2019-3170.

[109] de Vries, R., van Arnhem, N., Avallone, F., Ragni, D., Vos, R., Eitelberg, G., and Veldhuis, L. L., "Aerodynamic Interaction Between an Over-the-Wing Propeller and the Wing Boundary-Layer in Adverse Pressure Gradients," *AIAA Aviation Forum*, American Institute of Aeronautics and Astronautics, Dallas, Texas, 2019, pp. 1–19. DOI: 10.2514/6.2019-3035.

[110] Aljabri, A., Lyman, V., and Parker, R., "Evaluation of propeller/nacelle interactions in the PTA program," *22nd Joint Propulsion Conference*, American Institute of Aeronautics and Astronautics, Reston, Virigina, 1986. DOI: 10.2514/6.1986-1552.

[111] Jones, P. K., Boughton, T. B. A., Ketley, G. R., Mitchell, D. J., and Sinton, N. D., "Introduction To Installation Effects on Thrust and Drag for Propeller-Driven Aircraft," ESDU Data Item 85015, Engineering Sciences and Data Unit, 2006.

[112] Stokkermans, T., "Aerodynamics of Propellers in Interaction Dominated Flowfields," Phd thesis, Delft University of Technology, 2019. DOI: 10.4233/uuid, URL https://resolver.tudelft.nl/uuid:46178824-bb80-4247-83f1-dc8a9ca7d8e3.

[113] Eggleston, B., "Some Considerations in Propeller and Airframe Integration," Paper 18 18, Advisory Group for Aerospace Reserach and Development, 1984. DOI: 10.1063/1.3066038.

[114] Radespiel, R., Heinze, W., and Bertsch, L., "High-Lift Research for Future Transport Aircraft," *66. Deutscher Luft- and Raumfahrtkongress (DLRK)*, 2017, pp. 1–15.

[115] Plijter, J., "Aerodynamic Interaction Effects Between a Propeller Slipstream and Flap Boundary Layer," Msc thesis, Delft University of Technology, 2023. URL https://resolver.tudelft.nl/uuid:2eabfd64-0be9-401b-8a23-9c4d01833f34.

[116] Nederlof, R., "Improved modeling of propeller-wing interactions with a lifting-line approach," Msc thesis, Delft University of Technology, 2020.

[117] Allen, H. J., and Vincenti, W. G., "Wall interference in a two-dimensional-flow wind tunnel, with consideration of the effect of compressibility," NACA Technical Report 782, National Advisory Committee of Aeronautics, 1944.

[118] Yon, S. A., and Katz, J., "Study of the unsteady flow features on a stalled wing," *AIAA Journal*, Vol. 36, No. 3, 1998, pp. 305–312. DOI: 10.2514/2.372.

[119] Broeren, A. P., and Bragg, M. B., "Spanwise variation in the unsteady stalling flow-fields of two-dimensional airfoil models," *AIAA Journal*, Vol. 39, No. 9, 2001, pp. 1641–1651. DOI: 10.2514/2.1501.

[120] Winkelmann, A. E., and Barlow, J. B., "Flowfield model for a rectangular planform wing beyond stall," *AIAA Journal*, Vol. 18, No. 8, 1980, pp. 1006–1008. DOI: 10.2514/3.50846.

[121] de Vries, R., Sinnige, T., and Veldhuis, L. L., "Aerodynamic Performance and Interaction Effects of an Over-the-Wing Distributed-Propeller System in Cruise Conditions," *Proceedings of the 34th Congress of the International Council of Aeronautical Sciences*, International Council of the Aeronautical Sciences, Florence, Italy, 2024, pp. 1–29.

[122] Braslow, A. L., and Knox, E. C., "Simplified Method for Determination of Critical Height of Distributed Roughness Particles for Boundary-Layer Transition at Mach Numbers from 0 to 5," NACA Technical Note 4363, National Advisory Committee for Aeronautics, Langley Field, Va., 1958.

[123] Eça, L., and Hoekstra, M., "A procedure for the estimation of the numerical uncertainty of CFD calculations based on grid refinement studies," *Journal of Computational Physics*, Vol. 262, 2014, pp. 104–130. DOI: 10.1016/j.jcp.2014.01.006.

[124] Roache, P. J., "Quantification of uncertainty in computational fluid dynamics," *Annual Review of Fluid Mechanics*, Vol. 29, 1997, pp. 123–160. DOI: 10.1146/annurev.fluid.29.1.123.

# ACKNOWLEDGEMENTS

This chapter is only included in the printed version of this dissertation.

# Curriculum Vitæ

## Ramon Robert Duivenvoorden

27-07-1992      Born in Uden, The Netherlands.

## Research & Work Experience

2020–2024      **PhD Candidate**
*Delft University of Technology, Delft, The Netherlands*
*Technical University of Braunschweig, Braunschweig, Germany*
Dissertation: "*Aerodynamic Phenomena of Propeller-Wing-Flap Interaction*".
Promotor: Prof. dr. ir. Leo L. M. Veldhuis
Co-promotor: Dr. ir. Tomas Sinnige
External supervisor: Prof. Dr.-Ing. Jens Friedrichs

2019–2020      **Project Engineer**
*Stolthaven Terminals, Rotterdam, The Netherlands*

2016–2019      **Student IT Desk**
*Delft University of Technology, Delft, The Netherlands*

2014–2015      **Jr. Performance Engineer**
*Maserati, Modena, Italy*

# EDUCATION

| | |
|---|---|
| 2020–2024 | Doctoral Education Programme<br>*Delft University of Technology, Delft, The Netherlands* |
| 2015–2019 | M.Sc. Aerospace Engineering<br>*Delft University of Technology, Delft, The Netherlands* |

2015–2019   M.Sc. Aerospace Engineering
*Delft University of Technology, Delft, The Netherlands*
*Thesis:*        Rotorcraft Formation Flight for Aerodynamic Benefit
*Supervisors:*   Prof. dr. ir. Mark Voskuijl
                 Prof. dr. ir. Carlos Simão Ferreira

2011–2014   B.Sc. Aerospace Engineering
*Delft University of Technology, Delft, The Netherlands*

Exchange programme
*Iowa State University, Ames, IO, United States of America*

2004–2010   Gymnasium
*Gymnasium Bernrode, Heeschwijk-Dinther, The Netherlands*

# AWARDS

2020   Best Paper in Aerodynamics Session
*Awarded by the Vertical Flight Society at the VFS 76th Annual Forum &*
*Technology Display, October 6-8, 2020*

# LIST OF PUBLICATIONS

## JOURNAL ARTICLES

4. R.R. Duivenvoorden, A.F.P. Ribeiro, T. Sinnige and L.L.M. Veldhuis, *Slipstream Deformation in Propeller-Wing-Flap Aerodynamic Interaction.* (Under review)

3. R.R. Duivenvoorden, T. Sinnige and L.L.M. Veldhuis, *Impact of Helix Characteristics on Slipstream Deformation in Propeller-Wing-Flap Interaction*, AIAA Journal. (Accepted, awaiting publication)

2. R.R. Duivenvoorden, T. Sinnige, J. Friedrichs and L.L.M. Veldhuis, *Multi-Element Airfoil in Jet Flows: Identifying Dominant Factors and Interactions*, Journal of Aircraft **61 (5)**, p. 1517-1534, 2024, doi:10.2514/1.C037741.

1. R.R. Duivenvoorden, M. Voskuijl, L. Morée, J. de Vries and F. van der Veen, *Numerical and Experimental Investigation into the Aerodynamic Benefits of Rotorcraft Formation Flight*, Journal of the American Helicopter Society **67 (1)**, p. 1-17, 2020, doi:10.4050/JAHS.67.012011

## CONFERENCE PAPERS

6. J.C. Plijter, R.R. Duivenvoorden and T. Sinnige, *Aerodynamic Interaction Effects Between a Propeller Slipstream and Single Slotted Flap by a High-Fidelity URANS Simulation*, 2025 AIAA SciTech Forum, Orlando, FL, January 6-10, 2025.

5. R.R. Duivenvoorden, F. do N. Monteiro, T. Sinnige and L.L.M. Veldhuis, *Experimental Measurements of Slipstream Deformation for an Installed Distributed Propeller Configuration*, 34th Congress of the International Council of the Aeronautical Sciences, Florence, Italy, September 9-13, 2024.

4. F. do N. Monteiro, R.R. Duivenvoorden, D. Ragni, T. Sinnige and F. Avallone, *Experimental Analysis of Synchrophasing Impact on Noise of Distributed Propeller Systems in Tractor Configuration*, 30th AIAA/CEAS Aeroacoustics Conference, Rome, Italy, June 4-7, 2024, doi:10.2514/6.2024-3421.

3. A.F.P. Ribeiro, R.R. Duivenvoorden and D. Martins, *High-Fidelity Simulations of Propeller-Wing Interactions in High-Lift Conditions*, AIAA Aviation 2023 Forum, San Diego, CA, June 12-17, 2023, doi:10.2514/6.2023-3541.

2. R.R. Duivenvoorden, N. Suard, T. Sinnige and L.L.M. Veldhuis, *Experimental Investigation of Aerodynamic Interactions of a Wing with Deployed Fowler Flap under Influence of a Propeller Slipstream*, AIAA Aviation 2022 Forum, Chicago, IL, June 27-1, 2022, doi:10.2514/6.2022-3216.

1. R.R. Duivenvoorden, M. Voskuijl, L. Morée, J. de Vries and F. van der Veen, *Numerical and Experimental Investigation into the Aerodynamic Benefits of Rotorcraft Formation Flight*, Vertical Flight Society's 76th Annual Forum and Technology Display, Virginia Beach, VA, October 6-8, 2020.